UNIVERSIDADE DE LISBOA
INSTITUTO SUPERIOR TÉCNICO

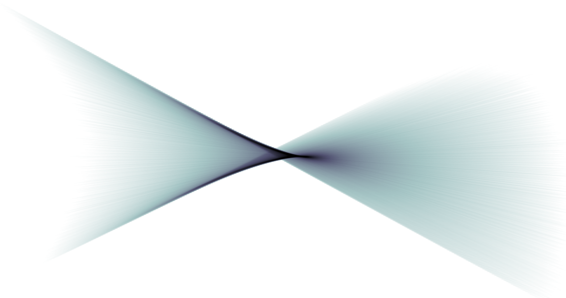

Plasma Light Sources: A Spatiotemporal Analysis

Miguel José Ferreira Pardal

Supervisor : Doctor Jorge Miguel Ramos Domingues Ferreira Vieira
Co-Supervisor : Doctor Ricardo Parreira de Azambuja Fonseca

Thesis approved in public session to obtain the PhD Degree in
Technological Physics Engineering

Jury final classification: Pass with Distinction and Honour

2024

UNIVERSIDADE DE LISBOA
INSTITUTO SUPERIOR TÉCNICO

Plasma Light Sources: A Spatiotemporal Analysis

Miguel José Ferreira Pardal

Supervisor : Doctor Jorge Miguel Ramos Domingues Ferreira Vieirae
Co-Supervisor : Doctor Ricardo Parreira de Azambuja Fonseca

Thesis approved in public session to obtain the PhD Degree in Technological Physics Engineering

Jury final classification: Pass with Distinction and Honour

Jury

Chairperson: Doctor Luís Miguel de Oliveira e Silva, Instituto Superior Técnico, Universidade de Lisboa;

Members of the Committee:

Doctor Luís Miguel de Oliveira e Silva, Instituto Superior Técnico, Universidade de Lisboa;
Doctor Olle Lundh, Department of Physics, Lund University, Sweden;
Doctor Jorge Miguel Ramos Domingues Ferreira Vieira, Instituto Superior Técnico, Universidade de Lisboa;
Doctor Xavier Davoine, Commissariat à l'Energie Atomique et aux Energies Alternatives (CEA), DAM, DIF, France.

Funding Institution
FCT: Fundação para a Ciência e a Tecnologia

2024

Abstract

State-of-the-art X-ray sources such as Free Electron Lasers and synchrotrons allow probing and imaging ultra-fast processes occurring at the tiniest atomic and molecular scales. These sources are large scale devices, typically on the order of a few kilometers. Recently, efforts have been made to develop smaller and more cost-effective solutions, mostly based on beam-plasma interactions. In this thesis, we explore plasma-based radiation sources using theory and Particle-In-Cell simulations, relying on the possibilities opened by the recent discovery of Generalized Superradiance to propose new methods of generating intense ultra-short, high frequency pulses of radiation. Namely, we investigated radiation coming from particles that cross evanescent fields. These surface modes are common in laser-plasma interaction experiments. We took direct advantage of the extreme spatial localization of evanescent waves to generate directed x-rays and demonstrate, that electrons with $\gamma \simeq 10-100$ that scatter across an evanescent wave can produce keV-MeV radiation. Furthermore, we showed that, the intersection position between the electron bunch and the evanescent wave can act as a virtual particle. In the right conditions, this virtual particle can be superluminal and can produce a superradiant optical shock.

Additionally, we explored coherent betatron radiation through generalized superradiance. Where a spatiotemporal manipulation of the accelerated particle bunch can lead to superradiant emission. We showed that a particle beam with a sinusoidal modulation featuring a superluminal phase speed can produce optical shocks along the Cherenkov angle associated with the phase speed of the modulation. These optical shocks lead to ultra-short attosecond level pulses whose intensity grows quadratically with the number of particles in the beam, regardless of the interparticle distance. We relied heavily on RaDiO during the course of this thesis, and added several improvements to this code. Most importantly, we added GPU compatibility using the CUDA programming language. Utilizing a single GPU board, we achieve near-instantaneous radiation calculations across millions of spatial cells, a feat previously only achievable when using computer clusters housing hundreds of CPUs. This improvement allowed us to run many seemingly expensive radiation simulations in a local server with a single GPU board, opening up the possibility of seeing radiation at unprecedented spatial resolutions.

Keywords:
Plasma, Superradiance, Betatron, Evanescent, GPU

Resumo

As fontes de raios X mais avançadas, tais como os lasers de electrões livres e os sincrotrões, permitem sondar e obter imagens de processos ultra-rápidos que ocorrem às mais ínfimas escalas atómicas e moleculares. Estas fontes são dispositivos de grandes dimensões, normalmente da ordem de alguns quilómetros. Recentemente, têm sido feitos esforços para desenvolver soluções mais pequenas e económicas, maioritaraimente baseadas em feixe-plasma. Nesta tese, exploramos as fontes de radiação baseadas em plasma usando teoria e simulações Particle-In-Cell, baseando-nos nas possibilidades abertas pela recente descoberta da Superradiância Generalizada para propor novos métodos de geração de impulsos de radiação intensos, ultra-curtos e de alta frequência. Nomeadamente, investigámos a radiação proveniente de partículas que atravessam campos evanescentes. Estes modos de superfície são comuns em experiências de interação laser-plasma. Tirámos partido da localização espacial extrema das ondas evanescentes para gerar raios-X dirigidos e demonstrámos que os electrões com $\gamma \simeq 10-100$ que atravessam uma onda evanescente podem produzir radiação keV-MeV. Além disso, mostrámos que a posição de intersecção entre o feixe de electrões e a onda evanescente pode atuar como uma partícula virtual. Nas condições certas, esta partícula virtual pode ser superluminosa e produzir um choque ótico superradiante.

Além disso, explorámos a radiação coerente de betatrões através de superradiância generalizada. Onde uma manipulação espácio-temporal do feixe de partículas aceleradas pode levar à emissão superradiante. Mostrámos que um feixe de partículas com uma modulação sinusoidal com uma velocidade de fase superluminal pode produzir choques ópticos ao longo do ângulo de Cherenkov associado à velocidade de fase da modulação. Estes choques ópticos conduzem a impulsos ultra-curtos de nível de attossegundo cuja intensidade cresce quadraticamente com o número de partículas no feixe, independentemente da distância entre as partículas. Durante a realização desta tese, baseámo-nos fortemente no RaDiO e introduzimos várias melhorias neste código. Uma das mais importantes foi acompatibilidade com GPU utilizando a linguagem de programação CUDA. Utilizando uma única placa de GPU, conseguimos cálculos de radiação quase instantâneos em milhões de células espaciais, um feito que anteriormente só era possível quando se utilizavam clusters de computadores com centenas de CPUs. Esta melhoria permitiu-nos executar inúmeras simulações de radiação, anteriormente dispendiosas, permitindo observar a radiação a resoluções espaciais sem precedentes.

Palavras-Chave:

Plasma, Superradiância, Betatrão, Evanescente, GPU

Acknowledgments

This thesis contains research work performed during the past 4 years at the Group of Lasers and Plasmas of Instituto de Plasmas e Fusão Nuclear (GoLP/IPFN) in Instituto Superior Técnico (IST) of Universidade de Lisboa. It received funding from Fundação para a Ciência e Tencologia under grant agreement PD/BD/150411/2019.

I would like to express my deepest gratitude to all those who have contributed to the successful completion of this thesis. This journey has been filled with challenges and triumphs, and I could not have reached this point without the support and assistance of many individuals and organizations.

First and foremost, I want to thank my thesis advisor, Prof. Jorge Vieira, for his unwavering guidance, patience, and expertise. His mentorship has been invaluable throughout this research, and I am grateful for the countless hours he devoted to helping me shape my ideas and refine my work. I cannot thank him enough for giving me the freedom to follow my own research interests.

In this sense, I also extend my heartfelt appreciation to my co-supervisor, Prof. Ricardo Fonseca, for his crucial role in this thesis. His deep knowledge of the computational aspects of plasma simulations and High Performance Computing were instrumental in shaping the research and ensuring its success.

I am also indebted to the members of my thesis jury committee, for their thoughtful feedback and insightful suggestions. Their collective knowledge and dedication to my project greatly enriched the quality of this thesis.

In addition, I wish to acknowledge the numerous individuals with whom I shared ideas, engaged in meaningful discussions, and received valuable feedback, namely Prof. Chandrashekhar J. Joshi, Prof John Palastro, Dr. Igor Andriyash, Dr. Xinlu Xu, Dr. Kyle Miller. These interactions opened new perspectives, challenged my thinking, and helped shape the direction of my research. Collaborative discussions with colleagues, fellow students, and industry experts have played a significant role in the development of this work.

I would like to acknowledge the Group of Lasers and Plasmas and all its faculty and staff for providing me with a supportive academic environment and the resources necessary for conducting my research. Without their commitment to education and research, this thesis would not have been possible.

To my friends and colleagues who stood by me during this journey, I am profoundly grateful. Your encouragement, discussions, and camaraderie were essential in maintaining my motivation and enthusiasm for this work.

My family deserves special recognition for their support and belief in my abilities. They provided me with the love and encouragement needed to persevere through the most challenging times, and for that, I am profoundly thankful.

To Patricia, I am greatly thankful. For all your love and support, for always encouraging me to be better, for never letting me forget who I am, for always criticizing my work when I ask for opinions, for always praising it when I don't ask for opinions, and for always asking me to display my plots as works of art.

Finally, I am thankful to you, the reader, for showing interest in this topic, I hope you have a good time.

Contents

List of Figures

List of Tables

1

Introduction

Contents

1.1 Motivation

Understanding radiation from plasma sources is an endeavour that has kept the minds of physicists from virtually all fields busy for generations. In astrophysical scenarios, for example, the radiation observed from celestial sources provides invaluable insights into the intricate physical mechanisms operating under extreme conditions in the universe [1]. Meanwhile, in laboratory settings, radiative processes are fundamental to the development of advanced light sources [2, 3], which, in turn, serve as essential tools for probing and manipulating dynamics at the atomic and molecular scale [4].

These radiative processes often emerge as a consequence of collective effects associated with the dynamics of charged particles within plasmas. The conventional approach for modeling their behavior involves the Particle-In-Cell (PIC) scheme [5]. In its standard form, the PIC scheme makes no physical approximations and instead solves the complete set of Maxwell's equations, accounting for the complex interplay between electromagnetic fields and the relativistic Lorentz force experienced by the charged particles. This method stands as a cornerstone in the study of radiative processes, enabling a detailed understanding of the underlying physical principles governing these phenomena.

Accessing the radiation profile in time and space, however, is relevant and interesting in a number of fields and applications. For example, the spatiotemporal radiation profile can reveal the properties of rotating black holes [6, 7], and play an essential role in advanced microscopy based on twisted light with helical wavefronts [8]. Furthermore, accessing the spatiotemporal radiation profile provides a natural path to account for interference effects between the radiation emitted by all the particles, leading to built-in spatiotemporal coherence effects. The recently developed Radiation Diagnostic for OSIRIS (RaDiO) [9, 10] can retrieve the emitted spatiotemporal electromagnetic field structure of the emitted radiation in OSIRIS [11] simulations which are typically run with a high level of efficiency in most of the biggest CPU-based supercomputers in the world [12]

RaDiO has been successfully used in recent years to explore novel radiation generation mechanisms with great impact. A notable example is the study of generalized superradiance. Traditionally, superradiance is a phenomenon in which coherent photon emission occurs from a gas. It has crucial applications in atomic physics, quantum mechanics, and astrophysics. Superradiant light sources are powerful because the intensity of their beams scales with the square of the number of particles involved. In regular superradiance, this happens when the distance between emitting particles is much smaller than the photon wavelength. However, this recent research has revealed a new kind of superradiance that remains relevant even when the number of particles per wavelength approaches zero. This novel type of superradiance involves manipulating the spatiotemporal distribution of relativistic charged particle beams to create an optical shock along the Vavilov-Cherenkov angle in a vacuum. The shock concentrates broadband radiation into singular ultra-short, high intensity light pulses. This effect has identifiable experimental signatures and can be decisive in advanced light sources, atomic physics systems, and unlock coherent emission in plasma accelerators, paving the road to intense attosecond pulses.

Through this thesis, we aim to further explore and advance our comprehension of radiative processes in plasmas, seeking to develop a mechanism that can produce high frequency, broadband radiation in cost-effective way, especially focusing on superradiant regimes, while building upon the robust foundation of RaDiO, the Radiation Diagnostic for OSIRIS.

1.2 State of The Art

X-ray sources have a pivotal role in investigating and visualizing intricate, rapid microscopic phenomena. While Free Electron Lasers [13] and Synchrotrons [14–16] have been highly effective in this regard, endeavors to downsize these sources have the potential to significantly amplify their influence.

Plasma Wakefield Acceleration has been studied as an alternative to conventional particle acceleration since the 1970s [17]. Conventional radio-frequency accelerators are made of several individual accelerators that accelerate the moving particles by applying a synchronized electromagnetic field. The energy gained by the particles in these devices is directly linked to the maximum field applied at each accelerating unit, which is limited by the electrical breakdown [18], limiting the total energy gain. On the other hand, in plasma-based accelerators, the maximum field is no longer restrained by the electric breakdown limit, and higher energy gains are possible. The underlying mechanism consists in using a short and intense laser pulse or particle beam [19] to generate a plasma wake moving at almost the speed of light that is capable of accelerating particles to very high energies. The particles that undergo acceleration are subjected to extreme forces that can make them undergo the so-called betatron motion and radiate [20]. This radiation can be used as a diagnostic for the acceleration [21] or, if the conditions are right, betatron radiation from high-energy electrons ($\simeq 1$ GeV) accelerated by ultra-intense lasers ($a_0 > 1$) in laser plasma accelerators [22–26] can achieve keV x-ray beams [27], other applications include imaging biological samples (*e.g.* tomographic reconstruction of bone samples [28]), high energy density states (*e.g.* as in laser-solid interactions). In a plasma accelerator, the phase-space properties of the accelerated beams, such as the longitudinal momentum or radial dynamics, as well as the angular momentum degrees of freedom, can be potentially controlled using complex temporal wakefield modulations [29] and spatial shapes [30, 31]. Tailoring the wakefield topology [32] can have a vast impact in many fields, in particular, in light sources, where spatiotemporally structured light beams can help break the diffraction limit [4, 8].

Betatron radiation [20, 28, 33, 34] coming from compact laser-plasma accelerators can then play a key role in the efforts of miniaturizing these high-end sources, especially under coherent emission regimes. The Ion Channel Laser (ICL) [20, 35–41] provides a framework to produce temporally coherent Betatron x-rays but requires seeding the microbunching instability to modulate the particle bunch at the radiated wavelength. It was initially introduced in 1990 as a more compact alternative to the Free Electron Laser for the creation of intense and coherent high-energy radiation. Both Free Electron Lasers and Ion Channel Lasers depend on a phenomenon known as electron beam microbunching, which emerges from the intricate interaction between electrons and the radiation they emit during their transverse oscillations.

Apart from plasma wakefield acceleration, other laser-plasma based radiation sources have been investigated. For example, high harmonic generation by a plasma mirror [42–46] and Thomson scattering of plasma electrons [47–49], can lead to emission of harmonics up to the x-ray region of an ultra-intense laser pulse. Furthermore, ultra relativistic electrons can be used to obtain transition radiation in the x-ray region [50–53].

Despite being a promising alternative to FEL's and Synchrotrons, these mechanisms can be demanding in their own way. For example, it is possible to obtain Transition Radiation in the X-ray region, but only when ultra relativistic electrons are used [53]. Somewhat similarly, Betatron emission in laser plasma accelerators routinely produces keV x-ray beams [27], but requires electrons to be accelerated to ultra relativistic energies ($\lesssim 1$ GeV) which needs ultra-intense lasers ($a_0 \gtrsim 1$) [26]. The same limitation can be found in HHG by a plasma mirror [45, 46] and Thomson Scattering [47], where only the interaction of an ultra-intense laser pulse with the electrons can put in motion the non-linear processes that lead to the emission of harmonics of the laser pulse in the X-ray region.

Historically, approaches for characterizing radiation emissions in plasmas have primarily concentrated on their spectral properties. Notable examples include JRAD [54], which uses trajectories from PIC simulations to obtain the radiation spectrum, PIConGPU [55–57], capable of computing the emitted spectrum as the simulation progresses, and the QED module for OSIRIS [58], which models photon emission during the simulation using a Monte-Carlo approach. While these approaches have successfully predicted the radiation properties in both laboratory and astrophysical plasmas, they often lack insights into the spatiotemporal characteristics of emitted radiation. The recently developed Radiation Diagnostic for OSIRIS (RaDiO) [9, 10] allows for the study of radiation emission mechanisms under a different lens, looking into the influence of the spatiotemporal properties of the system in the emitted radiation within OSIRIS simulations. While these codes demonstrate high efficiency on most major CPU-based supercomputers worldwide [12], it is important to note that many supercomputing centers have embraced CPU-GPU hybrid solutions, with some of the largest machines being GPU-based [59]. Adapting RaDiO for GPUs can greatly enhance performance on these architectures. Therefore, in recent years, a number of efforts have been made in order to adapt OSIRIS to this sort of supercomputer so that we can take full advantage of the new architectures. The calculations associated with the radiation algorithm involve simple operations for each particle, which means that they can easily be performed by processors specialized in SIMD operations. Thus, adapting the radiation diagnostic for GPUs would allow the code to run efficiently in most supercomputers.

With previously existing tools the number of particles in the plasma mirror was one of the most prominent bottlenecks for the simulations, RaDiO on the other hand can retrieve radiation from a huge number of particles (potentially several orders of magnitude more than its predecessors), which allows us to tackle this problem more efficiently.

Currently, the radiation diagnostic is capable of calculating the spatiotemporal profile of the electromagnetic fields and potentials radiated by the particles during the OSIRIS simulation. However, the algorithm is completely general and could be implemented in any PIC code. A key step to ensure compatibility with other simulation codes would be to create a code-agnostic post-processing version that can use the trajectories provided by any code in a standard format to obtain radiation.

Some other much-needed improvements include compatibility features with other OSIRIS modules. Currently, it is only possible to obtain radiation from simulations in standard 1D, 2D and 3D geometries, but quasi-3D simulations lack support for radiative species. It is also not possible to selectively capture radiation from a subset of particles in a radiative species, forcing calculations to be performed in all the particles of the species. Additionally, up until now, we have considered scenarios where the energy radiated by the particles is negligible when compared to the particle kinetic energy, and the radiation diagnostic does not take into account particle deceleration by radiation emission. OSIRIS has a module that can take such factor into account. Still, it is not yet compatible with the radiation module; implementing this feature could lead to more realistic results.

Nevertheless, all of these necessities can be circumvented by calculation radiation in post-processing from a set of trajectories obtained using these features on OSIRIS.

1.3 Original Contributions

During the course of the doctoral programme, we explored several aspects of plasma based radiation sources, focusing on the concept of generalized superradiance. We investigated different sources where generalized superradiance could be used to achieve ultra-intense short pulses of broadband with special interest in the high frequency regions.

One of those sources was betatron radiation from plasma accelerated electrons, where we discovered that spatiotemporal manipulation of the accelerated particle bunch can lead to superradiant emission. We showed that a particle beam with a sinusoidal modulation featuring a superluminal phase speed can produce optical shocks along the Cherenkov angle associated with the phase speed of the modulation. These optical shocks lead to ultra-short attosecond level pulses whose intensity grows quadratically with the number of particles in the beam, regardless of the interparticle distance. Moreover, we showed that the spectrum of radiation at the Cherenkov angle is composed by a large number of high harmonics of the modulation wavelength.

Through theory and computer simulations, we arrived at the conclusion that this effect persists even when the quality of the modulation is non-ideal (for example in the case where the particle beam as an energy spread or temperature). Additionally, we demonstrated that it is possible to correctly modulate the particle beam by relying on resonant coupling between the betatron oscillations and the periodic force exerted by a co-propagating laser pulse with superluminal phase-speed. Our simulations show that such process is feasible in the wakeless regime of plasma wakefield acceleration, where a pure ion channel with no longitudinal accelerating is created by a high energy driver particle beam.

Our results suggest a method of enhancing betatron radiation, leading to a huge boost in radiated intensity, potentially elevating this radiation source to a higher level.

Furthermore, we investigated for the first time radiation coming from particles that cross evanescent fields like the ones present at the boundary between a laser and an overdense target. These surface modes are common in laser-plasma interaction experiments. Their degree of spatial localization in the direction normal to the surface is set by the material skin-depth λ_{ev}, which can be more than an order of magnitude smaller than the wavelength, $\lambda_0 = 2\pi c/\omega_0$, of the laser that excites the evanescent mode. We showed that interaction between a relativistic particle and these evanescent fields lead to the emission of an extremely short pulse of radiation, with a broad frequency spectrum.

Our proposed scheme presents a highly promising mechanism for the emission of high-frequency radiation. It exhibits a distinct spectral signature that holds great potential for experimental detection. The mechanism outlined in this thesis, which generates X-rays using moderately relativistic electrons as the sole energy source, opens up exciting avenues for further research. We took direct advantage of the extreme spatial localization of evanescent waves to generate directed x-rays and demonstrate, with theory and through particle-in-cell (PIC) simulations in Osiris [11, 60] complemented by the Radiation Diagnostic for Osiris (RaDiO) [10], that electrons with $\gamma \simeq 10-100$ that scatter across a surface wave can produce keV-MeV radiation.

We also found that electron bunches with certain spatial distributions can produce a superradiant optical shock. The creation of optical shocks by tilted electron bunches was investigated by Bolotowsky and Ginzburg in transition radiation [61], but here we show that, because the radiation from each bunch electron interferes constructively, its intensity scales quadratically with number of bunch particles as in superradiance. More generally, we found that the intersection position between the electron bunch and the evanescent surface can act as a virtual particle, whose trajectory defines key radiation properties, just as if it were a single real particle.

These results were obtained using the recently developed radiation diagnostic for OSIRIS, which we developed as a result of a master's thesis. Nevertheless, we added several improvements to this code during the course of this doctoral programme.

In our efforts to enhance the reliability and stability of RaDiO, we dedicated time to debug and add important features. This work has improved code quality and reduced unexpected errors, resulting in an enhanced user experience.

We made substantial changes to the post-processing version of RaDiO to better integrate it with the OSIRIS framework, adopting OSIRIS-style input decks and standardizing file I/O methods. Furthermore, we added OpenPMD support, allowing the code to read trajectory files from other PIC codes. This increased the versatility and compatibility of post-processing version of RaDiO, leading to its rebranding as RaDi-x.

We also integrated additional features into the run-time version, enhancing compatibility with other OSIRIS simulation modes and optimizing performance. In collaboration with the UCLA group, particularly with Kyle Miller, we optimized parallelization and added support for batch processing of particles on the CPU, resulting in a significant overall performance improvement. To further enhance the developing experience, we prioritized improving code readability to facilitate development, customization, and troubleshooting.

Additionally, we introduced the option to select a subset of radiative species for calculations and model radiation from ionized particles during simulations, expanding research possibilities. Moreover, we also introduced support for RaDiO in quasi-3D simulations, providing users a new simulation mode for their radiation simulations.

Lastly, one of the major improvements in RaDiO was the addition GPU compatibility. The GPU version of the code stands as a formidable instrument, introducing new opportunities for exploring radiation emission within Particle in Cell (PIC) codes, especially when dealing with large spatial detectors.

Utilizing a single GPU board, we achieve near-instantaneous radiation calculations across millions of spatial cells, a feat previously only achievable when using computer clusters housing hundreds of CPUs.

The research work performed during the course of these past 4 years resulted in several scientific publications, some of which are still in preparation or under the review process in a journal:

- M. Pardal, R. A. Fonseca, J. Vieira, *Superrdiance in the Ion Channel Laser*, in preparation (2023)

- M. Pardal, R. A. Fonseca, J. Vieira, *Superrdiant scattering from evanescent waves*, submitted (2023)

- M. Pardal, A. Sainte-Marie, A. Reboul-Salze, R. A. Fonseca, and J. Vieira, *Radio: An efficient spatiotemporal radiation diagnostic for particle-in-cell codes*, Computer Physics Communications, vol. 285, p. 108634, 4 (2023)

- J. Vieira, M. Pardal, J. T. Mendonça, and R. A. Fonseca, *Generalized superradiance for producing broadband coherent radiation with transversely modulated arbitrarily diluted bunches*, Nature Physics, vol. 17, no. 1, pp. 99–104 (2021).

- B. Malaca, M. Pardal, D. Ramsey, J. R. Pierce, K. Weichman, I. A. Andriyash, W. B. Mori, J. P. Palastro, R. A. Fonseca, and J. Vieira, *Coherence and superradiance from a plasma-based quasiparticle accelerator*, Nature Photonics, (2023).

- D. Ramsey, B. Malaca, A. Di Piazza, M. Formanek, P. Franke, D. H. Froula, M. Pardal, T. T. Simpson, J. Vieira, K. Weichman, and J. P. Palastro, *Nonlinear Thomson scattering with ponderomotive control*, Physical Review E 105, 065201 (2022)

It also resulted in several scientific presentations in international conferences:

- M. Pardal *et al.*, *Radiation Diagnostic for OSIRIS: Applications in coherent betatron emission*. **Invited** talk presented at the Laser Plasma Accelerator Workshop in Lagos, Algarve, Portugal, March 2023

- M. Pardal *et al.*, *Radiative reflection: high frequency radiation emission using evanescent light waves in plasma mirrors*. **Invited** talk Presented at the LPA Seminars, Online, June 2021

- M. Pardal *et al.*, *Capturing high frequency radiation coming from extreme scenarios in OSIRIS*. **Invited** talk presented at the AAC Seminar Series, Online, December 2020

- M. Pardal *et al.*, *Superradiance in the Ion Channel Laser*. Talk presented at the 65th Annual Meeting of the APS Division of Plasma Physics, Denver, Colorado, USA, October 2023

- M. Pardal *et al.*, *Radiation Diagnostic for OSIRIS: Applications in coherent betatron emission*. Talk presented at the Advanced Accelerator Concepts Workshop in Long Island, New York, USA, November 2022

- M. Pardal *et al.*, *Superradiant X-ray Emission in Ion Channels*. Talk presented at the 48th EPS Conference on Plasma Physics, Online, July 2022

- M. Pardal *et al.*, *Superradiant x-ray emission in nonlinear plasma wakefields*. Talk presented at the 63rd Annual Meeting of the APS Division of Plasma Physics, Online, November 2021

- M. Pardal *et al.*, *Broadband radiation from electrons in evanescent fields*. Poster presented at the 47th EPS Conference on Plasma Physics, Online, June 2021

- M. Pardal *et al.*, *Radiative reflection: high frequency radiation emission using evanescent light waves in plasma mirrors*. Talk presented at the 62nd Annual Meeting of the APS Division of Plasma Physics, Online, November 2020

1.4 Thesis Outline

This Thesis features computational and theoretical work developed during the past 4 years at the Group of Lasers and Plasmas in IST. It has three main chapters, each corresponding to a publication as first author in a peer-reviewed journal as first author, either already published, under review or in preparation.

Chapter 2 presents a detailed description of the radiation algorithm, focusing on its implementation both for CPUs and GPUs as well as presenting a description of all the new features that were developed. It also provides several usage examples, benchmarks and comparisons with theoretical expectations and similar radiation codes.

Chapter 3 contains the study of a previously unexplored type of radiation which we called evanescent radiation. This kind of radiation is emitted when a particle crosses an extremely localized evanescent field. Here, we explore the key features of this kind of radiation and show how it could reach high frequency emission. In this chapter, we also find that particle beams with certain spatiotemporal modulations can emit superradiant evanescent radiation.

In Chapter 4, we explore the possibility of achieving superradiant betatron emission. There, we present a new method of resonantly shaping a particle beam into a sinusoidal shape with superluminal phase velocity. We then show that a particle beam under such conditions emits superradiant light at the Cherenkov angle associated with the phase speed of the modulation and find that, theoretically, near attosecond ultra intense pulses could be obtained using this method. Finally, we investigate the robustness of the method under non-ideal conditions, and find that superradiance still happens even when the modulation is not perfect.

In Chapter 5 we conclude and point future directions of research.

2

RaDiO

Contents

2.1 Introduction

Radiative processes in plasma are ubiquitous in astrophysics [6] and in laboratory settings. In plasma acceleration experiments, for example, they are important to the development of compact light sources [20], commonly employed in probing ultra-fast processes. Radiation emission mechanisms in plasma result from collective effects associated with the self-consistent dynamics of a large number of charged particles in the presence of strong electric and magnetic fields. *Ab-initio* numerical models, that can capture the motion of single particles, play an important role in this context, not only to validate theoretical advances, but also to predict radiation emission from experiments and in conditions where analytical models are not available.

Among the different numerical techniques, the Particle-in-Cell (PIC) [5] scheme provides a standard model to compute the motion of ensembles of charged particles. In its standard version, the PIC scheme consists in a loop that iteratively computes electric and magnetic fields by solving a discretized version of the full set of Maxwell's equations in a grid, and then determines the next positions of the charged particles according to the relativistic Lorentz force. PIC codes are thus capable, by design, to retain most classical radiation emission processes.

The resolution required to capture radiation in the PIC algorithm poses quite stringent limitations on the shortest wavelengths that can be captured directly in a simulation, given that increasing the grid resolution will lead to a significant increase in the computational load. Consider a relativistic charged particle, with relativistic factor γ_p, undergoing a periodic motion with period T: The corresponding radiation wavelength, λ_{rad}, is proportional to $\lambda_{\mathrm{rad}} \propto cT/\gamma_p^2$ Hence, the spatial resolution required to capture λ_{rad} is γ_p^2 times higher than the resolution needed to describe the particle trajectory. Furthermore, because of the Courant–Friedrichs–Lewy condition, the required temporal resolution is also γ_p^2 higher than standard. This results in an increase of γ_p^4 operations per simulation, pushing the limits of current computational capabilities, thereby motivating the development of advanced algorithms to compute radiation emission in PIC codes.

The standard approach to avoid the increased computational load and obtain high-frequency radiation emission from PIC simulations consists in performing additional radiation calculations outside the PIC loop using particle trajectory information obtained with the PIC algorithm. Many simulation codes have been developed over the recent years following this strategy. The code JRAD [54] receives a set of charged particle trajectories in order to compute the radiated spectra from the Fourier transform of the Liénard-Wiechert potentials; PIConGPU [55–57] follows a similar strategy, but can compute the emitted spectrum as the simulation progresses; the PIC codes OSIRIS [11] and EPOCH employ Monte-Carlo approaches to compute the spectrum of radiation from QED processes at run time (see, e.g. Ref. [58]). These tools have been successfully used to predict the radiation properties of laboratory plasmas (in plasma based accelerators [27]), Quantum Electrodynamics [62] and astrophysical plasmas.

However, the spatiotemporal profile of radiation is also important in fields such as astrophysics, where it can reveal the properties of rotating black holes [6, 7] for example. It can also play an important role in advanced microscopy based on twisted light with helical wavefronts [8]. Furthermore, this approach also

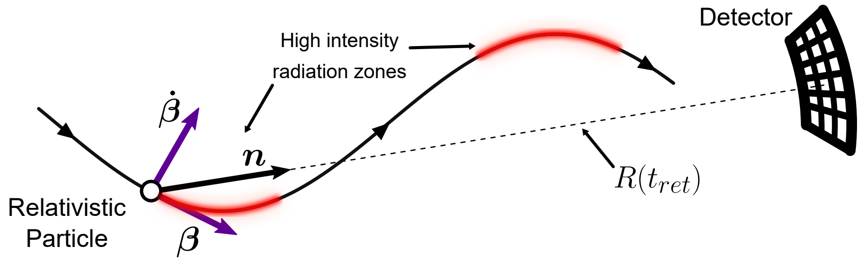

Figure 2.1: Illustration of the geometry of the radiation emission process and relevant quantities.

provides a natural description of orbital angular momentum of light. To address this, we propose a new algorithm that retrieves the spatiotemporal radiation profile instead of its spectrum. This complementary approach includes built-in spatial and temporal coherence effects that are important to describe unexplored features of radiation emission, such as superradiant emission [63], for example. Our scheme can be used whenever the charged particle motion is well resolved, regardless of whether the spatial or temporal resolution is sufficient to resolve the resulting electromagnetic radiation.

The PIC simulation framework provides a direct and natural application to our present work and we focused on the implementation of this algorithm into the OSIRIS code naming our tool RaDiO, which stands for Radiation Diagnostic for OSIRIS. This diagnostic is composed of two distinct but equally useful counterparts: one implemented as a post-processing tool that uses previously generated trajectories to find the radiation that was emitted along them, and the other implemented as a run-time diagnostic for the PIC code OSIRIS, that uses the simulation data at each time step to compute the radiation.

This paper is structured as follows. In Section 2.2, we describe the theoretical framework behind radiation emission processes, which lays the groundwork for the development of the algorithm. Section 2.3 describes the implementation of the algorithm in detail, exploring key aspects like the temporal interpolation scheme. In Section 2.4, we benchmark our code against theoretical predictions and the results obtained with other radiation codes. Section 2.5 contains the study of the radiation emitted during the reflection of laser pulses by a plasma mirror. And, finally, Section 2.7 presents the conclusions.

2.2 Spatiotemporal electromagnetic field structure

The Fourier transformed Liénard-Wiechert fields [64] are commonly employed to predict the radiation spectra from charged particle trajectories. Here, instead, we calculate the Liénard-Wiechert fields directly, as these formulas provide the emitted electromagnetic fields at a certain position in space-time. The spatiotemporal Electric (**E**) and Magnetic (**B**) field structure of the radiation emitted by a charged particle according to the Liénard-Wiechert formulas is given by:

$$\begin{aligned}
\mathbf{E}(\mathbf{x},t_{det}) &= e\left[\frac{\mathbf{n}-\boldsymbol{\beta}}{\gamma_p^2(1-\boldsymbol{\beta}\cdot\mathbf{n})^3R^2}\right]_{\text{ret}} + \frac{e}{c}\left[\frac{\mathbf{n}\times[(\mathbf{n}-\boldsymbol{\beta})\times\dot{\boldsymbol{\beta}})]}{(1-\boldsymbol{\beta}\cdot\mathbf{n})^3R}\right]_{\text{ret}}, \\
\mathbf{B}(\mathbf{x},t_{det}) &= [\mathbf{n}\times\mathbf{E}]_{\text{ret}},
\end{aligned} \tag{2.1}$$

with $\gamma_p = 1/\sqrt{1-\beta^2}$. In Equation (2.1), the subscript ret denotes calculations using values at the retarded time, $\mathbf{n}$ is the unit vector oriented from the particle position to the region in space where we are interested in capturing the emitted radiation. The virtual region in space-time where radiation is deposited is henceforth denoted as the *detector* and will be described in more detail in Section 2.3. In addition, $\boldsymbol{\beta} = \mathbf{v}/c$ and $\dot{\beta} = \dot{\mathbf{v}}/c$ are respectively, the particle velocity normalized to the speed of light, c and the corresponding acceleration. Here the dot represents the time derivative. The direction of $\boldsymbol{\beta}$ and $\dot{\boldsymbol{\beta}}$ with respect to the virtual detector and $\mathbf{n}$ are schematically represented in Figure 2.1. Moreover, e is the electron charge and the quantity R is the distance from the particle to the detector. For the purpose of determining the radiated fields, the first term in Equation (2.1) can be dropped if $R\gamma_p^2\dot{\beta}/c \gg 1$. This condition is usually satisfied in the far field ($R \gg c/\dot{\beta}$) for sufficiently relativistic particles ($\gamma_p \gg 1$). The second term in Equation (2.1) thus corresponds to emission of propagating electromagnetic waves, describing the so-called acceleration fields.

Equation (2.1) describes the emitted electric, $\mathbf{E}$, and magnetic, $\mathbf{B}$, fields at a given position, x and time t, calculated from quantities obtained at the retarded time t_{ret}. For a given light ray that reaches the detector at a time t_{det}, t_{ret} is the instant of time when emission has occurred. The time of arrival t_{det} is given by:

$$t_{det} = t_{ret} + |\mathbf{r}_{part} - R_{cell}\mathbf{n}_{cell}|/c, \tag{2.2}$$

where $\mathbf{r}_{part}$ is the position of the particle and $R_{cell}\mathbf{n}_{cell}$ is the position of the detector's cell. In order to enhance computational performance, it is useful and possible to simplify Equation (2.2) in the far field, which gives [64]:

$$t_{det} = t_{ret} + R_{cell}/c - \mathbf{r}_{part} \cdot \mathbf{n}_{cell}/c, \tag{2.3}$$

Supplemented by the additional conditions given by Equations. (2.2-2.3), Equation. (2.1) can thus be used to retrieve the full set of spatiotemporal degrees of freedom of the radiation emitted by accelerated charges. By mapping the emitted radiation at each timestep in the particle trajectory to the corresponding time of arrival at the detector, the actual temporal resolution of the relativistic particle trajectory can be much coarser than the required one to describe the radiated fields.

An estimate of the maximum temporal resolution that can be accurately obtained using Equations (2.2-2.3) can be found using the simplified picture shown in Figure 2.2: The particle located at x_0 emits a photon 1 at $t = t_0$. As the photon travels at c, in the next time step it will have travelled an extra $dt(\mathrm{c} - v_p)$ than the particle, which emits a second photon at $t = t_1$. Considering that a particle emits a photon at every time-step, the time interval between the arrival of two consecutive photons at the detector, provided that they are emitted by a relativistic particle, is given by Equation (2.4):

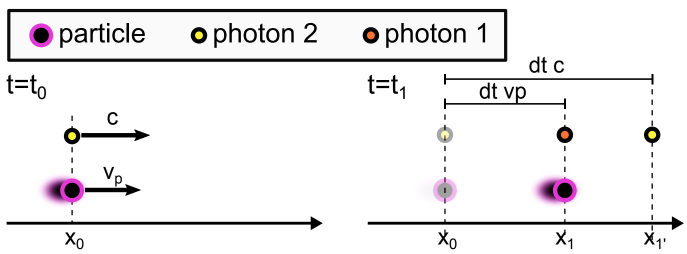

Figure 2.2: Illustration of radiation emission.

$$dt_{rad} = dt(1 - v_p/c) \simeq dt/\left(2\gamma_p^2\right), \tag{2.4}$$

with dt being the temporal distance between emissions *i.e.* the temporal resolution of the simulation providing for the particle trajectory.

Therefore, we are able to capture radiation with frequencies up to $2\gamma_p^2$ times larger than the ones allowed by the time-step used to sample the particle's motion, as our detector time grid can be as fine as $dt_{\text{det}} = dt/2\gamma_p^2$. As a consequence, the simulation time step can be much larger than the typical period of the emitted radiation. It is also important to note that the resolution in the detector should not be increased indefinitely as resolving time grids finer than $dt/2\gamma_p^2$ could generate non-physical information.

The sampling frequency f_s required to capture a frequency ω in rad$/s$ is given by the Nyquist-Shannon theorem: $f_s > 2(\omega/2\pi)$. The sampling frequency of our virtual detector after the interpolation, is related to the resolution of its temporal grid dt_{det}: $f_s = 1/dt_{\text{det}}$. Therefore, the resolution in the detector required to accurately model a frequency ω is given by: $dt_{\text{det}} < \pi/\omega$.

The deposition time is obtained at each time step by computing the time that light takes to reach the detector cells from the particle's position. Thus, the sampling frequency before the interpolation can be slightly more complex. A particle with a trajectory described with a given dt will deposit radiation in steps of about $dt/(2\gamma_p^2)$. Therefore, the time resolution in the PIC simulation required to model a frequency ω in the detector is roughly given by $dt < \gamma_p^2 2\pi/\omega$.

Due to the natural variations in the particle's momentum and position throughout the simulation, these depositions will be unevenly spaced, so the interpolation scheme maps these depositions to the detector's discretized time grid. If the detector's time grid is much finer than the typical time between depositions, the interpolated field may contain nonphysical information. This is particularly adverse for our algorithm, which employs the simplest interpolation order, as it assumes a constant field between depositions.

The showcase this effect, we used the example of a particle undergoing a sinusoidal trajectory

$$\begin{cases} x(t) & = \beta_{x0}\left[t - \frac{r_\beta^2}{8\gamma_{x0}}\left(t - \frac{\cos(2\omega_\beta t)}{2}\right)\right] \\ y(t) & = r_\beta \cos\left(\omega_\beta t\right) \end{cases} \tag{2.5}$$

where β_{x0} is the initial velocity of the particle along the longitudinal x direction, $\gamma_{x0} = (1 - \beta_{x0}^2)^{-1/2}$ its

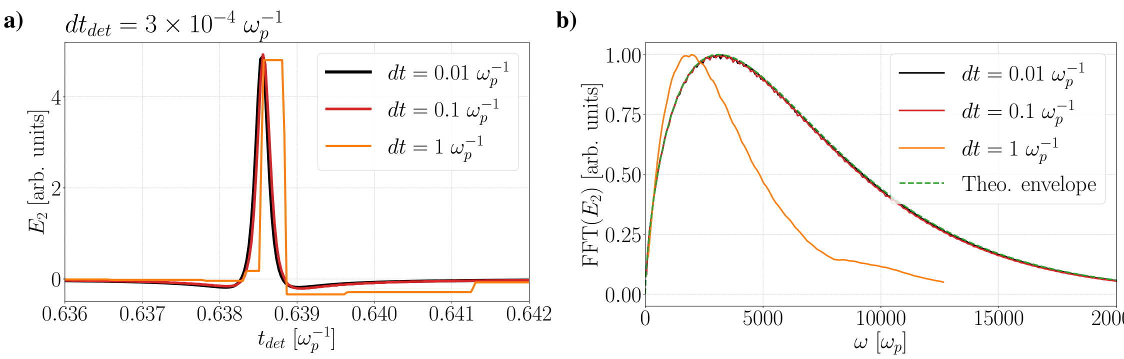

Figure 2.3: Comparison of the results from RaDiO for different temporal resolutions of the trajectory dt in the spatiotemporal domain (a) and in the spectral domain (b) superimposed with the theoretical prediction.

longitudinal Lorentz factor, r_β the amplitude of the sinusoidal trajectory, and ω_β its frequency. We used a relativistic electron ($\gamma_p = 50$) with an amplitude of $r_\beta = 2\,c/\omega_p$, $k_\beta = \omega_\beta/c = 0.1\,\omega_p/c$ in the transverse $x-y$ plane, where ω_p is a normalizing frequency. We simulated a line of a spherical detector, placed in the $z-x$ plane, $10^5\,c/\omega_p$ away from the axis origin with an angular aperture of 0.1 rad around the x axis. In this case, the spectrum extends to about $10\omega_c$ so the maximum dt allowed for the trajectory should be $dt_{max} = \gamma_p^2 2\pi/10\omega_c \simeq 0.4\ \omega_p^{-1}$. By varying the time resolution of the trajectory beyond the limits discussed above, we saw that the resulting radiation signal, together with the corresponding frequency spectrum could be heavily affected. The results are summarized in Figure 2.3.

The next section describes our implementation of the radiation algorithm and illustrates the reasons behind the different limits in resolution.

2.3 Algorithm and Implementation

The calculations of Equation (2.1) can be fully integrated either into a pre-existing code that computes the trajectories of charged particles (e.g. the PIC scheme) or be used as a post-processing tool that that computes Equation (2.1) on a set of pre-calculated trajectories. The algorithm consists of two main parts: calculating and obtaining the radiated fields and depositing them in a discretized grid. In this section we discuss the general steps and approach to incorporate the radiation algorithm considering these two components.

2.3.1 Radiation calculation algorithm

The virtual detector is a key feature of the radiation diagnostic. It is the region of space where radiation is tracked during a given time period. We consider two geometries of the virtual detector, (i) a spherical one Figure 2.4a, where the grid is defined using spherical coordinates ($\mathbf{e}_\theta, \mathbf{e}_\phi, \mathbf{e}_\mathbf{r}$) and (ii) a cartesian one Figure 2.4b, where the grid is defined using cartesian coordinates ($\mathbf{e}_\mathbf{x}, \mathbf{e}_\mathbf{y}, \mathbf{e}_\mathbf{z}$). RaDiO has the capability to compute the radiation in both types of geometries.

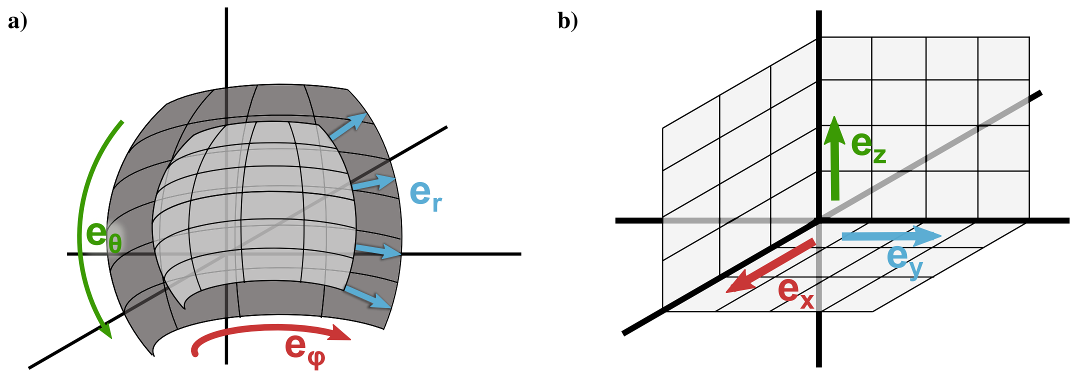

Figure 2.4: Spherical (a) and cartesian (b) detectors. The darker spherical grid has a higher radius than the lighter one. All spherical grids are centered in the origin of the coordinate system.

In order to track the emitted radiation at each time step of the trajectory we need to evaluate Equation (2.1) in every cell of the virtual detector. The radiation emitted at each time step of a given trajectory lies on a spherical shell that expands from the position of the particle at the time of emission, t_{ret}, at the speed of light. The intersection of the radiation shell with the detector consists of a circumference, whose radius increases with t_{det}. Figure 2.5 illustrates this picture, by showing the intersection of the radiation shell with a cartesian detector. The top of Figure 2.5 shows the detector at three different t_{det}. The bottom of Figure 2.5 shows the radiation arriving at each one of the highlighted cells as a function of t_{det}, which can be calculated using Equation (2.2) or Equation (2.3).

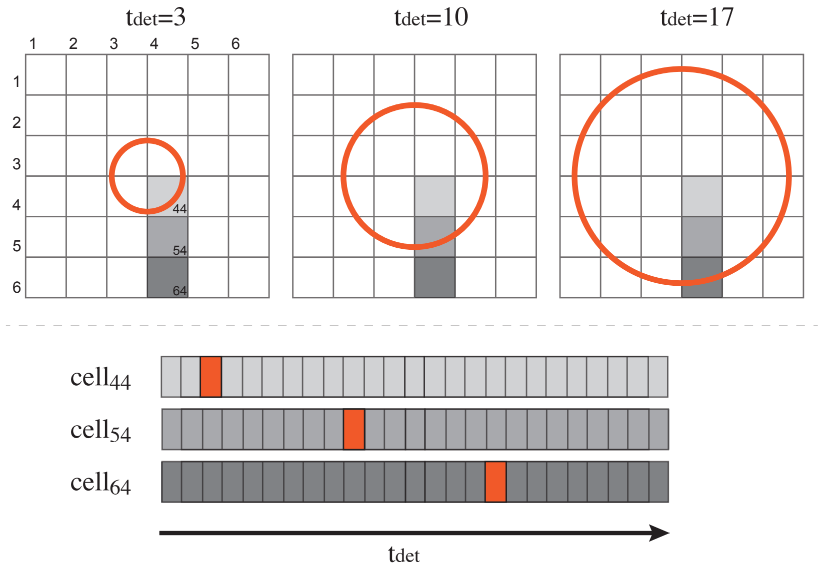

Figure 2.5: Visual representation of the arrival of radiation emitted by a single particle in a single time step of the simulation at a detector cartesian detector. Top panel: expansion of the intersection between the radiation shell and the detector (in orange). Bottom panel: Time of detection for three distinct cells of the detector.

The illustration of Figure 2.5 suggests a clear approach to track the radiation reaching the detector from the emission of one particle at a given time step t_{ret}: Loop through each spatial cell of the detector and to compute t_{det} at which radiation arrives. All the required quantities to compute Equation (2.1) are known or can be easily calculated (see additional details below). This approach features the quality of avoiding loops through the temporal cells in the detector. Thus, radiation computing time becomes independent of the temporal resolution of the detector and the total computing time is proportional to the number of time steps in the PIC simulation, $N_{\text{t\_PIC}}$ multiplied by the number of particles, N_{part} multiplied by the number of spatial cells in the detector, $N_{\text{sp\_cell}}$.

This approach is summarized in Algorithm 2.1. It comprises two different loops: one through the particles that emit radiation (denoted as radiative particles) and another through the detector spatial cells. The quantities t, R, $\mathbf{n}$, β, $\dot{\beta}$ and t_{det} are required in order to evaluate Equation (2.1). All of these quantities are either readily available or can be directly calculated from other quantities that are available in the simulation, such as the position of the particle ($\mathbf{x_{part}}$), the momentum of the particle ($\mathbf{p}$) and the time of emission t, as well as quantities that are part of the radiation module, such as the position of each detector cell $\mathbf{x_{cell}}$ or the previous velocity of the particle β_{prev}. These calculations are also shown in Algorithm 2.1.

Because t_{det} can be computed at each time of emission, t_{ret}, using Equation (2.2) or Equation (2.3), it is in principle possible to conceive a temporally gridless detector. This approach could provide a very accurate description of the radiated fields, particularly if complemented by a post-interpolation

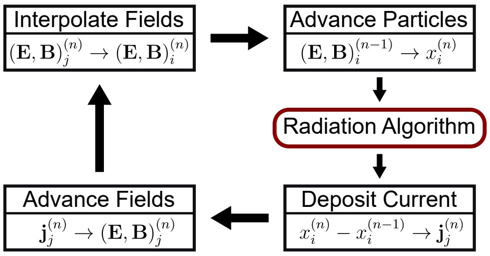

Figure 2.6: Placement of the radiation algorithm (Algorithm 2.1), performed at each time-step inside the PIC loop.

scheme with the goal of retaining the continuous nature of radiation emission. Such approach, however, would require storing as many spatial detector arrays as the number of steps in the particle trajectory, for every particle in the simulation ($N_{\text{t\_PIC}} \times N_{\text{part}} \times N_{\text{sp\_cell}}$). High memory consumption would thus be the main limitation of such algorithm. To face this issue, RaDiO deposits radiation in a grid detector with up to 3 dimensions (1 temporal dimension and up to 2 spatial dimensions) with the spatial cells being distributed according to a spherical or cartesian geometry, and uses a temporal interpolation scheme to mimic continuous radiation emission between two consecutive PIC time-steps for every particle in the simulation.

Algorithm 2.1 Radiation calculation and depositing

procedure RADIATIONCALCULATOR
  for all *particle* **in** simulation **do**
    $\beta = \text{velocity}(particle) = \mathbf{p}/\sqrt{|\mathbf{p}|^2+1}$
    $\dot{\beta} = \text{acceleration}(particle) = (\beta - \beta_{prev})/dt$
    for all *cell* **in** detector **do**
      $R = \text{distance}(particle, cell) = |\mathbf{x_{part}} - \mathbf{x_{cell}}|$
      $\mathbf{n} = \text{direction}(particle, cell) = (\mathbf{x_{part}} - \mathbf{x_{cell}})/R$
      $t_{det} = R/c + t$
      $t_{det,prev} = R_{prev}/c + t - dt$
      if $t_{\text{det}}min < t_{\text{det}} < t_{\text{det}}max$ **then**
        $\text{RADIATIONINTERPOLATOR}(\mathbf{E}(\mathbf{n}, \beta, \dot{\beta}), t_{\text{det}}, t_{\text{det,prev}})$
      end if
    end for
  end for
end procedure

The implementation shown in Algorithm 2.1 can be applied to both post-processing diagnostics, which calculates the radiation given a set of pre-calculated trajectories, and to run-time diagnostics, in which the radiation calculations are performed at run time during the trajectory calculation. In the latter scenario, the calculation and deposition of the emitted radiation can take place in a sub-step of the particle push loop, created specifically for that purpose, as shown in Figure 2.6, This sub-step comes right after pushing the particles, in such a way that the newly calculated positions and momenta can be used, in conjunction with the corresponding stored values from the previous iteration, to compute the required quantities to determine the radiated fields. In the post-processing version, all required quantities can be readily calculated by considering the positions and momenta from consecutive time-steps.

2.3.2 Deposition of the radiated fields in a virtual detector

According to Equations (2.2) and (2.3), each PIC simulation timestep corresponds to a given detector time. In general, consecutive time steps in the trajectory will deposit radiation in non-consecutive detector time cells. A simple prescription that only deposits the radiated fields in the temporal cells that are closest to the predictions given by Equations (2.2) and (2.3) will therefore generate noisy radiation patterns that are non-physical because particles emit radiation continuously. To re-gain the continuous character of radiation emission, and remove the artificial noise induced by the discretization of the trajectories in time, RaDiO interpolates the fields emitted by each particle between every two consecutive PIC time steps.

The interpolation scheme in RaDiO assumes that particles radiate constant fields between each consecutive PIC timestep. In order to deposit the fields across different temporal cells, we weigh the contribution of each deposition by the time until the next deposition. In fact, the value of the radiation in a time slot is the integral of the radiation in the interval delimited by two consecutive detector time-steps. Incidentally, real-life applications often employ an *integrator detector*, which takes the information about radiation arriving in-between detector time steps into account. This deposition scheme can be implemented by following Algorithm 2.2, below.

Algorithm 2.2 Radiation interpolation

procedure RADIATIONINTERPOLATOR
    $n_{\text{slot}} = \text{slot}(t_{\text{array}}, t_{\text{det}})$
    $n_{\text{slot,prev}} = \text{slot}(t_{\text{array}}, t_{\text{det,prev}})$
    $n_{\text{itr}} = t_{\text{slot,prev}}$
    $t_{\text{tmp}} = t_{\text{det,prev}}$
    while $n_{\text{itr}} < n_{\text{slot}}$ **do**
        $\text{scale\_factor} = (t_{\text{array}}[n_{\text{itr}}+1] - t_{\text{tmp}})/dt_{\text{det}}$
        $\boldsymbol{E}(cell, n_{itr}) = \mathbf{E}(\mathbf{n}, \beta, \dot{\beta}) \cdot \text{scale\_factor}$
        $n_{\text{itr}} = n_{\text{itr}} + 1$
        $t_{\text{tmp}} = t_{\text{array}}[n_{\text{itr}}]$
    end while
    $\text{scale\_factor} = (t_{\text{det}} - t_{\text{array}}[n_{\text{slot}}])/dt_{\text{det}}$
    $\boldsymbol{E}(cell, n_{itr}) = \mathbf{E}(\mathbf{n}, \beta, \dot{\beta}) \cdot \text{scale\_factor}$
end procedure

Each variable in Algorithm 2.2 is calculated at each PIC time-step and for each particle. Here, *slot(...)* is a function that returns the index of the slot in the detector's time-array (t_{array}) where t_{det} falls, t_{det} is the time of the current deposition and n_{slot} is the corresponding time-slot position in the detector array. In addition, n_{itr} is an iterator that runs from $n_{\text{slot,prev}}$, the detector time slot where particle deposited radiation in the previous PIC time-step, until n_{slot}. The quantity t_{tmp} is an auxiliary variable for the calculation of the time difference between depositions. It runs from, $t_{\text{det,prev}}$, the time of the previous deposition, to $t[n_{\text{itr}}]$, the time for the actual deposition.

Figure 2.7 shows an example case that clarifies this deposition scheme. Each of these depositions correspond to radiation emitted at a different PIC time step by a single particle. This interpolation can be performed while the simulation is running, as it only requires information about the radiated field in the

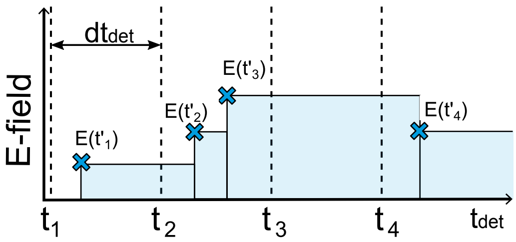

Figure 2.7: Integrator detector: radiation is scaled by the time until the next deposition. t_i refers to the detector's time grid and t_i' to the different deposition times.

previous time step. In fact, for the example present in Figure 2.7 the deposition algorithm would go as follows:

1) At PIC iteration 4, a radiated field $E(t_4')$ arrives at the detector at $t_{\text{det}} = t_4'$.

2) n_{itr} is set to 2, the slot of the previous deposition, at t_3', t_{tmp} is set to t_3', the time of the previous deposition, we enter the loop, the scale factor is calculated: $(t_3 - t_{\text{tmp}})/dt_{\text{det}}$, with $t_{\text{array}}[n_{\text{itr}}+1] = t_3$ and $E(t_3')(t_3 - t_3')/dt_{\text{det}}$ is deposited in the second time slot, t_2.

3) n_{itr} is incremented to 3, t_{tmp} is set to t_3, the time of the previous deposition, the scale factor is calculated: $(t_4 - t_3)/dt_{\text{det}}$, with $t_{\text{array}}[n_{\text{itr}}+1] = t_4$ and $E(t_3')(t_4 - t_3)/dt_{\text{det}}$ is deposited in the third time slot, t_3.

4) n_{itr} is incremented to 4, t_{tmp} is set to t_4, we exit the loop, the scale factor is calculated: $(t_{\text{det}} - t_4)/dt_{\text{det}}$ and $E(t_3')(t_4' - t_4)/dt_{\text{det}}$ is deposited in the time slot t_4.

Using this approach, radiation can be computed and deposited using only the information from the current and the previous time steps. This algorithm interpolates radiation coming from a single particle, but can be repeated for all particles in the simulation, as stated in Algorithm 2.1, in order to capture radiation from all particles. It can also be applied to calculate the radiated magnetic fields.

2.3.3 Practical example: Helical trajectory

Here we look at a practical example, in which an electron with $\gamma_p = 57.3$ undergoes a helical motion with amplitude $0.014\,\mathrm{c}/\omega_p$ and frequency $\omega_0 = \omega_p$, corresponding to a K parameter of $K = 0.8$, K is a trajectory parameter that can be taken as a scaled pitch angle the maximum angle of the particle trajectory, normalized to the Lorentz factor γ_p and given by $K = \gamma_p r_0 \omega_0 / c$. The helical motion was described by the

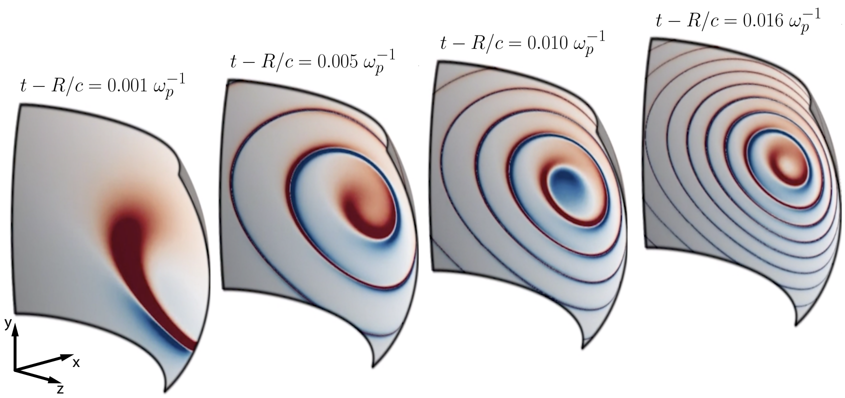

Figure 2.8: Spatiotemporal signature of the radiation emitted by a particle undergoing a helical trajectory.

PIC algorithm with a temporal resolution of 0.1 ω_p^{-1}. Here, ω_p, is an arbitrary normalizing frequency. The radiation generated by a particle undergoing such trajectory has a distinctive, expanding spiral spatiotemporal signature. This is shown in Figure 2.8, which represents the radiated electric field along the y direction deposited onto a spherical 2D detector with an angular aperture of 0.1 rad placed in the direction of the longitudinal motion of the particles (x axis), with radius $R = 10^6$ c$/\omega_p$. The temporal resolution of the detector was 1.33×10^{-5} ω_p^{-2} and the spatial resolution was 58 µrad. Figure 2.8 shows a snapshot of the detector at four different temporal positions. The starting point of the spiral follows the circular motion of the particle in the $y - z$ plane. Between each snapshot the radiation spiral makes two turns, thus the temporal distance between each snapshot is approximately equal to two periods of the emitted radiation. Given the trajectory parameters, the radiation period was expected to be of about $\sim 2 \times 10^{-3}$ ω_p^{-1}, about 10 times smaller than the smaller period that could be resolved using only the PIC algorithm.

2.4 Benchmarking

As far as we are aware, the only explicit analytical formulas capturing the spatiotemporal radiation profile of synchrotron radiation are found in [65], which gives a semi-analytical model for the emitted field lines. The work by R. Y. Tsien [65] is one of the first to describe the spatiotemporal nature of the radiated fields mathematically. This description, however is fundamentally different from the one found in our algorithm. While R. Y. Tsien's algorithm presents a visual depiction of the radiated electric field lines in the plane of motion, RaDiO provides the actual value of the electric field in a given region of space. The density of the field lines is a surrogate for the intensity of electric field in a given region, making visual comparisons easier.

We compared the results of RaDiO and R. Y. Tsien's algorithm for the case of a charge undergoing circular motion in the xy plane around the origin with radius $r = 1$ $c/$ ω_p and $\gamma_p = 2.294$ and found good agreement on the overall shape and periodicity of the radiated electric field, as displayed in Figure 2.9.

However, direct quantitative comparisons between the visual depiction of field lines and the actual

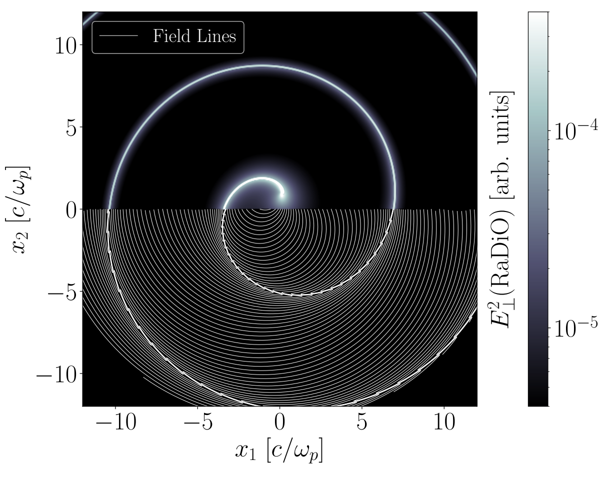

Figure 2.9: Comparison with the field line algorithm of R. Y. Tsien. The top half contains a color plot of the field intensity E^2 obtained with RaDiO. The bottom half shows the field lines obtained with R. Y. Tsien's algorithm

value of the emitted field in a region of space can be difficult. On the other hand, the spectral properties of radiation are well documented [66, 67], so we Fourier transformed the data in the virtual detector with respect to time and compared these spectra to the theoretical predictions.

We then consider the example of a single relativistic particle emitting synchrotron radiation. Synchrotrons have a magnetic field structure that imposes a sinusoidal trajectory to relativistic electrons that go through the device, thus leading to the emission of high frequency photon beams in the X-UV or X-ray regions of the spectrum. The trajectory of the particle would then be given by Equation (2.5).

The corresponding intensity spectrum (I) with respect to the frequency ω and solid angle Ω of the emitted radiation, valid for ultra relativistic particles as an asymptotic limit expression ($\gamma_p \gg 1$) and assuming very large number of periods in the trajectory, [20], is given by:

$$\frac{d^2I}{d\omega d\Omega} = \frac{e^2\omega^2\gamma^2}{3\pi^2 c\omega_\beta K}\left(\frac{1}{\gamma_p^2}+\theta^2\right)^2\left[\frac{\theta^2}{\gamma_p^{-2}+\theta^2}K_{2/3}^2(\Upsilon)+K_{1/3}^2(\Upsilon)\right], \tag{2.6}$$

where, θ is the observation angle in the direction perpendicular to the trajectories plane. In addition, K_n is the modified Bessel function and Υ is a numerical parameter given by $\Upsilon = \frac{\omega\gamma_p}{3\omega_\beta K}\left(\gamma_p^{-2}+\theta^2\right)^{-3/2}$, with K being the aforementioned K parameter.

Equation (2.6) can be integrated over all angles, returning the frequency spectrum [20]:

$$\frac{dI}{d\omega} = \sqrt{3}\frac{e^2\gamma_p\omega}{c\omega_c}\int_{\omega/\omega_c}^{\infty} K_{5/3}(x)dx,\ \omega_c = \frac{3}{2}K\gamma_p^2\omega_\beta \tag{2.7}$$

We have benchmarked our algorithm against Equations (2.6) and (2.7). The benchmarks were performed using the two-dimensional sinusoidal trajectory of a relativistic electron ($\gamma_p = 50$) with an amplitude of $r_\beta = 2\,c/\omega_p$, $k_\beta = 0.1\,\omega_p/c$ ($K = 10$) in the transverse $x-y$ plane and $dt = 0.01c/\omega_p$, where ω_p is a normalizing frequency. We simulated a line of a spherical detector, placed in the $z-x$ plane, $10^5\,c/\omega_p$ away from the axis origin with an angular aperture of 0.1 rad around the x axis. This detector had 512 spatial cells and 131072 temporal cells, resulting in a temporal detector resolution of $2.98\times10^{-5}c/\omega_p$. The results are shown in Figure 2.10 which features a plot of the detected electric field in the $\mathbf{e}_\phi$ direction (perpendicular to the motion plane) for each spatiotemporal cell.

The radiation is composed of several periodically spaced peaks, whose shape can be observed in the lineout Figure 2.10b. The short burst nature of the radiation (equivalent to a broadband spectrum), consistent with the large value of the K parameter, is clear from Figure 2.10. Instead of displaying a purely sinusoidal profile with a single wavelength, the electric field consists of sharply peaked bursts containing many different wavelengths. Moreover, it is possible to observe that consecutive peaks have opposite sign. This is a direct result of the sinusoidal nature of the electron trajectory in which the acceleration $\dot{\boldsymbol{\beta}}$ switches sign between peaks. Furthermore, it is possible to note that for larger angles, the radiation bursts arrive later, creating the parabola-like structures that can be seen in the upper plot. This delay becomes more significant as the particle approaches the detector's surface, resulting in a decrease of the curves' aperture.

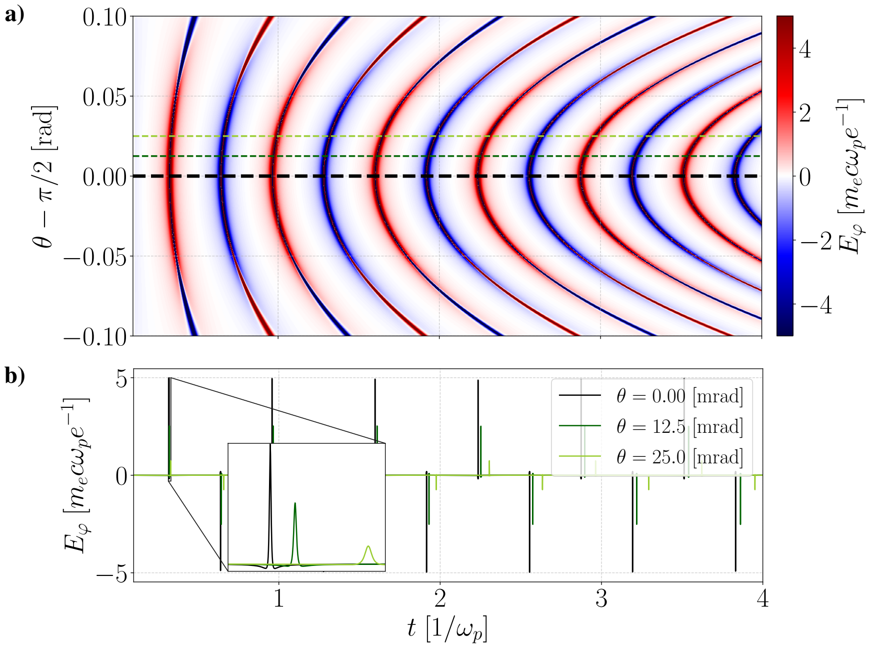

Figure 2.10: Spatiotemporal signature of the radiation emitted by a particle undergoing a sinusoidal motion in a transverse detector (a). The lineouts are shown on the bottom plot (b). Peaks located at smaller t arrive earlier at the detector.

This result can also be understood in terms of the spatiotemporal reasoning regarding the estimation for the typical radiation frequency presented in Figure 2.2. However, instead of depicting the emitted radiation parallel to the motion of the particle, we picture them emitted at an angle θ. The temporal distance between the emission and arrival of light ray emitted at a given longitudinal position x is then given by: $c\Delta t_{rad} = \sqrt{R^2 + x^2 - 2xR\cos\theta}$, where all quantities are defined as in Equation (2.3). This expression shows that the time of arrival increases with θ and also that it is scaled by the longitudinal position x. Thus, as the particle approaches the detector and x grows larger, the parabolic structures left on the detector become tighter.

Figure 2.10 b, which depicts lineouts of E_ϕ, also shows that the peaks become wider and less intense for larger angles. This is in concordance with the predictions for the spectrum [see Equation (2.6)], which features a decrease in the number of harmonics for larger angles, resulting in broader and less intense peaks off-axis.

In order to further understand the angular dependent frequency spectra, Figure 2.11 compares the theoretical result, given by Equation (2.6), with the simulated result, given by the Fourier transform over time of the field shown in Figure 2.10a. The spectrum is symmetric with respect to $\theta = 0$. Thus, the upper half of Figure 2.11 a ($\theta > 0$) shows the simulated results and the bottom half ($\theta < 0$) the theory. As expected, the theoretical line, being the assymptotic limit of a continuous harmonic distribution with a very large number of oscilations in the trajectory [20], corresponds to the envelope of the numerical result, showing excellent agreement. This is evident from the lineout of the radiated spectra displayed in Figure 2.11b.

The simulated integrated spectrum over all angles, which yields the frequency distribution of the emitted radiation, can be benchmarked against Equation (2.7). Figure 8 shows excellent agreement

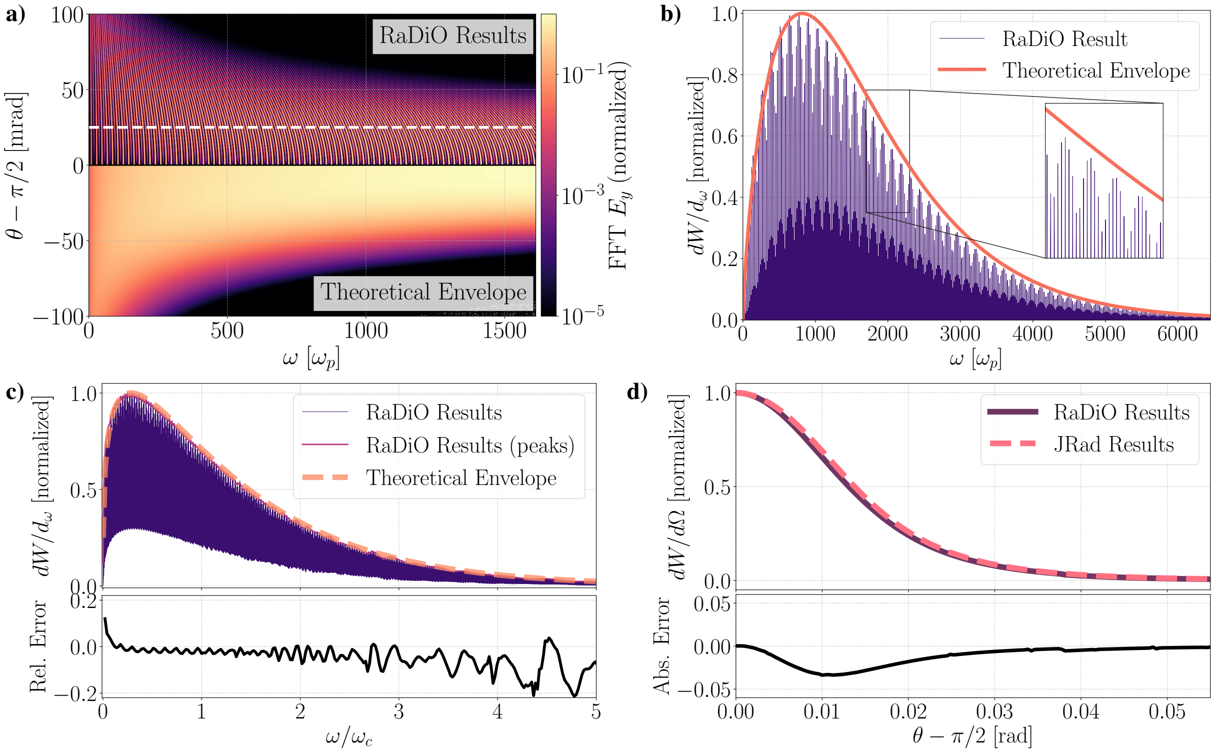

Figure 2.11: a) Comparison between the theoretical and simulated spectra. b) Comparison between a lineout at $\Delta\theta = 0.02$ from both spectra. c) Angle integrated spectra, both spectra are normalized to 1. The relative error ($I_{\text{RaDiO}}/I_{\text{theor}} - 1$) is shown on the inset. (d) Frequency integrated spectra, both spectra are normalized to 1. The absolute error ($I_{\text{RaDiO}} - I_{\text{JRad}}$) is shown on the inset.

between numerical and theoretical results, as the intensity of most peaks matches the expected result with small relative error which rises as frequency increases.

To further confirm the validity of our numerical approach, we benchmarked the frequency integrated spectrum, $dI/d\Omega$ against the spectrum provided by the post-processing spectral code JRad [54], which computes the radiated fields using the spectral version of the Liénard-Wiechert potentials. The results of this comparison, shown in Figure 2.11 d), are in excellent agreement.

2.4.1 Coherence tests

Because RaDiO captures the emitted fields in space and in time it can also naturally describe temporal and spacial interference effects. This feature is essential to accurately portrait temporal and spatial coherence, present in superradiant emission scenarios for example. This is an intrinsic feature of our spatiotemporal approach, which allows us to directly obtain the fields radiated by every simulation particle, including interference effects by design.

To test our ability to accurately model temporal and spatial coherence, we ran simulations using two particles with opposite charges and sinusoidal trajectories, similar the one defined in Equation (2.5). The two particles, with particle 1 being positively charged and particle 2 being negatively charged underwent this sinusoidal trajectory in perpendicular planes (particle 1 in plane $x-y$ and particle 2 in plane $x-z$) and the detector was the same as the one used in the previous section.

Figure 2.12 shows the simulated radiated electric field profile as a function of θ and t_{det} for three

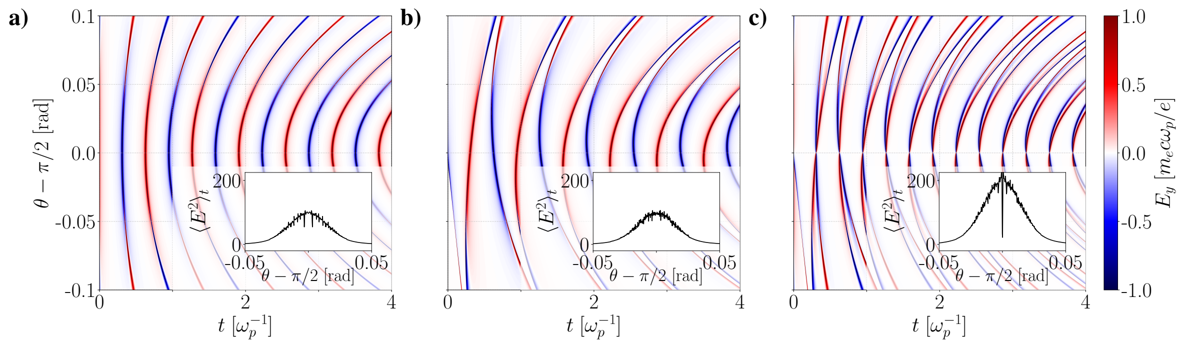

Figure 2.12: a) Spatiotemporal profile of the radiation coming from particle 1 (trajectory perpendicular to the detector). b) Spatiotemporal profile of the radiation coming from particle 2 (trajectory parallel to the detector). c) Spatiotemporal profile of the radiation coming from both particles. The insets contain the time averaged squared field, $\langle E^2\rangle_t$.

different configurations: one with only particle 1 [Figure 2.12 (a)], one with only particle 2 [Figure 2.12 (b)] and other with both particles [Figure 2.12 (c)]. As the two trajectories lie in different planes, the spatiotemporal signatures of the radiation emitted by each particle are noticeably distinct because the detector plane lies on the plane of the trajectory of particle 2, then being perpendicular to the plane of particle 1. By comparing Figure 2.12 (a) with Figure 2.12 (b), we can hence readily identify the radiation coming from each particle in Figure 2.12 (c).

As both particles have opposite charges, the field on axis for a given particle will have the opposite sign as the on-axis field for the other particle. Thus, the radiation emitted by both particles will interfere destructively on-axis. This happens exactly at $\theta = \pi/2$. Thus, if we look at the time averaged squared field (insets in each panel of Figure 2.12), we see that although $\langle E^2\rangle_t$ is maximum at $\theta = \pi/2$ for the simulations with only one of the particles (insets of Figure 2.12a and Figure 2.12b), the opposite happens when we capture the fields radiated by both particles (inset of Figure 2.12c).

Our algorithm captures coherence effects of the simulation particles by default. However, in a PIC code, each particle in the simulation represents a cloud of N real particles with a size close to cell size that follow the same dynamics, this is the so called macroparticle aprroximation. A macroparticle is then the computational way of representing a group of particles, as displayed in Figure 2.13, that are assumed to move with same momentum throughout the simulation, keeping their spatial distribution static over time. This assumption is usually valid in scenarios where the collective effects dominate over the individual motion for scales larger than the cell size. Depending on the physical process at study, the number of particles grouped inside a macroparticle should be selected in order to ensure the validity of this approximation.

In our code, however, spatial scales smaller than the cell size play a key role, but as it is virtually impossible to determine the spatial distribution of each macroparticle, we calculate the radiation emitted by the macroparticles in the simulation as if they were point charges with charge equal to the total charge inside the macroparticle (Nq). This is in fact equivalent to assuming that each of the N particles inside the macroparticle radiates coherently. However, as discussed by Ref. [68], the shape of this distribution may affect the coherence of the emitted radiation. Therefore, the radiated spectrum should be given by:

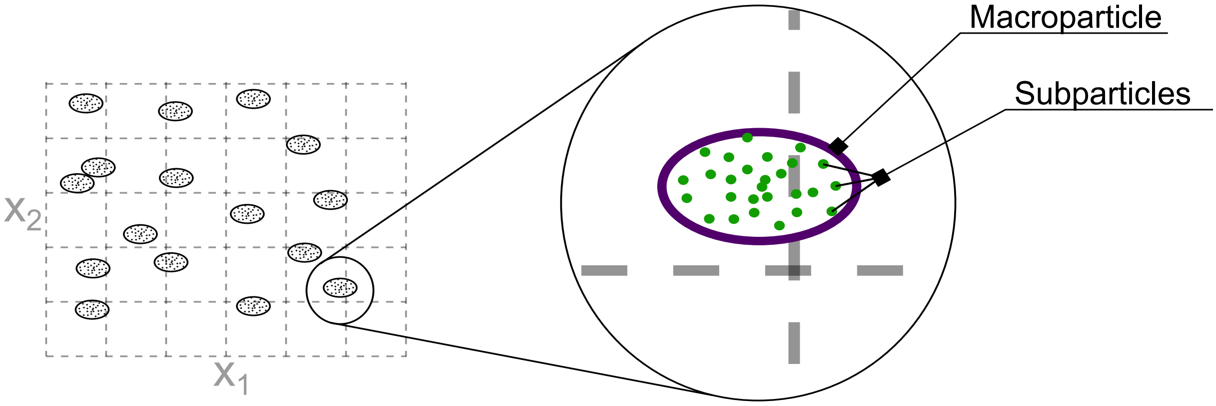

Figure 2.13: Illustration of the macropaticle concept

$$\frac{d^2I}{d\omega d\Omega} = \frac{q_e^2}{4\pi^2 c}\left|\int_V \rho(\mathbf{r_0}-\mathbf{r})dV\int_{-\infty}^{\infty}\frac{\mathbf{n}\times[(\mathbf{n}-\boldsymbol{\beta})\times\dot{\boldsymbol{\beta}}]}{(1-\boldsymbol{\beta}\cdot\mathbf{n})^2}e^{i\omega\left(t_{\text{ret}}-\frac{\mathbf{n}\cdot(\mathbf{r_0}-\mathbf{r})}{c}\right)}dt_{\text{ret}}\right|^2 \tag{2.8}$$

where $\rho(\mathbf{r})$ is the charge density distribution of the particles inside the macroparticle, which can be assumed to be centered around the center of the macroparticle $\mathbf{r_0}$, in this case the spatial integral can be taken as the Fourier transform of the charge distribution, $\mathscr{F}_\rho$:

$$\begin{aligned}\frac{d^2I}{d\omega d\Omega} &= \frac{q_e^2}{4\pi^2 c}\left|\int_{-\infty}^{\infty}\frac{\mathbf{n}\times[(\mathbf{n}-\boldsymbol{\beta})\times\dot{\boldsymbol{\beta}}]}{(1-\boldsymbol{\beta}\cdot\mathbf{n})^2}e^{i\omega\left(t_{\text{ret}}-\frac{\mathbf{n}\cdot\mathbf{r_0}}{c}\right)}dt_{\text{ret}}\int_V \rho(\mathbf{r}-\mathbf{r_0})e^{i\omega\left(t_{\text{ret}}-\frac{\mathbf{n}\cdot\mathbf{r}}{c}\right)}dV\right|^2 \\ &= \frac{q_e^2}{4\pi^2 c}\left|\int_{-\infty}^{\infty}\frac{\mathbf{n}\times[(\mathbf{n}-\boldsymbol{\beta})\times\dot{\boldsymbol{\beta}}]}{(1-\boldsymbol{\beta}\cdot\mathbf{n})^2}e^{i\omega\left(t_{\text{ret}}-\frac{\mathbf{n}\cdot\mathbf{r_0}}{c}\right)}dt_{\text{ret}}\right|^2\mathscr{F}_\rho^2(\omega/c)\,.\end{aligned} \tag{2.9}$$

For a point-like macroparticle the charge density may be written as a Dirac-delta function, $\rho = \delta(\mathbf{r}-\mathbf{r_0})$, whose Fourier transform is equal to 1. In this case, the charge distribution has no effect on the amplitude of the emitted, harmonics. However, if the charge density is a discrete set of N particles distributed according to the continuous charge distribution ρ the radiated spectrum would be given by [68]:

$$\frac{d^2I}{d\omega d\Omega} = \frac{q_e^2}{4\pi^2 c}\left|\int_{-\infty}^{\infty}\frac{\mathbf{n}\times[(\mathbf{n}-\boldsymbol{\beta})\times\dot{\boldsymbol{\beta}}]}{(1-\boldsymbol{\beta}\cdot\mathbf{n})^2}e^{i\omega\left(t_{\text{ret}}-\frac{\mathbf{n}\cdot\mathbf{r_0}}{c}\right)}dt_{\text{ret}}\right|^2\left[N+\left(N^2-N\right)\mathscr{F}_\rho^2(\omega/c)\right]. \tag{2.10}$$

The N factor accounts for the incoherent emission that happens after the shape function cuts-off (for higher frequencies), whereas the (N^2-N) accounts for coherent emission that happens for lower frequencies.

In order to simulate the effect of the macroparticle shape function on the emitted radiation we added an extension to the post-processing diagnostic that allowed the user to specify the shape of the macroparticle and number of subparticles to be used in the simulation. This tool's functioning is based on the assumption that a spatial charge distribution results in an equivalent deposition time distribution, that is: if the particles are distributed uniformly along space, then the times at which they will deposit radiation are equally distributed.

For these simulations, we used the sinusoidal trajectory of Equation (2.5), with a slice of spherical detector of radius $R = 10^5\, c/\omega_p$ located in the $y-z$ plane with azimuthal angle $\phi = 0$ and polar angle

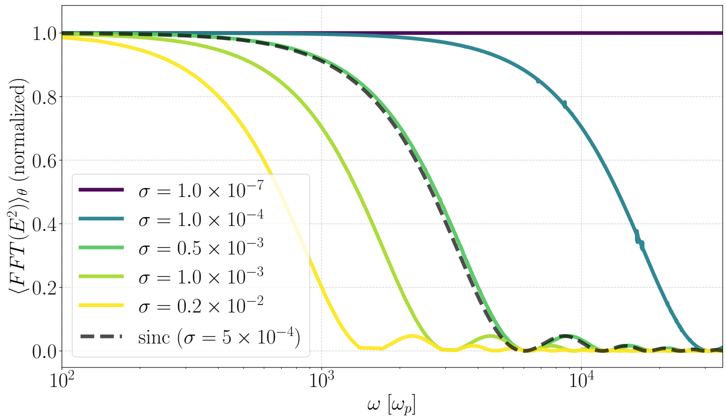

Figure 2.14: Comparison between the spectra emitted by macroparticles with different sizes. a) Direct comparison of the spectra. b) Ratio between each spectrum and the spectrum obtained for a point-like macroparticle.

θ ranging from $\pi/2-0.08$ to $\pi/2+0.08\,\text{rad}$ with 512 spatial cells that accepted radiation from $t = R/c+0.01\,\omega_p^{-1}$ to $t = R/c+4\,\omega_p^{-1}$ with 131072 temporal cells. The macroparticles were composed of 128 subparticles and we varied their width σ from $\sigma = 10^{-7}\,c/\omega_p$ to $\sigma = 2\times 10^{-3}\,\mathrm{c}/\omega_p$.

The simulated electric field was transformed into a frequency-angular spectrum by means of an FFT and then integrated along the angular direction. The resulting spectra are displayed on the left panel of Figure 2.14. Even though the spectrum of this kind of radiation decays naturally for higher frequencies, it is possible to verify that when the macroparticle becomes wider (higher σ), this decay happens earlier.

By normalizing each spectrum to the spectrum generated with $\sigma = 0$ we were able to obtain the filter function for each σ. The results are plotted in the right panel on Figure 2.14 where it is possible to see that in the available range of frequencies, the effect of the shape functions clearly match the expected sinc filter. In these radiation emission phenomena, this filtering occurs due to coherence effects: a macroparticle with a given size emits coherent radiation if the wavelength of the radiation is larger than its typical size and emits incoherent radiation if the wavelength of the radiation is smaller than its typical size.

The mathematical framework developed by R. Paush allows for an easy understanding of why the spectrum's intensity should decay for higher frequencies. However, some more physical insight can be given by the spatiotemporal picture of the emitted radiation. Figure 2.15 shows the difference between the spatiotemporal signature of a macroparticle with $\sigma = 10^{-7}\,c/\omega_p$ and a macroparticle with $\sigma = 10^{-2}\,c/\omega_p$. With a smaller macropaticle the radiation is much more intense, with shorter pulses (temporally). The opposite happens for larger macroparticles, as the radiation from each subparticle is no longer focused on the same time slot which also leads to destructive interference. This fact is evidenced by the lineout on the right panel of Figure 2.15, where the strong pulse generated by the small macroparticle becomes broader when the macroparticle becomes wider with a much longer and less steep transition between the positive and negative parts of the pulse caused by the interference between the singular pulses of each subparticle.

The fact that the shape function corresponds to the quotient of the spectrum of the radiation obtained with larger macroparticles and the spectrum obtained with a point particle seems to suggest that the addition of subparticles to the macroparticle acts as a filter, leaving out the high-frequency components. In this way, it may be possible to obtain the macroparticle spatiotemporal signature from the point particle's

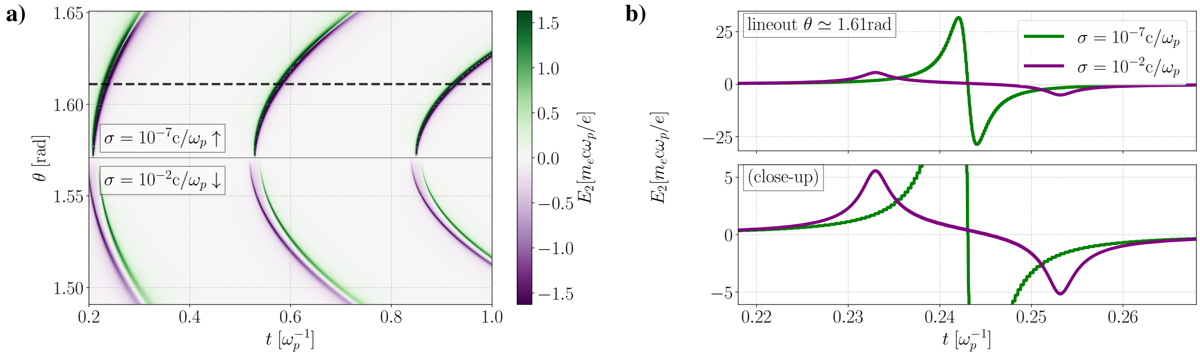

Figure 2.15: Comparison between the spatiotemporal profiles of the radiation emitted by two types of macroparticles. The left plot (a) shows the two complementary halves of the full detector. The lineout is shown on the right panels (b), featuring a close-up.

signature through Fourier filtering. However, this operation requires strong assumptions about the shape of the macroparticle which may not be valid at sub-grid scales.

The assumption that they all radiate coherently holds either for all wavelengths if $N = 1$, or for wavelengths larger than the cell size if $N \gg 1$. Thus, for wavelengths shorter than the cell size, in general, we cannot say it holds, as such an assumption depends on information about particles that are not being simulated. For example, if standard macroparticle approximation is still valid at scales smaller than the cell size, the emitted radiation should be incoherent for wavelengths shorter than the cell size and the result should be corrected with a filter function.

The detailed study of the conditions that allow assuming that each of the N particles inside the macroparticle radiates coherently is out of the scope of this work. It will be up to the user to decide whether it holds or not. If this assumption does not hold, then results given by our code will be correct for wavelengths larger than the cell size, but could be overestimated for wavelengths smaller than the cell size. Nevertheless, our code can, in general, accurately predict the qualitative aspects of the emitted radiation for all wavelengths.

2.5 Example: Radiation from a plasma mirror

When an electromagnetic wave collides with a target such as a metallic surface or an overdense plasma, it is unable to propagate and gets reflected. The process of reflection has long been well understood and thoroughly explained at the macroscopic level by Maxwell's laws and classical electrodynamics. In the plasma, the phenomenon is commonly explored using a fluid theory approach, provided that relativistic and kinetic effects are negligible. Such description predicts the damping of the wave near the surface of the reflective material (it becomes an evanescent wave) and the appearance of a reflected wave. At the electron level, however, the phenomenon is not always trivial, in particular at relativistic laser intensities (with peak normalized vector potential $a_0 = eA_0/(m_e c) = 1$), which lead to High Harmonic Generation (HHG) in plasma mirrors [43, 46]. Several theoretical frameworks have been proposed to describe the underlying mechanisms of HHG, each with different regimes of applicability (see e.g. [69, 70])

PIC simulations are commonly employed to deepen the understanding of the physical processes underlying laser reflection and harmonic generation in plasma mirrors. An accurate description of HHG in standard PIC simulations, for instance, is computationally challenging because spatial and temporal PIC grids need to properly resolve the high harmonics. Thus, to accurately capture high harmonics up to the 10^{th} or 100^{th} order, PIC simulations require spatiotemporal resolution up to one-two orders of magnitude higher than one required to resolve the fundamental harmonic. The use of RaDiO may thus be computationally advantageous in HHG simulations, as it allows capturing high frequency harmonics without increasing the PIC resolution.

In this section, we present 3D Osiris simulations of an HHG scenario where the laser propagates in the longitudinal x direction and is linearly polarized along the transverse z direction. The laser uses a $\sin^2$ temporal profile with 12 full periods ($T_0 = 8\pi\ \omega_p^{-1}$, $\omega_0 = \omega_p/4$) and Gaussian perpendicular profile with spot-size ($W_0 = 2\lambda_0$, λ_0 is the central laser wavelength). The plasma mirror consists of an overdense plasma slab with plasma frequency ω_p (and density n_p, 16 times larger than the critical density n_c for that laser pulse) with thickness 100 c/ω_p, much higher than the non-relativistic plasma skin-depth ($l_s \sim\ c/\omega_p$ in this case). As the laser gets reflected, we capture the reflected fields both in the PIC grid through Maxwell's equations and in a virtual detector through RaDiO. We chose to compute the radiation emitted by all plasma electrons located within the plasma cylinder with a radius of three laser spot sizes around the focus. The virtual cartesian detector was located at $x = -160\ c/\omega_p$, ranging from $y = -160\ c/\omega_p$ to 160 c/ω_p, with temporal resolution $dt_{\text{det}} = 0.0384\ \omega_p^{-1}$, about five times smaller than the PIC temporal resolution $dt_{\text{PIC}} = 0.1792\ \omega_p^{-1}$. The PIC simulation box ranged from $x = -288\ c/\omega_p$ to $x = 108\ c/\omega_p$, with a resolution $dx = 0.96\ c/\omega_p$ in the longitudinal direction and from $y, z = -160\ c/\omega_p$ to $y, z = 160\ c/\omega_p$ with resolution $dy, dz = 0.32\ c/\omega_p$ in the transverse direction. This PIC grid is able to resolve 26 points per laser wavelength. Each cell contains 16 simulation particles. A 2-D slice of the setup is shown in Figure 2.16, the laser propagates from left to right.

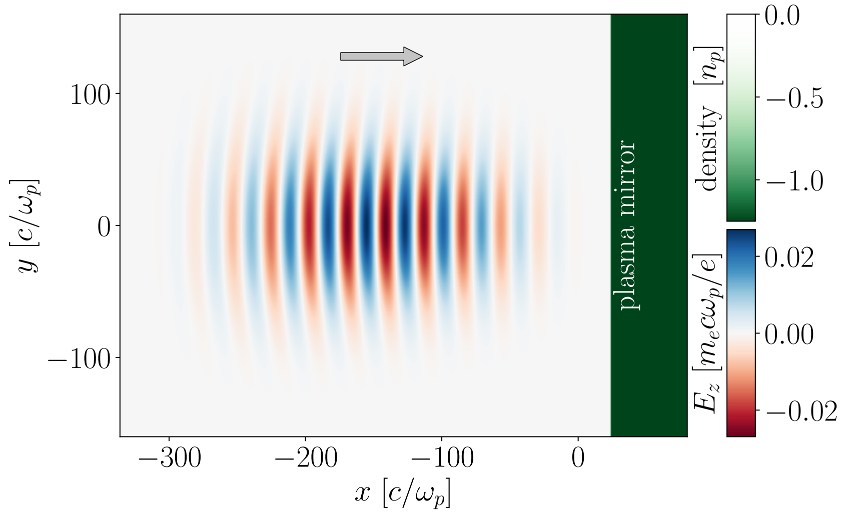

Figure 2.16: Reflection radiation simulation setup. A tightly focused gaussian laser pulse propagates from left to right towards an overdense plasma target.

We start by capturing the radiation in the absence of HHG, by using a non-relativistic laser intensity, with peak normalized vector potential $a_0 = 0.1$. Figure 2.17, top, shows the trajectories of a random sample of 512 plasma particles. The zoomed-in region clearly displays the typical *figure-8*-like motion induced in the plasma particles by the laser pulse. This motion originates the radiation, which is captured both in the PIC grid and in the virtual radiation detector. By comparing the radiation in the detector to the reflected pulse in the PIC grid (Figure 2.17, bottom), we show that the beam reflection is a direct result of the charged particles' trajectories induced by the incident beam.

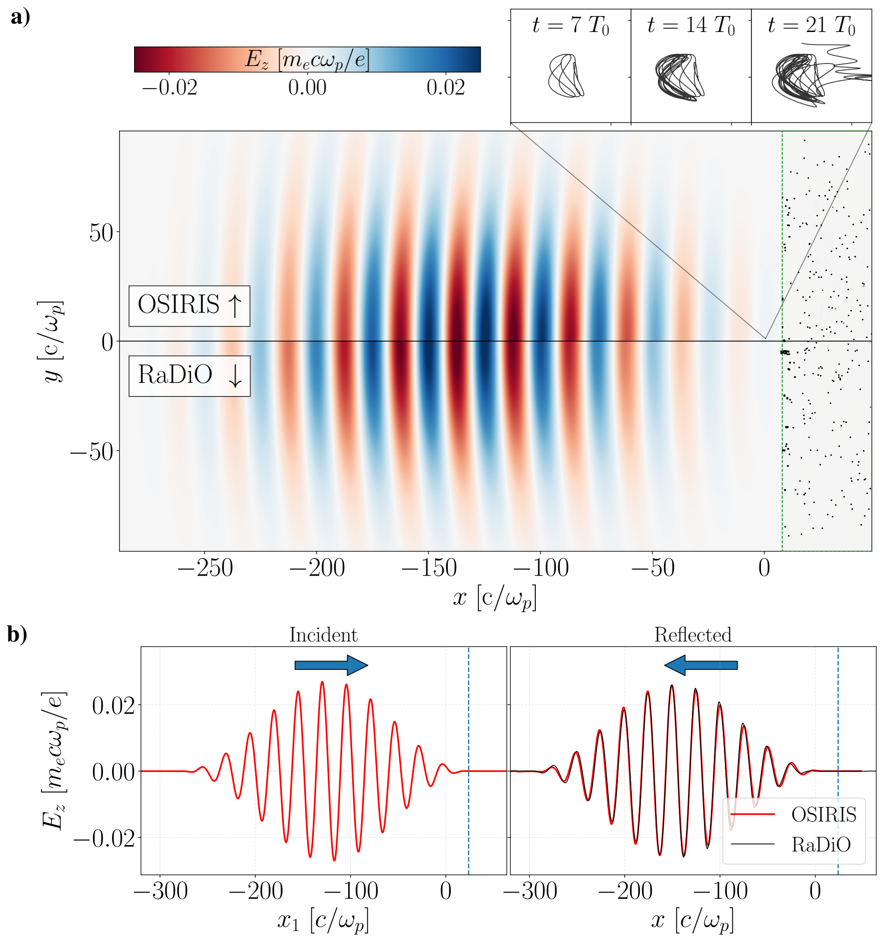

Figure 2.17: Trajectories of a random sample of 512 plasma particles under the influence of a low intensity laser ($a_0 = 0.1$). The zoomed-in region shows a particle performing the figure-8 motion induced by the incident laser (a). Comparison between the reflected laser profile given by the PIC grid (upper half) and by RaDiO (lower half) at $x = -160\ c/\omega_p$. Comparison between incident and reflected beams as captured by the standard PIC algorithm and by RaDiO (b). The laser pulses are properly described in both situations with more than 20 points per wavelength.

Next to investigate a scenario with strong HHG, we used a high-intensity laser ($a_0 = 4.2$) in a setup similar to the one shown on Figure 2.16. In this case, we see the clear effect of the increased intensity on the trajectory of the sampled particles (Figure 2.18, top), with a similar figure-8 motion for the first few laser periods, but with increased amplitude overall and stronger deviation from the standard figure-8 motion.

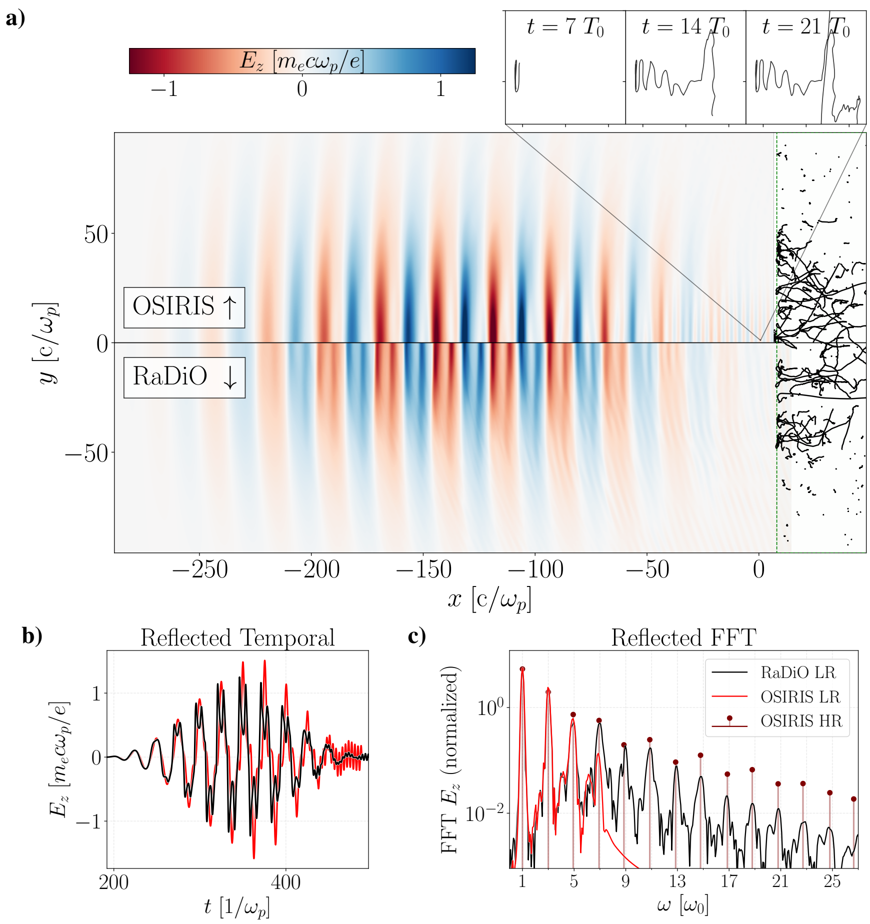

Figure 2.18: Trajectories of a random sample of 512 plasma particles (a) after the reflection a low intensity laser ($a_0 = 4.2$). The zoomed-in region shows a particle performing the figure-8 motion induced by the incident laser. Comparison between the reflected laser profile given by the PIC grid (upper half) and by RaDiO (lower half) $x = -160\ c/\omega_p$. Spatiotemporal (b) and frequency spectrum (c) of the reflected high intensity laser beam.

As a result of this more extreme motion, the reflected laser beam is noticeably different from the incident beam. This is made clear in the comparison shown at the bottom of Figure 2.18. The differences between incoming and reflected laser pulse electric field profile are due to the existence of high laser harmonics present in the reflected beam. The presence of the high harmonics is also clearly visible in the spectrum of Figure 2.18. The frequency spectrum shows that the reflected laser captured by RaDiO contains at least 13 harmonics, while the PIC algorithm, which only resolves the plasma relevant scales correctly captures the emission of the first 4 odd harmonics. The PIC grid is able to resolve the original harmonic with 26 points per wavelength, but as the harmonic order increases, past the 7th order only RaDiO's resolution can capture the signal correctly. In this case the RaDiO frequency spectrum captures frequencies at least 4 times higher than the OSIRIS PIC grid, being able to capture harmonics at least until the 25th order, as expected from the employed laser intensity ($a_0 = 4.2$).

For these intensities, the result of the low resolution OSIRIS simulation differs greatly from the result obtained with RaDiO both in the spectral and spatiotemporal domain. Here we present a comprehensive analysis of the results obtained with higher resolution OSIRIS simulations.

We used the same setup as described previously but enhanced the spatial resolution by the number of cells in the OSIRIS simulation in the x direction by factors of 2 and 4 to 896 and 1792 respectively, while

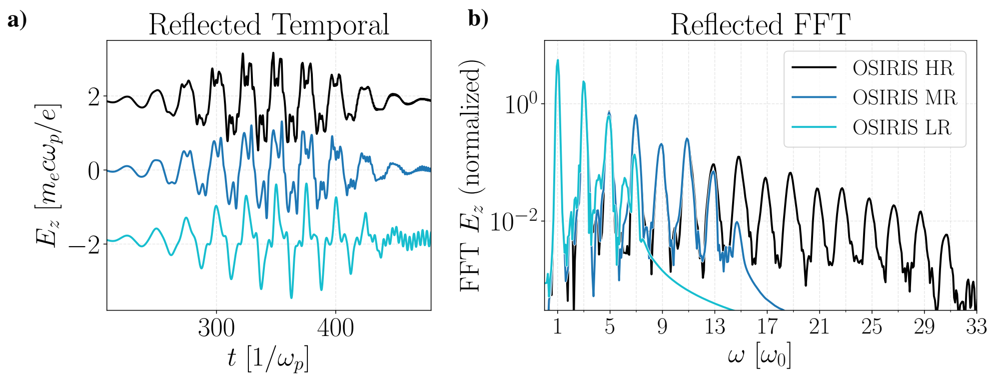

Figure 2.19: Comparison between the reflected laser profile in the temporal (a) and spectral (b) domain at $x = -160\ c/\omega_p$ given by the PIC grid for 3 different resolutions (LR=448 cells, MR=896 cells, HR=1792 cells). The temporal profiles (a) were offset by $\pm\ 2\ m_e c\omega_p/e$ to facilitate comparison.

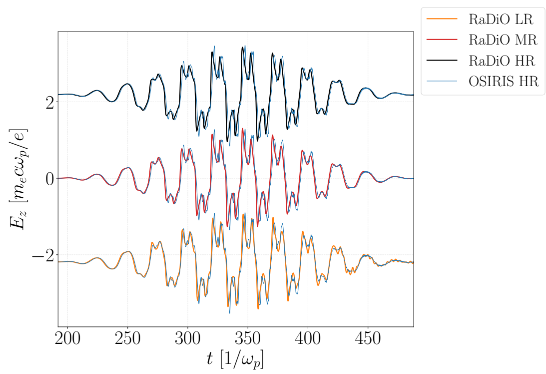

Figure 2.20: Comparison between the reflected laser temporal profile at $x = -160\ c/\omega_p$ as captured by RaDiO for the 3 different PIC grid resolutions (LR=448 cells, MR=896 cells, HR=1792 cells) overlaid with the result from the High Resolution PIC simulation.

keeping the total number of particles in the simulation constant. The resolution of the virtual detector was kept constant as well.

With 896 cells in the x direction ($d_x = 0.4816\ c/\omega_p$), the PIC grid is able to resolve about 52 points per wavelength of the laser pulse, this results in a better description of both the process and the reflected laser pulse. Therefore, the spectrum of the reflected laser pulse as given by the PIC grid contains twice as much harmonics, which impact the spatiotemporal profile as well. The same is true for the case with 1792 cells in the x direction ($d_x = 0.24\ c/\omega_p$), which adds even more harmonics to the spectrum and more complexity to the spatiotemporal profile. This is clear from Figure 2.19 which compares the results given by the PIC grid at the 3 employed resolutions.

The spectra obtained with RaDiO in these 3 setups are present in Figure 2.21 and show a substantially different result. These spectra contain harmonics far past the limits of the PIC grid. For higher frequency harmonics, the amplitudes start to diverge, but the spectral content is present nonetheless, which is a great advantage from the OSIRIS results at low resolutions.

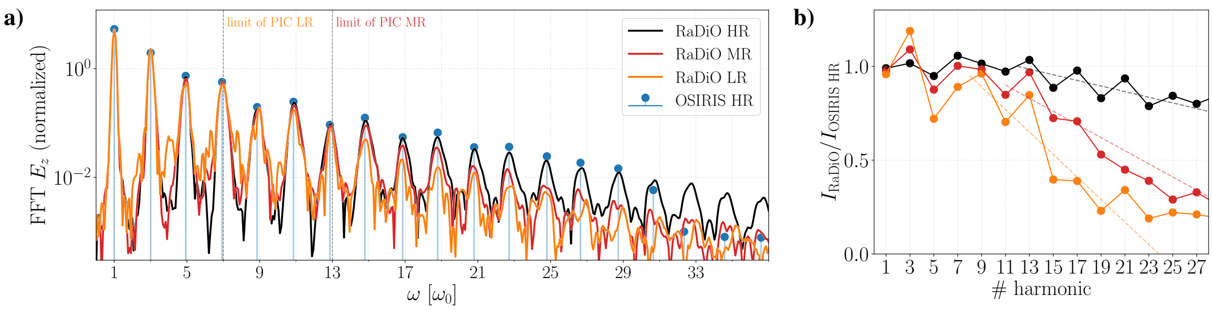

Figure 2.21: Comparison between the reflected laser spectrum at $x = -160\ c/\omega_p$ as captured by RaDiO for the 3 different PIC grid resolutions (LR=448 cells, MR=896 cells, HR=1792 cells) (a). Ratio between the intensity of the n^{th} harmonic captured by RaDiO and the High Resolution PIC simulation.

2.6 Additional Features

In an effort to ensure the reliability and stability of RaDiO, we have dedicated some time to general debugging, and adding some important features. This work has resulted in improved code quality and a reduction in unexpected errors, enhancing the overall user experience.

2.6.1 Post-processing Version

The post-processing version of RaDiO has undergone substantial changes to better integrate with the OSIRIS framework and align with the OSIRIS code philosophy. This includes adopting OSIRIS-style input decks and standardizing file I/O methods. These changes facilitate smoother data exchange between RaDiO and OSIRIS.

Additionally, we have added comprehensive openPMD [71] support to increase RaDiO's versatility. The openPMD standard, (open standard for particle-mesh data files) is a standard for metadata and naming schemes. It provides naming and attribute conventions which aim to enable particle and mesh based data exchange from scientific simulations of any code and experiments. To reflect the compatibility of the post-processing version of RaDiO with various simulation codes, we have renamed it as RaDi-x.

2.6.2 Run-time Version

We added several features to the run-time version of RaDiO. These features mainly added compatibility with other simulation modes of OSIRIS, but included also some performance optimizations.

Working closely with the UCLA group we made several significant improvements to the run-time version of RaDiO. These include an improvement in code readability, ensuring a smoother experience for future developers and users, but most importantly, we focused on optimizing the parallelization scheme. In particular, we added support for batch processing of particles on the CPU, meaning that the particles are transferred in batches to the CPU's cache memory and then the radiation calculations are made for this batch of particles. This takes advantage of the CPU's cache memory which can be accessed by the CPU much faster than regular memory. This significantly enhanced overall performance, resulting in a factor of 2 speedup from the previous version in some cases.

Additionally, we added the possibility to select a subset of the radiative species for radiation calculations. This introduced the possibility of skipping radiation calculations for non-relevant particles. The selection can be made in four distinct ways:

- Randomly select a fraction of the particles;
- Select particles based on their energy (avoids calculation radiation from low-energy particles);
- Select particles using a mathematical expression using their position momenta and time as parameters;
- Select particles previously tagged in post-processing.

In OSIRIS PIC simulations, electrons can be created from neutral species due to ionization. These electrons that are created during the simulation are part of a species which in earlier versions of RaDiO could not be set as radiative, and therefore it was not possible to track the radiation coming from them. A notable feature we added is the ability to model radiation from ionized particles during simulations, expanding the scope of research possibilities.

Lastly, we've also introduced support for RaDiO in quasi-3D [72] simulations, providing users a new simulation mode for their radiation simulations. The quasi-3D simulation mode allows for a 3D description of a system by expanding the fields and currents into azimuthal harmonics (modes) where the amplitudes of each harmonic are complex and functions of r and z. This expansion is fed into Maxwell's equations to determine a series of equations for the complex amplitudes for each harmonic. The particles are then pushed in 3D Cartesian geometry and are then used to obtain the complex amplitudes for each harmonic of the current. This expansion enables more comprehensive and realistic modeling, making RaDiO a more versatile tool for a wider range of applications.

2.6.3 GPU version

In the world of computing hardware, CPUs and GPUs, whose architecture is depicted in Figure 2.22, serve distinct purposes, each optimized for particular types of tasks.

The CPU (Central Processing Unit) is the core component of most computing systems and is valued for its versatility. CPUs are designed to handle a wide range of operations efficiently. They are equipped with complex control logic, making them excellent at executing a variety of instructions in a sequential manner. CPUs excel in serial tasks where operations occur one at a time. While they typically have a limited number of execution units, CPUs compensate with higher clock speeds, ensuring quick execution of individual instructions.

GPUs (Graphics Processing Unit) are purpose-built for parallel processing. Their strength lies in managing multiple parallelizable tasks simultaneously. They employ simpler control logic optimized for parallel operations. GPUs stand out in scenarios that demand high compute density, thanks to their numerous execution units. They often adopt the Single Instruction Multiple Data (SIMD) architecture, enabling a single instruction to operate on multiple data elements concurrently. This architecture makes GPUs highly efficient for parallel tasks, such as graphics rendering, video processing, scientific simulations, and machine learning.

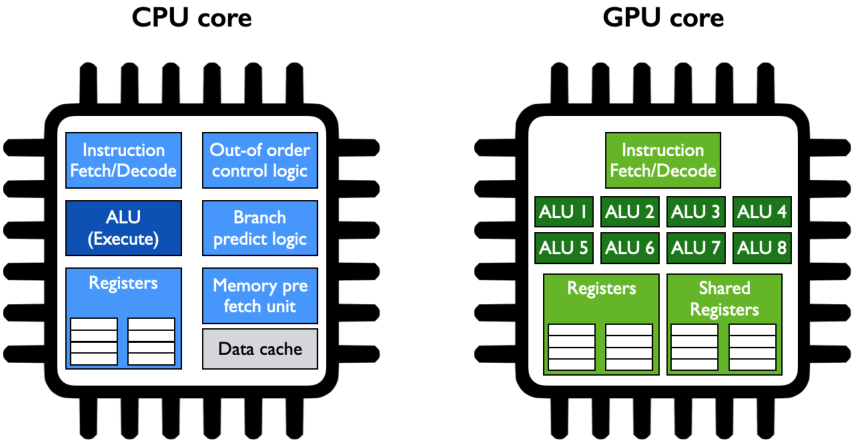

Figure 2.22: Schematic representation of the most common CPU and GPU core architectures. The CPU typically has more complex control logic, such as branch prediction and memory pre-fetching, being more optimized for serial tasks, whereas the GPU is more densely populated with execution units (ALUs) that can run in parallel.

CPUs are versatile and well-suited for general-purpose computing tasks that involve intricate control logic. On the other hand, GPUs excel in parallel processing and are commonly utilized in applications that benefit from simultaneous processing of large datasets. Table 2.1 summarizes the main differences between these two processing units. The choice between a CPU and a GPU is determined by the specific requirements of the application, with both playing vital roles in the field of computing.

Modern CPUs are now incorporating elements traditionally associated with GPUs, such as increasing the number of execution units and adopting SIMD-like capabilities, allowing them to better handle parallel tasks. On the other hand, GPUs are evolving to become more programmable, extending their utility beyond graphics rendering to tasks involving complex control logic. This convergence is particularly evident in applications like machine learning, where a mix of CPU and GPU processing is common.

In fact, GPU accelerator boards are now employed in supercomputers to the point where some of the most powerful machines nowadays are GPU-based systems.

CPU (Central Processing Unit)	**GPU (Graphics Processing Unit)**
Low Compute Density Complex control logic Optimized for serial (scalar) tasks: · Fewer execution units · Higher Clock Speeds	High Compute Density Simple control logic Optimized for parallel tasks: · Many execution units · Single Instruction Multiple Data (SIMD)

Table 2.1: Comparison of CPU and GPU Features

2.6.3.A Programming in a GPU

NVIDIA is an American technology company mostly known for its contributions to the graphics processing unit (GPU) industry. It has become a global leader in GPU design, development, and manufacturing, sharing the spotlight with competitors such as AMD. CUDA (Compute Unified Device Architecture) is a parallel computing platform by NVIDIA that harnesses the computational power of

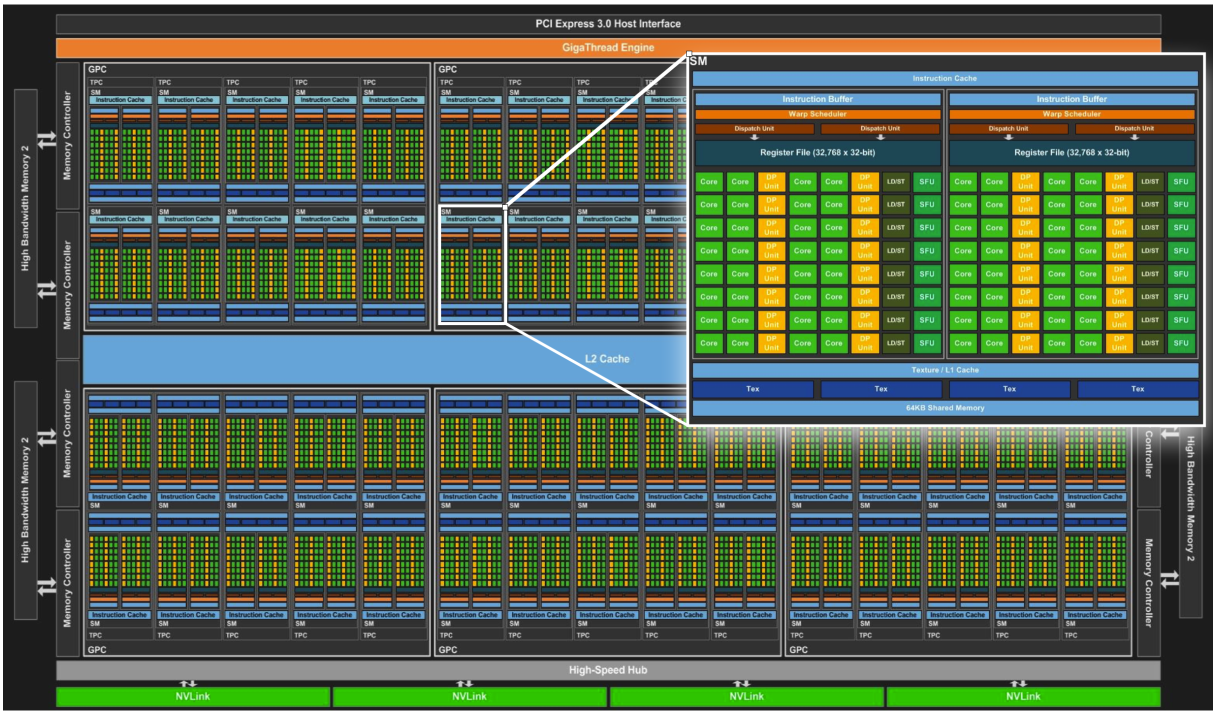

Figure 2.23: Block diagram of a GP100 Board and Streaming Multiprocessor.

GPUs. It provides a programming model for creating highly efficient parallel applications and libraries for common tasks.

One significant drawback of CUDA is its platform dependency. It is specific to NVIDIA GPUs, limiting portability, as code developed for CUDA cannot run on non-NVIDIA GPUs, like AMD devices. Additionally, CUDA is owned and maintained by NVIDIA, which means that its development and evolution are controlled by the company. This proprietary nature can restrict choices for developers and researchers seeking open standards or alternative platforms.

Nevertheless, CUDA provides developers with full control of GPU resources, enabling them to finely tune applications for optimal performance. This level of control allows for low-level optimizations, making it possible to achieve maximum efficiency for specific tasks and GPU architectures. Therefore, we decided to use CUDA to make a GPU compatible version of the radiation diagnostic.

A deeper understanding of how a GPU board works can be obtained by looking at a specific case. Figure 2.23 shows all the components in a GPU following the Pascal GP100 architecture. The GP100 architecture consists of several key components, including Graphics Processing Clusters, Texture Processing Clusters, Streaming Multiprocessors, and memory controllers. A complete GP100 unit comprises six Graphics Processing Clusters, 60 Pascal Streaming Multiprocessors, 30 Texture Processing Clusters (each with two Streaming Multiprocessors), and eight 512-bit memory controllers (for a total of 4096 bits).

Within each Graphics Processing Cluster, there are 10 Streaming Multiprocessors, and each Streaming Multiprocessor is equipped with 64 CUDA Cores and 4 texture units. With a total of 60 Streaming Multiprocessors, GP100 boasts 3840 single-precision CUDA Cores and 240 texture units. Additionally, each memory controller is associated with 512 KB of L2 cache, and each High Bandwidth Memory 2 (HBM2) DRAM stack is governed by a pair of memory controllers. In total, the GPU offers a combined

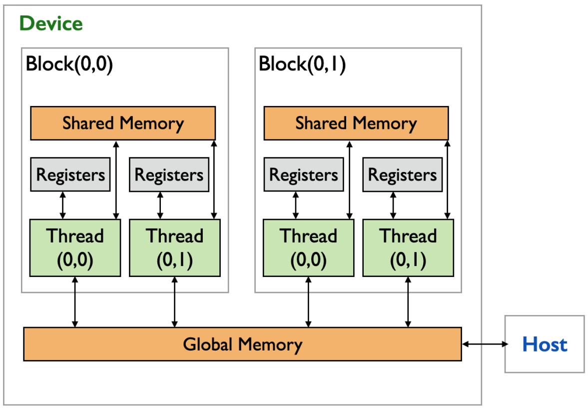

Figure 2.24: Memory hierarchy in CUDA.

4096 KB of L2 cache.

A streaming multiprocessor is the equivalent to the GPU core shown in Figure 2.22. In this case, each Streaming Multiprocessor within the GP100 architecture is equipped with 32 CUDA Cores dedicated to double-precision (FP64) calculations. Notably, this allocation is precisely half of the FP32 single-precision CUDA Cores. In a complete GP100 GPU, there are a total of 1920 FP64 CUDA Cores. A schematic representation of a GP100 Streaming Multiprocessor can be found of Figure 2.23. We can see that most of its components are CUDA cores with either single (referred to as "Cores") or double precision (referred to as "DP Units"). The rest of the board is composed of components that take care of the instructions and memory components such as registers, cache or shared memory.

While a GPU can significantly accelerate certain workloads, by performing parallel operations in large sets of data, proper memory management and communication are vital for realizing its full computational potential. Efficient memory communication within the memory hierarchy is then a critical aspect of CUDA programming. The memory hierarchy in CUDA consists of various memory spaces, including global memory, shared memory, and registers, each with unique characteristics, shown in Figure 2.24:

– **Global Memory:** This is the largest, but slowest memory in the hierarchy. Efficient data transfers to and from global memory are vital to minimize latency and ensure data availability for threads. Managing data locality and access patterns can significantly impact global memory performance.

– **Shared Memory:** Shared memory is a small, fast, on-chip memory space shared among threads within a thread block. Effective usage of shared memory reduces latency and enhances data sharing among threads, leading to better memory hierarchy utilization.

– **Registers:** Registers are ultra-fast, on-chip memory elements where thread-specific data is stored. Efficient use of registers helps minimize memory latency and is critical for achieving high-performance CUDA kernels.

Optimizing memory communication within this hierarchy is crucial for maximizing GPU-accelerated application performance.

A CUDA kernel is a fundamental component of GPU programming that encapsulates a specific task designed for execution on a Graphics Processing Unit (GPU). Kernels are similar to specialized functions but are crafted to leverage the parallel processing power of the GPU. These parallel tasks are executed concurrently by multiple threads, which act as individual workers. When a kernel is launched, it orchestrates the simultaneous execution of these threads, and each thread performs the same operation on different data elements.

Threads executing kernel operations are organized into groups called "thread blocks", and several of these blocks form a "grid." This hierarchical arrangement provides a way to manage and coordinate the execution of threads. In the example of Figure 2.24, we show a kernel with 2 thread blocks (block 0,0 and 0,1) with 2 threads each. Although each thread is allocated to, and runs, in a single CUDA core, the CUDA scheduler can manage thread allocation such that a single core can deal with many threads sequentially.

Kernels are intricately managed by the CPU, referred to as the host, which controls various aspects of their execution. The host is responsible for allocating memory on the GPU, transferring data between the CPU and GPU, and launching kernels as needed. Kernels are finely tuned to harness the GPU's architectural features, such as its memory hierarchy and numerous parallel processing units.

Depending on the kernel design, each thread may require the use of more of the GPU resources, such as memory registers. In a GPU, there is typically a fixed number of registers per core, so if a core is running a thread that requires the use of more registers, it needs to "borrow" registers from other cores. Essentially, this means that both cores can not perform their operations simultaneously, hindering performance. This is an example of the concept of CUDA occupancy, which refers to the measure of how effectively a GPU is being utilized during the execution of a CUDA kernel. It quantifies the degree to which the GPU's resources, such as its streaming multiprocessors (SMs) and registers, are being utilized by the threads running the kernel.

Higher occupancy indicates that the GPU is operating more efficiently, with more threads executing in parallel. Occupancy can be influenced by various factors, including the number of threads per block, the amount of shared memory used, and the register usage per thread block.

Optimizing kernel occupancy is crucial for achieving high-performance GPU computations. It involves finding the right balance between the number of threads, shared memory, and registers used to fully utilize the GPU's capabilities while avoiding resource contention and underutilization.

2.6.3.B GPU implementation of RaDiO

We added GPU compatibility RaDiO using CUDA taking all these factors in consideration. We started with post-processing version of the code, which we renamed RaDi-x as it could be used to obtain radiation from trajectory files calculated by any simulation code and not just OSIRIS. This version uses the pre-calculated trajectories of charged particles to calculate radiation in a set of detector cells.

The CPU implementation of RaDiO uses a hybrid distributed/shared memory strategy to parallelize computations using MPI and OpenMP. The radiation calculation algorithm featured in Algorithm 2.1 is performed every time step of the trajectory. It has two main loops that are totally independent and thus parallelizable: one that circles through the N_p particles and another one that, for each particle, circles through the N_c detector cells, performing $\sim N_p N_c$ operations. While the particle loop can only be

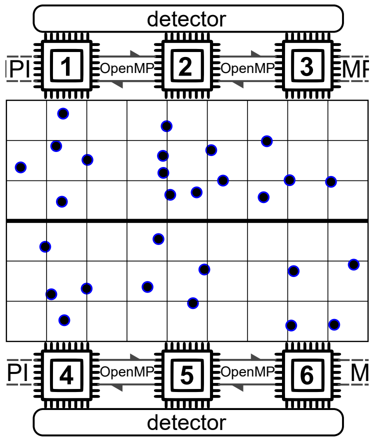

Figure 2.25: Distributed/shared memory hybrid parallelization. Each group of CPUs shares a detector object and is responsible for the calculations of a different group of particles. The CPUs in each group are responsible for the calculations in different regions of the detector

parallelized using distributed memory parallelization (each processor or group of processors has access to a different copy of the detector) due to concurrence problems that arise when two or more particles deposit radiation in the same detector cell at the same time, the detector loop can be parallelized using shared memory parallelization (each processor has access to a different region of the same detector)

Distributed-shared memory hybrid parallelization is shown in Figure 2.25. This scheme assigns a copy of the detector object to each group of CPUs which take care of the calculations for a subset of particles. The CPUs within each subgroup, act as shared memory processors share the same detector object, but each one only accesses a distinct memory region. In practice, the detector copy is split spatially among the CPUs. This is made possible by the total independence of the calculations in the spatial loop.

Whenever the code reports the detector, each copy is summed into a single detector using MPI before writing the data to the disk. This method almost fully avoids communications between processors during the rest of the simulation and therefore does not affect the overall parallel efficiency.

In CUDA, the implementation follows a similar strategy: The many CUDA cores inside a GPU act as shared memory processors, and, if possible, each GPU is assigned a subset of the radiative particles and acts as a distributed memory processor, having a copy of the detector object.

This way, a natural way of implementing a GPU compatible program to calculate radiation from a trajectory file would be to have the CPU loop through every trajectory in the file and through all its timesteps. At each timestep the CPU would load the necessary information to the GPU and launch a kernel to calculate and deposit radiation in all the cells in the detector. This approach, which we labelled "naive", is summarized in Algorithm 2.3. When we compile this kernel in a Tesla P100 GPU board which follows the Pascal GP100 architecture, we find that this kernel uses exactly 32 registers per thread, which is the maximum number of registers we can allocate to each thread while maintaining full occupancy. However, launching a CUDA kernel typically takes an overhead of approximately 10 μs, and doing it every timestep for every trajectory can quickly hinder performance, especially for detectors with fewer spatial cells.

Algorithm 2.3 Naive radiation calculation CUDA

for all *particle* **in** track **do**
  for all timestep **in** track **do**
    procedure RADIATIONCALCULATOR KERNEL $(\beta, \dot{\beta}, x_{part})$
      $R \leftarrow \text{distance}(particle, cell) = |\mathbf{x_{part}} - \mathbf{x_{cell}}|$
      $\mathbf{n} \leftarrow \text{direction}(particle, cell) = (\mathbf{x_{part}} - \mathbf{x_{cell}})/R$
      $t_{det} \leftarrow R/c + t$
      $t_{det,prev} \leftarrow R_{prev}/c + t - dt$
      if $t_{\text{det}}min < t_{\text{det}} < t_{\text{det}}max$ **then**
        RADIATIONINTERPOLATOR$(\mathbf{E}(\mathbf{n}, \beta, \dot{\beta}), t_{\text{det}}, t_{\text{det,prev}})$
      end if
    end procedure
  end for
end for

It is, however, possible to avoid launching kernels so often if we loop through the timesteps inside the GPU. This implies transferring the full trajectory data to the GPU global memory and adding more complexity to the kernel, which in this case needs to perform a loop. This approach, which we labelled "Track Loop", is summarized in Algorithm 2.4. Due to the increased complexity, this kernel now requires each thread to use 48 registers, only allowing 68% occupancy of the GPU.

Algorithm 2.4 Track loop in GPU algorithm

procedure RADIATIONCALCULATOR
  for all *particle* **in** simulation **do**
    $\beta = \text{velocity}(particle) = \mathbf{p}/\sqrt{|\mathbf{p}|^2 + 1}$
    $\dot{\beta} = \text{acceleration}(particle) = (\beta - \beta_{prev})/dt$
    for all *cell* **in** detector **do**
      $R = \text{distance}(particle, cell) = |\mathbf{x_{part}} - \mathbf{x_{cell}}|$
      $\mathbf{n} = \text{direction}(particle, cell) = (\mathbf{x_{part}} - \mathbf{x_{cell}})/R$
      $t_{det} = R/c + t$
      $t_{det,prev} = R_{prev}/c + t - dt$
      if $t_{\text{det}}min < t_{\text{det}} < t_{\text{det}}max$ **then**
        RADIATIONINTERPOLATOR$(\mathbf{E}(\mathbf{n}, \beta, \dot{\beta}), t_{\text{det}}, t_{\text{det,prev}})$
      end if
    end for
  end for
end procedure

Nevertheless, we can reduce register use by relying on shared memory. Instead of having each thread directly load trajectory data from global memory, we can periodically load chunks of data to shared memory and then loop through those chunks. Apart from reducing register usage, this also avoids regular global memory access (which is slow) while privileging shared memory access (which is faster). This approach, which we labelled "Shared Memory", is summarized in Algorithm 2.5.

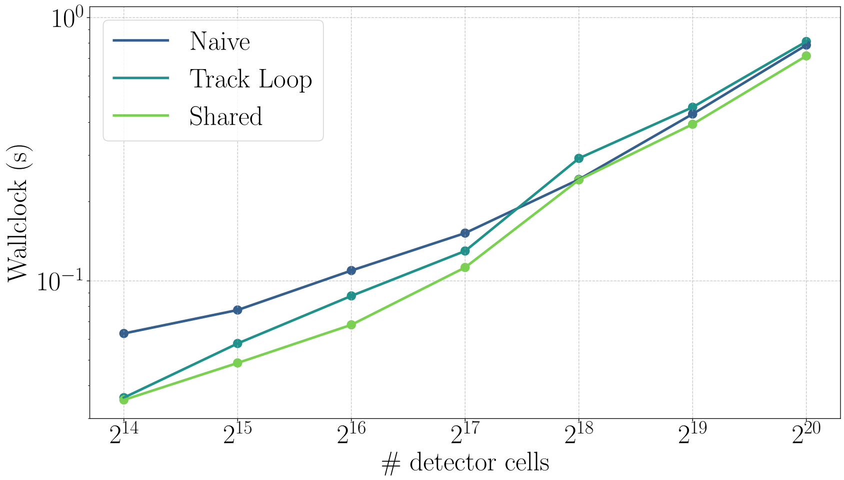

Figure 2.26: Performance comparison of CUDA kernel designs (Naive, Track Loop, and Shared Memory) for Varying Workloads. The plot illustrates the relative performance of three different CUDA kernel designs across a range of detector sizes.

Algorithm 2.5 Shared Memory algorithm

for all *particle* **in** track **do**
  procedure RADIATIONCALCULATOR KERNEL (TRACK)
    for all timestep **in** track **do**
      $R \leftarrow \text{distance}(particle, cell) = |\mathbf{x}_{\mathbf{part}} - \mathbf{x}_{\mathbf{cell}}|$
      $\mathbf{n} \leftarrow \text{direction}(particle, cell) = (\mathbf{x}_{\mathbf{part}} - \mathbf{x}_{\mathbf{cell}})/R$
      $t_{det} \leftarrow R/c + t$
      $t_{det,prev} \leftarrow R_{prev}/c + t - dt$
      if $t_{\text{det}}min < t_{\text{det}} < t_{\text{det}}max$ **then**
        RADIATIONINTERPOLATOR$(\mathbf{E}(\mathbf{n}, \beta, \dot{\beta}), t_{\text{det}}, t_{\text{det,prev}})$
      end if
    end for
  end procedure
end for

After implementing these three kernel designs, we performed benchmarks in a Tesla P100 GPU board to determine which one would be more suited to our application. We used these three kernel designs to calculate radiation from a trajectory file with only one particle and 26041 timesteps in a 2D spherical detector. We increased the number of spatial cells in the detector from 16384 (2^{14}) to 1048576 (2^{20}). The results are shown in Figure 2.26.

For smaller workloads, the kernel launch overhead associated with the "Naive" approach significantly impacts performance, making it the slower approach by a factor of ~ 3. In the "Track Loop" design, threads loop through the entire track, eliminating the need for separate kernel launches and avoiding kernel launch overhead, so it is faster than the "Naive" approach. Nevertheless, as we increase the workload the overhead becomes less important and the occupancy becomes more relevant, so the "Naive" approach becomes faster than the "Track Loop" approach. The "Shared Memory" design has threads loop through the track in smaller chunks, reducing register usage. It achieves higher occupancy than the "Track Loop", which improves parallelization and GPU utilization. Additionally, it avoids kernel launch overhead by

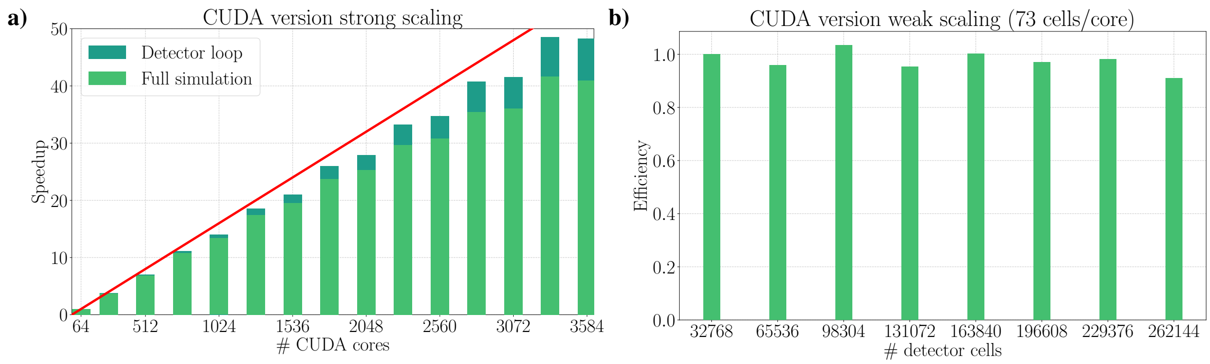

Figure 2.27: Strong (a) and Weak (b) scaling analysis of the GPU version of RaDi-x. The strong scaling tests were performed using a detector with 2^{20} spatial cells.

handling multiple time steps within a single kernel. This combination of factors makes it the fastest kernel, it is consistently the fastest kernel for every detector size, so it is the one we included in the GPU implementation of RaDi-x.

In parallel computing, strong scaling measures how well an algorithm's performance improves as more processors are added while keeping the problem size constant. If execution time decreases proportionally with more processors, it indicates strong scaling efficiency. In contrast, weak scaling assesses how effectively an algorithm handles both larger problem sizes and increased processors, maintaining a constant workload per processor. The goal of weak scaling is to efficiently process larger datasets or perform simulations on more extensive domains. Both concepts are critical for understanding parallel system performance and optimizing their use in diverse applications. We performed further benchmarks using the same trajectory file to determine the Strong Scaling and Weak scaling of this implementation. The results of this analysis are summarized in Figure 2.27.

Regarding strong scaling, it is encouraging to see that the simulation scales well. The almost linear behavior when considering speedup in the "Detector Loop", which takes care of the radiation calculations, is a positive sign. It suggests that adding more resources, such as GPUs or processors, directly translates to improved performance for this specific part of the simulation. Nevertheless, when we take into account the full simulation, which includes reading trajectory data from the file and writing detector data to disk, the code does not scale as well. Serial routines such as CUDA initialization and memory copying can also have a considerable role in the simulation's runtime. The relative impact of these routines, should however, decrease for larger workloads, so we can consider our results to be quite satisfactory.

In fact, the weak scaling analysis shows that the efficiency of our algorithm remains close to 1 as we increase the size of the detector while keeping the number of GPU cores per detector cell constant.

From Figure 2.27 we see that in the strong scaling analysis, we launched kernels with at most 3584 CUDA threads, using up all the CUDA cores in our Tesla P100 board. However, it is possible to launch kernels with more threads than there are available cores. In fact, launching more CUDA threads than available physical cores on a GPU is a common practice to fully utilize the GPU's computing power. When we launch more threads than physical cores, the GPU employs a scheduling mechanism to execute these threads concurrently. The reason for doing this is that GPUs are designed to handle a large number

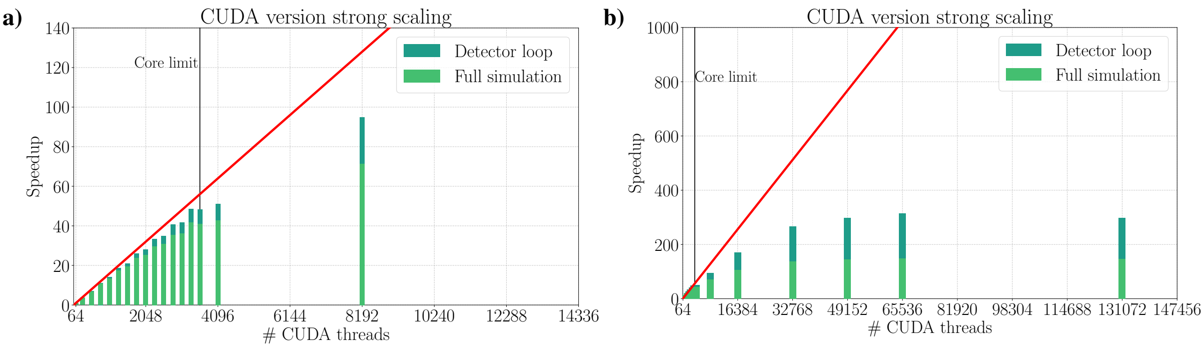

Figure 2.28: Speedup obtained when launching than physical GPU cores.

of threads simultaneously, and not all threads are actively executing at the same time. By launching more threads than cores, we can keep the GPU occupied with work, ensuring that the cores are not idle while waiting for memory access or other operations to complete. However, it's important to note that launching an excessive number of threads can lead to diminishing returns or even decreased performance due to increased overhead from thread management. Figure 2.28 shows the results of going past the physical core limit. There we can see that, while the scaling is no long linear, we still get speedups, ending up with a code that runs 500× faster than the serial CPU version using a single processor.

While the design of the algorithm ensures that increasing the temporal resolution of the detector does not increase the number of operations, as there is no loop performed in the temporal dimension, increasing the number of temporal cells leads to an overall increase of detector size in memory. In the case of 2D detectors with millions of spatial cells, an increased number of temporal cells can quickly make the detector object occupy more space than we can fit inside the GPU memory, typically the limit is on the order of a few to ten GigaBytes.

Nevertheless, the GPU version of RaDi-x is a powerful tool that opens new possibilities for exploring radiation emission in Particle in Cell codes, especially when detectors with a large amount of spatial cells are required. Using a single GPU board, we are able to calculate radiation in millions of spatial cells almost instantly, a feat which was only possible when using computer clusters with hundreds of CPUs.

2.7 Conclusions

The radiation diagnostic for OSIRIS (RaDiO) was successfully implemented, benchmarked and tested in several scenarios, including production runs. While not described here, it should be also be noted that the algorithm was fully parallelized allowing for large simulations. RaDiO is a novel radiation diagnostic that captures the spatiotemporal features of high frequency radiation in PIC codes. A key aspect of our algorithm is the development of a temporal interpolation scheme for depositing radiation. This is essential to preserve the continuous character of radiation emission and to obtain correct values for the amplitude of the radiated fields. The algorithm is general and only requires knowledge about the trajectories of an arbitrarily large ensemble of charged particles ($> 10^6$) thus we can apply it to generally enhance the capabilities of any algorithm that predicts the trajectories of charged particles, apart from PIC codes. We described the implementation of RaDiO into OSIRIS and provided benchmarks with well established theoretical models for synchrotron emission. These comparisons showed excellent agreement, therefore adding a high level of confidence to future runs.

We also provided an illustration where we used RaDiO to probe the spatiotemporal features of radiation emitted in the context of laser reflection by a plasma mirror. At lower laser intensities, RaDiO fully recovers the PIC simulation result. This further confirms the validity of RaDiO in a setting where temporal and spatial coherence effects are critical. A simulation at higher laser intensity demonstrated the generation of high harmonics beyond the predictions of the PIC algorithm, showing that RaDiO allows for a complete characterization of the reflected beam along with all the harmonics, without increasing the overall PIC resolution, and effectively demonstrating that RaDiO can be effectively used to predict high frequency radiation from PIC codes.

RaDiO is a flexible diagnostic tool that can be further expanded to include additional features such as higher order interpolation schemes, for example using an advanced particle pusher recently developed [73], the option to compute the electromagnetic field potentials in addition to the electromagnetic fields, or the capability to convert radiation to/from relativistic Lorentz boosted frames. Although this diagnostic does not interact with the particles, it could also be employed together with a QED code that captures radiation reaction and affects the particle's trajectories and capture radiation compatible with QED effects as long as the emission is purely classical. Because it captures the radiation in space and in time, RaDiO may also be useful in describing the production of spatiotemporally structured beams [74].

3

Radiation from evanescent waves

Contents

3.1 Introduction

Advanced x-ray [75] sources are central to probe and image ultra-fast processes occurring at the atomic and molecular scale [4, 76, 77]. Large scale free electron lasers [13] and synchrotrons [14–16] are amongst the most successful, but efforts have been made to develop smaller and more cost-effective radiation sources in recent years, relying on a plethora of radiation generation mechanisms. For example, high harmonic generation by a plasma mirror [42–46] and Thomson scattering of plasma electrons [47–49], can lead to emission of harmonics up to the x-ray region of an ultra-intense laser pulse. Furthermore, ultra relativistic electrons can be used to obtain transition radiation in the x-ray region [50–53] and betatron radiation from high-energy electrons ($\simeq$ 1 GeV) accelerated by ultra-intense lasers ($a_0 > 1$) in laser plasma accelerators [22–26] routinely achieves keV x-ray beams [27]

Nevertheless, mechanisms capable of producing x-rays from moderately relativistic electron beams ($\gamma \sim 10$) or moderately intense laser pulses ($a_0 < 1$) can open new exciting research opportunities by democratizing access to high energy photon beams. A notable example, Thomson Scattering of a relativistic electron beam by a laser pulse [78, 79], can generate double Doppler shifted versions of the incident laser, producing nm wavelength pulses from a 800nm laser. In this case, for a fixed γ, the emitted wavelength is set by the laser's wavelength, but could it be possible to develop a mechanism to obtain emission at even smaller wavelengths? Here, we address this question by exploring a new light emitting process based on the scattering of an electron from an evanescent wave. Evanescent waves are at the core of plasmonics, where they play a key role in applications ranging from photon induced near-field microscopy [80] to super-resolution microscopy thanks to superlensing effects [81]. These waves were also exploited towards radiation emission in graphene, thanks to a Thomson-scattering effect experienced by electrons that propagate parallel to the evanescent wave [82]. These surface modes are ubiquitous in laser-plasma interaction experiments, namely in those with plasma mirrors, which are commonly used to improve the contrast of high-power laser pulses [83].

The degree of spatial localization of surface waves in the direction normal to the surface is set by the material skin-depth. The skin depth λ_{ev} can be more than an order of magnitude smaller than the wavelength, $\lambda_0 = 2\pi c/\omega_0$, of the laser that excites the evanescent mode. For example, according to the linear dispersion relation for electromagnetic waves in plasma, $\lambda_{\text{ev}} = c/\sqrt{\omega_p^2 - \omega_0^2}$, where ω_0 is the central frequency of the incident laser pulse, $\omega_p = \sqrt{e^2 n_0/m_e \varepsilon_0}$ is the plasma frequency, e the elementary charge, m_e the electron mass, ε_0 the vacuum electric permittivity and n_0 the plasma density. Thus, it can be as short as $\simeq 10$ nm for a plasma density $n_0 \sim 2 \times 10^{23}$ cm^{-3}. This is more than two orders of magnitude below the central wavelength of a typical laboratory laser pulse, where $\lambda_0 \simeq 800$ nm.

In this section, we take direct advantage of the extreme spatial localization of evanescent waves to generate directed x-rays and demonstrate, with theory and through particle-in-cell (PIC) simulations in Osiris [11, 60] complemented by the Radiation Diagnostic for Osiris (RaDiO) [10], that electrons with $\gamma \simeq 10 - 100$ that scatter across a surface wave can produce keV-MeV radiation. Furthermore, we also find that suitably modulated electron bunches can produce a superradiant optical shock. The creation of optical shocks by tilted electron bunches was investigated by Bolotowsky and Ginzburg in

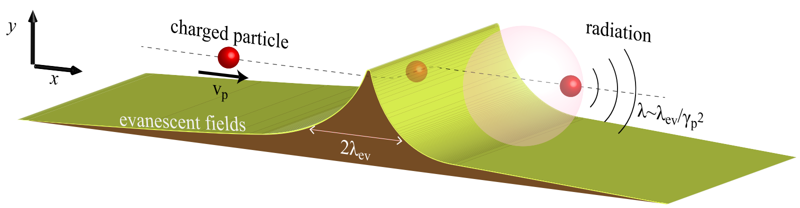

Figure 3.1: Simulation setup and evanescent field. A single particle collides with a localized evanescent field and suffers sharp acceleration, producing radiation.

transition radiation [61], but here we show that, because the radiation from each bunch electron interferes constructively, its intensity scales favorably with the square of bunch particles as in superradiance. More generally, we found that the intersection position between the electron bunch and the evanescent wave can act as a virtual particle, whose trajectory defines key radiation properties, just as if it were a single real particle [84]. This can bring previously unexplored spectral features and coherence in evanescent scattering configurations.

3.2 Single Particle Evanescent Radiation

The electromagnetic vector potential of a standing evanescent wave, $\mathbf{A}_{\text{ev}}$, can adequately characterize the evanescent field structure. In its simplest form, $\mathbf{A}_{\text{ev}}$ may then be given by:

$$\mathbf{A}_{\text{ev}} = A_{0,\text{ev}} \left[1 - \text{sign}(x) \left(e^{-|x|/\lambda_{\text{ev}}} - 1\right)\right] \cos(\omega_{\text{ev}} t)\mathbf{e}_y \equiv A_{\text{ev}}(x,t)\mathbf{e}_y, \tag{3.1}$$

where $A_{0,\text{ev}}$ is the vector potential peak amplitude, ω_{ev} is the evanescent wave frequency, λ_{ev} is its typical scale-length (also denoted by skin-depth), x is the distance along the surface normal, and $\mathbf{e}_y$ is a unit vector tangent to the surface. The green surface in Figure 3.1 is a schematic illustration of the evanescent wave structure.

Owning to its highly localized spatial structure, evanescent waves can impart a strong transverse acceleration to an electron that propagates across the surface fields. Such an intense, albeit localized acceleration, underlies radiation emission in evanescent wave-scattering processes. The acceleration can be deduced from the electron trajectory. Figure 3.1a depicts the trajectory of an electron (red sphere) moving across an evanescent wave (green surface).

We can determine the electron trajectory by using the conservation of the transverse canonical momentum for an electron initially at rest, since the vector potential $\mathbf{A}_{\text{ev}}$ is independent of y and z:

$$\begin{aligned} \mathscr{P}_\perp &= \mathbf{p}_\perp - eA_{0,\text{ev}} = 0 \\ \Rightarrow \mathbf{p}_\perp &= eA_{0,\text{ev}} \end{aligned} \tag{3.2}$$

Here $\mathbf{p}_\perp = m_e \gamma_p \mathbf{v}_\perp = m_e \gamma \mathrm{d}\mathbf{r}_\perp/\mathrm{d}t$ is the transverse electron momentum, hereafter assumed to be along $\mathbf{e}_y$. $\mathbf{p}_{\perp,0} \equiv \mathbf{p}_y(t=0)$, m_e is the electron mass, and γ the relativistic factor. To integrate the equation of motion, we assume $\mathbf{p}_{\perp,0} = 0$, and ignore variations in the particle longitudinal momentum, a valid assumption as long as the evanescent mode amplitude is sufficiently small (i.e. $|e\mathbf{A}_{\text{ev}}/(m_e c)| \ll \gamma$). We also assume that the evanescent wave oscillates slowly ($\omega_{\text{ev}} \ll v_x/\lambda_{\text{ev}}$), leading to:

$$
\begin{aligned}
\frac{\mathrm{d}v_y}{\mathrm{d}t} =& \frac{1}{\gamma m_e}\frac{\mathrm{d}p_y}{\mathrm{d}t} = \frac{e}{\gamma m_e}\frac{\mathrm{d}A_{\mathrm{ev}}}{\mathrm{d}t} \equiv a_y \\
=& \frac{e}{\gamma m_e}A_{0,\mathrm{ev}}e^{-v_x|t|/\lambda_{\mathrm{ev}}}\left[\frac{v_x\cos(\omega_{\mathrm{ev}}t)}{\lambda_{\mathrm{ev}}} + \omega_{\mathrm{ev}}\sin(\omega_{\mathrm{ev}}|t|)\right] \\
\simeq& \frac{ev_xA_{0,\mathrm{ev}}\exp(-v_x|t|/\lambda_{\mathrm{ev}})}{\gamma_0 m_e\lambda_{\mathrm{ev}}} = \frac{v_xv_{y0,\mathrm{ev}}\exp(-v_x|t|/\lambda_{\mathrm{ev}})}{\lambda_{\mathrm{ev}}}
\end{aligned}
\tag{3.3}
$$

where we used $x = v_p t$ to relate the longitudinal electron position with the interaction time t. Equation (3.3) shows that the transverse electron acceleration grows as λ_{ev} decreases. Hence, even though an evanescent wave may not change the electron trajectory appreciably (due to its high spatial localization), it can still impart a strong acceleration to produce high energy radiation.

To make quantitative predictions, we consider the radiated energy in the far field (I_{rad}), per unit frequency ω, per solid angle Ω, which, for an arbitrary electron trajectory $\mathbf{r}(t)$, is generally given by the Liénard-Wiechert potentials [85, 86]:

$$
\frac{\mathrm{d}^2 I_{\mathrm{rad}}}{\mathrm{d}\omega\mathrm{d}\Omega} = \frac{e^2}{4\pi^2 c}\left|\int_{-\infty}^{+\infty}\frac{\mathbf{n}\times\left[(\mathbf{n}-\boldsymbol{\beta})\times\dot{\boldsymbol{\beta}}\right]}{(1-\boldsymbol{\beta}\cdot\mathbf{n})^2}e^{i\omega[t-\mathbf{n}\cdot\mathbf{r}(t)/c]}\mathrm{d}t\right|^2, \tag{3.4}
$$

where c is the speed of light, t the time of emission (retarded time), and $\mathbf{n}$ the unit vector that points to the observation direction. In spherical coordinates, $\mathbf{n} = [\sin(\theta)\cos(\varphi), \sin(\theta)\sin(\varphi), \cos(\theta)]$, where φ is the angle with the x-axis in the $x-y$ plane, and θ is the angle with the z axis. In addition, $\boldsymbol{\beta} = \mathbf{v}/c$ is the electron velocity normalized to c, and $\dot{\boldsymbol{\beta}} = (1/c)\mathrm{d}\mathbf{v}/\mathrm{d}t$ the corresponding acceleration.

For $\mathbf{n} = (1,0,0)$ the spectrum becomes:

$$
\left|\frac{\mathrm{d}^2 I_{\mathrm{rad}}}{\mathrm{d}\omega\mathrm{d}\Omega}\right|_{\mathbf{n}=\mathbf{e_x}} = \frac{e^2}{4\pi^2 c}\left|\int_{-\infty}^{+\infty}\frac{\dot{\beta}_y(\beta_x-1)-\dot{\beta}_x\beta_y}{(1-\beta_x)^2}e^{i\omega[t-x(t)/c]}\mathrm{d}t\right|^2, \tag{3.5}
$$

The full particle trajectory, given by Equation (3.3), is too complex for a symbolic integration of Equation (3.4). To allow a fully analytical treatment, while still retaining all the essential spectral features, we ignore the transverse electron displacement in the complex exponential in Equation (3.4). This assumption holds as long as the radiation phase accumulated during the transverse electron motion, $\Delta\phi$, is sufficiently small. As a guide, $\Delta\phi = n_\perp(\omega/c)y(t) \lesssim 2\pi$, where $n_\perp$ is the unit vector along y, and $y(t)$ is the transverse electron displacement. We also consider $\dot{\beta}_x \sim 0$. Under these assumptions, Equation (3.5) can be simplified to yield:

$$
\begin{aligned}
\left|\frac{\mathrm{d}^2 I_{\mathrm{rad}}}{\mathrm{d}\omega \mathrm{d}\Omega}\right|_{\mathbf{n}=\mathbf{e_x}} &= \frac{e^2}{4\pi^2 c}\left|\int_{-\infty}^{+\infty} \frac{\dot{\beta}_y}{\beta_x - 1} e^{i\omega[t-x(t)/c]}\mathrm{d}t\right|^2 \\
&= \frac{e^2 v_x^2 \beta_{y0,\mathrm{ev}}^2}{4\pi^2 c \lambda_{\mathrm{ev}}^2}\left|\int_{-\infty}^{+\infty} \frac{e^{-v_x|t|/\lambda_{\mathrm{ev}}}}{\beta_x - 1} e^{i\omega[t-\beta_x t]}\mathrm{d}t\right|^2 \\
&= \frac{e^2}{4\pi^2 c}\left|\frac{2\beta_{y0,\mathrm{ev}}^2}{(\beta_x - 1) + (\beta_x - 1)^3\,\omega^2 \lambda_{\mathrm{ev}}^2 / v_x^2}\right|^2 \\
&\underset{1-\beta_p \to \gamma_p^{-2}/2}{\simeq} \frac{e^2}{4\pi^2 c}\left|\frac{4\beta_{y0}\gamma_p^2}{1+\omega^2\lambda_{\mathrm{ev}}^2/\left(2\gamma_p^2 v_x\right)^2}\right|^2,
\end{aligned}
\tag{3.6}
$$

The single particle spectrum emitted along the forward x-direction [$\mathbf{n} = (1,0,0)$] is then given by:

$$
\left|\frac{\mathrm{d}^2 I_{\mathrm{rad}}}{\mathrm{d}\omega \mathrm{d}\Omega}\right|_{\mathbf{n}=\mathbf{e_x}} = \frac{e^2}{4\pi^2 c}\left|\frac{4\beta_{y0}\gamma_p^2}{1+\omega^2\lambda_{\mathrm{ev}}^2/\left(2\gamma_p^2 v_x\right)^2}\right|^2, \tag{3.7}
$$

where $\beta_{y0} = A_{\mathrm{ev},0}/(\gamma_p c)$ and $\beta_p = v_p/c$. Equation (3.7) shows that an electron moving across an evanescent wave produces a broadband Lorentzian spectrum. In the time domain, the profile of the radiation that gives rise to spectrum given by Equation (3.7) corresponds to that of an evanescent field $E_{\mathrm{rad}} \propto \exp\left(-c|t|2\gamma_p^2/\lambda_{\mathrm{ev}}\right)$. This unusual field profile can be regarded as a flying electromagnetic copy of the surface wave, compressed by a double Doppler shift.

While the evanescent mode amplitude controls the peak radiated intensity through β_{y0}, the corresponding spectral width, $\Delta\omega$, is proportional to $\Delta\omega \propto 2\gamma_p^2(c/\lambda_{\mathrm{ev}})$. Accordingly, solid plasma targets with various densities, or different non-ionized materials, each with a characteristic λ_{ev}, can produce measurably different spectra. As a figure of merit, the typical radiation wavelength, λ_{rad}, is then proportional to the evanescent wave skin-depth compressed by a double Doppler shift factor. Hence, with $\lambda_{\mathrm{ev}} \simeq 10$ nm, even a moderately relativistic electron, with a relativistic factor $\gamma_p = 10$, could radiate at $\lambda_{\mathrm{rad}} \propto \lambda_{\mathrm{ev}}/(2\gamma_p^2) \simeq 0.1$ nm.

To verify this prediction, we ran numerical simulations using the particle-in-cell (PIC) code Osiris together with the Radiation Diagnostic for Osiris (RaDiO). We simulated a single particle with $\gamma = 100$ (with velocity along the horizontal direction x) colliding with an externally imposed a magnetic field evanescent wave characterized by the following expression:

$$
B_z(x) = \begin{cases} 0.2\exp\left[(x-10)/\lambda_{\mathrm{ev}}\right], & \text{if } x < 10 \\ 0.2\exp\left[(10-x)/\lambda_{\mathrm{ev}}\right], & \text{if } x > 10 \end{cases} \tag{3.8}
$$

with $\lambda_{\mathrm{ev}} = 0.05$ c$/\omega_0$, ω_0 being a normalizing frequency. The simulation box had a length of 11 c$/\omega_0$ (459 cells) and a width of 24 c$/\omega_0$ (359 cells). We tracked the radiation in a far-away detector with only one spatial cell aligned with $\mathbf{e}_x$ and temporal resolution $dt_{\mathrm{det}} = 2 \times 10^{-8}$ $1/\omega_0$ about 10^4 times smaller than the PIC simulation temporal resolution. We compared the spectrum of radiation with the theoretical prediction of Equation (3.7). Figure 3.2 shows the results of that simulation. The relevant quantities for

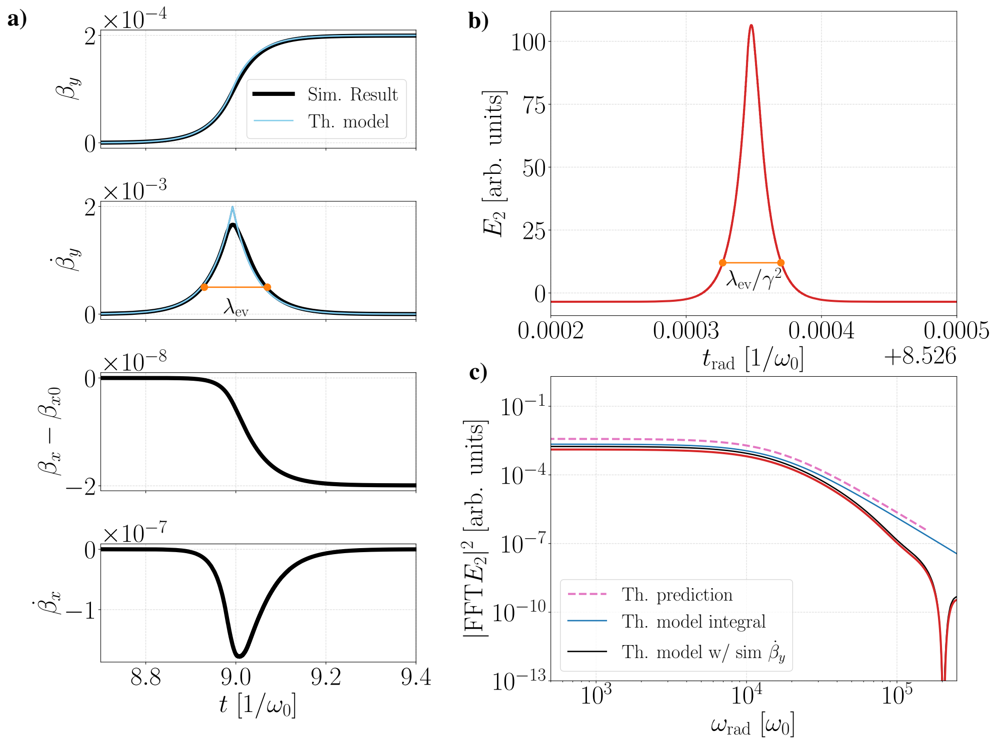

Figure 3.2: Evanescent radiation emission by single particle. a) Spectrum of radiation emitted on-axis and comparison with theoretical predictions. b) Radiation spatial intensity distribution. c) Temporal profile of the radiation emitted on-axis.

the spectrum calculation are plotted in the left column. We can see that the longitudinal component of both the velocity and acceleration suffer a very small variation, small enough to be neglected, and that the perpendicular component of velocity shows an almost perfect agreement with the theoretical expression. The perpendicular acceleration in the simulation, however, displays a considerable deviation from the theoretical model, where instead of a sharp transition in the evanescent surface, we see a smooth curve, later we will see that this has some impact in the quality of the predicted spectrum of radiation.

The temporal profile of the emitted radiation can be seen on Figure 3.2a where its made clear that the evanescent radiation is flying copy of the evanescent wave profile, compressed in time through double Doppler shifting by a factor of γ^2. The frequency spectrum of radiation is shown on Figure 3.2b. There, we can see that the theoretical model of Equation (3.7) predicts the overall trend of the frequency spectrum, with excellent agreement on the cutoff frequency, but tends to overestimate the radiated intensity for larger frequencies. We can verify, however, that the expression in Equation (3.7) is the correct result if the trajectory is exactly as we assumed, as the numerical integral of Equation (3.23) yields very similar results (pink and blue lines). However, as we alluded to previously, the major deviation from theory to simulation is the y component of acceleration $\dot\beta_y$. In fact, if we do the numerical integral with the trajectory components exactly as described in the theoretical model, but use $\dot\beta_y$ from the simulation, we get a spectrum that agrees almost perfectly with the one on the simulation.

Nevertheless, Equation (3.7) can still predict the relevant features of the spectrum, while a full symbolic integration of the spectrum including the correction for the perpendicular component of the acceleration remains out-of reach.

Equation (3.7) also shows that evanescent wave scattering produces a radiation spectrum with noticeably distinct properties from other known radiation mechanisms, sharing some similarities, however, with transition radiation [64] whose energy spectrum is given by Equation (3.9) below:

$$d^2 I_{\mathrm{rad}}/(d\omega d\Omega) \propto \omega_p^4 \gamma_p^6 \theta^2 / \left(\omega^4 (1+\gamma_p^2\theta^2)^4\right) \tag{3.9}$$

The radiated spectrum decays with ω^{-4} in both cases. However, whereas in transition radiation the spectral intensity always decays with ω^{-4}, in evanescent radiation it only decays with ω^{-4} for $\omega \gg 2\gamma_p^2\sqrt{\omega_p^2-\omega_0^2}$. Thus, in the case of evanescent radiation, the decay in intensity happens only at higher frequencies. Additionally, transition radiation does not lead to on-axis emission, whereas evanescent wave scattering produces highly directional radiation, along the main propagation axis (x in the present case).

3.2.1 Laser Reflection

In classical electrodynamics, evanescent fields refer to the electromagnetic fields that appear at the surface of a reflective material when an electromagnetic wave gets reflected. A natural way of generating an evanescent wave would then be to reflect a laser in a surface. These fields decay exponentially inside the material as the wave is unable to propagate. In a plasma, only waves with a frequency lower than the plasma frequency are reflected.

The expression for the evanescent mode vector potential adequately models surface modes in mirrors. It also holds in plasma, provided that the plasma electrons are non-relativistic. The width λ_{ev} depends on the material where the surface mode lives. In a plasma, for example, $\lambda_{\mathrm{ev}} = c/\sqrt{\omega_p^2-\omega_0^2}$, where ω_p is the plasma frequency.

If a particle co-propagating with the laser has a perpendicular momentum consistent with the lasers vector potential, such that the initial canonical momentum is $\mathscr{P}_\perp = 0$, then as the laser gets reflected, the particle will lose all its transverse momentum as it passes through the evanescent interface.

Figure 3.3 illustrates the typical features of radiation obtained from evanescent wave scattering when using a laser pulse to generate the evanescent wave. The radiation spectrum on-axis is shown in Figure 3.3a and the time integrated radiated intensity on Figure 3.3b. These results were obtained from numerical simulations with the particle-in-cell (PIC) code Osiris and with the Radiation Diagnostic for Osiris (RaDiO). The resolution of the PIC simulation box is 0.052×2.4 $(\mathrm{c}/\omega_0)^2$ in the (x,y) directions, and the time step is $dt_{\mathrm{PIC}} = 0.004\ \omega_0^{-1}$. A virtual spherical detector records the radiation in time. The detector is placed in the far field and is aligned with the longitudinal x direction. The detector angular aperture is $\Delta\varphi = 20$ mrad, and temporal resolution $dt_{\mathrm{rad}} = 8\times 10^{-7}\ \omega_0^{-1} \sim dt_{\mathrm{PIC}}/2\gamma_p^2$. In this simulation a single electron with $\gamma_p = 80$ scatters through an evanescent mode with $A_{\mathrm{ev},0} = 0.2 m_e c/e$ and $\lambda_{\mathrm{ev}} \simeq 0.17\ c/\omega_0$. We considered two types of evanescent modes, one created by a plasma mirror reflecting a linearly polarised laser pulse and an externally imposed standing mode like the one described by Equation (3.1). The laser pulse's normalized vector potential is $a_0 = eA_0/(m_e c) = 0.2$ and spot size $W_0 = 6\ \lambda_0$. The plasma mirror density is $n_p = 32 n_{\mathrm{crit}}$, where $n_{\mathrm{crit}} = \omega_0^2 m_e \varepsilon_0/e^2$ is the critical plasma density. The initial

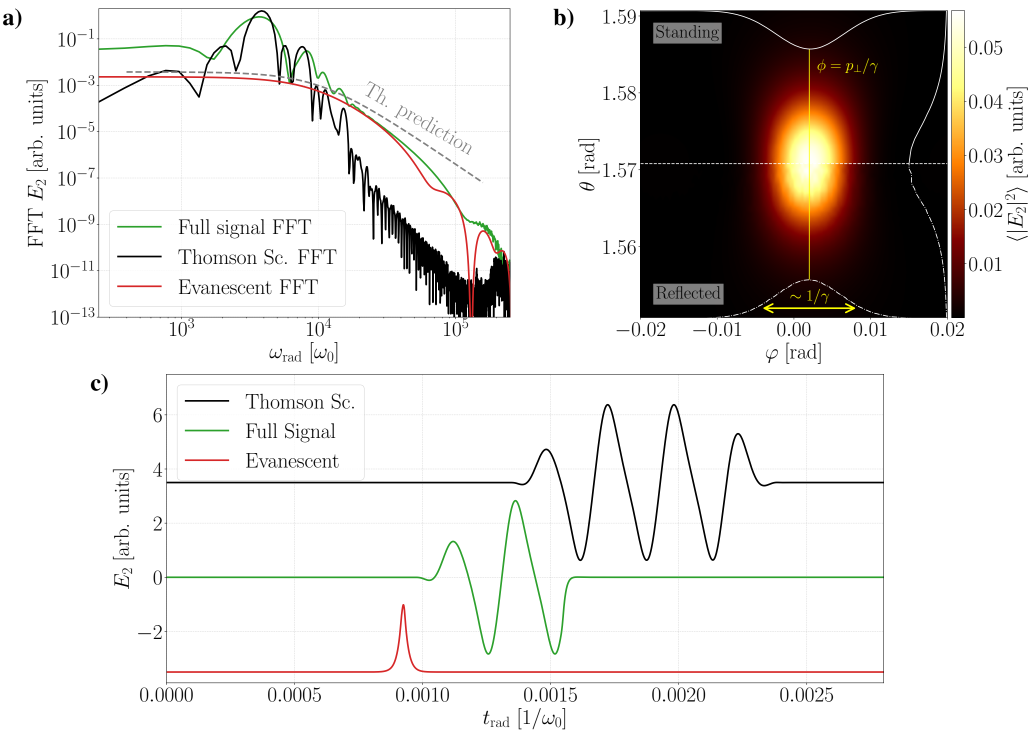

Figure 3.3: Simulation results of the radiation generated during scattering of a single electron by and evanescent mode create through laser reflection. a) Temporal profile on the emitted radiation and its components. b) Frequency spectrum of the emitted radiation. Contributions from the evanescent and pre-evanescent regimes are plotted separately from the full spectrum. c) Spatial intensity distribution of the emitted evanescent radiation at a far away spherical detector.

electron transverse momentum, $p_y(t=0) = 0.16 m_e c$, matches the normalized laser vector potential at its injection position.

We utilized two spherical detectors with $R = 10^5 c/\omega_p$. The first detector, used for frequency spectrum analysis, had a time resolution of $dt_{\rm rad} = 8 \times 10^{-7}\ \omega_0^{-1}$ (65536 temporal cells) and one spatial cell on-axis. The second detector, used for spatial intensity distribution analysis, had a time resolution of $dt_{\rm rad} = 4 \times 10^{-5}\ \omega_0^{-1}$ (8192 temporal cells) and an aperture of $\Delta\varphi = \Delta\theta = 20$ mrad, with 320 cells on $\mathbf{e}_\varphi$ and 32 cells on $\mathbf{e}_\theta$ for spatial spectrum analysis.

In the plasma mirror configuration, the electron first scatters in the standing wave created by the superposition of the incident and reflected laser (Thomson scattering), before reaching the evanescent wave at the plasma surface (evanescent wave scattering). The full radiation spectrum (green) in Figure 3.3a then contains Thomson scattering (black) and evanescent wave scattering (red) components. We obtained the Thomson scattering spectrum by considering only the interaction with the reflected laser pulse leaving out the interaction with the evanescent wave, this was achieved by using a counter-propagating laser pulse instead of a plasma mirror. Additionally, we obtained the evanescent spectrum using an externally imposed standing evanescent wave. Thomson scattering leads to an intensity peak at the double Doppler shifted laser frequency ($\propto \omega_0 \gamma_p^2 = 6.4 \times 10^3 \omega_0$). Evanescent wave scattering dominates at higher frequencies. For instance, at $\omega_{\rm rad} \simeq 10^6\ \omega_0$, the evanescent field radiation spectral power is 2 orders of magnitude higher than that of the Thomson scattering. Figure 3.3a also shows that the predictions of Equation (3.7) (dashed gray) are in excellent agreement with the evanescent wave scattering spectrum calculated numerically.

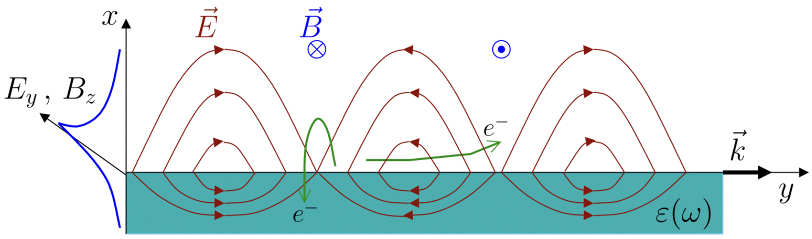

Figure 3.4: Sketch of the electromagnetic fields of a surface plasmon propagating in the y direction along the interface between vacuum and a sharp boundary plasma at $x = 0$. Taken from [87].

The time-integrated spatial intensity distribution is fully contained in the region of $1/\gamma_p$, and is offset in the direction of the particle's perpendicular momentum, as depicted in Figure 3.3b. The spatiotemporal profile of the radiation obtained in these scenarios is shown in Figure 3.3c.

3.2.2 Surface Plasmons

Plasma mirrors only last over the incident pulse duration, but it is possible to create long-lived evanescent fields using shaped solid targets (usually metallic) excited by a laser pulse. These long-lived modes are called surface plasmons. Several methods of producing radiation using surface plasmons have been proposed, for example, electrons propagating parallel to a surface-plasmon in graphene, experience these modes as if they were standard electromagnetic waves. Electrons can then undergo Thomson-scattering, and radiate [82].

The typical electro-magnetic fields associated with surface plasmon propagating in the y direction along a surface boundary located at $x = 0$, with frequency ω and wavenumber k, are given by [87]:

$$\begin{aligned} E_y &= E_0 \exp(iky - i\omega t) \exp(q_< x) \\ B_z &= \frac{i\omega}{cq_<} E_0 \exp(iky - i\omega t) \exp(q_< x) \\ E_x &= -\frac{ik}{q_<} E_0 \exp(iky - i\omega t) \exp(q_< x) \end{aligned} \tag{3.10}$$

for $x < 0$, and:

$$\begin{aligned} E_y &= E_0 \exp(iky - i\omega t) \exp(-q_> x) \\ B_z &= \frac{i\omega}{cq_<} E_0 \exp(iky - i\omega t) \exp(-q_> x) \\ E_x &= -\frac{ik}{q_>} E_0 \exp(iky - i\omega t) \exp(-q_> x) \end{aligned} \tag{3.11}$$

for $x \geq 0$. With :

$$q_< = \frac{k}{\sqrt{\omega_p^2/\omega^2 - 1}}, \qquad q_> = k\sqrt{\omega_p^2/\omega^2 - 1} \tag{3.12}$$

A sketch of the electromagnetic fild profile, taken from [87] can be found on Figure 3.4.

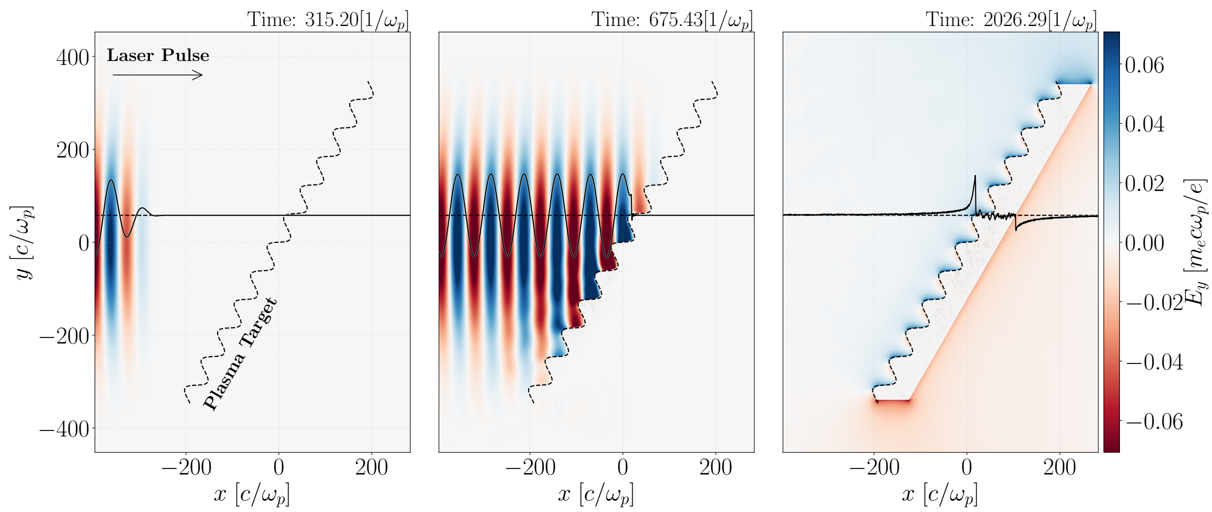

Figure 3.5: Snapshots of the generation of a surface plasmon in grating target using a laser pulse. The laser pulse (red-blue colormap) is a gaussian beam with spot size $w_0 \simeq 200\ \mathrm{c}/\omega_p$ propagating from left to right at an angle $\theta = \pi/6$ relative to the plasma surface (dahsed line). A lineout of the y component of the electric field at $y = 50\ \mathrm{c}/\omega_\mathrm{p}$ is represented by the solid black line.

An evanescent mode created by a surface plasmon is also much closer to the theoretical expression given in Equation (3.8) than the evanescent mode created by a reflecting a laser pulse. One key advantage is the absence of the reflected laser, which avoids spectrum contamination by the radiation emitted during the reflected laser-particle interaction.

3.2.2.A Creation of a Surface Plasmon

Surface plasmons [88] can be created through the interaction of an intense laser with a sinusoidally modulated target. In this setup, the surface plasmon excited by the laser remains present even after the laser plasma interaction has stopped and the resulting electromagnetic field decays exponentially away from the vaccum-plasma interface. We used OSIRIS to simulate the generation of a surface plasmon field in a 2D geometry. The laser pulse in this simulation had a normalized peak vector potential $a_0 = 1$ and frequency $\omega_L = 0.09\omega_p$. It lasted for about 15 laser periods, and incided in an overdense plasma at an angle $\theta = \pi/6$. The overdense plasma target featured a sinusoidal grating surface with spatial periodicity $\lambda_S = 2\lambda_L$ and depth $\lambda_L/4$. Its density was $n_p = 128\ n_c$, or 128 times larger than the critical density for the employed laser. We modeled the plasma target using 1 particle per cell in each direction in a box with length of 905 c/ω_p with 2048 cells in both directions.

Figure 3.5 shows the results of this simulation. We can see that before the laser reaches the target, there are no surface fields, but afterwards, an evanescent field is clearly present, even after the laser has been fully reflected.

3.2.2.B Surface Plasmon Evanescent Radiation

We then investigated the scattering of a charged particle across the envanescent fields of a surface plasmon. To do so, we performed 2D OSIRIS simulations where we collided a relativistic particle with a lorentz factor $\gamma = 100$ with externally imposed surface plasmon fields given by Equations (3.10) and

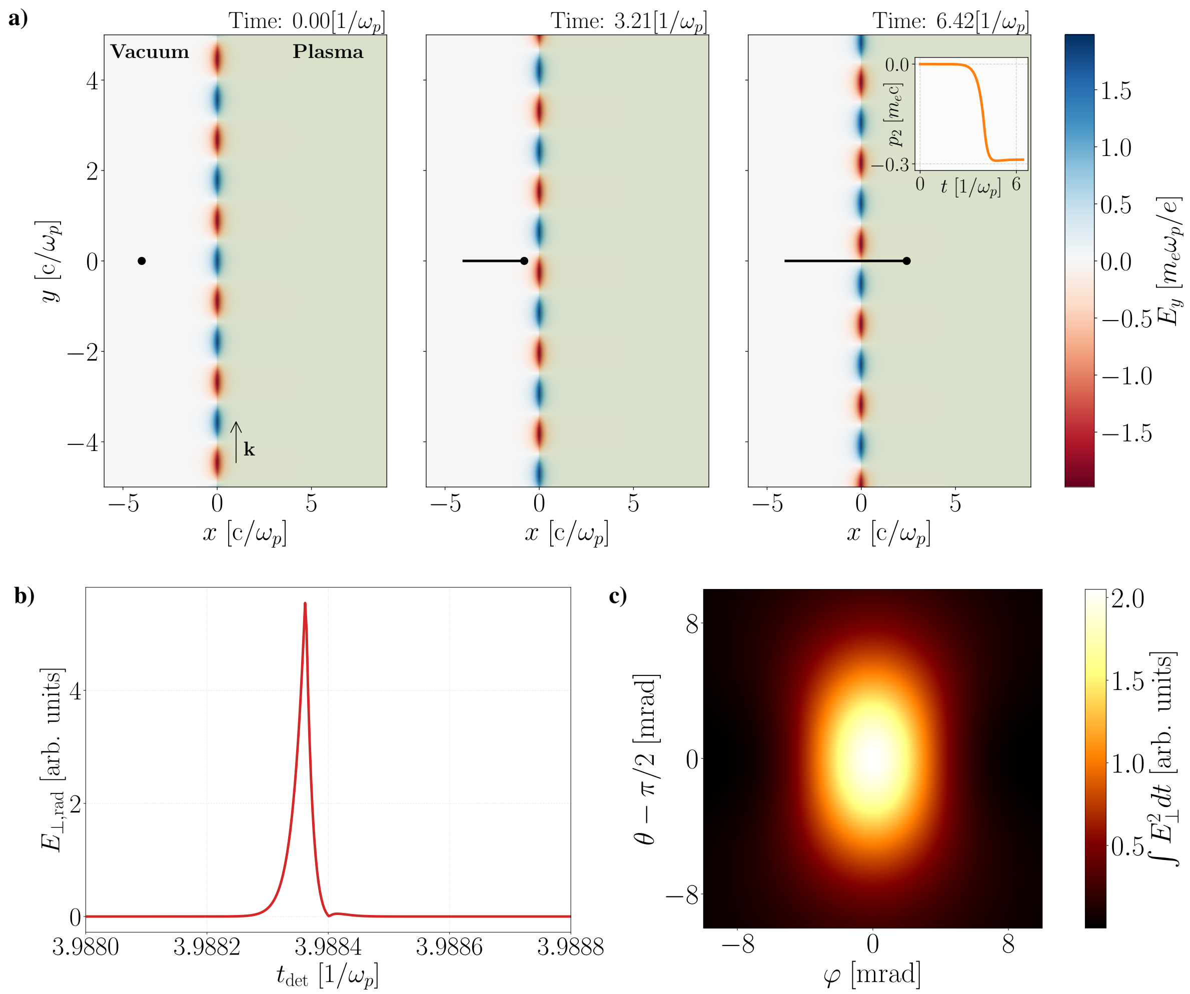

Figure 3.6: Single particle evanescent scattering from surface plasmons. a) Simulation setup: Snapshots of the simulation at increasing timesteps from left to right. A single charged particle (black dot) travels from left to right scattering across a surface plasmon (red-blue colormap) at the vaccum plasma boundary at $x = 0$. The inset on the last snapshot shows the temporal evolution of the particles transverse momentum. b) Temporal profile of the emitted radiation on-axis ($y = 0$). c) Angular profile of the total radiated intensity at a far-away spherical detector.

(3.11). The surface plasmon wave had a frequency $\omega = 0.7\omega_p$ and wavevector $\mathbf{k} = 3.53\ \omega_p/c\ e_y$, leading to an evanescent decay rate of $q_< = 3.46\omega_p/c$ in vaccum and $q_> = 3.6\omega_p/c$ inside the plasma. The simulation box had a length of 15 c/ω_p along x (1703 cells) and a width of 10 c/ω_p along y (513 cells). The simulation setup is summarized in Figure 3.6a.

We tracked the radiation emitted by this single particle using RaDiO. The spherical detector was placed far-away, with radius $R = 10^5\ c/\omega_p$ and pointed along the x-axis with an angular aperture of 10 mrad in both directions using 128 cells in each direction. The temporal resolution of the detector was $dt_{\text{det}} = 2.4 \times 10^{-6}\ 1/\omega_p$.

Figure 3.6a shows the particle travelling across the evancescent fields of the surface plasmon. It is possible to see also that the surface plasmon is itself travelling along the plasma boundary with phase speed $v_\phi = \omega/k = 0.19$ c. As a consequence, the profile of the evanescent field felt by the particle changes as the particle scatters across it. Additionally, the asymmetric evanescent decay rates $q_<$ and $q_>$ lead to an asymmetric temporal radiation profile (Figure 3.6b) as opposed to what was observed in Figure 3.2.

Nevertheless, the spatial intensity distribution appears to be similar to the previous observation of Figure 3.3, remianig mostly confined to an angular region of $\Delta\varphi \simeq 1/\gamma = 10$ mrad.

With these simulations we showed that the evanescent fields associated with surface plasmons can be used to produce evanescent radiation from single particles, with similar properties to the radiation obtained in the ideal scenario of Figure 3.2. We showed also that it is possible to generate these surface plasmons by hitting a grating plasma surface with a laser pulse.

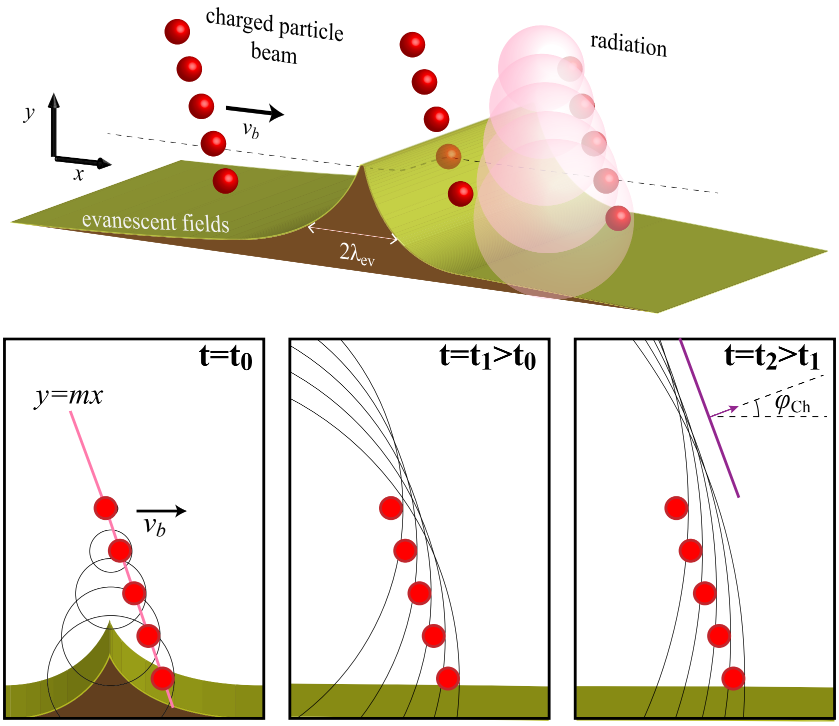

Figure 3.7: A tilted particle beam with slope m and velocity v_p collides with an evanescent wave, the radiation from each particle when crossing the evanescent mode is represented as sphere which expands as time progresses.

3.3 Evanescent Radiation Superradiance

Evanescent wave scattering radiation from an electron bunch (with N_e bunch electrons) generally leads to incoherent emission. Here, the radiated intensity is directly proportional to the number of bunch electrons, $I_{\mathrm{rad}} \propto N_e$. However, in certain conditions, the spatial shape of the bunch can bring temporal coherence phenomena and superradiance to evanescent wave scattering, where the radiated intensity scales with the number of particles squared $I_{\mathrm{rad}} \propto N_e^2$.

3.3.1 Spectrum Calculations

To demonstrate how certain modulations can control the onset of superradiance, we consider a tilted electron bunch moving towards an evanescent wave at a surface. Because the evanescent wave is extremely localized in space, the particles in the beam emit most of their radiation when they cross the surface. This is equivalent to having a moving light source constrained to the evanescent surface. The trajectory of this virtual light source or virtual particle (vp) is determined by the shape of the particle beam. For a tilted particle beam with slope m moving with velocity v_{b}, the light source moves along a straight line in the evanescent plane with speed $v_{\mathrm{vp}} = mv_{\mathrm{b}}$. For example for a particle beam moving close to the speed of light with a large enough slope, this virtual light source may be superluminal.

Under these conditions, the radiation from each particle in the beam will interfere constructively at a given angle, leading to a Cherenkov-like optical shock. Figure 3.7 illustrates qualitatively the onset of superradiance for a tilted electron bunch. It provides a clear pictorial demonstration that this superradiance effect is due to the onset of an optical shock.

From a theoretical standpoint, we can demonstrate how these modulations can control the onset of superradiance, by determining the corresponding radiated spectrum. We integrate Eq. (3.4) for a thin electron bunch with N_e electrons, where all electrons follow along the same trajectory, except for temporal and spatial off-sets, which determine the bunch shape. The radiation spectrum emitted by the particle beam is then given by:

$$\frac{\mathrm{d}^2 I_{\mathrm{rad}}}{\mathrm{d}\omega \mathrm{d}\Omega} = \frac{e^2}{4\pi^2 c}\left|\sum_i^{N_e}\int_{-\infty}^{+\infty}\frac{\mathbf{n}\times\left[(\mathbf{n}-\boldsymbol{\beta}_i(t))\times\dot{\boldsymbol{\beta}}_i(t)\right]}{(1-\boldsymbol{\beta}_i(t)\cdot\mathbf{n})^2}e^{i\omega[t-\mathbf{n}\cdot\mathbf{r}_i(t)/c]}\mathrm{d}t\right|^2, \tag{3.13}$$

We then assume that the trajectory of an electron that arrives at the evanescent wave at $t=t_i$, is given by $\mathbf{r}_i(t)=\mathbf{r}(t-t_i)+\mathbf{r}_{\mathrm{vp}}(t_i)\equiv\mathbf{r}(t')+\mathbf{r}_{\mathrm{vp}}(t_i)$. Here, $\mathbf{r}(t')$ is the electron displacement relative to a spatial off-set $\mathbf{r}_{\mathrm{vp}}(t_i)$, and $t'=t-t_i$ is the time elapsed relative to t_i, and $\mathbf{r}_{\mathrm{vp}}(t_i)$ is the instantaneous position where the electron bunch intersects the evanescent wave.

$$\begin{cases} \boldsymbol{r_i}(t)=\boldsymbol{r}(t')+\boldsymbol{r}_{\mathrm{vp}}(t_i); \\ \boldsymbol{\beta_i}(t)=\boldsymbol{\beta}(t-t_i)=\boldsymbol{\beta}(t'); \\ \dot{\boldsymbol{\beta}}_{\boldsymbol{i}}(t)=\dot{\boldsymbol{\beta}}(t-t_i)=\dot{\boldsymbol{\beta}}(t'); \end{cases} \tag{3.14}$$

For a tilted electron bunch with slope m travelling along x with velocity v_{b} and an evanescent mode at the yOz plane, $\mathbf{r}_{\mathrm{vp}}(t_i)=v_{\mathrm{vp}}t_i\mathbf{e}_y$, where $v_{\mathrm{vp}}=mv_{\mathrm{b}}$ is the vertical velocity of the virtual particle. Under these conditions, Eq. (3.13) can be written as:

$$\frac{\mathrm{d}^2 I_{\mathrm{rad}}}{\mathrm{d}\omega \mathrm{d}\Omega} = \frac{e^2}{4\pi^2 c}\left|\sum_i^{N_e}\int_{-\infty}^{+\infty}\frac{\mathbf{n}\times\left[(\mathbf{n}-\boldsymbol{\beta}(t'))\times\dot{\boldsymbol{\beta}}(t')\right]}{(1-\boldsymbol{\beta}(t')\cdot\mathbf{n})^2}e^{i\omega[t'-\mathbf{n}\cdot\mathbf{r}(t')/c]}e^{i\omega[t_i-\mathbf{n}\cdot\mathbf{r}_{\mathrm{vp}}(t_i)/c]}\mathrm{d}t'\right|^2, \tag{3.15}$$

In equation (3.15) above, we can identify the spectrum of radiation emitted by a single particle as given by the Liénard-Wiechert potentials, $\mathscr{F}_{\mathrm{sing}}$:

$$\mathscr{F}_{\mathrm{sing}} = \frac{e^2}{4\pi^2 c}\left|\int_{-\infty}^{+\infty}\frac{\mathbf{n}\times\left[(\mathbf{n}-\boldsymbol{\beta})\times\dot{\boldsymbol{\beta}}\right]}{(1-\boldsymbol{\beta}\cdot\mathbf{n})^2}e^{i\omega[t'-\mathbf{n}\cdot\mathbf{r}(t')/c]}\mathrm{d}t'\right|^2, \tag{3.16}$$

Equation (3.15) can then be re-written as:

$$\frac{\mathrm{d}^2 I_{\mathrm{rad}}}{\mathrm{d}\omega \mathrm{d}\Omega} = \mathscr{F}_{\mathrm{sing}}\left|\sum_i^{N_e}e^{i\omega[t_i-\mathbf{n}\cdot\mathbf{r}_{\mathrm{vp}}(t_i)/c]}\right|^2 = \mathscr{F}_{\mathrm{sing}}\left|\frac{N_e}{T}\sum_i^{N_e}e^{i\omega[t_i-\mathbf{n}\cdot\mathbf{r}_{\mathrm{vp}}(t_i)/c]}\Delta t_i\right|^2,$$

where Δt_i the time distance between the arrival of each electron at the evanescent wave and T the time interval between the arrival of the first and last electrons. For a large enough number of electrons we can replace the summation for an integral:

$$\sum_i^{N_e}(\ldots)\Delta t_i \to \frac{N_e}{T}\int_{-T/2}^{T/2}(\ldots)\mathrm{d}t_i, \tag{3.17}$$

the radiated spectrum then becomes:

$$\frac{\mathrm{d}^2 I_{\mathrm{rad}}}{\mathrm{d}\omega \mathrm{d}\Omega} = \mathscr{F}_{\mathrm{sing}}\left|\frac{N_e}{T}\int_{-T/2}^{T/2}e^{i\omega[t_i-n_y v_{\mathrm{vp}}t_i/c]}\mathrm{d}t_i\right|^2 = \mathscr{F}_{\mathrm{sing}}\frac{N_e^2}{4}\mathrm{sinc}^2\left(\frac{\omega T\left(1-n_y v_{\mathrm{vp}}/c\right)}{2}\right), \tag{3.18}$$

with $n_y = \sin\theta\sin\varphi$ in spherical coordinates, and where we integrated from $t_i = [-T/2, T/2]$. Equation (3.18) tells us that the radiated spectrum is maximum along a specific direction, namely when $n_y = \mathrm{c}/v_{\mathrm{vp}}$, or:

$$\varphi = \arcsin\left(\frac{c}{v_{\mathrm{vp}}\sin(\theta)}\right) = \varphi_{\mathrm{Ch}}. \tag{3.19}$$

The critical angle φ_{Ch} corresponds to the Cherenkov cone angle [89] in vacuum measured from the vertical y direction. The phase of the light rays emitted by the different bunch electrons is the same at $\varphi = \varphi_{\mathrm{Ch}}$. This holds for every emitted frequency, and hence leads to an optical shock directed towards $\varphi = \varphi_{\mathrm{Ch}}$.

Equation (3.18) recovers the typical superradiant scaling of the radiated intensity with the number of bunch electrons squared when $\varphi = \varphi_{\mathrm{Ch}}$. To see why this happens, consider the frequency integrated intensity. At the Cherenkov angle $\varphi = \varphi_{\mathrm{Ch}}$ or $n_y = \mathrm{c}/v_{\mathrm{vp}}$, it can be written as:

$$\left.\frac{\mathrm{d}^2 I_{\mathrm{rad}}}{\mathrm{d}\omega\mathrm{d}\Omega}\right|_{\varphi=\varphi_{\mathrm{Ch}}} = \mathscr{F}_{\mathrm{sing}}(\omega,\Omega)\frac{N_e^2}{4}, \tag{3.20}$$

the frequency integrated spectrum at this angle is then given by:

$$\int \mathrm{d}\omega \left.\frac{\mathrm{d}^2 I_{\mathrm{rad}}}{\mathrm{d}\omega\mathrm{d}\Omega}\right|_{\varphi=\varphi_{\mathrm{Ch}}} = \frac{N_e^2}{4}\int \mathrm{d}\omega \mathscr{F}_{\mathrm{sing}}(\omega,\Omega), \tag{3.21}$$

from which we can directly conclude, even without evaluating the integral, that the radiated intensity directly scales quadratically with the number of particles the beam, $\propto N_e^2$, as neither $\mathscr{F}_{\mathrm{sing}}$ nor its integral in ω have any dependence on N_e.

On the other hand, if we move away from the Cherenkov angle, this is no longer true. For example, on-axis, where $\varphi = 0$ or $n_x = \mathbf{e}_x$, the spectrum becomes:

$$\left.\frac{\mathrm{d}^2 I_{\mathrm{rad}}}{\mathrm{d}\omega\mathrm{d}\Omega}\right|_{\varphi=0} = \mathscr{F}_{\mathrm{sing}}(\omega,\Omega)\frac{N_e^2}{4}\mathrm{sinc}^2\left(\omega T/2\right), \tag{3.22}$$

and the frequency integrated spectrum at this angle is then given by:

$$\int \mathrm{d}\omega \left.\frac{\mathrm{d}^2 I_{\mathrm{rad}}}{\mathrm{d}\omega\mathrm{d}\Omega}\right|_{\varphi=0} = \frac{N_e^2}{4}\int \mathrm{d}\omega \mathscr{F}_{\mathrm{sing}}(\omega,\Omega)\mathrm{sinc}^2\left(\omega T/2\right), \tag{3.23}$$

In this case, we can no longer directly determine how the radiated intensity directly scales with the number of particles the beam, because the integral in ω now includes a term which depends on N_e ($T = N_e/j_b$). Here, we assumed that the number of bunch particles is proportional to the bunch duration, $N_e = j_b T$, where $j_b = n_b v_x$ is the beams current given by the product between the beam density n_b and velocity v_x. Thus, in order to discover how the frequency integrated spectrum scales with the number of particles one needs to evaluate the integral. To do this, we must assume $\mathscr{F}_{\mathrm{sing}}$ to be constant. This is valid if the sinc component decays much faster than $\mathscr{F}_{\mathrm{sing}}$, which happens in the case of evanescent radiation as the frequency spectrum on-axis, given by:

$$\mathscr{F}_{\mathrm{sing}} = \frac{e^2}{4\pi^2 c}\left|\frac{4\beta_{y0}\gamma_p^2}{1+\omega^2\lambda_{\mathrm{ev}}^2/\left(2\gamma_p^2 v_x\right)^2}\right|^2 \tag{3.24}$$

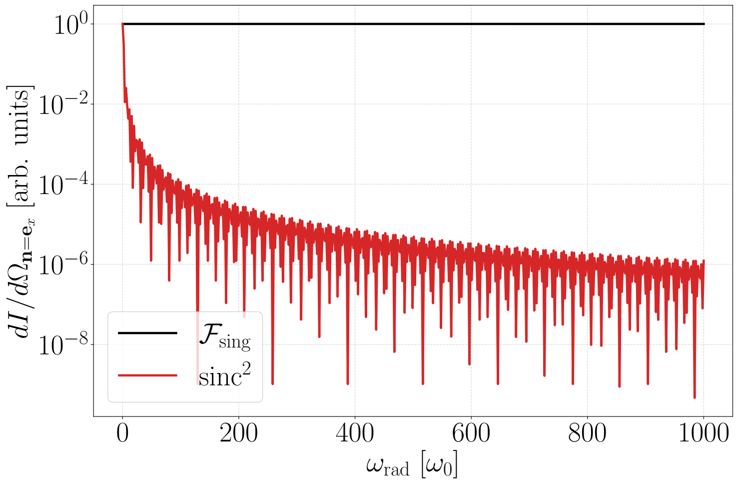

Figure 3.8: Comparison between the sinc^2 and $\mathscr{F}_{\text{sing}}$ components for the parameters used in this section ($\gamma_p = 80$, $\lambda_{\text{ev}} = 0.17\omega_0$, $v_x \sim$ c and $T = 1.2$ c$/\omega_0$).

remains constant for $\omega \ll 4\gamma_p^2/\lambda_{\text{ev}}$, whereas $\text{sinc}^2(\omega T/2)$ decays rapidly for $\omega > 6\pi/T$. Figure 3.8 shows the behavior of both the sinc^2 and $\mathscr{F}_{\text{sing}}$ components for the parameters used in the simulations of this section, proving the validity of the assumption. Thus, if $T > 6\pi\lambda_{\text{ev}}/2\gamma_p^2$, that is, if the particle beam is relativistic and/or the if its length is greater than the length of the evanescent wave, the assumption is valid and the integrated frequency spectrum is given by:

$$\int d\omega \left.\frac{d^2 I_{\text{rad}}}{d\omega d\Omega}\right|_{\varphi=0} = \frac{e^2}{4\pi^2 c} 4\beta_{y0}\gamma_p^2 j_b N_e \pi, \tag{3.25}$$

which scales linearly with the number of particles for constant j_b. Moreover, the result obtained under the assumption that $\mathscr{F}_{\text{sing}}$ is constant can be understood as an upper limit to the integral in Eq. (3.23). Thus, regardless of the validity of the assumption we can conclude that the integrated intensity on-axis scales, at most, with N_e.

3.3.2 Toy Model

We developed a toy model to help visualize the onset of the optical shock. This model provides a simple depiction of light emitted at the evanescent interface by displaying it as spherical surfaces (which we may also call radiation wavefronts) centered at intersection point between the particle and the evanescent surface also referred to as the virtual superluminal particle. The radius of these surfaces expands at the speed of light c. Because the virtual particle is moving faster than c, as the radiation wavefronts from the multiple particles expand, they begin to intersect, creating the optical shock as portrayed in Figure 3.7.

Our toy model allows us to see the optical shock from multiple prespectives. In the aforementioned case of a tilted beam, our toy model can showcase the optical shock in the plane where the beam lies offering a side-view of the phenomenon. Here, the expanding spherical wavefronts appear as expanding circumferences (the intersection between the beam plane and the spherical wavefrons is a circumference). The collective addition of these wavefronts may, under the Huygens principle, be approximated a plane

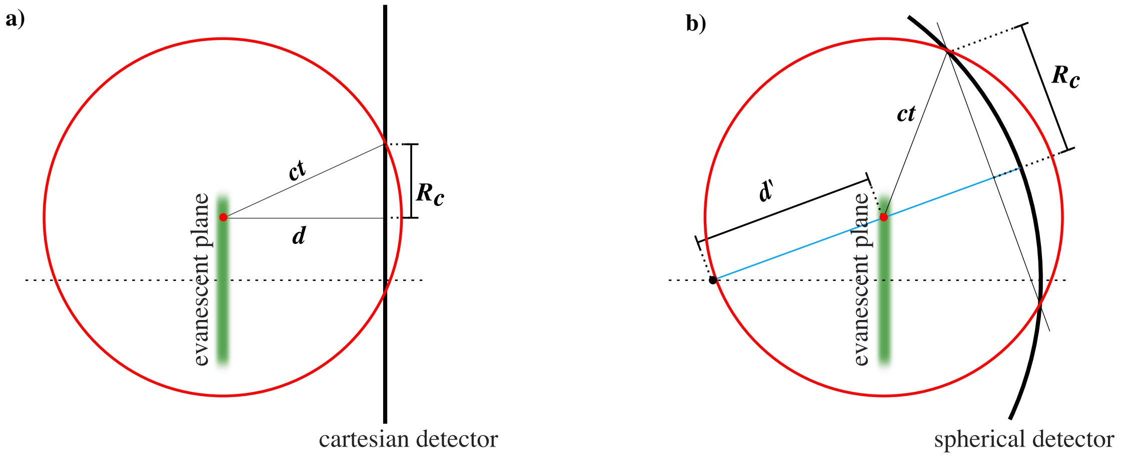

Figure 3.9: 2D geometry of the intersection between a spherical shell of radiation (red circumference) emitted from an evanescent plane (in green) and a cartesian (a) and spherical (b) detector (in black).

wavefront tiled in the direction of the Cherenkov angle as depicted in the bottom panels of Figure 3.7. A simple python script can create these visualizations by superimposing a set of circunferences whose center is determined by the interseciton between the particle beam and the evanescent plane and whose radius is proportional to the time elapsed since their creation (*i.e.* the time since a given particle in the beam crossed the evanescent plane). In the case of the tilted beam, the trajectory is a vertical line.

Another interesting aspect is the visualization of these shocks at the surface of a detector, this can be accomplished by superimposing in a plot the instantaneous intersection between the spherical shells of radiation emitted by the multiple particles in the beam and the detector surface. For a cartesian (plane) detector parallel to the evanescent surface, the intersection for each radiation shell is a circumference centered at the projection of the particle position in the detector plane with radius given by:

$$R_c = \sqrt{c^2t^2 - d^2} \tag{3.26}$$

with t being the time elapsed since the radiaiton was emitted and d begin the distance between the evanescent plane and the detector plane. Figure 3.9a shows the geometry of the intersection between the spherical wave and the plane detector as well as the relevant quantities.

In the case of the spherical detector the intersection is still a circumference, but it is a bit more difficult to determine. Figure 3.9b shows the geometry of the intersection between a spherical shell of radiation and a spherical detector. This intersection is a circumference whose center lies on a straight line that connects the center of the spherical detector to the position of the particle that is emitting the radiation (in blue in Figure 3.9b). This line is normal to the plane where the circumference lies. The radius of this circumference can be found using the following expression:

$$R_c = \frac{\sqrt{4d'^2R^2 - (d'^2 - c^2t^2 + R^2)^2}}{2d'} \tag{3.27}$$

Figure 3.10 shows an example of the insights provided by the spherical toy model for a superluminal virtual particle performing a circular motion at the evanescent plane. This sort of motion for the virtual particle could be obtained by scattering a helical particle beam acrros an evanescent field at a plane. In

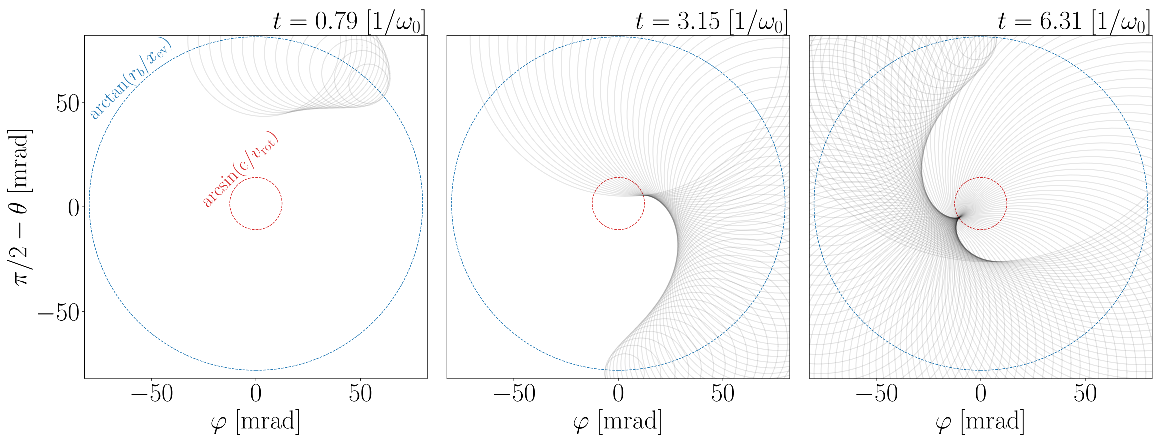

Figure 3.10: Snapshots of the toy model of superradiant emission in a spherical detector from a virtual superluminal particle performing uniform circular motion in a plane. The red circle represents the Cherenkov angle and the blue circle represents the pitch angle of the particle positon with respect to center of the detector.

this case the detector had a radius $R = 10^5$ c/ω_0 and the virtual particle performed a circular motion with radius $r_b = 80$ c/ω_0 with frequency ω_0 at an evanescent plane located at $x_{ev} = 1000$ c/ω_0. Here, we can see that the radiation circumferences always appear at a fixed angular distance from the longitudinal axis $\Delta\theta = \arctan(r_b/x_{ev}) \sim 80$ mrad. As the virtual particle travels and emits more radiation, we can see that the radiation circumferences start to intesect, forming the shape of a cardioid. The cusp of this cardioid, which is the point where the intersection is maximum is located at the Cherenkov angle φ_{Ch} corresponding to the velocity of the virtual particle $v_{rot} = \omega_0 r_b = 80$ c. The Cherenkov angle is then $\varphi_{Ch} = \arcsin(c/v_{rot})$.

This toy model allows us to quickly predict the spatiotemporal features of superradiant emission from particle beams in evanescent waves, even for more exotic virtual particle trajectories.

3.3.3 Simulations of Superradiant evancescent radiation from structured particle beams

With the insight obtained from the theoretical predictions and the toy model, we designed and simulated several scenarios where superradiance plays a major role. We start with the simple example of a tilted particle beam and then increase complexity (and move closer to a possible experimental realization) with sinusoidally modulated and helicaly modulated particle beams.

3.3.3.A Tilted Beam

In this study, we conducted a 2D simulation using the same parameters as the single particle example of Figure 3.2, except for the particle beam. The particle beam had a γ factor of 80 and a transverse momentum $p_\perp = 0.0$, and a transverse thickness w_0 of about $3 \times 10^{-3} c/\omega_p$. The number of particles per cell (ppc) in this beam was 2^{15}. We utilized a spherical detector located at $R = 10^4 c/\omega_p$. The detector had a time resolution of $dt_{rad} = 3 \times 10^{-6}$ ω_p^{-1} (262144 temporal cells) and an aperture of $\Delta\phi = 50$ mrad, with 256 cells on $\mathbf{e}_\phi$.

Figure 3.11a shows the onset of the optical shock in the virtual detector produced by a tilted electron bunch ($\gamma_p = 80$), which scatters from an evanescent wave (under the same parameters as in Figure 3.3).

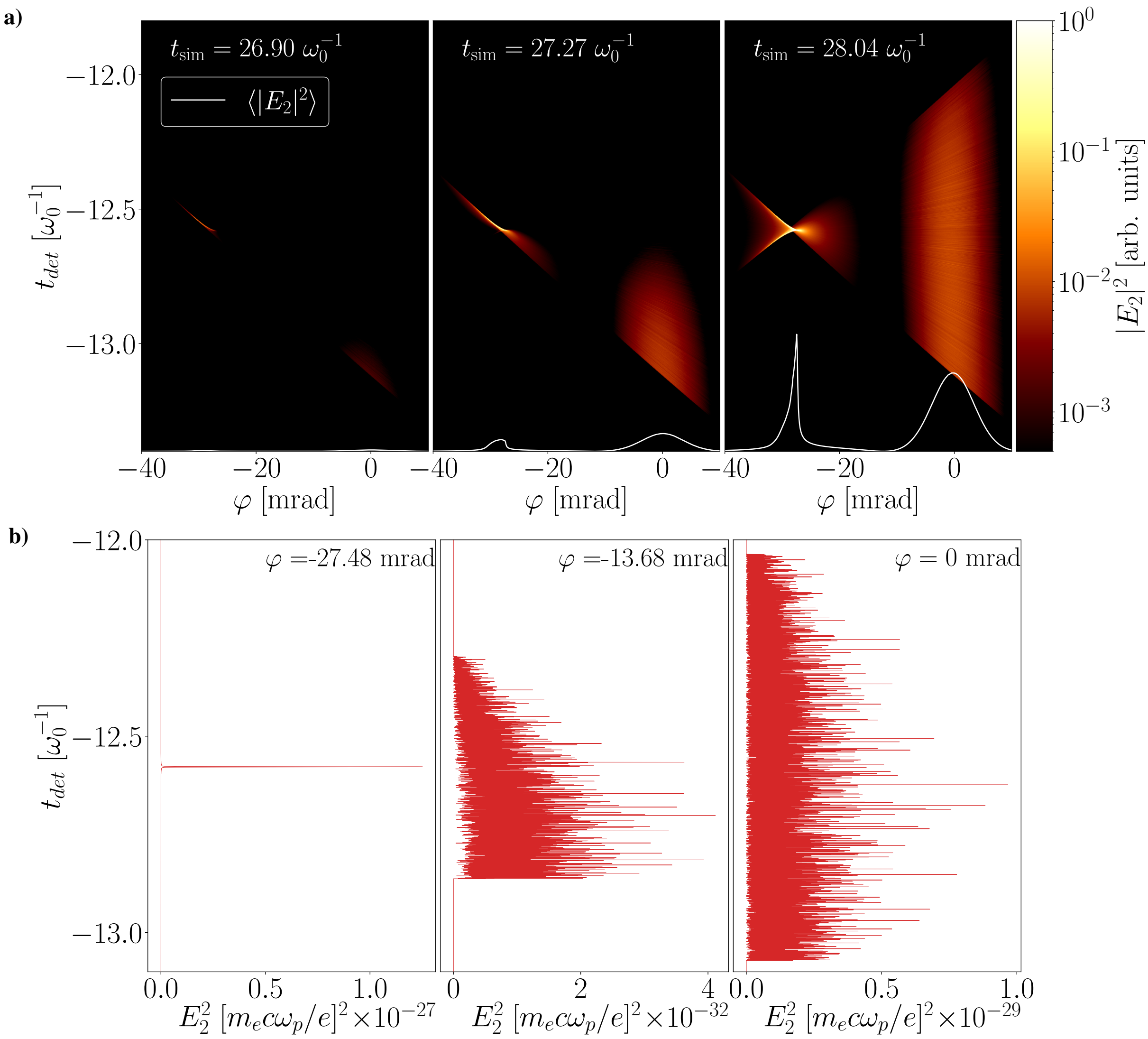

Figure 3.11: Onset of optical shock by a tilted charged particle beam. a) Snapshots of the spatiotemporal profile showing the optical shock formation at the Cherenkov angle (colormap) and time integrated profile (white line). b) Lineouts of the final snapshot in a) at 3 different angles: at the Cherenkov angle, on-axis, an in-between

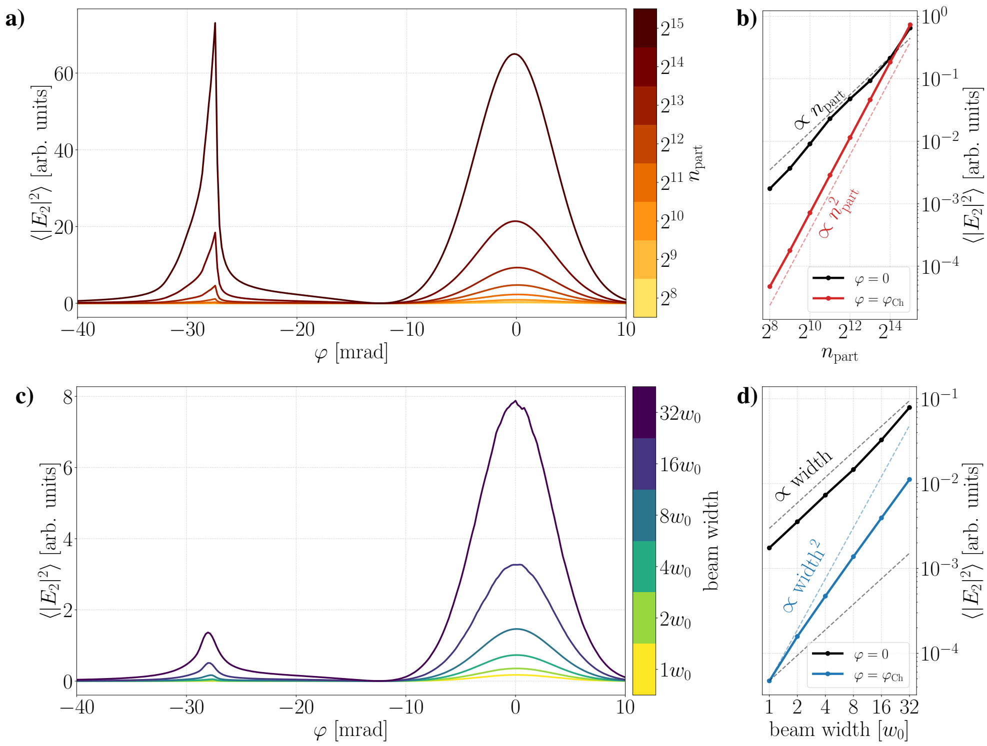

Figure 3.12: Angular profile of the integrated radiation intensity spectrum for different particle beams. a) Variation with the number of particles per cell with fixed width. b) Comparision between the intensity peaks on-axis and at the Cherenkov angle for increasing beam for increasing number of particles. c) Variation with the beam width for a fixed number of particles per cell. d) Comparision between the intensity peaks on-axis and at the Cherenkov angle for increasing beam widths.

The velocity of the superluminal virtual particle is $v_\text{vp}/c \simeq 36$, and the corresponding Cherenkov angle is $\theta_\text{Ch} \simeq 27$ mrad. This prediction is in excellent agreement with simulation results shown in Figure 3.11b. The optical shock leads to a sharp intensity spike. Interestingly, despite appearing in a region where single electrons nearly do not radiate (see Figure 3.3c), the peak intensity at the optical shock is higher than the peak intensity on-axis, which is where single bunch electrons produce most of their radiation.

We can see from Figure 3.11a that this optical shock is the result of the accumulation of the radiation from all particles in a very narrow time window. This figure shows the temporal profile of radiation at the different angles: $\varphi = \varphi_\text{Ch}$ (Cherenkov angle), $\varphi = \varphi_\text{Ch}/2$, and $\varphi = 0$ (on-axis). On-axis, the radiation profile is composed of many individual peaks that are spread out occupying a time window whose duration is close to the particle beams duration. As we move closer to the Cherenkov angle, these peaks starting bunching together eventually forming a single high intensity peak, orders of magnitude more intense than each individual peak on-axis, despite being in a region where the single particle radiation intensity is order of magnitude smaller than on-axis.

What distinguishes superradiance from other emission regimes is the scaling of the radiation intensity peak at the cherenkov angle with the number of radiating electron in a bunch. To investigate this scaling in superradiant evanescent scattering, we performed additional simulations. We tested the variation in the total radiated intensity with the number of particles in the beam, both by increasing the particles-per-cell parameter (increasing the number of particles longitudinally) and the particle beam width (increasing the

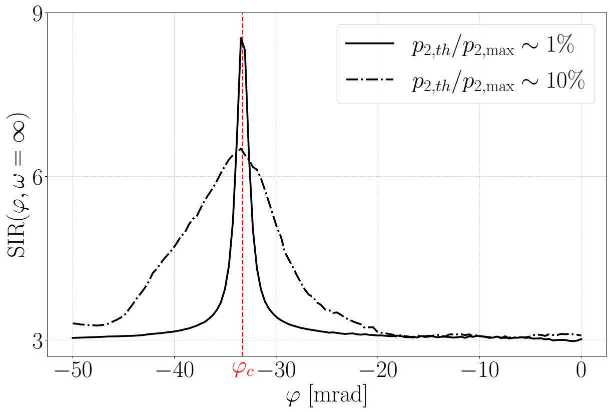

Figure 3.13: Full Frequency Spectrum Integral Ratio for particle beams with $p_{\perp,\mathrm{th}} = 0.1p_{\perp,\max}$ and $p_{\perp,\mathrm{th}} = 0.01p_{\perp,\max}$, with $L_2/L_1 = 3$.

number of particles transversely). We varied the number of particles in the beam from 2^8 to 2^{15} for a fixed width of w_0 and increased the transverse thickness from w_0 to $32w_0$ starting with number of particles in the beam 2^8.

Figure 3.12 shows the resulting angular profile of time integrated intensity spectrum under these conditions as well as the total radiated energy on-axis ($\varphi = 0$) and at the Cherenkov angle ($\varphi = \varphi_{\mathrm{Ch}}$). In accordance to the theoretical predictions of Eqs. (3.25) and (3.21), while the integrated intensity scales with N_e^2 at the Cherenkov angle when we increase the number of particles longitudinally, Fig. 3.12b demonstrates that the radiated intensity scales linearly with the number of bunch electrons far from the Cherenkov cone angle given by Eq. (3.19). Moreover, Figure 3.12d shows that the total radiated intensity on-axis grows still with N_e when we increase the beam width ($N_e \propto$width), however, at the Cherenkov angle we obtain larger than N_e, but smaller than N_e^2 growth.

These simulations were performed with cold particle beams whose shape was externally imposed. In a realistic scenario, for a particle beam to acquire such shape it would need to have a transverse momentum profile like the one given by Eq. (3.28) below:

$$p_\perp(x,t) = \frac{x - (x_c + v_b t)}{L_x/2} p_{\perp,\max} \tag{3.28}$$

where L_x is the particle beam's initial length along x, x_c is the position of beam's centroid along the x-axis at $t = 0$ and $x_c + v_b t$ the beam center at any given time.

To further demonstrate the robustness of this method, we tested tilted particle beams under non-ideal scenarios, namely by increasing particle temperature and energy spread and adding a transverse momentum profile. We used electron beams with 1% energy spread longitudinally and added a perpendicular thermal momentum distribution characterized by a gaussian distribution with standard deviation p_{th}. We increased the p_{th} from 1% to 10% of the maximum transverse momentum of the particles in the beam. Additionally, we varied the number of particle by increasing the beam length.

To better understand the impact of such non-ideality on the expected superradiance, we defined the Spectrum Integral Ratio (SIR), which consists in the ratio between the integrated frequency spectra

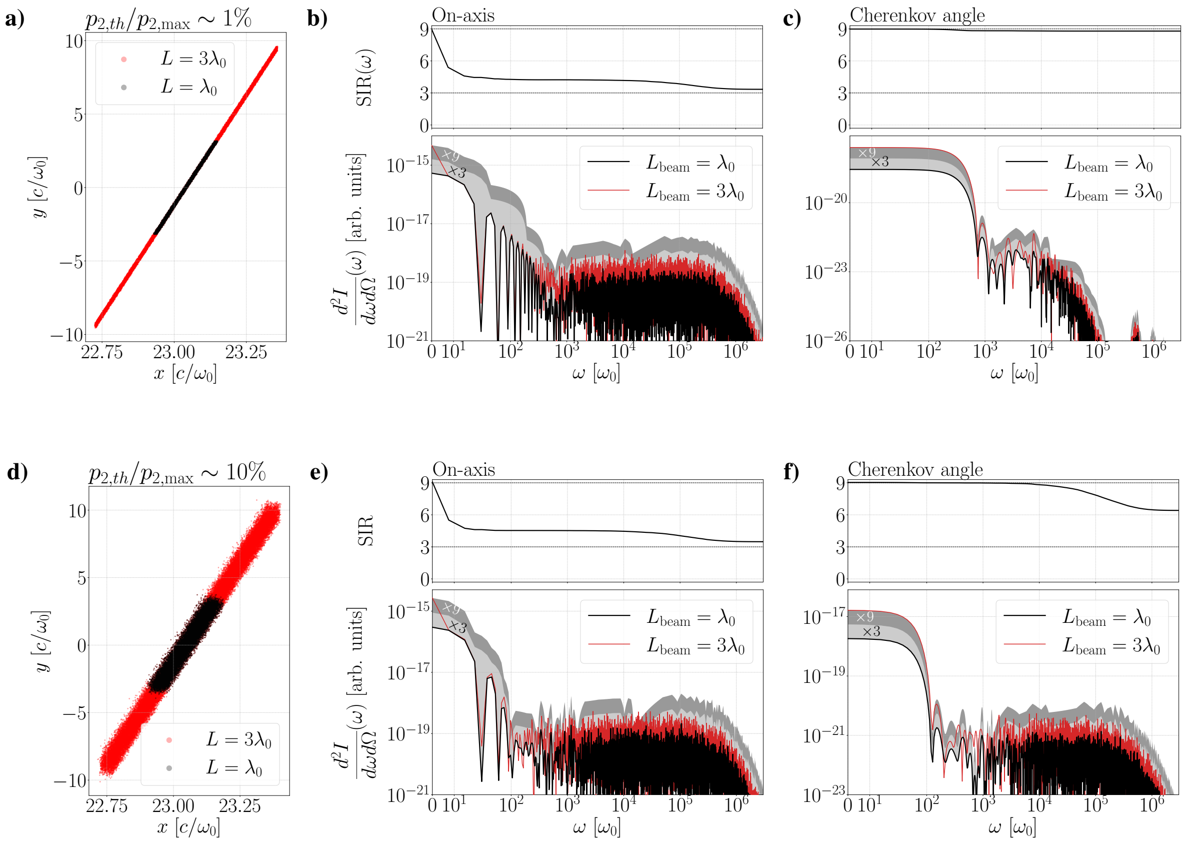

Figure 3.14: Frequency Spectra for hot and cold particle beams on-axis and at the Cherenkov angle. a) Particle beam shape when passing through the evanescent field. b) Frequency Dependent Specturm Integral Ratio and frequency spectra on axis. c) Frequency Dependent Specturm Integral Ratio and frequency spectra at the Cherenkov angle. d), e) and f) the same as a), b) and c) respectively, but for a hot particle beam. The light grey region delimits the region of incoherent addition of intensity (where intensity grows with a factor $f < N_e$) and the dark grey region delimits the region of superadiant addition of intensity (where intensity grows with a factor $N_e < f < N_e^2$).

obtained from particle beams with different lengths L_1 and $L_2 > L_1$:

$$\mathrm{SIR}(\varphi, \omega) = \int_0^{\omega} \frac{d^2 I_{L1}}{d\omega' d\Omega} d\omega' \Bigg/ \int_0^{\omega} \frac{d^2 I_{L2}}{d\omega' d\Omega} d\omega' \tag{3.29}$$

$\mathrm{SIR}(\varphi, \omega = \infty)$ corresponds to the ratio of the total energy emitted at a given angle φ. In the ideal case, the SIR should be equal to$(L_2/L_1)^2$ around the Cherenkov angle and L_2/L_1 otherwise.

Our results, summarized in Figure 3.13, show that when we introduce a transverse thermal spread of 1%, for $L_2/L_1 = 3$, the SIR remains as expected close to 3 (meaning that it grows linearly with the number of particles) for most angles, but grows quadratically with the number of particles near the Cherenkov angle. For a transverse thermal spread of 10%, we see that the radiated intensity no longer grows with the number of particles squared, but still grows faster than only linearly with the number of particles. Moreover, the region of space where it does so is larger, meaning that it is possible to collect the same energy as in the ideal case if our target is larger.

Additionally, despite the fact that the total radiated energy does not always grow quadratically with the number of particles, there are still some regions of the frequency spectrum that display superradiant

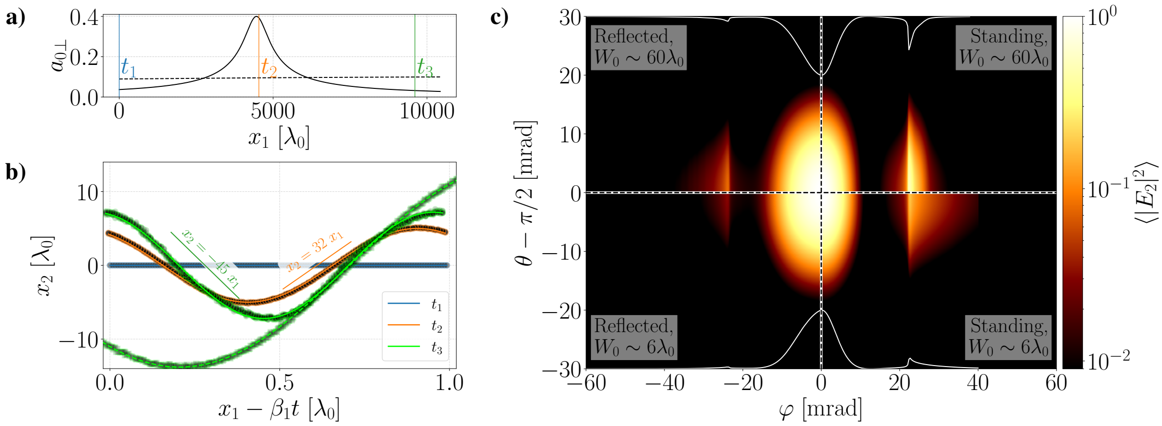

Figure 3.15: Evanescent radiation from a particle beam shaped by a gaussian laser pulse. a) Intensity profile of the two laser pulses employed. The solid line represents a more tightly focused laser pulse $W_0 \sim 4\lambda_0$ and the dashed line represents a more loosely focuses laser pulse $W_0 \sim 60\lambda_0$. b) Particle beam shape at different times. c) Resulting radiation.

behaviour. The frequency dependent SIR shows the frequencies up until which the emission is superradiant. Figure 3.14 shows the frequency spectra of emitted radiation both on-axis and at the Cherenkov angle for both particle beams. On-axis, the frequency spectrum behaves superradiantly only for $\omega = 0$, which makes sense given that for $\omega = 0$ the phase of the emitted radiation is the same for every particle. This means that the frequency dependent spectrum integral ratio quickly goes from $(L_2/L_1)^2$ to (L_2/L_1) as we increase ω. This happens both for $p_{2,th}/p_{2,\max} = 1\%$ and $p_{2,th}/p_{2,\max} = 10\%$. At the Cherenkov angle, the frequency spectrum behaves superradiantly for a much larger range of frequencies. In fact, the intensity of radiation grows strictly quadratically for frequencies up to $10^3\omega_0$ in the case where $p_{2,th}/p_{2,\max} = 1\%$ and for frequencies up to $10^2\omega_0$ in the case where $p_{2,th}/p_{2,\max} = 10\%$. The factor of 10 difference between the threshold frequency in these two cases is directly related to the difference in the final bunch width, which is similarly a factor of 10.

3.3.3.B Sinusoidal Beam

From a physical standpoint, a particle beam with a sinusoidal modulation can be approximated as a sequence of tilted bunches with opposite slopes with each tilted section of the bunch crosses the evanescent mode with a velocity $v_{\mathrm{vp}} \sim c$. This approximation fails at the points of maximum transverse electron displacement. However, is still a useful model to predict the onset of superradiance. Additionally, the sinusoidal modulation of particle beam may be easier to realize experimentally.

Here, we demonstrate a possible all-optical beam-shaping mechanism, which uses a laser pulse (with $a_0 \ll 1$) to modulate a relativistic electron bunch and control the onset of superradiance. In the most simple configuration, the laser pulse, which co-propagates with the electron bunch, exerts a spatially periodic force that pushes bunch electrons along the polarization direction. A downward (upward) push occurs if the laser electric field is positive (negative) at the electron position, thereby modulating the electron bunch at λ_0. The modulation persists when the laser vanishes. Hence, a linearly or a circularly polarized laser pulse can introduce a sinusoidal or helical modulation on a pencil electron beam. Interestingly, each portion of the bunch located between consecutive crests and troughs of the laser vector potential behaves as a tilted beam.

Figure 3.15a-b illustrates how a linearly polarized laser pulse imparts a sinusoidal modulation on a thin, pencil-like electron bunch with length $L \sim \lambda_0$, with $\gamma = 80$ and longitudinal thermal spread $u_x = 10^{-3}\, m_e$c. The resolution of the PIC simulation box is 0.09×0.24 $(\mathrm{c}/\omega_0)^2$ in the (x, y) directions, and the time step is $dt_{\mathrm{PIC}} = 0.08\ \omega_0^{-1}$ We tested two types of laser profiles: Laser 1, a more intense, tightly focused laser, with wavelength λ_0, waist $W_0 \sim 6\lambda_0$, and peak normalized vector potential is $a_0 = 0.4$ (solid line in Fig. 3.15a) and Laser 2, a more loosely focused laser pulse with wavelength $2\lambda_0$, waist $W_0 \sim 60\lambda_0$, and peak normalized vector potential is $a_0 = 0.1$ (dashed line in Fig. 3.15a).

The setup with Laser 1 imprints a modulation with amplitude $\Delta r_{\mathrm{vp}} \sim 7\ \lambda_0$ at t_3 after the laser has focused and defocused. A larger amplitude beam would be desirable as it would allow each tilted section to be longer, containing more particles, which would contribute to a more prominent superradiance peak. Using a laser beam with larger waist allows for the laser-particle interaction to last longer, leading to larger amplitude modulations, even at lower intensities ($\Delta r_{\mathrm{vp}} \sim 14\ \lambda_0$ at t_3 for Laser 2 compared to $\Delta r_{\mathrm{vp}} \sim 7\ \lambda_0$ at t_3 for the Laser 1). In order to preserve the location of the Cherenkov angle, the slope of each tilted section, given by $m_{\mathrm{sec}} \sim \Delta r_{\mathrm{vp}} 2\pi/\lambda_0$, needs to be kept constant, therefore the wavelength of the modulation and, consequently, of the laser needs to increase by the same factor as Δr_{vp}. Thus, Laser 2 has double the wavelength of Laser 1.

The evanescent mode appears either self-consistently as the plasma target reflects the laser pulse or as an externally imposed standing evanescent wave like the ones generated by surface plasmons. Figure 3.15c shows that the corresponding time-integrated radiation profile consists of two bright horizontal lobes appearing at $\varphi = \pm 30$ mrad. The angular location of the intensity peaks coincides exactly with the predictions of Eq. (3.19). Thus, for $\theta = \pi/2$, $\varphi_{\mathrm{Ch}} = 22$ mrad, exactly as shown in the simulations. In addition, the time-integrated radiation profile strongly contrasts with Fig. 3.3c for a single electron, emphasizing the important role of the spatial bunch shape on radiation emission.

For a sinusoidal beam, evanescent radiation from a standing evanescent wave always leads to stronger superradiance peaks when compared to the ones generated through laser reflection. This happens because when colliding with a standing wave, all particles suffer the same acceleration, whereas in the laser reflection case, the particles suffer an acceleration dependent on the particle's position within the laser pulse. This way, when the radiation from all particles is collected in short temporal window at the Cherenkov angle, the one coming from interactions with a standing wave adds up constructively, while the one coming from laser reflection can be a bit more irregular. Additionally, contamination from the radiation of Thomson scattering-like interaction with the reflected laser pulse can have an impact on the formation of the optical shock.

3.3.3.C Helical Beam

We have seen how a linearly polarized laser pulse imprints a sinusoidal modulation on a particle beam in the direction of polarization of the laser. This spatial modulation leads to superradiant emission when the particle beam collides with an evanescent field at a surface. This superradiant emission can

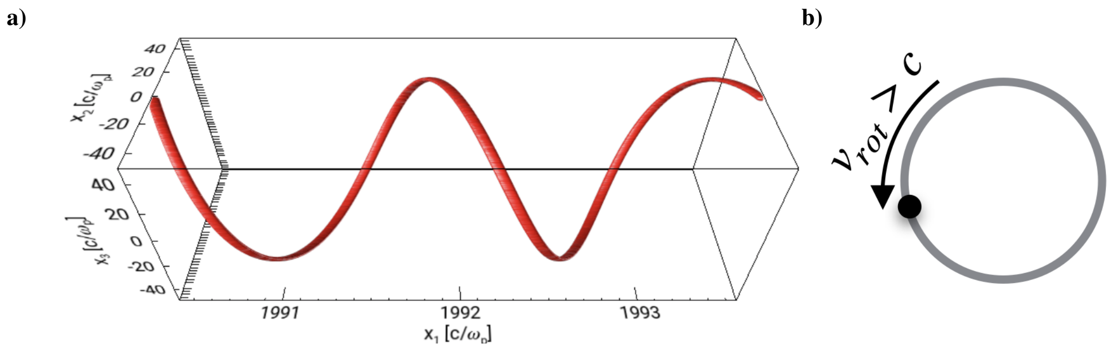

Figure 3.16: Helical particle beam. a) Setup with a helical beam of charged particles co-propagating with a circularly polarized laser pulse, and about to hit a plasma mirror. b) The particle-wave interaction at the mirror surface creates a "ghost" or "virtual" particle that undergoes superluminal circular motion.

be attributed to optical shocks caused by the motion of a superluminal virtual particle in the evanescent surface. The position of this virtual particle at any given time is determined by the intersection between the particle beam and the evanescent surface. For a sinusoidal beam, this particle performs a 1D oscillating motion in the direction of the beam's modulation and the optical shock happens at a specific angle along this direction.

If instead of a linearly polarized laser pulse we use a circularly polarized one, the particle beam will be shaped like a helix. Under these conditions, the virtual particle will perform a circular motion in the plane of the evanescent wave, and the optical shock becomes more interesting.

Here we performed 3D simulations with a helix shaped particle beam, as shown in Figure 3.16. The resolution of the PIC simulation box is 0.1 (c/ω_0) in the (y,z) directions, and 0.015 (c/ω_0) in the x direction and the time step is $dt_{\text{PIC}} = 0.014\ \omega_0^{-1}$. A virtual spherical detector records the radiation in time.

The initial electron bunch length corresponds to $\sigma_{\|} = 4\pi\ c/\omega_0$ (i.e. 2 laser wavelengths). We used a circularly polarized laser pulse with a Gaussian profile with $a_0 = 0.2$, frequency $\omega = \omega_0$ and a transverse spot-size given by $w_0 = 80\ c/\omega_0$, focused at the surface of the plasma mirror. After co-propagating with the laser, the particle beam becomes shaped like a helix with spatial frequency $\omega_h = \omega_0$. Its transverse momentum distribution is thus consistent with the laser's transverse a_0 profile. The helix radius is $r_h \sim 200c/\omega_0$. This beam is travelling along x with relativistic speeds ($\gamma = 500$). A plasma mirror (overdense plasma with $n_p = 4n_{\text{crit}}$) reflects the laser pulse creating an evanescent field where the particle beam radiates.

We utilized a spherical detector located at $R = 10^6 c/\omega_p$. The detector had a time resolution of $dt_{\text{rad}} = 1\times10^{-3}$ (2048 temporal cells) and an aperture of $\Delta\phi = \Delta\theta = 10$ mrad around the x axis, with 256 cells on each direction.

Figure 3.17a, which depicts the resulting instantaneous radiation snapshot in the far field, shows that the radiation is shaped like a cardioid-like caustic. The cusp rotates along the radiated pulse, being located at a fixed angular distance from the longitudinal axis. The time integrated spectrum (see Fig. 3.17 d) then shows a ring structure originated by the rotation of the cardioid cusp. The angular position of the cusp coincides exactly with the predicted Cherenkov cone angle.

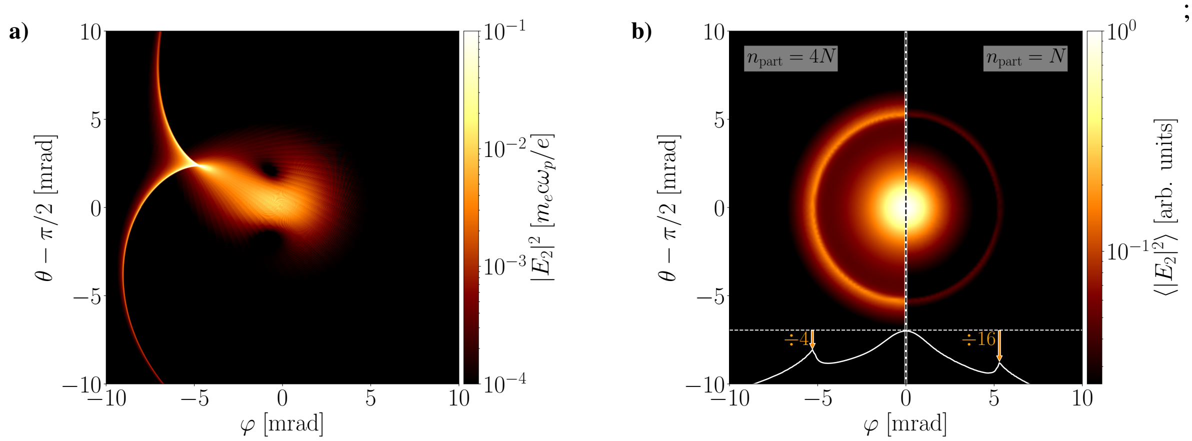

Figure 3.17: Influence of particle beam shape in the time-integrated radiation profile and in the instantaneous snaptshot. a) Instantaneous snapshot of the radiation emitted in setup of Figure 3.16 at a far-away spherical detector. b) Time-integrated spectrum of the radiation emitted by the particles in the setup described of Figure 3.16 for a beam with N particles and a beam with $4N$ particles. A lineout of the integrated spectrum for theta=$\pi/2$ is also present.

Figure 3.17b shows the time integrated radiation spectrum of a simulation with similar setup as in sinusoidal bunch case but this time using a circularly polarized laser pulse to create a helical modulation. The angular position of the resulting ring structure coincides exactly with the predicted Cherenkov cone angle. The lineout shows that the intensity in the ring region grows with the number of electrons in the beam squared, as opposed to the on-axis radiation, which grows linearly with the number of bunch electrons, in perfect agreement with the predictions of Eq. (3.18).

3.3.3.D Titled Beam and Surface Plasmons

An interesting effect occurs when we consider the role of a non-uniform transverse field profile in generalized superradiance. Fields such as those associated with a surface plasmon described by Equations (3.10) and (3.11) have a spatial periodicity along the plasma-vacuum interface, meaning that different parts of the particle beam may be subjected to different accelerations and produce radiation that does not interfere constructively.

A key component on the calculations we performed to obtain the spectrum of radiation emitted by a titled particle beam was the assumption that every particle underwent the same trajectory except for offsets in time and in the transverse position. However, if each particle feels a different evanescent field depending on their vertical position, then each particle will suffer a different acceleration and produce radiation with different profiles.

In the case of the surface plasmon of Figure 3.6, which had a spatial periodicity of 1.78 c/ω_p, a tilted particle beam with slope $m = 200$ with length $L = 9\ c/\omega_p$ from $y = -4.5\ c/\omega_p$ to $y = 4.5\ c/\omega_p$ will hit about 5 full periods of the surface plasmon. In this case the intersection between the particle beam and the plasma surface travels along the surface with velocity $v_{\rm vp} = 200$ c whereas the surface plasmon travels with phase speed $v_\phi = 0.2$ c. This means that, in practice, the titled electron beam feels a static surface plasmon. This way, the peak evanescent field felt by each particle varies periodically with their position along y, giving rise to different acceleration profiles for the particles in the beam.

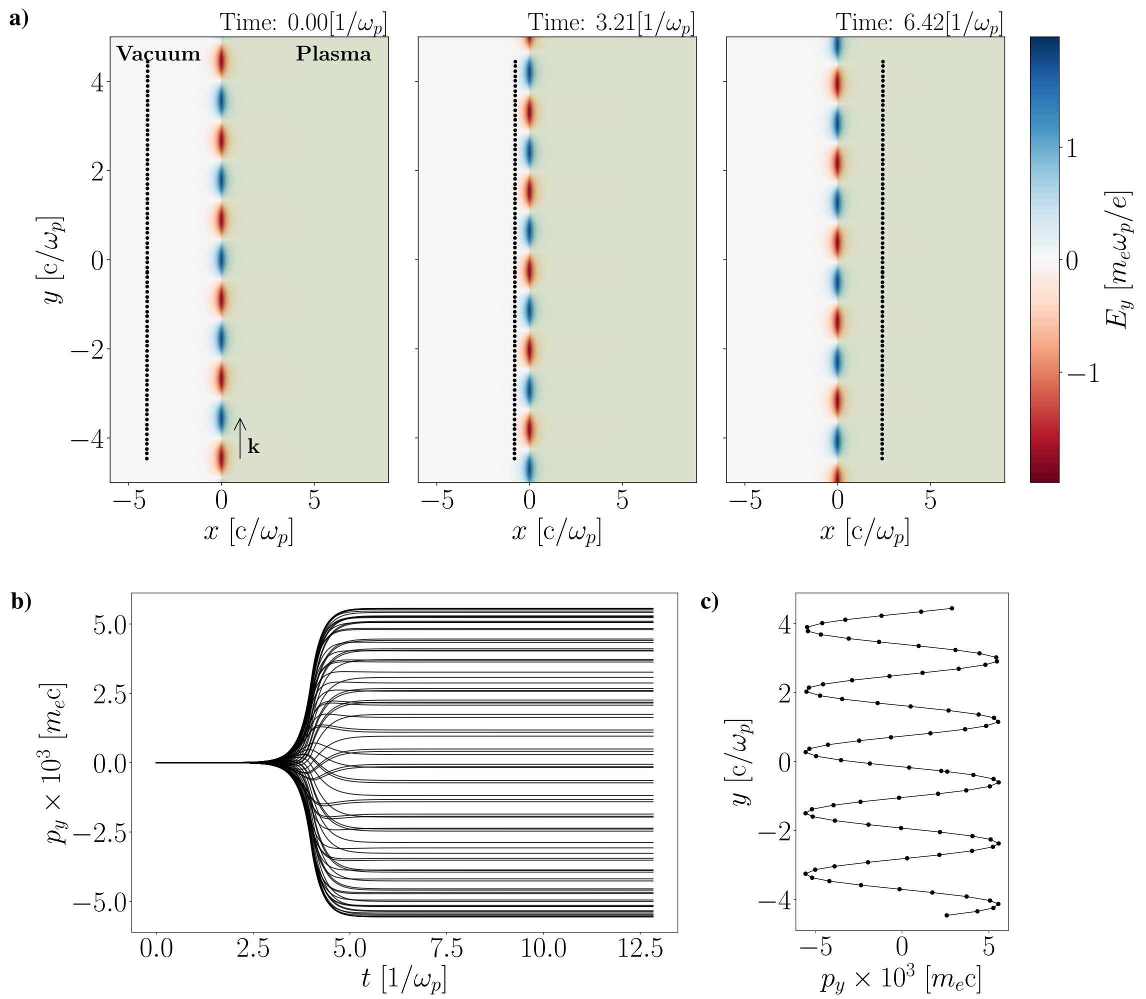

Figure 3.18: Simulation setup and results for tilted beam superradiance with surface plasmons. a) snapshots The tilted beam colliding with the sufrcae plasmon. b) temporal evolution of the beam particles transverse momentum. c) Final transverse momentum of the beam particles as a function of their transverse position.

We performed 2D OSIRIS PIC simulations using the same setup as the one described in Figure 3.6, but instead of a single particle we used a particle beam with slope $m = 200$. The particles in this beam were initialized with no transverse momentum. Figure 3.18a shows 3 snapshots of this simulation as the particle beam collides with the surface plasmon. As the particles feel different evanescent fields depending on their vertical position, the acceleration profiles, shown in Figure 3.18b, are also heterogenous, with some particles acquiring positive transverse momentum while others acquire negative transverse momentum. We can also see from Figure 3.18c that the final momentum obtained by the particles varies periodically with the particles transverse position. Ultimately this means that some particles suffer positive acceleration while others suffer negative acceleration in the y direction. Consequently, the radiation fields, whose value is proportional to the acceleration felt by the particles, will also be positive for some particles and negative for others.

Because the particle beam spans 5 full periods of the surface plasmon, there will be an equal number of particles radiating a positive electric field and a negative electric field. At the Cherenkov angle corresponding to the velocity of the intersection point between the particle beam and the plasma-vacuum

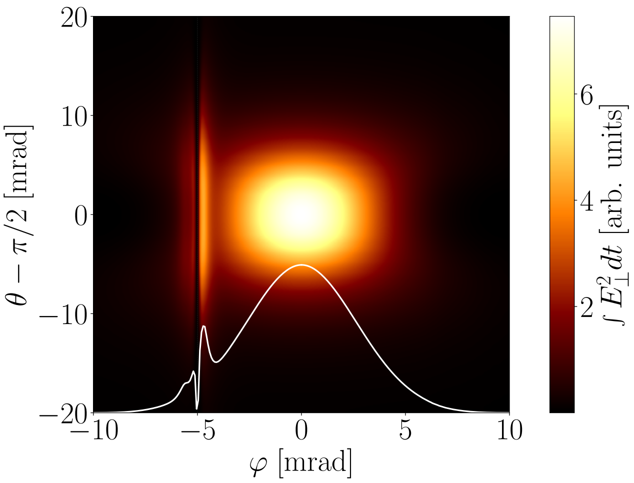

Figure 3.19: Evidence of Sub-radiance at the Cherenkov angle. Spatial profile of the total intensity of radiation emitted by a tilted electron beam scattering across a surface plasmon.

interface, the radiation from all the particles beam will then add up to 0, leading to a phenomenon we called subradiance. Figure 3.19 shows the spatial intensity profile of the radiation emitted in this scenario. It was captured using RaDiO, with a spherical detector placed far away from the simulation box with a radius $R = 10^5\ c/\omega_p$, pointed along the x-axis. The detector had an angular aperture of 20 mrad in the azimuthal angle φ (128 cells) and 40 mrad in the polar angle θ (16 cells). The temporal resolution in the detector was $dt_{\text{det}} = 1.5 \times 10^6$.

The spatial intensity distribution of radiation displays a clear absence of light along the vertical line defined by $\varphi = -5$ mrad, the Cherenkonv angle for a tilted beam with slope $m = 200$. The lineout in Figure 3.19, taken at $\theta = \pi/2$, shows that the radiation intensity completely drops to 0 at this angle. Moreover, the radiated intensity at this angle can be tuned by varying the length of the particle beam, shifting the balance between the particles that emit positive fields and the one that emit negative electric fields. This effect can also be mitigated by increasing the surface plasmon wavelength or matching its phase speed to the one of the virtual particle.

This phenomenon provides an interesting insight on the effect of generalized superradiance, which tells us that it not enough that the radiation from every particle falls in the same narrow temporal region, it is also necessary that the radiation from every particle is at the same phase when reaching the detector.

3.4 Conclusions & Future Work

In conclusion, our scheme appears as a promising mechanism for high frequency radiation emission, with a clear spectral signature that should be experimentally measurable. Furthermore, the radiation from scattering electrons on evanescent modes only occurs where the target exists. This radiation thus carries information about the target shape, this property could be exploited as a diagnostic of evanescent wave scattering or, conversely, to image targets with high (sub-incident-laser-wavelength) resolution. The mechanism described in this paper, capable of producing x-rays by solely relying on moderately relativistic electrons can open new exciting research opportunities.

In this work, we used the reflection properties of plasma mirrors to create the evanescent field, as well as surface plasmons. More intense evanescent modes, for example appearing when electrons are entirely removed from a solid target (e.g., by using an ultra-intense laser pulse), can produce stronger signals.

Since evanescent waves in plasma can be excited at low laser intensities $I \ll 10^{18}\ \mathrm{W/cm^2}$, a keV x-ray source based on evanescent wave-scattering could be experimentally realized in standard Laser Wakefield Accelerator (LWFA) experiments. This mechanism could be particularly appealing in the context of high-repetition rate (KHz) LWFAs [24, 90], where the energy of Betatron photons is too low for applications.

Additionally, the laser-based electron modulator can shape a moderately relativistic electron beam in multiple ways. Hence, a suitable superposition of modes with different frequencies and polarization can control the virtual particle trajectory and therefore control superradiance, coherence and the spectral properties of radiation. For example, orthogonally polarized laser modes at ω_0 and $2\omega_0$ could create a virtual particle whose trajectory resembles the well-known figure-8 motion of an electron in a laser field, which is at the core of high harmonic generation in lasers.

4

Superradiance in the Ion Channel Laser

Contents

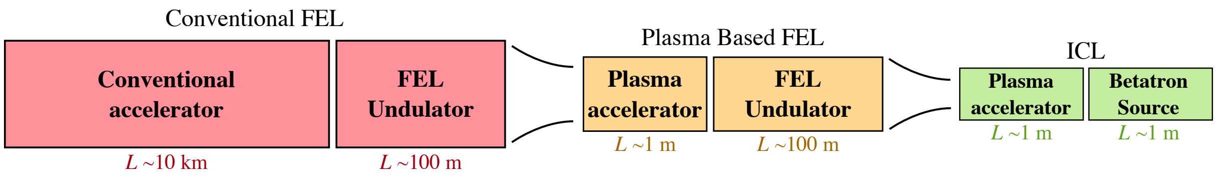

Figure 4.1: Roadmap for miniaturization of ultra bright coherent light sources.

4.1 Introduction

X-ray sources play a pivotal role in investigating and visualizing intricate, rapid microscopic phenomena. While Free Electron Lasers [13] and Synchrotrons [14–16] have been highly effective in this regard, endeavors to downsize these sources have the potential to significantly amplify their influence. Plasma-Based Free Electron Lasers offer a compact alternative by replacing the conventional accelerator with a plasma based accelerator, which can be orders of magnitude smaller, while keeping the magnetic undulator device. Further miniaturization is possible by replacing the undulator device by a plasma based undulator called the betatron. Betatron radiation [20, 28, 33, 34] coming from compact laser-plasma accelerators can play a key role in these efforts, but typically, betatron emission is incoherent, so the peak brightness in these sources is usually much smaller than the one obtained in conventional FELs. Nevertheless, these sources have found their use in many applications and under coherent emission regimes, betatron radiation can achieve peak brightnesses close to conventional FELs. The Ion Channel Laser (ICL) [35] provides a framework to produce temporally coherent Betatron x-rays but requires seeding the microbunching instability to modulate the particle bunch at the radiated wavelength. Here we present recent theory and simulation work on a generalization of the ICL for broadband, off-axis emission, which is made possible by the use of generalized superradiance [63]. The generalized ion channel laser concept can then be seeded by more traditional infra-red laser pulses, and lead to temporally coherent, broadband radiation that can extend all the way up to x-ray frequencies.

4.1.1 Ion Channel Laser

The typical Free Electron Laser mechanism allows electron beams to produce coherent Synchrotron radiation. It makes use of the microbunching instability [91] to split the original beam into several beamlets with size comparable to the wavelength of the radiation emitted by each particle. Because the interparticle distance in each beamlet is smaller than the typical radiated wavelength, the radiation adds up coherently and its intensity scales with the number of particles squared.

The concept of the Ion Channel Laser [20, 35–41] was introduced back in 1990 as a more space-efficient alternative to the Free Electron Laser for generating intense and coherent high-energy radiation. Both FELs and ICLs rely on a phenomenon called electron beam microbunching instability, which arises from the interplay between electrons and the radiation they emit during their transverse oscillations.

In the case of FELs, electrons emit synchrotron radiation while passing through a magnetic undulator, leading to longitudinal microbunching. This process amplifies the radiation in a positive feedback loop. Conversely, in the ICL, electrons emit Betatron radiation as they oscillate around the central axis of an ion channel, which is often seen in the blowout regime of a Plasma Wakefield Accelerator (PWFA).

Betatron oscillations are normally performed by accelerated charged particles in plasma-based accelerators. In these devices, a "driver" (either an electron beam or a laser pulse) expels plasma electrons in the direction transverse to its velocity as it propagates in the medium leaving a region almost exclusively composed by ions behind. The expelled electrons feel the electric field of the positively charged ion region and are driven back to the axis of propagation. This results in a spatially delimited region of positive charge that travels with the driver commonly denoted as *bubble*. Electrons trapped in this region (either through self-injection or external injection) will feel electromagnetic fields originated by the *bubble* structure.

In the ICL, the ion channel creates a linear radial focusing force on the electrons, resulting in transverse harmonic motion. This motion leads to the electrons bunching together in structures of the scale of the wavelength of the emitted radiation.

While FELs [92] demand electron beams with minimal energy spread and small emittance, ICLs are more forgiving [36] in this aspect. However, the ICL has additional constraints related to the allowed spread in the undulator parameter, K. In theory, the advantages of the ICL over the FEL are numerous, including much shorter gain lengths, extensive wavelength tunability, but this scheme can be much harder to realize in practice.

Apart from requiring particle beams with particle with small ΔK, one key restriction of this method, is the difficulty in seeding the ICL microbunching instability at wavelengths comparable to those of the betatron radiation.

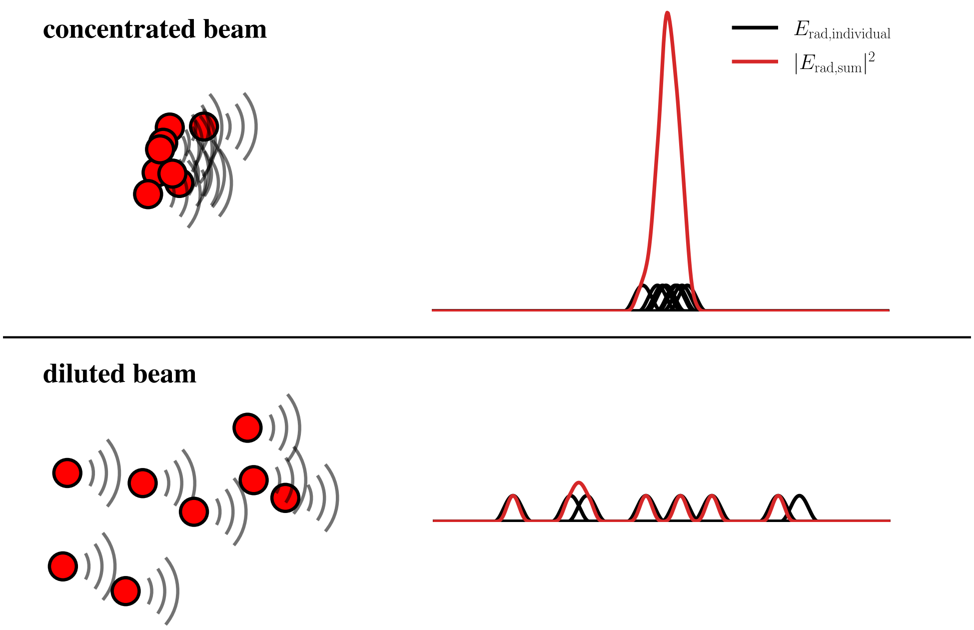

Figure 4.2: Typical mechanism for quadratic intensity scaling with microbunching and its limits.

4.2 The role of superradiance

The concept of generalized superradiance allows us to relax some of the restrictions on the ICL mechanism while still retaining coherent addition of radiation intensity. To understand this, consider first the case of standard superradiance [93–95], illustrated in Figure 4.2: an ultra relativistic electron bunch performing synchronized betatron motion emits the typical pulses of betatron radiation. If the electron bunch is highly concentrated, such that its many particles are located in a region of space much smaller than the length of the pulse emitted by each particle, then the radiation from each particle interferes constructively at all angles and the total intensity scales with the number of particles squared. If, instead, the electron bunch diluted, such that its interparticle distance is much larger than the length of pulse emitted by each particle, then the radiation no longer interferes constructively and we get incoherent addition of radiation. This effect is the reason why microbunching is necessary in the typical configuration of the ion channel laser.

Generalized superradiance, on the other hand, allows for the pulses of all the particles in the beam to interfere constructively under certain conditions, even if the beam is highly diluted. Consider again the case of the diluted particle beam. Assume an infinitely thin train of particles travelling in the x_1 direction with velocity v_0 and performing periodic Betatron oscillations in the transverse direction x_2, with frequency ω_β. The interparticle distance is $\Delta x_0 = \Delta t_0 c \gg \lambda_{\beta,\mathrm{rad}}$, where $\lambda_{\beta,\mathrm{rad}}$ is the typical wavelength of the emitted Betatron radiation. The longitudinal position of each particle p, would then be given by Eq. (4.1) below:

$$x_p(t) = v_0(t - t_{0p}) \tag{4.1}$$

If we assume each particle p is injected in the ion channel at the same transverse position $y = r_\beta$, but at time $t_{0p} = t_0 + p\Delta t_0$, where p is the index of the particle inside the particle beam, with $p = 0$ referring to the particle at the front end of the beam (the first particle to enter the ion channel) and $p = N_p$ referring to the particle at the back end of beam (the last one to enter the ion channel), then each particle will perform the same betatron oscillation but with a temporal offset equal to the distance from the end of the beam. The full trajectory of each particle p would then be given by Eq. (4.2) below:

$$\begin{cases} x_p(t,t_{0p}) = v_0(t - t_{0p}) \\ y_p(t,t_{0p}) = r_\beta \cos\left[\omega_\beta(t - t_{0p})\right] \end{cases} \tag{4.2}$$

In the context of betatron emission, most of the radiation is emitted when the particles are at the maximum displacement of their trajectory, that is, when $y = r_\beta$. In this case, the point where particles radiate the most can be retrieved by solving the system of equations:

$$\begin{aligned} y = r_\beta \Rightarrow \omega_\beta(t - t_{0p}) = 2m\pi,\ \ m \in \mathbb{Z} \\ \Rightarrow x = v_0 2m\pi/\omega_\beta \end{aligned} \tag{4.3}$$

Thus, the point of emission of radiation is located at the same longitudinal position for every particle, emulating a stationary light source. One can also say that the particle beam shape can be described as a sine wave with zero phase speed.

The top row of Figure 4.3 illustrates this situation representing each particle as a colored circle (dark red means that the particle is radiating), and the emitted radiation as circular shells, circumferences whose center lies on the position where that radiation was emitted. The thickness of these circumferences represents the pulse length, which is much smaller than the interparticle distance. The circular shells of radiation never intersect. In this case it is not possible to obtain constructive interference.

Consider now the case where the transverse injection position of the particle now depends on the particle's relative position in the beam. Each particle now has a slight phase difference dependent on its position in the beam or the injection time, and the trajectory of each particle p would be given by Equation (4.4) below:

$$\begin{cases} x_p(t,t_{0p}) = v_0(t - t_{0p}) \\ y_p(t,t_{0p}) = r_\beta \cos\left[\omega_\beta(t - t_{0p}) + \omega_m t_{0p}\right] \end{cases} \tag{4.4}$$

where v_0 is the longitudinal velocity of the bunch, r_β the radius of the Betatron oscillations, ω_β the Betatron frequency, ω_m a modulation frequency and t_{0p} the time of injection of the particle. In this case the particle beam has an effective phase speed given by:

$$v_\phi = \frac{v_0}{1 - \omega_\beta/\omega_m} = \frac{\omega_m}{k_m} \tag{4.5}$$

Because of this phase speed, the point where each particle radiates the most is not located at a fixed position emulating a moving light source. This is illustrated in the two bottom rows of Figure 4.3, where

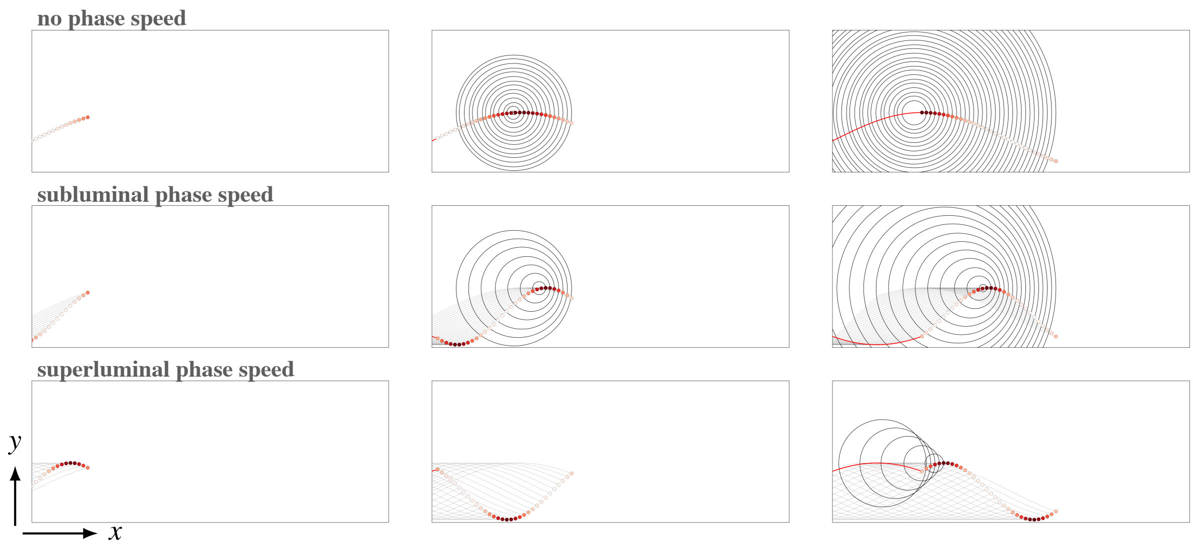

Figure 4.3: A phase speed induced superluminal light source. Each row shows three snapshots of the particle beam and its radiation with time increasing from left to right. The particles are represented using colored circles. The color of each particle represents the intensity of radiation being emitted (dark red: high intensity, white: no intensity). The trajectory of each particle is shown with a light grey line except for one which is shown with a red line. The pulses of radiation are emitted omnidirectionally, so they are represented with circumferences whose center lies on the point where radiation was emitted. The thickness of these circumferences represents the pulse length. The top row shows a particle beam with no phase speed. The middle row shows a particle beam with subluminal phase speed and the bottom row shows a particle beam with superluminal phase speed.

we can see that the dark red region, as well as the center of the radiation shells is moving forward. Under the right conditions this moving light source can be superluminal (bottom row) and the radiation from each particle can interfere constructively at a specific angle in a Cherenkov-like effect, even if the interparticle distance is much larger than the radiated pulse length. We denoted this effect Generalized superradiance [63] as it allows for coherent addition of radiation intensity just like classical superradiance, but under less stringent conditions.

4.2.1 Spectrum Calculations

To understand the spectral features of Generalized Superradiance, and how it can be used to generalize the standard superradiance effect in conventional undulator or betatron sources, we consider the spectrum of radiation described by the Liénard-Wiechert Potentials. The spectrum of radiation obtained when a particle beam has a superluminal phase speed can then be obtained by solving the integral in the Lienard-Wiechert potentials using the trajectories defined in Equation. (4.4) for a set of N_p electrons. The corresponding spectrum of radiation is given by:

$$\frac{\mathrm{d}^2 I}{\mathrm{d}\omega \mathrm{d}\Omega} = \frac{e^2}{4\pi^2 c}\omega^2 \left| \int \sum_{j=1}^{N_p} \mathbf{n} \times [\mathbf{n} \times \beta_j(t)]\, e^{i\omega\left(t - \mathbf{n}\cdot\mathbf{r}_j(t)/c\right)} \mathrm{d}t \right|^2 \tag{4.6}$$

where e is the electron charge, c the speed of light, $\mathbf{r}_j(t) = x_{1,j}(t)\mathbf{e}_x + x_{2,j}(t)\mathbf{e}_y$ is the position of particle j at time t, $\beta_j(t)$ the normalized velocity of particle j with respect to c at time t. $\mathbf{n}$ is the unitary direction vector pointing towards the direction of observation, which can be expressed in spherical coordinates, as a combination of the polar angle (θ) and the azimuthal angle (ϕ).

$$\mathbf{n} = (n_x, n_y, n_z) = \sin\theta\cos\varphi\mathbf{e}_x + \sin\theta\sin\varphi\mathbf{e}_y + \cos\theta\mathbf{e}_z \tag{4.7}$$

Here we assume the convention of using the azimuthal angle (φ) as the angle measured from the positive x-axis in the xy-plane, with θ as the polar angle measured from the positive z-axis. The ranges for the angles are typically: $\theta \in [0, \pi]$, $\varphi \in [0, 2\pi[$.

Considering emission only in the $x0y$ plane ($\theta = \pi/2$), the cross product $\mathbf{n} \times [\mathbf{n} \times \boldsymbol{\beta}(t)]$ becomes:

$$\mathbf{n} \times [\mathbf{n} \times \boldsymbol{\beta}(t)] = \left(\beta_y \cos\varphi \sin\varphi - \beta_x \sin^2\varphi\right)\mathbf{e}_x + \left(\beta_x \cos\varphi\sin\varphi - \beta_y \cos^2\varphi\right)\mathbf{e}_y \tag{4.8}$$

So we can re-write Eq. (4.6) as:

$$\begin{aligned}\frac{\mathrm{d}^2 I}{\mathrm{d}\omega_{\mathrm{rad}}\mathrm{d}\Omega} = \frac{e^2}{4\pi^2 c}\omega^2 \Bigg(&\left| \int \sum_{j=1}^{N_p} \left(\beta_{y,j}(t)\cos\varphi\sin\varphi - \beta_{x,j}(t)\sin^2\varphi\right) e^{i\omega\left(t - \mathbf{n}\cdot\mathbf{r}_j(t)/c\right)}\mathrm{d}t \right|^2 + \\ &+ \left| \int \sum_{j=1}^{N_p} \left(\beta_{x,j}(t)\cos\varphi\sin\varphi - \beta_{y,j}(t)\sin^2\varphi\right) e^{i\omega\left(t - \mathbf{n}\cdot\mathbf{r}_j(t)/c\right)}\mathrm{d}t \right|^2 \Bigg)\end{aligned} \tag{4.9}$$

Expanding the modulus of the integrals and using the fact that the integral of a sum is equal to the sum of the integrals, we get:

$$\begin{aligned}\frac{\mathrm{d}^2 I}{\mathrm{d}\omega_{\mathrm{rad}}\mathrm{d}\Omega} = \frac{e^2}{4\pi^2 c}\omega^2 \Bigg(&\cos^2\varphi \left| \sum_{j=1}^{N_p} \int \beta_{y,j}(t) e^{i\omega\left(t - \mathbf{n}\cdot\mathbf{r}_j(t)/c\right)}\mathrm{d}t \right|^2 + \sin^2\varphi \left| \sum_{j=1}^{N_p} \int \beta_{x,j}(t) e^{i\omega\left(t - \mathbf{n}\cdot\mathbf{r}_j(t)/c\right)}\mathrm{d}t \right|^2 - \\ &- 2\cos\varphi\sin\varphi \int \sum_{j=1}^{N_p} \beta_{x,j}(t) e^{i\omega\left(t - \mathbf{n}\cdot\mathbf{r}_j(t)/c\right)}\mathrm{d}t \int \sum_{j=1}^{N_p} \beta_{y,j}(t) e^{i\omega\left(t - \mathbf{n}\cdot\mathbf{r}_j(t)/c\right)}\mathrm{d}t \Bigg)\end{aligned} \tag{4.10}$$

Introducing the variables $I_{x,j}$ and $I_{y,j}$ to represent the integrals for each particle, and the variables I_x, I_y to represent the summed integrals, we can simplify the previous equation to:

$$\frac{\mathrm{d}^2 I}{\mathrm{d}\omega_{\mathrm{rad}}\mathrm{d}\Omega} = \frac{e^2}{4\pi^2 c}\omega^2 \left(\left| \sum_{j=1}^{N_p} I_{y,j} \right|^2 \cos^2\varphi + \left| \sum_{j=1}^{N_p} I_{x,j} \right|^2 \sin^2\varphi - 2\sum_{j=1}^{N_p} I_{x,j} \sum_{j=1}^{N_p} I_{y,j} \cos\varphi\sin\varphi \right) \tag{4.11}$$

$$= \frac{e^2}{4\pi^2 c}\omega^2 \left(|I_y|^2 \cos^2\varphi + |I_x|^2 \sin^2\varphi - 2 I_x I_y \cos\varphi\sin\varphi \right) \tag{4.12}$$

This way, we can compute each component separately. Starting with I_x:

$$\begin{aligned} I_x &= \sum_{j=1}^{N_p} \int \beta_{x,j}(t) e^{i\omega\left(t - \mathbf{n}\cdot\mathbf{r}_j(t)/c\right)}\mathrm{d}t \\ &= \sum_{j=1}^{N_p} \int \beta_0 e^{i\omega\left(t - n_x\beta_0(t - t_{0,j})\right)} e^{-i\omega n_y r_\beta/c \sin\left[\omega_\beta(t - t_{0j}) + \omega_m t_{0j}\right]}\mathrm{d}t \\ &= \sum_{j=1}^{N_p} e^{i\omega t_{0,j}} \int \beta_0 e^{i\omega\left((t - t_{0,j}) - n_x\beta_0(t - t_{0,j})\right)} e^{-i\omega n_y r_\beta/c \sin\left[\omega_\beta(t - t_{0j}) + \omega_m t_{0j}\right]}\mathrm{d}t \end{aligned} \tag{4.13}$$

introducing the variable $t' = t - t_{0j}$ leads to:

$$I_x = \sum_{j=1}^{N_p} e^{i\omega t_{0,j}} \int \beta_0 e^{i\omega(t'-n_x\beta_0 t')} e^{-i\omega n_y r_\beta/c \sin\left[\omega_\beta t'+\omega_m t_{0j}\right]} \mathrm{d}t' \tag{4.14}$$

using the Jacobi-Anger expansion, as shown below:

$$e^{-i\omega n_y r_\beta/c \sin\left(\omega_\beta t'-\omega_m t_{0p}\right)} = \sum_{n=-\infty}^{\infty} i^n J_n(-\omega n_y r_\beta/c) e^{-in\left(\omega_\beta t'-\omega_m t_{0j}\right)} \tag{4.15}$$

we can further simplify the expression by isolating the integral in t' to:

$$I_x = \sum_{n=-\infty}^{\infty} i^n J_n(-\omega n_y r_\beta/c) \sum_{j=1}^{N_p} e^{i(\omega-n\omega_m)t_{0j}} \int \beta_0 e^{i\omega(t'-n_x\beta_0 t')} e^{-in\omega_\beta t'} \mathrm{d}t' \tag{4.16}$$

Equation (4.16) states that the spectrum of radiation emitted by each particle is the same, except for a phase difference related to the time of injection t_{0j}. This way, as all particle follow the same trajectory apart from this phase difference, the integral in t' is the same for all particles and can be obtained effortlessly:

$$\int \beta_0 e^{i\omega(t'-n_x\beta_0 t')} e^{-in\omega_\beta t'} \mathrm{d}t' = \frac{\beta_0 T_{\mathrm{int}}}{2} \mathrm{sinc}\left(T_{\mathrm{int}} \frac{\omega(1-n_x\beta_0)-n\omega_\beta}{2}\right) \tag{4.17}$$

where we integrated from $t' = -T_{\mathrm{int}}/2$ to $t' = -T_{\mathrm{int}}/2$. T_{int} is the period of time during which radiation is emitted. It is assumed to be the same for all particles. For a sufficiently large number of particles in the beam one can replace the summation over the particles by an integral:

$$\sum_{j=1}^{N_p} e^{i(\omega-n\omega_m)t_{0j}} \to \frac{N_p}{L} \int_{-T/2}^{T/2} f(t_0) e^{i(\omega-n\omega_m)t_0} dt_0 \tag{4.18}$$

where $T = L/v_0$ is the temporal length of the particle beam and f the longitudinal beam density profile. For a uniform density profile (*i.e.* $f(t) = 1$), we get:

$$\frac{N_p v_0}{L} \int_{-T/2}^{T/2} f(t_0) e^{i(\omega-n\omega_m)t_0} dt_0 = \frac{N_p}{T} \mathrm{sinc}\left(\frac{T(\omega-n\omega_m)}{2}\right) = \frac{N_p v_0}{L} \mathrm{sinc}\left(\frac{L(\omega-n\omega_m)}{2v_0}\right) \tag{4.19}$$

Thus, Equation (4.16) becomes:

$$I_x = \frac{N_p v_0}{L} \frac{\beta_0 T_{\mathrm{int}}}{2} \sum_{n=-\infty}^{\infty} i^n J_n(-\omega n_y r_\beta/c) \mathrm{sinc}\left(\frac{L\mu_n}{2v_0}\right) \mathrm{sinc}\left(\frac{T_{\mathrm{int}}\tau_n}{2}\right) \tag{4.20}$$

where we introduced the variables μ_n and τ_n to simplify the arguments inside the sinc functions and the variable α to represent the argument inside the Bessel function. τ_n/v_0 is also known as the FEL detuning parameter, which in the conventional FEL theory determines the spectral line-width of single particle radiation emission.

$$\mu_n = \omega - n\omega_m, \quad \tau_n = \omega(1-n_x\beta_0) - n\omega_\beta, \quad \alpha = -\omega n_y r_\beta/c \tag{4.21}$$

The I_y component can be obtained in a similar, although slightly more complex way due to the sinusoidal nature of β_y:

$$
\begin{aligned}
I_y &= \sum_{j=1}^{N_p} \int \beta_{y,j}(t) e^{i\omega\left(t-\mathbf{n}\cdot\mathbf{r}_j(t)/c\right)} \mathrm{d}t \\
&= \sum_{n=-\infty}^{\infty} i^n J_n(-\omega n_y r_\beta/c) \sum_{j=1}^{N_p} e^{i(\omega-n\omega_m)t_{0j}} \int \beta_{y,j}(t) e^{i\omega(t'-n_x\beta_0 t')} e^{-in\omega_\beta t'} \mathrm{d}t'
\end{aligned}
\tag{4.22}
$$

To evaluate the integral in t' we must explicitly replace the expression for β_y:

$$
\begin{aligned}
&\int \beta_{y,j}(t) e^{i\omega(t'-n_x\beta_0 t')} e^{-in\omega_\beta t'} \mathrm{d}t' \\
&= - r_\beta\,\omega_\beta \int \sin\left(\omega_\beta t' + \omega_m t_{0j}\right) e^{i\omega(t'-n_x\beta_0 t')} e^{-in\omega_\beta t'} \mathrm{d}t' \\
&= - r_\beta\,\omega_\beta \int \frac{e^{i\left(\omega_\beta t'+\omega_m t_{0j}\right)} - e^{-i\left(\omega_\beta t'+\omega_m t_{0j}\right)}}{2i} e^{i\omega(t'-n_x\beta_0 t')} e^{-in\omega_\beta t'} \mathrm{d}t' \\
&= - \frac{r_\beta\,\omega_\beta}{2i} \left[e^{i\omega_m t_{0j}} \int e^{it'\left(\omega(1-n_x\beta_0)-(n-1)\omega_\beta\right)} \mathrm{d}t' - e^{-i\omega_m t_{0j}} \int e^{it'\left(\omega(1-n_x\beta_0)-(n+1)\omega_\beta\right)} \mathrm{d}t' \right] \\
&= - \frac{r_\beta\,\omega_\beta}{2} \left[e^{i\omega_m t_{0j}} \int e^{it'\tau_{n-1}} \mathrm{d}t' - e^{-i\omega_m t_{0j}} \int e^{it'\tau_{n+1}} \mathrm{d}t' \right]
\end{aligned}
\tag{4.23}
$$

So the expression for I_y becomes:

$$
\begin{aligned}
I_y &= - r_\beta\,\omega_\beta \sum_{n=-\infty}^{\infty} \frac{i^n}{2i} J_n(\alpha) \sum_{j=1}^{N_p} e^{i(\omega-(n-1)\omega_m)t_{0j}} \int e^{it'\tau_{n-1}} \mathrm{d}t' + \\
&\qquad + r_\beta\,\omega_\beta \sum_{n=-\infty}^{\infty} \frac{i^n}{2i} J_n(\alpha) \sum_{j=1}^{N_p} e^{i(\omega-(n+1)\omega_m)t_{0j}} \int e^{it'\tau_{n+1}} \mathrm{d}t' \\
&= - r_\beta\,\omega_\beta \sum_{n=-\infty}^{\infty} \frac{i^{n+1}}{2i} J_{n+1}(\alpha) \sum_{j=1}^{N_p} e^{i(\omega-n\omega_m)t_{0j}} \int e^{it'\tau_n} \mathrm{d}t' + \\
&\qquad + r_\beta\,\omega_\beta \sum_{n=-\infty}^{\infty} \frac{i^{n-1}}{2i} J_{n-1}(\alpha) \sum_{j=1}^{N_p} e^{i(\omega-n\omega_m)t_{0j}} \int e^{it'\tau_n} \mathrm{d}t' \\
&= - r_\beta\,\omega_\beta \sum_{n=-\infty}^{\infty} \left(\frac{i^{n+1}}{2i} J_{n+1}(\alpha) - \frac{i^{n-1}}{2i} J_{n-1}(\alpha) \right) \sum_{j=1}^{N_p} e^{i\mu_n t_{0j}} \int e^{it'\tau_n} \mathrm{d}t'
\end{aligned}
$$

The summation over the particles and the integral in dt' can be obtained using the same approach as in the case of I_x, yielding:

$$
I_y = -\frac{N_p v_0}{L} \frac{r_\beta\,\omega_\beta T_{\mathrm{int}}}{2} \sum_{n=-\infty}^{\infty} \left(i^n J_{n+1}(\alpha) - i^{n-2} J_{n-1}(\alpha) \right) \operatorname{sinc}\left(\frac{L\mu_n}{2v_0}\right) \operatorname{sinc}\left(\frac{T_{\mathrm{int}}\tau_n}{2}\right) \tag{4.24}
$$

The sum of Bessel functions of different orders can also be further simplified:

$$
i^n J_{n+1}(\alpha) - i^{n-2} J_{n-1}(\alpha) = i^n \left(J_1(\alpha) - i^{-2} J_{n-1}(\alpha) \right) = i^n \left(J_{n+1}(\alpha) + J_{n-1}(\alpha) \right) = i^n \frac{n}{\alpha} J_n(\alpha) \tag{4.25}
$$

In the end, the term I_y becomes:

$$
I_y = -\frac{N_p v_0}{L} \frac{r_\beta\,\omega_\beta T_{\mathrm{int}}}{2} \sum_{n=-\infty}^{\infty} i^n \frac{n}{\alpha} J_n(\alpha) \operatorname{sinc}\left(\frac{L\mu_n}{2v_0}\right) \operatorname{sinc}\left(\frac{T_{\mathrm{int}}\tau_n}{2}\right) \tag{4.26}
$$

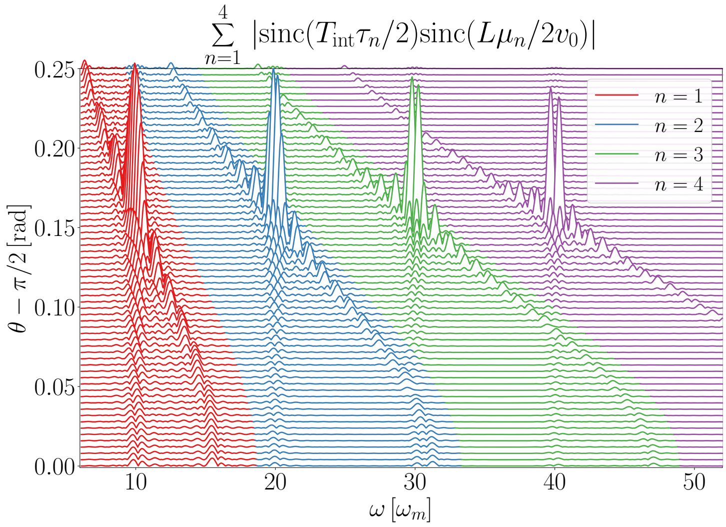

Figure 4.4: Plot of the square of the sum in I_x and I_y up to the 4th order for a particle beam with $\gamma = 5$ with modulation frequency $\omega_m \sim 31\omega_\beta$. The length of the particle beam is $L = 10\lambda_m = 10(2\pi c/\omega_m)$ and the interaction time $T_{\mathrm{int}} = 20T_\beta = 20(2\pi/\omega_\beta)$. The contribution from each order is represented with a different color.

To arrive at the final expression for the spectrum, we need to obtain the expressions for $|I_x|^2$ and $|I_y|^2$. Because both I_x and I_y are the result of an infinite sum in n, their expression would generally be given by:

$$\left|\sum_{n=-\infty}^{\infty} a_n(\omega,\theta)\right|^2 = \sum_{n=-\infty}^{\infty}\left(|a_n(\omega,\theta)|^2 + 2\sum_{k=-\infty}^{n-1} a_n(\omega,\theta)a_k(\omega,\theta)\right) \tag{4.27}$$

with $a_n(\omega,\theta)$ representing each term in the summation. However, as will be made clear shortly, we can neglect the cross terms $a_n(\omega,\theta)a_{k\neq n}(\omega,\theta)$.

Figure 4.4 shows that for a sufficiently long particle beam (when compared to the modulation wavelength) with sufficiently long interaction time (when compared to the betatron period), each term a_n in the spectrum components I_x and I_y gives rise to a single harmonic of the modulation frequency of order n at the Cherenkov angle. Under these conditions, these harmonics are very clearly separated, meaning that for any given combination of ω and θ the product $a_n(\omega,\theta)a_{k\neq n}(\omega,\theta)$ is zero. The separation of these harmonics is strictly dependent on the ratio between their spectral width $\Delta\omega$ and the spectral distance between consecutive harmonics ω_0. The spectral width is set by the parameters inside the sinc functions:

$$\Delta\omega \simeq \min\left(\frac{2\pi v_0}{L}, \frac{2\pi(1-n_x\beta_0)}{T_{\mathrm{int}}}\right) \tag{4.28}$$

whereas the separation is set by the modulation frequency ω_m and the fundamental harmonic of the single particle betatron spectrum at the Cherenkov angle $\omega_\beta/(1-\cos(\varphi_{\mathrm{Ch}})\beta_x)$. In order to obtain a clear separation in the harmonics the spectral width must be much smaller than the harmonic separation, that is:

$$\frac{v_0}{L} \ll \omega_m, \quad \frac{2\pi(1-n_x\beta_0)}{T_{\mathrm{int}}} \ll \omega_m, \tag{4.29}$$

Thus, $|I_x|^2$ and $|I_y|^2$ become:

$$|I_x|^2 = \frac{N_p^2 v_0^2}{L^2} \frac{\beta_0^2 T_{\text{int}}^2}{4} \sum_{n=-\infty}^{\infty} \left(J_n(\alpha) \text{sinc}\left(\frac{L\mu_n}{2v_0}\right) \text{sinc}\left(\frac{T_{\text{int}}\tau_n}{2}\right) \right)^2 \tag{4.30}$$

$$|I_y|^2 = \frac{N_p^2 v_0^2}{L^2} \frac{r_\beta^2 \omega_\beta^2 T_{\text{int}}^2}{4} \sum_{n=-\infty}^{\infty} \left(\frac{n}{\alpha} J_n(\alpha) \text{sinc}\left(\frac{L\mu_n}{2v_0}\right) \text{sinc}\left(\frac{T_{\text{int}}\tau_n}{2}\right) \right)^2 \tag{4.31}$$

The same reasoning can be applied to the term $I_x I_y$.

$$|I_x I_y| = \frac{N_p^2 v_0^2}{L^2} \frac{r_\beta \omega_\beta \beta_0 T_{\text{int}}^2}{4} \sum_{n=-\infty}^{\infty} \frac{n}{\alpha} \left(J_n(\alpha) \text{sinc}\left(\frac{L\mu_n}{2v_0}\right) \text{sinc}\left(\frac{T_{\text{int}}\tau_n}{2}\right) \right)^2 \tag{4.32}$$

$$\tag{4.33}$$

Coming back to Eq. (4.12) we can obtain the full expression for the emitted spectrum:

$$\frac{\mathrm{d}^2 I}{\mathrm{d}\omega_{\text{rad}} \mathrm{d}\Omega} = \frac{e^2 N_p^2 \beta_0^2 T_{\text{int}}^2 c}{16\pi^2 L^2} \omega^2 \sum_{n=-\infty}^{\infty} \text{sinc}^2\left(\frac{L\mu_n}{2v_0}\right) \text{sinc}^2\left(\frac{T_{\text{int}}\tau_n}{2}\right) J_n^2(\alpha) \left(\beta_0 \sin(\varphi) + r_\beta \omega_\beta \frac{n}{\alpha} \cos(\varphi) \right)^2 \tag{4.34}$$

From Eq. (4.34) we can conclude that, like the components I_x and I_y, the full radiated spectrum is composed by multiple separate harmonics, each one corresponding to a term in the infinite summation. These isolated harmonics appear as a consequence of the sinc^2 functions which are characterized by sharp intensity peaks around the zero or their argument. Because the argument of each sinc^2 term depends on n, each term of the summation gives rise to an intensity peak at a different frequency. We can discover these harmonics by finding the zeros of μ_n and τ_n:

$$\mu_n = \tau_n = 0 \Rightarrow \begin{cases} \omega = n\omega_m & \text{(4.35a)} \\ \omega = n\omega_\beta / (1 - \beta_0 \cos\varphi) & \text{(4.35b)} \end{cases}$$

Equation (4.35a) determines that the intensity peaks will always occur at multiples of the modulation frequency ω_m, while Equation. (4.35b) recovers the curves of maximum intensity in typical single particle Betatron spectrum. The intensity maxima of spectrum will be located at the intersection of the curves defined by the conditions in Eq. (4.35). These curves are themselves harmonics as well, one corresponding to the typical betatron spectrum harmonics and the other corresponding to harmonics of the modulation frequency. Figure 4.5 displays the intersection of the curves defined by these equations. With some manipulation, shown below in Eq. (4.36), we can find that the intersection, if it exists, always happens at a specific angle, independently of the of order of the harmonic. The angle can be found by equating Eqns. (4.35b) and (4.35a):

$$\begin{aligned} & n\omega_m = n\omega_\beta / (1 - \beta_0 \cos\varphi) \\ \Leftrightarrow & \cos\varphi = \frac{1 - \omega_\beta/\omega_m}{\beta_0} \\ \Leftrightarrow & \cos\varphi = \frac{c\left(1 - \omega_\beta/\omega_m\right)}{v_0} \\ \Leftrightarrow & \varphi = \arccos\left(c/v_\phi\right) \equiv \varphi_{\text{Ch}} \end{aligned} \tag{4.36}$$

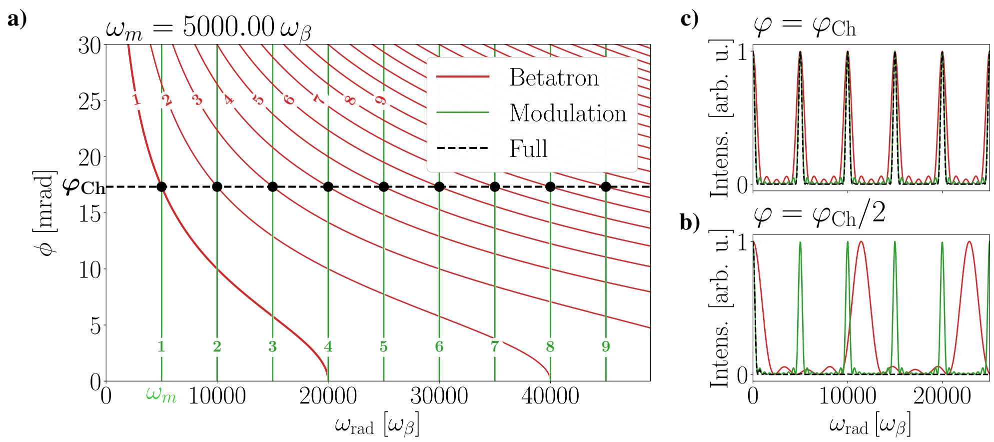

Figure 4.5: Harmonics of the Betatron spectrum, in red, defined by Eq. (4.35b), harmonics of the modulation frequency, in green, defined by Eq. (4.35a) and the intersection points between harmonics of the same order for a particle beam with superluminal phase speed. a) Intersections and harmonics in the $\varphi - \omega_{\rm rad}$ plane, b) Intersections and harmonics for $\varphi = \varphi_{\rm Ch}$. c) Intersections and harmonics for $\varphi = \varphi_{\rm Ch}/2$

where v_ϕ is the phase speed equivalent of the particle beam (see Eq. (4.5)). The intersection only happens for $v_\phi \geq c$, that is, for phase speeds greater than or equal to the speed of light. For $v_\phi < c$ the co-sine of φ would be greater than 1 and there is no angle that satisfies that condition. This is consistent with the physical picture given above in Section 4.2, where we showed that only superluminal phase velocities lead to optical shocks and constructive interference. When the phase speed is smaller than the speed of light, the radiation coming from consecutive particles in the beam never intersects and there is no optical shock. Figure 4.6a showcases a scenario where the phase speed is smaller than the speed of light. In this case, there are no intersections between curves of the same order.

This analysis also recovers the typical condition for obtaining standard undulator radiation superradiance. For particle beams with no modulation $\omega_m = 0$, the beam modulation contribution becomes:

$$\text{sinc}^2(L\omega/2v_0) \tag{4.37}$$

which corresponds to a single peak around $\omega = 0$, meaning that for longer particle beams and, consequently, sharper beam "modulation" contributions, there are no intersections between the beam modulation contribution and the single particle contribution and the radiated intensity is attenuated. However, if we shorten the length of our particle beam, L, the contribution from Eq. (4.37) becomes a wide peak and we can find relevant intensity peaks until $\omega \sim 2\pi/L$. In this case, the maxima of the spectrum are no longer determined by the intersection between Eq. (4.35b) and Eq. (4.35a) but by the sharp peaks of the single particle Betatron spectrum until a given frequency, determined by the beam length. As a consequence, the radiated intensity scales with N_p^2 for frequencies up to $\omega \sim \pi 2/L$. This is equivalent to stating that the beam particle are bunched in spatial region the size of a radiation wavelength, which is the typical limit for un-modulated particle beams.

The spectral analysis is then in agreement with the spatiotemporal illustration given by Figure 4.3. Where we see no constructive interference for the subluminal cases and constructive interference at the

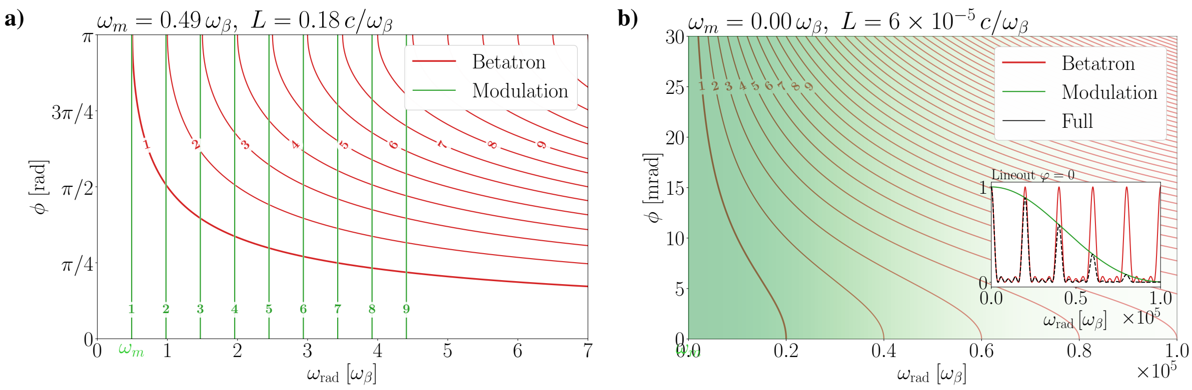

Figure 4.6: Harmonics of the Betatron spectrum, in red, defined by Eq. (4.35b), harmonics of the modulation frequency, in green, defined by Eq. (4.35a) and the intersection points between harmonics of the same order for a particle beam with subluminal phase speed (a) and a particle beam with 0 phase speed (b). The inset on (b) shows a lineout of the harmonics and intersections on-axis ($\varphi = 0$).

Cherenkov angle for the superluminal case.

It is also interesting to note that for on-axis superradiant emission, this scheme requires that the phase speed of the particle beam is equal to c.

We have seen how we can obtain superradiance at any angle $\varphi_{\rm Ch}$, even for arbitrarily diluted beams of particles with less than a particle per wavelength, as long as the bunch is modulated frequency is equal to the first harmonic of the single particle radiation at $\varphi_{\rm Ch}$. It is then necessary to investigate possible ways of modulating particle beams in such a way.

4.3 Modulating a particle beam

A laser pulse co-propagating with a relativistic particle beam exerts a transverse electromagnetic force on the charged particles, deflecting them. If the laser is linearly polarized, this deflection will occur in the polarization plane of the laser. In the case of a linearly polarized laser pulse propagating in vacuum with phase speed equal to the speed of light ($v_\varphi = c$), the electromagnetic field for a plane wave laser field would be given by:

$$\begin{cases} E_y = E_0 \sin(\omega t - kx) \\ B_z = kE_0/\omega \sin(\omega t - kx) \end{cases} \tag{4.38}$$

with ω being the laser frequency and k the laser wavenumber. Here, each particle in a highly energetic particle beam ($\gamma > 100$) travelling close to the speed of light will feel approximately the same phase of the laser for a long period of time as shown in the top row of Figure 4.7. Consequently, each particle feels a different force depending on their initial position along the propagation direction and the particle beam will be shaped like sinusoid with periodicity set by the laser pulse period.

Consider now the case where both the laser pulse and the particle beam are propagating in a plasma along the x direction. In this case the phase speed of the laser pulse is larger than the speed of light ($v_\varphi > c$). This means that, as each particle is co-propagating with the laser only at c, they will now feel periodically different phases of the laser pulse as they lag behind its phase fronts as shown in the top bottom of Figure 4.7. The phase of the laser felt by particle p is given by:

$$\phi_p(t) = \phi_{0p} - \frac{v_\varphi - v_0}{\lambda_0/2\pi}(t - t_{0p}) \tag{4.39}$$

where $\phi_{0p} = \omega_0 t_{0p} - k_0 x_{0p}$ is the phase of the laser pulse felt by the particle when it first interacts with the laser at $t = t_0$ and $x = x_0$. Thus, each particle p feels an oscillating field with periodicity set by the difference between the particle beam's velocity and the phase speed of the laser $|v_0 - v_\varphi|$ and the wavelength of the laser, λ_0. Assuming that the beam particle velocity remains constant along the propagation direction, the force felt by particle p in the transverse direction due to the laser fields is then:

$$\begin{aligned} [\mathbf{F}_{L,p}]_{\mathbf{e}_y}(t) &= [\mathbf{E}_L(t) + \mathbf{v} \times \mathbf{B}_L(t)]_{\mathbf{e}_y} \\ &= E_y(t) - v_0 B_z(t) \\ &= (1 - kv_0/\omega) E_y(t) \\ &= (1 - kv_0/\omega) E_0 \sin\left[\omega_0 \frac{v_\varphi - v_0}{v_\varphi}(t - t_{0p}) + \phi_{0p}\right] \\ &= (1 - kv_0/\omega) E_0 \sin\left[\omega_\phi (t - t_{0p}) + \phi_{0p}\right] \end{aligned} \tag{4.40}$$

A longitudinal field coming from the $\mathbf{e}_x$ component of $\mathbf{v} \times \mathbf{B}_L(t)$ is also present. It is given by $[\mathbf{F}_{L,p}]_{\mathbf{e}_x}(t) = v_y(t) B_z(t)$ which we can neglect for small laser intensities ($a_0 < 1$) and consequently small particle deflection velocities.

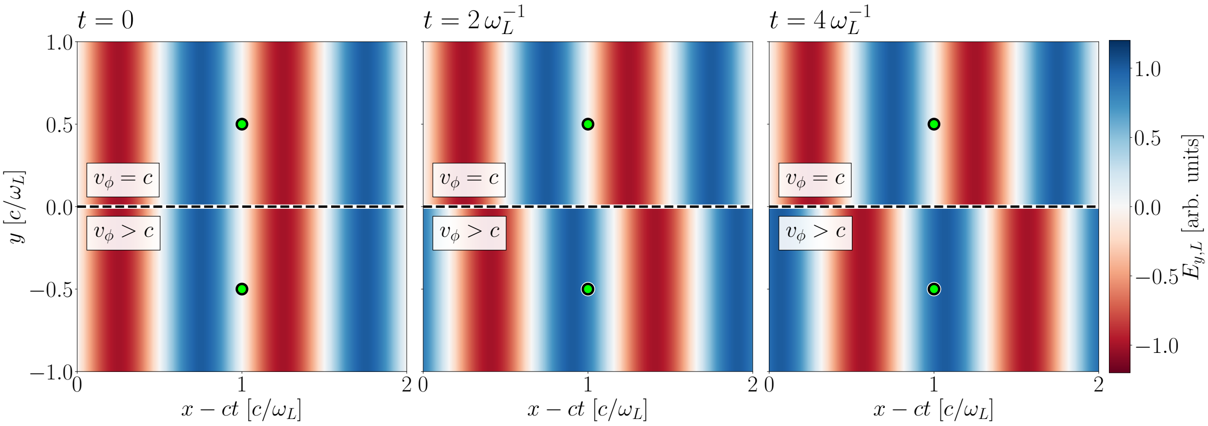

Figure 4.7: Phase lag of a particle co-propagating with a laser pulse. The particle (in green) is shown co-propagating with a laser pulse (Red-Blue colormap) in three snapshots at increasing times. The top half shows the case with phase speed equal to the speed of light and the bottom half shows the case with phase speed larger than the speed of light.

In comparision to the previous case, instead of being continuously deflected transversely, each particle p now feels an oscillating force and thus performs an oscillating motion in the transverse direction, with:

$$y_p(t) = r_L \sin\left[\omega_\phi(t - t_{0p}) + \phi_{0p}\right] \tag{4.41}$$

If we consider interaction starting at a fixed position $x_0 = 0$ (for example, the plasma boundary), the initial phase felt the particles in the beam is $\phi_{0p} = \omega_0 t_{0p}$, and the motion of each particle is then:

$$\begin{cases} x_p(t) = v_0(t - t_{0p}) & \text{(4.42a)} \\ y_p(t) = r_L \sin\left[\omega_\phi(t - t_{0p}) + \omega_0 t_{0p}\right] & \text{(4.42b)} \end{cases}$$

Thus, by combining Eqns. (4.42a) and (4.42b), we can find the y position of a particle at position x and at a given time t. Consequently, the shape of the particle beam at any given moment can be found through the following expression:

$$y_{\text{beam}}(t,x) = r_L \sin\left[\omega_\phi \frac{x}{v_0} + \omega_0\left(t - \frac{x}{v_0}\right)\right] = r_L \sin\left[\omega_0 t - \frac{\omega_0 - \omega_\phi}{v_0} x\right] = r_L \sin\left[\omega_b t - k_b x\right] \tag{4.43}$$

which has an associated phase-like speed $v_{\phi,\text{beam}}$:

$$v_{\phi,\text{beam}} = \frac{\omega_b}{k_b} = \frac{v_0}{1 - \omega_\phi/\omega_0} = \frac{v_0}{1 - (v_{\phi,L} - v_0)/v_{\phi,L}} = v_{\phi,L} \tag{4.44}$$

Therefore, a laser pulse with superluminal phase speed is able to imprint a sinusoidal perturbation with the same phase speed in a co-propagating charged particle beam.

It can be shown that, for a relativistic particle the maximum displacement is given by:

$$r_L = \frac{a_0}{\gamma(1 - v_0/v_\phi)} c/\omega_0 \tag{4.45}$$

where a_0 is the normalized vector potential of the laser pulse and γ the relativistic Lorentz factor of the particle beam. For $\gamma \gtrsim 1/(1 - v_0/v_\phi)$ and $a_0 \lesssim 1$ the modulation amplitude is on the order of or smaller than the modulation wavelength, which can be insufficient for the wiggler regime ($K \gg 1$).

However, the amplitude of this sinusoidal perturbation can be amplified through resonant interaction with an external oscillating force. In plasma accelerators, for example, the Betatron oscillations of trapped electrons can interact resonantly with the oscillations imposed by laser pulses with superluminal phase speeds [96], as long as the Betatron frequency, ω_β, is similar to the frequency of the motion imposed by the phase delay, ω_ϕ. Thus, we arrive at the following matching conditions for resonance with Betatron oscillations:

$$\omega_\beta = \frac{\omega_p}{\sqrt{2\gamma}} \sim \omega_\phi = \frac{\omega_L(v_{\phi,L} - v_0)}{v_{\phi,L}} \Rightarrow \begin{cases} \omega_L = \dfrac{v_{\phi,L}}{v_{\phi,L} - v_0}\dfrac{\omega_p}{\sqrt{2\gamma}} & \text{(4.46a)} \\ k_L = \dfrac{1}{v_{\phi,L} - v_0}\dfrac{\omega_p}{\sqrt{2\gamma}} & \text{(4.46b)} \end{cases}$$

with ω_p being the plasma frequency and γ the Lorentz factor of the charged particle.

4.3.1 Bessel Beams

In order for the previous analysis to be valid, the laser field phase felt by the particle should remain invariant under transverse motion, *i.e.* the laser pulse wavefronts should be as flat as possible. A typical gaussian laser pulse exhibits high levels of phase variability transversely, especially for longer propagation distances. It also diffracts in free space, meaning that its transverse profile expands and the peak intensity drops as the laser propagates. Therefore, a different kind of laser pulse is needed.

A Bessel Beam is a special type of laser pulse which is known for being difractless and having flat wavefronts. It was first theorized in 1987 [97] as an *exact, nonsingular solution of the scalar-wave equation for beams that are nondiffracting. This means that the intensity pattern in a transverse plane is unaltered by propagating in free space.* Figure 4.8a shows the transverse profile of a Bessel Beam.

For a 2D geometry, in the $x - y$ plane, for $\mathbf{r} = r_x\mathbf{e}_x + r_y\mathbf{e}_y$, the transverse electric field of a Bessel beam is described by:

$$E_y(\boldsymbol{r}, t) = a_0\omega_1\alpha J_0(r_y\alpha)\cos(k_1 r_x - \omega_1 t); \tag{4.47}$$

with $\alpha = \frac{\omega_1}{c}\sqrt{1 - c^2k_1^2/\omega_1^2}$ being the parameter that sets the half-width of the central peak (FWHM $\simeq 1/\alpha$). In free space, from Gauss's law we can determine the longitudinal electric field component of a Bessel Beam:

$$\nabla \cdot \mathbf{E} = 0 \Rightarrow \frac{\partial E_x}{\partial r_x} = -\frac{\partial E_y}{\partial r_y} \Rightarrow E_x = -\int \frac{\partial E_y}{\partial r_y} dr_x = a_0\omega_1\alpha J_1(r_y\alpha)\sin(k_1 x - \omega_1 t)/k_1 \tag{4.48}$$

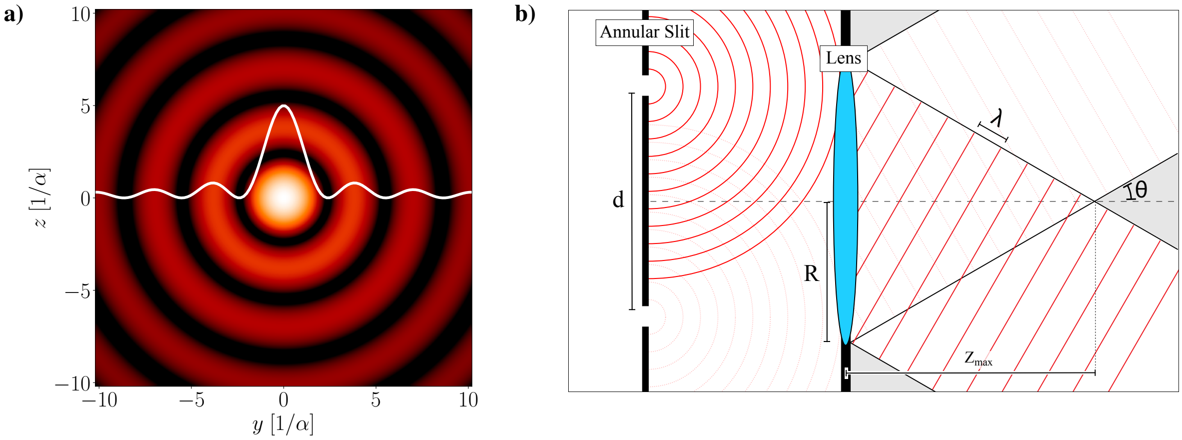

Figure 4.8: a) Transverse Profile (in respect to the direction of propagation) of a Bessel beam. b) 2D slice of the annular slit method for creating an approximation of a Bessel beam.

Faraday's law determines the magnetic field components:

$$\nabla \times \mathbf{E} = \frac{\partial \mathbf{B}}{\partial t} \Rightarrow \mathbf{B} = -\int \nabla \times \mathbf{E} dt = \int \frac{\partial \mathbf{E_y}}{\partial r_x} - \frac{\partial \mathbf{E_x}}{\partial r_y} dt \tag{4.49}$$

For small values of α, which is true for $\omega_1 \sim k_1$, the magnetic field is then:

$$\begin{aligned} B_z = k_1 &\left(J_0 (r_y \alpha) + \frac{\alpha^2}{2k_1^2} \left[J_0 (r_y \alpha) + J_2 (r_y \alpha) \right] \right) \cos (k_1 r_x - \omega_1 t) \\ \underset{\alpha/k_1 \ll 1}{\simeq} & \; k_1 J_0 (r_y \alpha) \cos (k_1 r_x - \omega_1 t) \end{aligned} \tag{4.50}$$

In the xOy plane, a Bessel beam is a superposition of two plane waves, with the same amplitude, and traveling towards the x axis at an angle $\theta = \pm \arcsin(\alpha/k_1)$, similar to what happens in Fig. 4.8b. In the full 3D space, a Bessel Beam corresponds to the superposition of an infinite number of plane waves travelling with the same angle towards the x axis but distributed along the azimuthal angle φ. One can think of it as a revolution of the 2D result in the xOy plane along the x axis. The intensity distribution of a Bessel Beam shown in Fig 4.8a decays with $1/r$, meaning that its integral over the transverse plane is infinite. In fact, the energy contained in each lobe remains constant independently of the ring order [97]. Thus, much like the plane wave, a true Bessel Beam is an exotic type of laser pulse, which would require an infinite amount of energy to create. Nevertheless, it is still possible to create satisfactory approximations using devices such as the annular slit [98, 99], Fabry-Perot Etalon [100] and Axicon [101–103]. As non-ideal Bessel Beams, the pulses created using these devices only propagate without diffracting for a limited distance which varies according to the device at use and its parameters.

The annular slit was one of the first proposed methods for producing an approximation to a Bessel Beam. It consists of a thin annular aperture of diameter d and width Λ. When placed at the focal plane of a lens with focal distance f and radius R, and illuminated with collimated light of wavelength λ, it generates a nondiffracting field with a maximum nondiffracting distance of $Z_{\max} \sim 2fR/d \sim 2\pi R/\lambda\alpha$. Figure 4.8b shows a 2D slice of this setup. Here, each slit creates a point-like source from a collimated beam coming from left to right. Each point source is offset from the lens axis by $d/2$, thus, the resulting spherical wave

a) b)

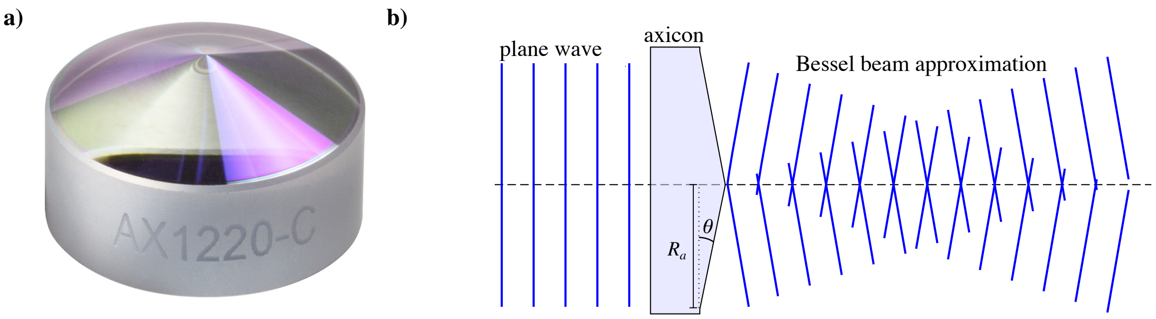

Figure 4.9: a) Picture of a modern axicon (taken from Thorlabs website [104]). b) 2D slice of the working principle of an axicon: a plane wave acquires a phase shift dependent on the distance from the optical axis r creating two plane waves propagating with a θ towards the optical axis.

is converted to an approximated plane wave traveling at an angle $\theta = \arctan(d/2f)$. Because the slit is in reality an annular aperture, this process happens for every azimuthal angle φ, creating an approximation to a Bessel Beam. One of the limiting factors in this setup is the radius of the lens R, which limits the transverse extent of the plane-like waves coming in the lens, eventually leading to the appearance of shadow zones (represented in grey in Fig. 4.8b). These shadow zones are the regions of space where the waves coming from opposing slits don't interfere and determine the maximum distance our Bessel Beam approximation can cover. Another limiting factor of this approach is the intensity distribution on-axis. Durnin, 1987 [97] shows that the intensity of the on-axis lobe produced by the annular slit setup oscillates about its initial value with increasing amplitude and decreasing frequency until reaching the maximum propagation distance.

Nowadays, the axicon [105] is the standard method producing Bessel beam approximations. It consists in a conical lens which focuses a collimated beam of light along a line by inducing a radially dependent phase shift (see Figure 4.9). The amount of lens material that each radial section of the beam crosses varies linearly with distance to the propagation axis r. Thus, the phase of each radial section of beam at the exit of the lens varies with linearly r which adds a tilt to the collimated light at the entrance, directing it towards the axis, similarly to what happens in the annular slit method. The axicon, however, is much more energy efficient as it allows the use of the full incident beam (instead of a single ring). Using an axicon also gives the possibility of avoiding the formation of an oscillating on-axis intensity pattern, yielding a far smoother intensity variation. An axicon of a radius R_a, index of refraction n and cone angle $\pi - 2\theta$ generates an approximate Bessel beam near optical axis with a maximum nondiffracting distance of $Z_{\max} \sim R_a/\theta$.

4.3.2 Creating a pure ion channel

In order to fulfill the matching conditions in Eqs. (4.46a) and (4.46b), the particle's velocity v_0 and Lorentz factor γ must remain as constant as possible so that the perturbation is amplified through resonance with Betatron oscillations.

In the blowout regime of plasma wakefield acceleration, the driver beam creates a bubble of ions on the plasma. The radius of this bubble depends on the properties of the driver beam. A laser beam

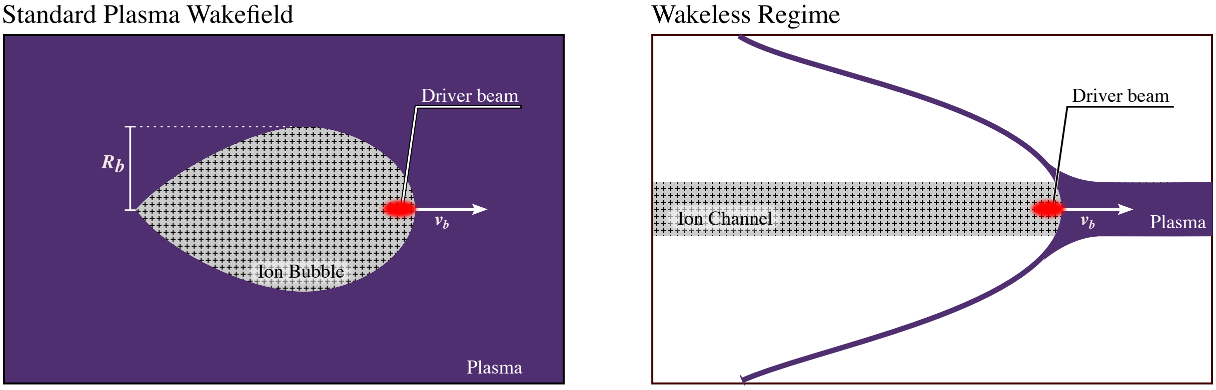

Figure 4.10: Standard plasma wakefiled acceleration setup (left) vs wakeless regime (right). A highly energetic electron driver particle beam (in red) travelling through a plasma (in purple) expels its electrons, leaving a region only with ions (in grey) behind.

with normalized peak intensity a_0 creates a bubble with radius $R_B \sim 2\sqrt{a_0}/k_p$. On the other hand, an electron beam with density n_b and transverse radius r_b creates a bubble with radius $R_B \sim r_b\sqrt{2n_b}$ [106]. The longitudinal electric field is negative near the rear of the *bubble* meaning that it accelerates electrons trapped inside it. In the transverse direction, the ion bubble results in a focusing field that drives electrons towards the axis of propagation. This results in a sinusoidal motion of the witness beam commonly referred to as Betatron motion.

As these relativistic particles oscillate inside the accelerating field their γ factor is usually increasing which may hinder the fulfilling of the matching conditions. Additionally, the angle at which the radiation interferes constructively depends on the phase speed of the particle beam. Thus, in order to get quadratic intensity scaling at a fixed angle we need to maintain constant phase speed in the modulation of our particle beam. To do this, we must make sure that our particle beam is not accelerating. In a typical plasma based accelerator setup (Figure 4.10, left), this may be a difficult task as there is always an accelerating field present inside the bubble. One might overcome this issue through beam loading, where the electric field coming from the witness beam itself is strong enough to cancel out the acceleration field, but it is difficult to place the witness beam correctly in the bubble, as well as to control its length to achieve this effect, additionally, electrons near the edges always end up feeling some accelerating field.

A different, more suitable, alternative is to use the wakeless regime (Figure 4.10, right) [107]. In this regime, the radius of the bubble created by the driver is larger than the width of the plasma column and when the electrons are expelled and exit the plasma column, they feel a much weaker field from the plasma ions and are never able to come back due to the limited positive charge inside the ion column. This leaves a pure ion channel behind the driver beam where there are no acceleration fields. A witness particle beam placed in this region will only feel the focusing field of the plasma column and perform stable Betatron oscillations, giving off Betatron radiation in the process.

Thus, in order to adequately modulate a particle beam for superradiant Betatron emission we use a Bessel Beam laser pulse in a pure ion channel created by a driver particle beam in the wakeless regime.

4.4 Particle Simulations

We performed preliminary numerical simulations in Mathematica to determine the particle beam's dynamics under the influence of a superluminal phase speed laser superimposed with a focusing Betatron field. Once our model for particle beam modulation was validated, we performed OSIRIS particle-in-cell simulations to investigate the creation of an ion channel by employing the wakeless regime. Then, we proceeded to add a Bessel Beam laser pulse and witness particle beam to investigate the formation of superluminal beam structures. Finally, we used the Radiation Diagnostic for OSIRIS to explore the emission of radiation under the superradiant regime by the particle beam.

4.4.1 Mathematica

We used the software Mathematica to obtain the dynamics for each particle are by numerically solving the equation of motion with the force term given by the electromagnetic Lorentz expression:

$$\frac{d\mathbf{p}}{dt} = q(\mathbf{E} + \mathbf{v} \times \mathbf{B}) \tag{4.51}$$

For these preliminary simulations, we assumed an ideal Bessel Beam described by eqs. (4.47), (4.48) and (4.50) and externally imposed focusing field given by:

$$E_f(x,y) = \begin{cases} \dfrac{en_p}{2\varepsilon_0}|r|\mathbf{e}_r \quad \text{(3D Cylindrical)} & \text{(4.52a)} \\ \dfrac{en_p}{\varepsilon_0} y\,\mathbf{e}_y \quad \text{(2D Cartesian)} & \text{(4.52b)} \end{cases}$$

where n_p is the background plasma density, e is the elementary charge (equal to the charge of each ion), and y and $|r|$ are the transverse displacement from the axis of the ion column. For an electron with mass m_e and charge $-e$, the 2D dynamics in the xOy plane are given by the following system of equations:

$$\begin{cases} m_e \dfrac{d\gamma(t)v_x(t)}{dt} = -e\left[E_{x,L}(x,y,t) + v_y(t)B_{z,L}(x,y,t)\right] & \text{(4.53a)} \\ m_e \dfrac{d\gamma(t)v_y(t)}{dt} = -e\left[E_{y,L}(x,y,t) + E_f(x,y) - v_x(t)B_{z,L}(x,y,t)\right] & \text{(4.53b)} \\ \dfrac{d\gamma}{dt} = \mathbf{E}\cdot\mathbf{v} & \text{(4.53c)} \end{cases}$$

with x being the longitudinal direction (or direction of propagation) and y and z being the two transverse directions. And, where γ is the Lorentz factor of the electron E_L and B_L are the laser electromagnetic fields and E_f the focusing field. We added a spatial envelope term $\mathscr{F}(x)$, defined in Eq. (4.54) below to modulate the amplitude of both the laser and the focusing fields such that $\mathbf{E}_L = \mathbf{E}_{\text{Bessel}}\mathscr{F}(x)$ and $\mathbf{B}_L = \mathbf{B}_{\text{Bessel}}\mathscr{F}(x)$. This emulates the spatial intensity profile of the Bessel Beam approximations created in experimental setups as well as the typical plasma density ramps.

$$\mathscr{F}(x) = \left[\arctan\left(\frac{x - x_i}{L}\right) + \arctan\left(\frac{x_f - x}{L}\right)\right]\frac{1}{\pi} \tag{4.54}$$

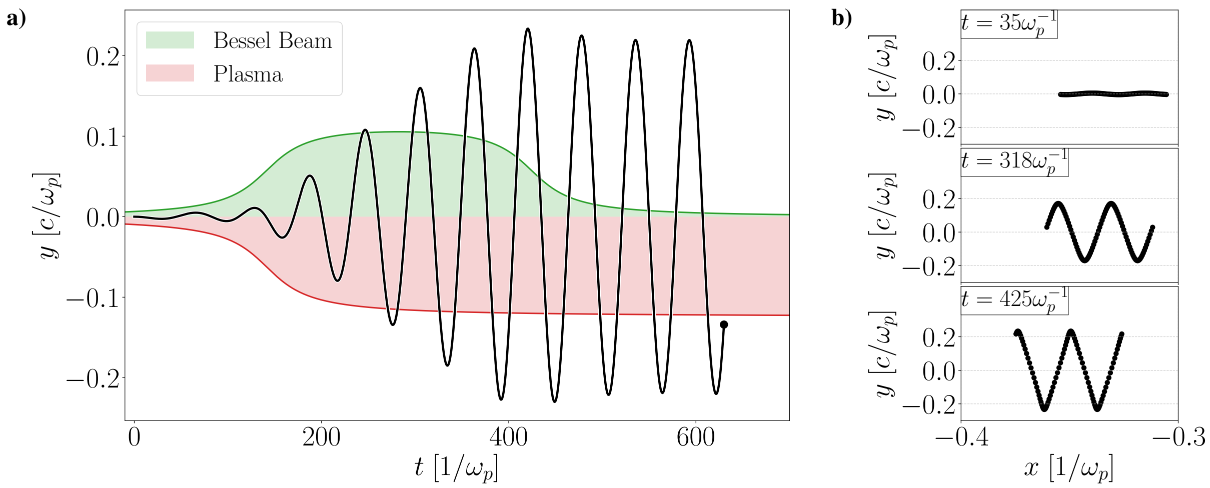

Figure 4.11: Results obtained by numerically solving the equations of motion in Mathematica for a single particle (a) and for a particle beam (b).

with x_i and x_f being respectively the starting and finishing positions of Bessel Beam/Ion Channel and L the typical length scale for the rise and fall of intensity. Figure 4.11 shows the numerical solution to the system of equations (4.53) given by Mathematica. For a set of particles initially with $\gamma = 300$ distributed along x_1 co-propagating with a Bessel Beam with frequency $\omega_L = 129\omega_p$ and phase speed $v_\phi = 1.00035c$, localized between $x_i = 200\ c/\omega_p$, $x_f = 600\ c/\omega_p$ with a typical rise and fall length of $L = 50c/\omega_p$ and an a_0 of 1 in a plasma with density n_p and plasma frequency ω_p. For an 800 nm laser, $\omega_p = 18 \times 10^{13}$ rad$/s$ and $n_p \simeq 1 \times 10^{17}$ cm^{-3}. Additionally, $x_i = 3$mm, $x_f = 1$cm and $L = 0.8$mm.

Figure 4.11 shows a trajectory for a sample particle, from there, we can see that the particle performs an oscillatory motion around $x_2 = 0$, the period of this oscillation is about $\sim 250\ \omega_p^{-1}$ which is close to the expected period for Betatron oscillations $T_\beta = 2\pi/\omega_\beta = 2\pi\sqrt{2\gamma}\,/\omega_p^{-1}$. The amplitude of these oscillations resonantly increases when the Bessel beam is present, and stabilizes afterwards. The particle beam as a whole becomes sinusoidally modulated with a superluminal phase speed. As the modulation grows, the particle beam loses longitudinal momentum and starts lagging behind the laser's pahsefornts.

4.4.2 OSIRIS PIC

In our Mathematica model we assumed an ideal focusing field, but in reality this field would be provided by an ion channel. We simulated the process of creating an ion channel in the context of plasma wakefield acceleration. We performed our simulation in the wakeless regime where the radius of this bubble is larger than the radius of the plasma column and the electrons that are expelled are unable to bounce back.

4.4.2.A Formation of a purely focusing field

We performed 2D OSIRIS PIC simulations with a typical SLAC FACET-II electron beam to assess the feasibility of this scheme to as means to create a pure ion channel. The simulation box was a moving window with length 42 c$/\omega_\mathrm{p}$ (4096 cells) and width 23 c$/\omega_\mathrm{p}$ (1025 cells). We used a plasma column with

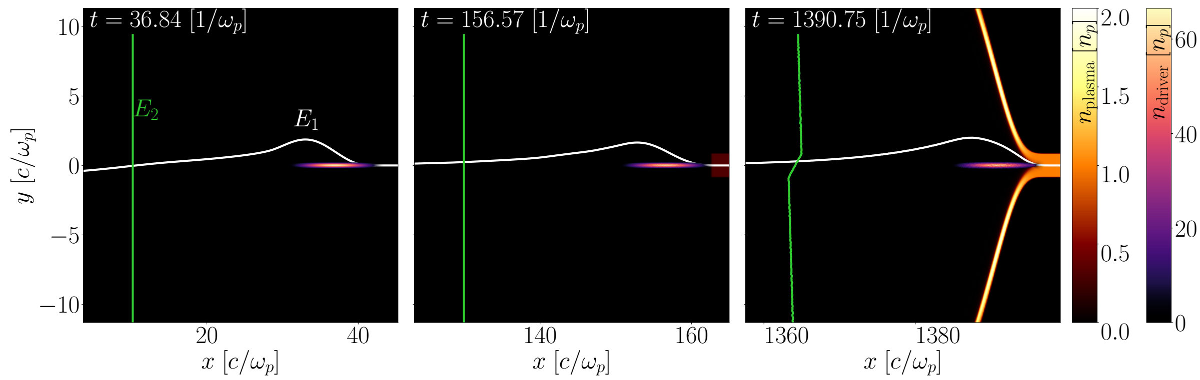

Figure 4.12: Snapshots of the onset of the wakeless regime. The white line shows the longitudinal (or accelerating) electric field on axis and the green line shows the transverse (or focusing) electric field farther back.

a smooth density upramp to n_p. The plasma column had radius of 0.4 c/ω_p, about 3 times larger than the radius of the particle beam and about 20 times smaller than the radius of the bubble. We modelled the pre-formed plasma column using 2 particles per cell in the longitudinal direction and 8 in the transverse direction. Such a plasma column could be ionized from a gas with a flying focus laser or with a low power Bessel beam [108] and its radius could be controlled with the spot size of this laser. The plasma density upramp is modelled with a Gaussian density profile, starting at $x = 170$ c/ω_p, that grows smoothly until reaching a constant value at $x = 700$ c/ω_p. This profile is described in Eq. (4.55) below:

$$n(x) = \begin{cases} 0 & \text{if } x < 170\ \mathrm{c}/\omega_p \\ n_p \exp\left(-\frac{(x-700)^2}{280^2}\right) & \text{if } 170\ \mathrm{c}/\omega_p \leq x < 700\ \mathrm{c}/\omega_p \\ n_p & \text{if } 700\ \mathrm{c}/\omega_p \leq x \end{cases} \tag{4.55}$$

The driver beam has the same energy as the SLAC FACET-II particle beam. It was initialized with $\gamma = 20000$ (10 GeV), a transverse radius $\sigma_y = 0.14$ c/ω_p, a length $\sigma_x = 3.4$ c/ω_p, thermal distribution of momenta $u_{\text{th}} = (3,3,3)\ m_e c$ and peak density $n_b = 64\ n_p$. We modeled the driver beam using 2 particles per cell in the longitudinal direction and 4 in the transverse direction.

Figure 4.12 shows the plasma column density profile, as well as the corresponding longitudinal electric field for different propagation times. The electrons that are expelled from the plasma are never able to come back and continue drifting away from the propagation axis. In free space, the longitudinal electric field takes longer to decay as these electrons still have an influence. However, if we consider our plasma column to confined in a device with absorbing walls, the expelled electrons disappear as they reach the walls and the longitudinal electric field decays much faster. Additionally, the transverse focusing field intensity grows smoothly with plasma density upramp.

We have then all the necessary conditions to add a second particle beam, trailing behind our main driver and superimpose a Bessel Beam with the focusing field of the plasma channel to recover our semi-theoretical predictions of Figure 4.11.

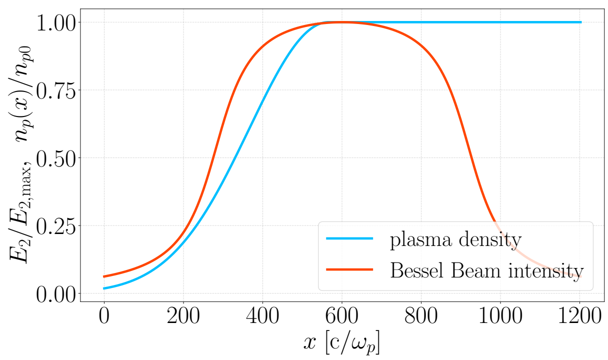

Figure 4.13: Plasma column density and Bessel Beam intensity profiles.

4.4.2.B Particle beam modulation with external fields

Due to the disparity in the scales of the distance between the driver and witness beam ($\sim 20\ \mathrm{c}/\omega_p$) and the wavelength of the witness beam modulation ($\sim 0.05\ \mathrm{c}/\omega_p$), we started by running simulations with a smaller box arround the witness and externally imposed the focusing fields consistent with the results from Figure 4.12. The simulation box had a length of $2.24\ \mathrm{c}/\omega_p$ (360 cells) and a width of $1.14\ \mathrm{c}/\omega_p$ (127 cells).

The laser Bessel Beam has a normalized vector potential of $a_0 = 0.85$, a phase velocity of $v_\phi = 1.0003\ c$, and a laser frequency of $\omega_L = 128.2\ \omega_p$, where ω_p is the plasma frequency. Its intensity profile is modelled using two arctangent functions such that it emulates the behaviour of a real Bessel beam and its intensity grows smoothly with the plasma density, it follows the expression given by Eq. (4.54) with $x_i = 350\ \mathrm{c}/\omega_p$, $x_f = 700\ \mathrm{c}/\omega_p$ and $L = 70\ \mathrm{c}/\omega_p$. The longitudinal intensity and density profile is depicted in Figure 4.13. The transverse profile is obtained using a Taylor expansion of the field expressions defined in Section 4.3.1 around $x_2 = 0$

The witness beam, has a normalized Lorentz factor ($\gamma = 300$), transverse spot size $\sigma_y = 0.001\ \mathrm{c}/\omega_p$, longitudinal spot size $\sigma_x = 0.3\ \mathrm{c}/\omega_p$, and a particle density $n_b = 0.01\ n_p$, where n_p is the peak density of the plasma column. For an 800 nm laser wavelength, this ideal witness beam would be about 5 µm long and 16 nm thick. Figure 4.14 shows snapshots of the shape of the witness beam at three different timesteps in a simulation. These snapshots show clearly that our particle beam acquires a sinusoidal shape with the same period as the laser. However, in order to verify that this modulation has a superluminal phase speed, a more thorough analysis over more temporal snapshots is required.

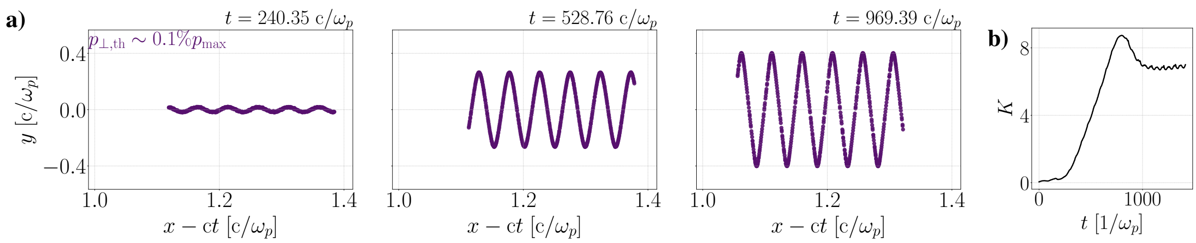

Figure 4.14: a) Snapshots of a particle beam at increasing timesteps (from left to right) as it becomes modulated. b) Temporal evolution of the K parameter of the particle beam.

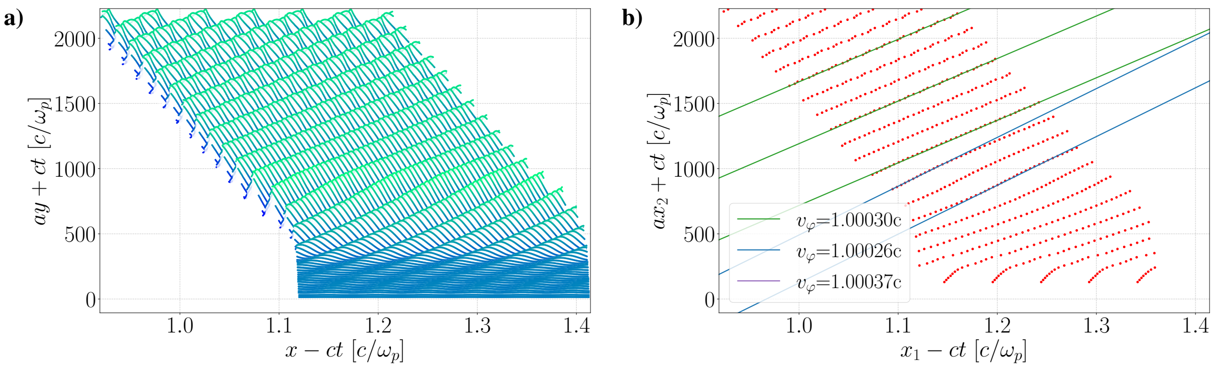

Figure 4.15: a) Evolution of a cold particle beam modulation. The colormap represents deviation from the horizontal axis (Light Blue $\rightarrow$ closer to center, Green $\rightarrow$ farther from center in the positive direction, Dark Blue $\rightarrow$ farther from center in the negative direction). b) Trajectories of the points of maximum displacement showcasing the phase speed of the perturbations.

Figure 4.15 condenses the results obtained from many snapshots in a single plot. In this plot, the beam is represented using a colored line where the colormap represents deviation from the horizontal axis, *i.e.* proportional to y (Light Blue $\rightarrow$ closer to center, Green $\rightarrow$ farther from center in the positive direction, Dark Blue $\rightarrow$ farther from center in the negative direction). We track our particle beam in a moving window with speed c, and transform the vertical coordinate with a function $f(y) = ay + ct$, meaning that we scale the vertical position by a factor a and add an offset ct in the transverse direction to the beam's y position. This way, the time evolution of the beam's modulation is mapped along the vertical direction.

We can see from Figure 4.15a that initially, the particle beam is un-modulated, but it quickly acquires a modulation whose amplitude rises until $t \sim 600\text{c}/\omega_p$. It is also clear from this plot that the green parts of our particle beam advance inside the moving window, meaning these structures are superluminal. These structures are of utmost importance as they are the regions where the beam particles produce the most radiation and therefore act as a virtual light source. It is also important to note that because these perturbations are moving with a phase speed v_ϕ greater than the velocity of the particle beam v_b, they eventually reach the front end of the beam and disappear as no more particles can participate in the perturbation. Similarly, new structures appear periodically from the back end of the beam and start travelling through the beam. This effect resembles the Barberpole illusion.

The velocity of these structures can be found by tracking the position of the particles that are most displaced from the beam center at each given time. Figure 4.15b represents these particles as red dots. Because we mapped time to the vertical direction, the velocity at which these structures are moving forward is given by the slopes of the trajectories of the red dots in the plot. When the modulation is still growing, the trajectories of the red dots are not linear, which means the perturbations move across the beam with varying velocity. After the desired modulation is achieved, the trajectories become linear, and every structure travels across the beam with constant velocity $v_\phi = 1.0003$ c, which is consistent with the phase speed of the Bessel Beam laser pulse. The varying phase velocity experienced by some superluminal beam perturbations could lead to a variation in the Cherenkov angle associated with superradiant emission. However, most of the variation occurs when the modulation amplitude is still growing and the emitted radiation is still far from reaching the maximum intensity. Additionally, in the case analyzed in Fig. 4.15b

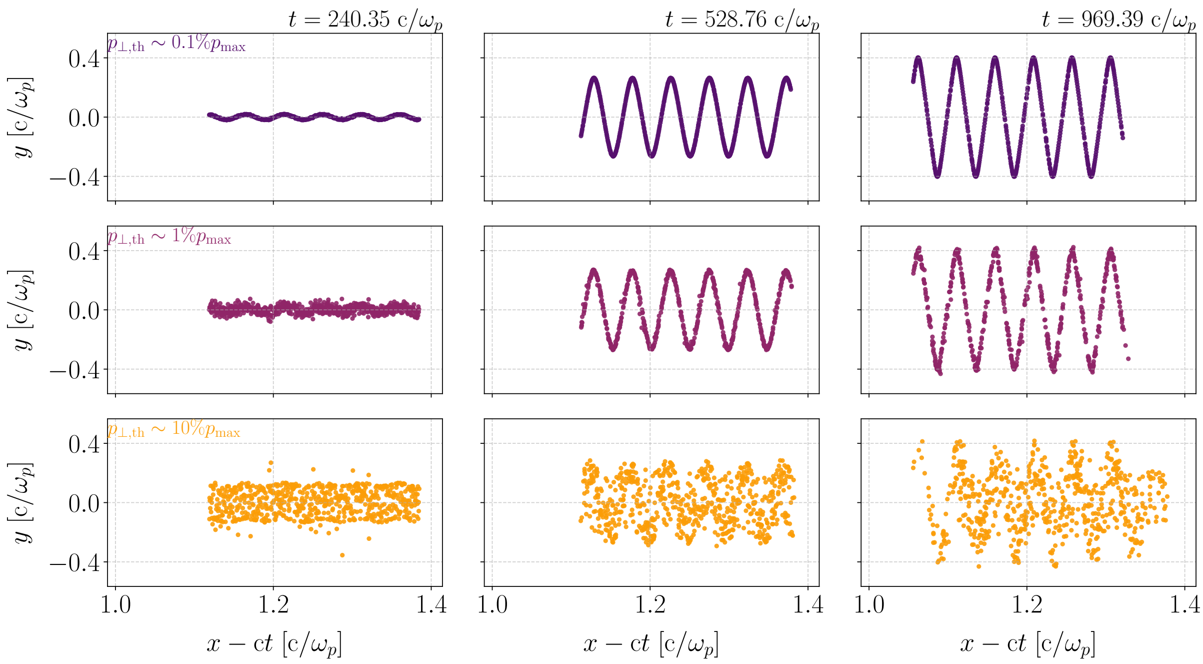

Figure 4.16: Snapshots of particle beams with increasing temperatures (from top to bottom) at increasing timesteps (from left to right).

the variation in the Cherenkov angle would be about 2 mrad around a central value of 25 mrad.

A particle beam with a modulation such as the one displayed in Fig. 4.15 should leave clear marks of superradiance in the radiation profile, as we will see in the following section. Nevertheless, this modulation was obtained under ideal conditions, using an extremely narrow particle beam with no temperature or energy spread. A more realistic description of the particle beam would allow us to gain an understanding of how this scheme responds to non-idealities in the setup. We then performed additional simulations with thicker particle beams with a finite energy spread, and increased the transverse temperature. We used three different configurations for the transverse temperature with values ranging from $p_{2,\rm th} = 0.02\ m_e$c, 2 orders of magnitude smaller than the maximum transverse momentum acquired by the particle beam, to $p_{2,\rm th} = 2\ m_e$c, on the same order of magnitude as the maximum transverse momentum acquired by the particle beam. Figure 4.16 shows three snapshots of the particle beams as the simulation progresses. The colder beam (top row) behaves as expected forming a clear sinusoid shape with a superluminal phase speed. When we increase the transverse temperature by a factor of 10 (middle row), we see that before the modulated has reached its maximum amplitude (left column) the sinusoidal structure is more difficult to identify, but as the modulation amplitude grows, the sinusoid shape becomes clear once again. As for the case with the highest transverse temperature, $p_{2,\rm th} = 2\ m_e$c close to particle beam's maximum transverse momentum, $p_{2,\rm max} = 6\ m_e$c, the sinusoid shape remains partially indistinct even when the modulation is fully developed. Nevertheless, it is still possible to identify a sinusoidal trend the particle distribution which should be enough to leave hints of superradiance, as we will see in the following section.

Our study shows that in order to achieve the desired modulation for the onset of superradiance, this second electron beam does not need to be as energetic as the main driver beam, but is required to have smaller energy spread and transverse temperature for the modulation shape to appear clearly.

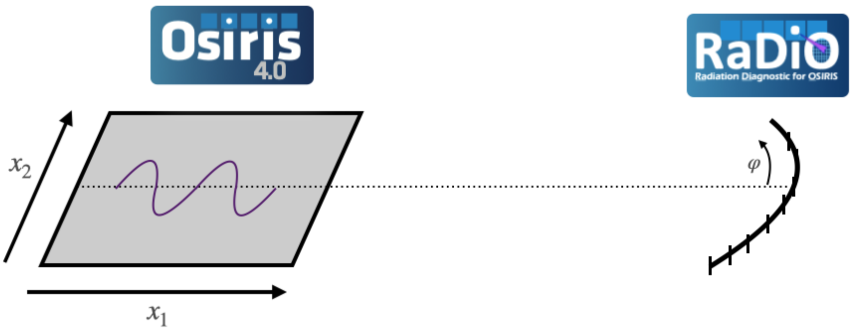

Figure 4.17: 2D simulation setup and detector positioning

4.5 Radiation Simulations

The simulations in the previous section show as self consistently as possible that it is possible to suitably shape a particle beam with a Bessel beam in the wakeless regime. However, in order to thoroughly explore the parameter space to find the parameters for the trailing beam that ensure the best quality of the generated radiation, the computational cost of each simulation must be reduced. A big part of the computation cost comes from the scale difference between the particle beam structures (laser wavelength) and the distance between the trailing beam and the main driver beam, which is necessary to keep the accelerating field $E_{\|}$ small or negligible, for example in the previous simulations this distance was $30\ \mathrm{c}/\omega_p$, about 1000 times larger than the wavelength of the laser used to modulate the particle beam. Such computational load can be greatly reduced if instead of self consistently creating the focusing field we externally imposed focusing field. This way, our simulation box can be as small as the trailing beam.

We used the Radiation Diagnostic for OSIRIS to track the radiation coming from modulated particle beams. The setup is depicted in Figure 4.17. The beam modulation is handled by OSIRIS in a 2D configuration, whereas RaDiO tracks the radiation in slice of a spherical detector placed far away from the simulation box, but resting on the same plane. The angle φ is measured from the horizontal x_1 axis.

The parameters used for the OSIRIS simulation were the same as tested previously, for the results shown on Figure 4.16 where we varied the particle beam's transverse temperature from $0.02\ m_e\mathrm{c}$ to $2\ m_e\mathrm{c}$. The spherical detector had a radius of $10^5\ \mathrm{c}/\omega_p$ and had an angular aperture of 40 mrad with 6400 spatial cells. The time resolution of the detector was $dt_{\mathrm{det}} = 5 \times 10^{-5}\ 1/\omega_p$. For particles with $\gamma = 300$ undergoing Betatron motion, the spectrum of emitted radiation should follow the typical Betatron spectrum with a critical frequency close to dt_{det} meaning that our detector is more than capable of capturing the full Betatron spectrum.

4.5.1 Spatiotemporal Profile of Radiation

We start by investigating the best-case scenario, which corresponds to the particle beam with the smallest temperature, where the modulation is more clearly visible. Figure 4.18 shows the full spatiotemporal profile of radiation emitted in this case. In this plot, we see that most radiation is emitted in a small

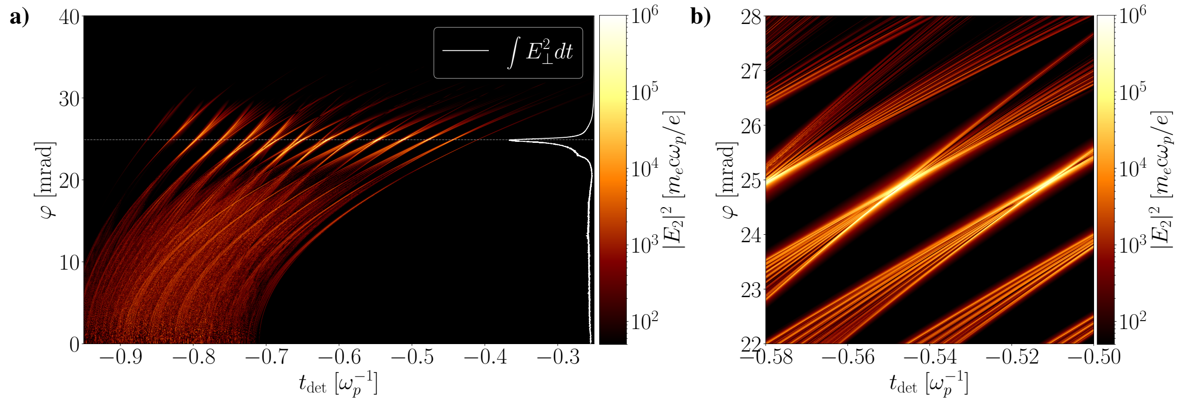

Figure 4.18: Spatiotemporal profile of the radiation emitted by a cold particle beam. (a) Full spatiotemporal profile. The white line represents the time integrated spectrum as a function of the angle φ (b) Close-up of a crossing point of radiation.

angular region with aperture close to 30 mrad which corresponds $K/\gamma = 10/300$, the typical opening angle for betatron radiation in the wiggler regime. However, unlike the typical betatron profile, the angle where we find the highest intensity radiation is no longer on-axis ($\varphi = 0$), but off-axis, at $\varphi \sim 25$ mrad. In this region, it is possible to identify several points of accumulation of radiation. This is a clear evidence of superradiance. These points are the result of constructive interference from the particles that make up the superluminal structures of the beam. Figure 4.18 shows a zoom of the spatiotemporal profile around one of these points of accumulation of radiation. Each of the stripes corresponds to the radiation profile produced by a single particle, the equivalent of the spherical shells of radiation depicted to in Figure 4.3 but in a φ, t plot.

4.5.1.A Crossing Points

The reason why the radiation from the particles in the beam generates these patterns can be understood by looking at the expression for the time at which radiation emitted at a given time t and longitudinal position $x(t)$ arrives at a point in the spherical detector with angle φ. This time, called the time of deposition t_{dep}, is given by the following expression:

$$\begin{aligned} t_{\text{dep}}(\varphi, t) &= t + \frac{\sqrt{[x(t) - R\cos\varphi]^2 + R^2\sin^2\varphi}}{\mathrm{c}}, \\ &= t + \frac{\sqrt{x^2(t) + R^2\cos^2(\varphi) - 2x(t)R\cos(\varphi) + R^2\sin^2(\varphi)}}{\mathrm{c}} \\ &= t + \frac{\sqrt{x^2(t) - 2x(t)R\cos(\varphi) + R^2}}{\mathrm{c}} \end{aligned} \tag{4.56}$$

For $\varphi = 0$, the time of deposition is simply:

$$t_{\text{dep}}(\varphi = 0, t) = R/c + t - x(t)/c \tag{4.57}$$

For two consecutive particles P_1 and P_2 radiating at positions x_1 and $x_2 > x_1$, and at times t_1 and $t_2 > t_1$ such that $|t_2 - t_1| = |x_2 - x_1|/v_\phi < |x_2 - x_1|/\mathrm{c}$ as they emulate a superluminal light source with velocity $v_\phi > \mathrm{c}$, the time distance between depositions on-axis is:

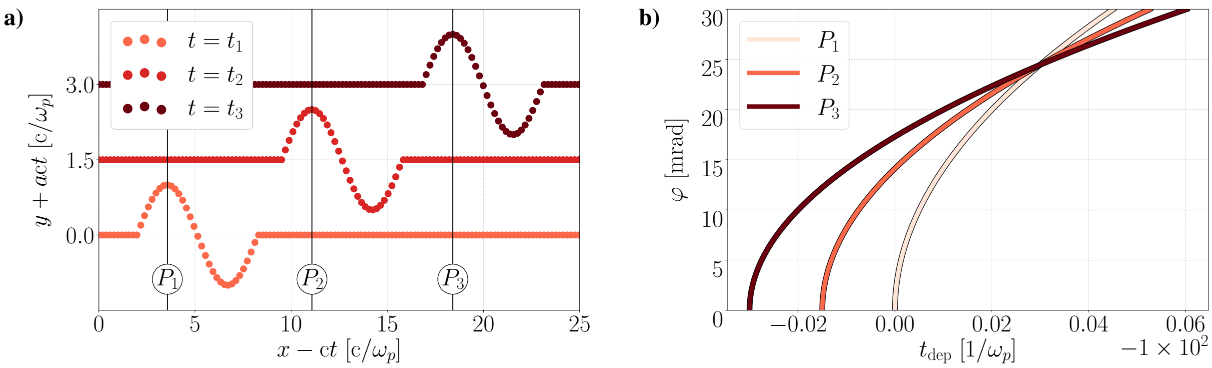

Figure 4.19: Points of accumulation of radiation generated by a superluminal perturbation. (a) Motion of the superluminal perturbation and position the particles that radiate at each time. The vertical position is offset by a factor proportional to t such that time is mapped along the vertical position (b) Deposition time curve for the three particles.

$$t_{\text{dep},2} - t_{\text{dep},1} = t_2 - t_1 - (x_2 - x_1)/c < 0 \tag{4.58}$$

Which simply means that the radiation from the particle that starts in front arrives sooner at the detector on-axis despite being produced at a later time.

Now, if we look at the deposition times for $\varphi = \pi/2$, the expression for t_{dep} becomes:

$$t_{\text{dep}} = t + \frac{\sqrt{x^2(t) + R^2}}{\text{c}} \tag{4.59}$$

For the same two consecutive particles P_1 and P_2, the time distance between depositions at $\varphi = \pi/2$ is then:

$$t_{\text{dep},2} - t_{\text{dep},1} = t_2 - t_1 + \sqrt{x_2^2/c^2 + R^2/c^2} - \sqrt{x_1^2/c^2 + R^2/c^2} > 0 \tag{4.60}$$

Which means that the radiation from the particle that starts in front arrives later at the detector for $\varphi = \pi/2$. This implies that at some angle between 0 and $\pi/2$ the radiation from these two particles arrives at the detector at the same time, creating an optical shock. The angle for which this happens can be shown to be the Cherenkov angle, given by $\varphi_{\text{Ch}} = \arccos c/v_\phi$. At this angle, constructive interference can be obtained if the phase of radiation is the same for all particles, which is true for betatron radiation.

Figure 4.19 shows the $t_{\text{dep}}(\varphi, t)$ curve defined by Eq. (4.56) for three particles that radiate consecutively at different times and positions due to a single perturbation that travels across the particle beam in such a way that they emulate a superluminal light source with velocity $v_\phi = 1.0003$. The spherical detector has a radius $R = 100$ c$/\omega_p$. Particle P_1 radiates first at time t_1 and position x_1, followed by particle P_2, which radiates at time $t_2 = t_1 + dt$ and at position $x_2 = x_1 + v_\phi dt$, finally, particle P_3 radiates at time $t_3 = t_1 + 2dt$ and at position $x_3 = x_1 + 2v_\phi dt$. As expected from our previous analysis, radiation from the particle that is closer to the detector, P_3, arrives first on-axis. Nevertheless, as we increase the angle φ the times of deposition of the three particle start to converge. When we reach the point of accumulation of radiation at $\varphi = 24$ mrad, all particles deposit their radiation at the same time. This angle corresponds to the

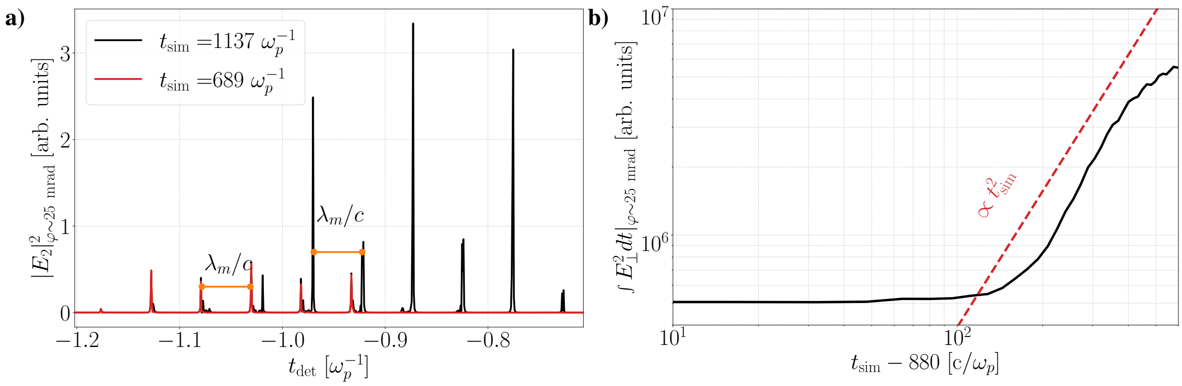

Figure 4.20: Temporal profile of radiation at the Cherenkov angle. (a) radiation collected at the detector as a function of the detector time. (b) Total energy deposited in the detector at the Cherenkov angle as a function of the simulation time. More negative times represent radiation that arrives first at the detector and thus correspond to emissions from the front end.

Cherenkov angle for a superluminal light source with velocity $v = v_\phi = 1.0003$. For larger angles, the radiation that arrives first at the detector is the one coming from the particle that radiates first, P_1.

4.5.1.B Temporal profile

In the case of the profile shown in Figure 4.18, the structures responsible superradiant emission are the periodic perturbations induced by the laser pulse, which travel across the beam at speed $v_\phi > v_0$, as shown in Figure 4.15. Instead of a single point of accumulation of radiation, the temporal profile of radiation at the Cherenkov angle is then composed of several short pulses, each one being originated by the superluminal perturbations that appear periodically from the back end of the particle beam. The temporal distance between these pulses is then equal to the laser period. Because these structures travel faster than the beam, they disappear when they reach the front end of the beam and new ones appear from the back of the beam. Each point of accumulation of radiation corresponds to a single structure, therefore, although we start with N points of accumulation, as the simulation progresses new ones appear. The frequency at which these new perturbations are generated is equal to the frequency at which the particles oscillate around the axis which is this case is the Betatron frequency ω_β.

Figure 4.20 shows the temporal profile of the radiated field at the Cherenkov angle for different times in the simulation, one just as the modulation is reaching its full amplitude (at $t = 688\ 1/\omega_p$) and other more towards the end of simulation (at $t = 1137\ 1/\omega_p$). The first thing we note is that the pulses are indeed separated by a laser period, and that in a period of time of about 450 $1/\omega_p$, 3 more pulses appear which is in agreement with the expected value as the Betatron period $T_\beta = 2\pi\sqrt{2\gamma}/\omega_p \sim 153\ 1/\omega_p$. Additionally, it is interesting to note that the pulses that appear after the modulation has reached its maximum amplitude (in black) have some delay with respect to the ones that appeared before. This happens because after the particles in the beam reach their maximum transverse momentum, they lose longitudinal momentum and the beam starts lagging behind, therefore the perturbations are also dragged further back and the radiation coming from them arrives a bit later at the detector. This is clear from Figure 4.15 where we can see that from $t = 700\ 1/\omega_p$ the particle beam starts travelling backwards in the moving window.

The intensity of each one of these pulses is closely related to the number of particles that participate

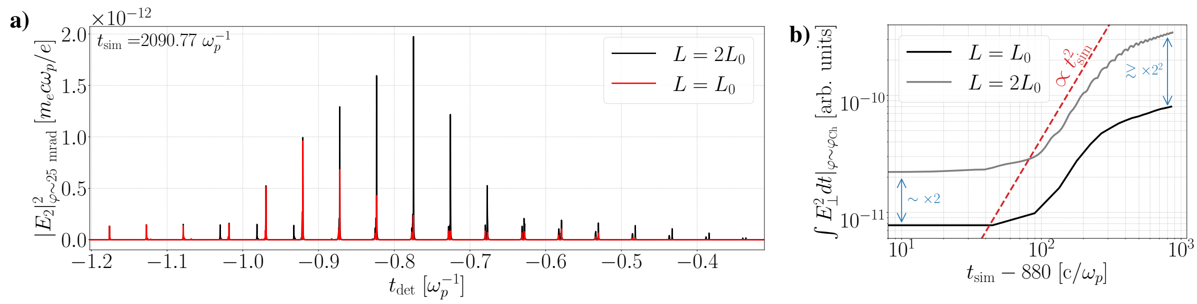

Figure 4.21: Temporal profile of radiation at the Cherenkov angle emitted by particle beams with lengths L_0 and $2L_0$. (a) radiation collected at the detector as a function of the detector time at the end of the simulation. (b) Total energy deposited in the detector at the Cherenkov angle as a function of the simulation time.

in the perturbation. In an ideal scenario, at the point of accumulation of radiation, the peak radiated electric field should be proportional to the number of particles that are caught by the perturbation, N_p. This means that the radiated energy should be proportional to N_p^2. The farther these structures are able to travel through the beam, the more particles contribute in the process of constructive interference and the more intense is the radiation at the crossing point.

For example, if a perturbation starts near the front end of the particle beam, it does not have many particles in front of it and so the radiated intensity of the pulse corresponding to this perturbation should be smaller when compared to other pulses. This is what happens with the leftmost pulse in Figure 4.20a, which is the one that arrives first at the detector and therefore generated by a perturbation created closer to the front end of the particle beam. As only a few particles participate in this perturbation, the intensity of this is very small.

Another implication of this fact is that the total radiated energy at the Cherenkov angle grows quadratically with the propagation time because the number of particles contributing to the optical shock to grows linearly with time. In fact, Figure 4.20b shows the integral of the squared radiated electric field at the Cherenkov angle, which is proportional to the total radiated energy, as a function of the simulation time in a log-log plot. For $t_{\rm sim} > 700$, the total radiated energy grows clearly with the square of the simulation time. Here it is important to note the difference between the horizontal axes of both plots in Figure 4.20. One represents the time at the detector for two different stages of the simulation and other represents simulation time.

Moreover, other factors may also influence the energy in each pulse at a given angle, as small variations in the phase speed of the perturbations may direct the point of accumulation of radiation to other regions of space, or energy losses by the particles that make them lag behind which can split the pulse temporally into multiple pulses like in the example of Figure 4.20.

A simple way of varying the number of particles that participate in the process of constructive interference is to have a particle beam with different length. We investigated this possibility by running an additional simulation with a particle with half the length as previously.

Figure 4.21 shows the temporal profile of radiation at the Cherenkov angle obtained from two particle beams with different lengths at the end of the simulation. There are two major differences between the radiation profile generated by the two particles beams, the first one is that the longest beam generates more pulses and the other one is that these pulses carry more energy. Although the longest beam is twice as long as the shortest beam, the total number of pulses generated by the two beam do not differ by the same factor of 2. This happens because the number of pulses does not depend only on the beam length, but also on the propagation time. The expression for the number of pulses generated is roughly given by:

$$N_{\text{pulses}} \simeq \frac{L_{\text{beam}}}{\lambda_m} + T_{\text{prop}} \frac{\omega_\beta}{2\pi} \tag{4.61}$$

where $L_{\text{beam}}/\lambda_m$ is the initial number of perturbations, roughly given by the ratio between the length of the beam L_{beam} and the wavelength of the modulation λ_m. And $T_{\text{prop}}\omega_\beta/2\pi$ the number of perturbations that appear as the beam travels forward, roughly given by the product between the total time of propagation after the full modulation of attained, T_{prop}, and the frequency at which new perturbations appear from the back end of the pulse, which in this case is equal to the Betatron frequency ω_β. Therefore, for two particle beams with different lengths that propagate for a long period of time ($T_{\text{prop}}\omega_\beta/2\pi \gg L_{\text{beam}}/\lambda_m$), the ratio between the total number of pulses generated is expected to be smaller than the ratio between the lengths of the beams. Nonetheless, if we look at the temporal profile of radiation shown by Figure 4.22 obtained shortly after the modulation has reached its desired amplitude, where $T_{\text{prop}} \sim 600$, we see that the initial number of pulses differs by a factor of $L_2/L_1 = 2$.

As for the total energy radiated at the Cherenkov angle, Figure 4.21b shows the evolution of squared electric field integrated in the detector's time array as a function of the simulation time, which is proportional to the energy radiated by the particle beam. We see that, similarly to what happened before, after the modulation has reached its desired amplitude, the total radiated energy grows quadratically with the simulation (or propagation) time until reaching a saturation point. The interesting thin to note here is that this saturation point appears at a later time for the longer beam, which leads to a larger growth in the total radiated energy.

Overall, the final radiated energy by the longer beam is about 4 times greater than the energy radiated by the shorter beam, despite the fact the beam is only twice as long. Moreover, Figure 4.21b shows that initially, the total radiated energy is $L_2/L_1 = 2$ times greater for beam 2, this is simply due to the fact that, at that time, beam 2 has generated $L_2/L_1 = 2$ times more pulses than beam 1, but they haven't yet travelled across the full particle beams so the number of particles contributing to each pulse is roughly the same and, therefore, all pulses have roughly the same amplitude. In this case, because all the pulses are clearly temporally separated, the integral of the squared electric field is roughly given by the product between the number of pulses N_{pulse} and the average squared amplitude of the pulses $|E_{\text{pulse}}|^2$:

$$\int |E_\perp|^2 dt = N_{\text{pulse}} |E_{\text{pulse}}|^2 \tag{4.62}$$

and the ratio between the energy obtained from each particle beam should be equal to $N_{\text{pulse},2}/N_{\text{pulse},1} = L_2/L_1 = 2$

However, as time passes and the perturbations travel across the beams, the squared amplitude of each pulse grows quadratically with the number of particles involved. Because beam 2 is able to have about $L_2/L_1 = 2$ more particles contributing to each pulse, the squared amplitude of the pulses generated by

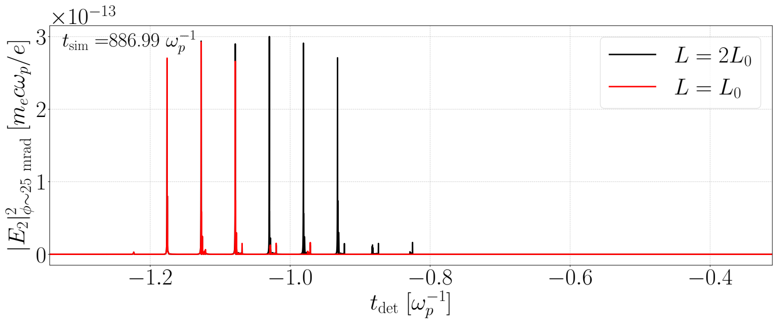

Figure 4.22: Temporal profile of radiation at the Cherenkov angle emitted by particle beams with lengths L_0 and $2L_0$ as a function of the detector time at the moment where the modulation has reached its desired amplitude.

beam 2 should be $(L_2/L_1)^2 = 4$ larger than the amplitude of the pulses generated by beam 1. Furthermore, as mentioned before, as the electron beams travel, more pulses are generated and for a long enough time, the number of pulses generated by each beam is roughly the same, regardless of the length of the beams. Therefore, in this case, the ratio between the energy obtained from each particle beam should, be equal to $|E_{\text{pulse},2}|^2/|E_{\text{pulse},1}|^2 = (L_2/L_1)^2 = 4$, assuming that the both beams produce approximately the same number of pulses.

While other factors may influence the growth in the amplitude of each pulse, such as the length each perturbation can travel inside the beam, or variations in the phase velocity, Figure 4.21 shows that in the end of the simulation the total radiated energy is about $(L_2/L_1)^2 = 4$ times greater for beam 2 than for beam 1.

4.5.1.C Pulse length

Apart from the possibility of achieving quadratic intensity scaling with the propagation time or with the particle beam length, another interesting prospect of superradiant emission is the production of ultra-short pulses of radiation. Because all the particles deposit their radiation almost at the same time at the Cherenkov angle, the resulting pulse of radiation is confined in a very narrow time window. For example, the shortest pulse in Figure 4.20 is shown in a zoomed in plot in Figure 4.23a. Its full width at half maximum is about 2.8 c/ω_p, about 174 times smaller than the wavelength of the laser employed to achieve the particle beam modulation. If we assume that this is an 800 nm laser, then the length of this pulse would be on the order of $1.53 \times 10^{-17} s$ which is about 15 attoseconds. Attosecond-level pulses of high intensity radiation can be extremely useful in a number of applications and this scheme can, with a more careful selection of the relevant parameters, deliver such pulses.

We also investigated the effect of having a thicker particle beam instead of having the ideal beam that only 1 particle thick. We increased the particle beam thickness to 0.11 c/ω_p, about 2.3 times larger than the wavelength of the laser employed to achieve the particle beam modulation. If we assume that this is an 800 nm laser, then this particle beam would be about 2 µm thick which is already close to the spot sizes of particle beams in high-end facilities. With this configuration, we obtained a pulse length of about 40 attoseconds.

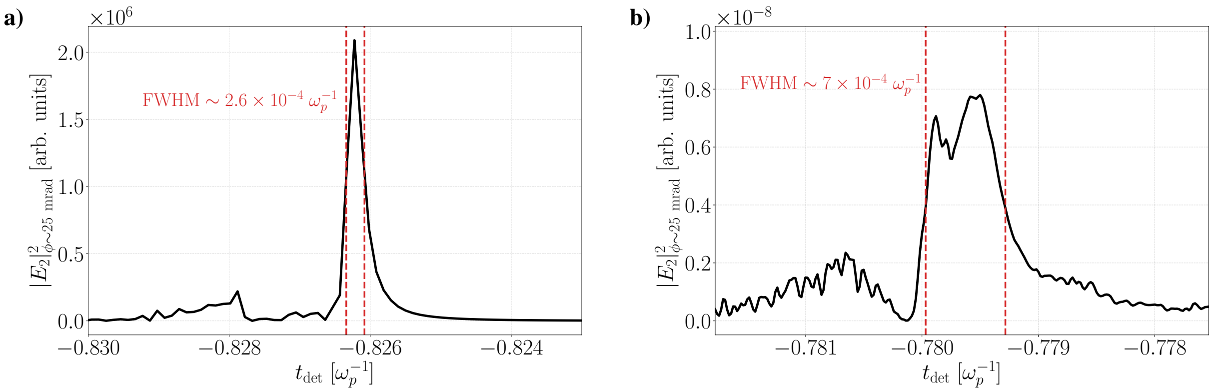

Figure 4.23: Close-up of the ultra-short pulses emitted at the Cherenkov angle. (a) Pulse emitted by a thin particle beam (only one particle thick). (b) Pulse emitted by a thick particle beam (with thickness on the order of μm).

4.5.2 Spectrum of radiation

In Section 4.2.1, we presented a theoretical analysis of the intensity spectrum of radiation obtained in superradiant Betatron emission. There, we predicted that the spectrum would essentially be the given by the intersection between the harmonics of the typical single-particle Betatron spectrum and the harmonics of the same order of the particle beam modulation frequency. These intersections are expected to occur always at the Cherenkov angle. We can verify this by examining the intensity spectrum of the radiation generated in our simulations.

Figure 4.24a shows the radiation intensity spectrum, $d^2I/d\omega d\Omega$, obtained by performing an FFT in the temporal array of the spatiotemporal profile of radiation presented in Figure 4.18. The highest intensity points of this spectrum all lie on the same angle φ_{Ch}, as expected, and appear at discrete frequencies, multiples of laser modulation frequency ω_m. The remaining parts of the spectrum are dwarfed by these components and remain invisible in the plot. This is in excellent agreement with the predictions of Section 4.2.1.

Furthermore, in Section 4.2.1 we also predicted that if the particle beam remains un-modulated, we should recover the typical Betatron spectrum with higher intensity for frequencies $\omega < 2\pi/L$. Therefore, we ran a simulation where we turned off the laser beam and let the particle beam perform simple Betatron oscillations. The particle beam had a length $L = 0.26\ \mathrm{c}/\omega_p$ and was initialized with a transverse position offset of $0.6\ \mathrm{c}/\omega_p$ from the center of the ion channel, such that its K parameter is about $K \sim 4$. The result is shown on Figure 4.24b where the typical harmonics of the Betatron spectrum are clear. Additionally, the region of space with larger radiated energy is the region inside $\varphi = K/\gamma \simeq 15$ mrad. Frequency-wise the spectrum has a maximum around $\omega = 0$ (which corresponds to the modulation frequency) which extends for frequencies up to $\omega = 20\ \omega_p$, in total agreement with the theoretical prediction of $2\pi/L = 24\ \omega_p$, the limit for superradiant emission using un-modulated particle beams.

4.5.3 Effect of beam temperature

As we saw on Section 4.4.2, a more realistic description of the particle beam, including for example beam temperature, can have some impact on the quality of the modulation achieved. Such defects can

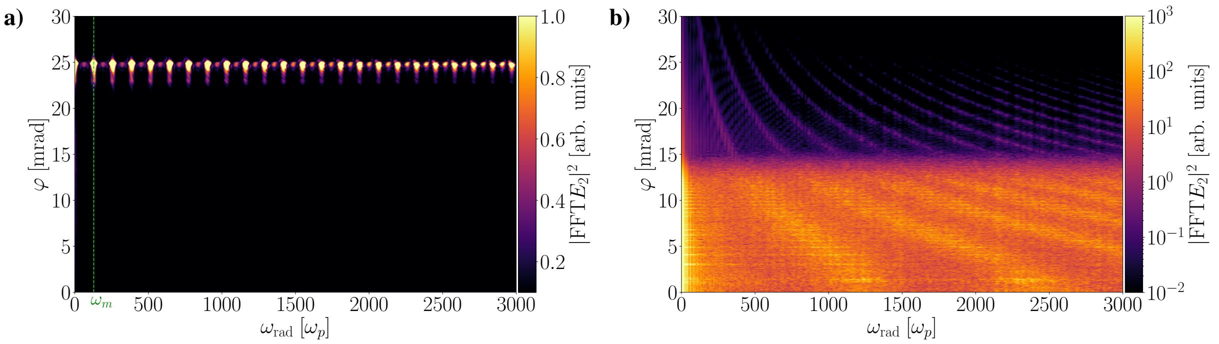

Figure 4.24: Spectrum of radiation emitted by cold particle beams. (a) Using a superluminal phase speed modulation. (b) Using no modulation.

result in an overall degradation of the superradiant radiation profile. In order to investigate the actual influence of particle beam temperature, we ran the simulations that yielded the data in Figure 4.16 but this time, we tracked the radiation coming from those particle beams.

Figure 4.25 shows the particle beams at the end of the simulation, together with the angular distribution of radiated intensity ($\propto \int E^2 dt$). The coldest particle beam, which is the one we have been using in the simulations of this section, generates a clear superradiance peak at the Cherenkov angle, whose intensity dwarves the Betatron spectrum contribution for smaller angles.

As we increase the temperature, the particles that participate in the superluminal perturbation become less organized, which makes it less likely that they all deposit their radiation at the same time at the Cherenkov angle. This can be understood in terms of Eq. 4.56 as a jitter added in $x(t)$ which translates as a jitter in the time of deposition t_{dep}. In this way, fewer particles contribute to a single point of accumulation of radiation and its intensity is no longer strictly a quadratic function of the number of particles in the beam, but of the fraction of the particles that are able to deposit radiation at the correct time window (*i.e.* superradiant particles).

Nevertheless, if we increase the number of particles in the beam we also increase the number of superradiant particles, so the intensity of the peak should still grow quadratically with the number of particles, albeit with an additional scaling factor. This results in lower intensity Cherenkov peaks for the larger temperatures, but does not result in the complete vanishing of such peaks. In fact, even for the largest temperature, with results in a barely identifiable modulation, we still get a distinct intensity peak at the Cherenkov angle, a region where, in the standard Betatron spectrum, there was supposed to be almost no radiation emitted. Moreover, these particle beams are incredibly diluted, with only a few thousand particles, in a realistic scenario, particle beams have order of magnitude more particles, meaning that those superradiant peaks could be much more intense when compared to the on-axis radiation intensity.

4.5.4 Full self-consistent simulations

In all the simulations with radiation performed up to this point in Section 4.5, we assumed an ideal plasma channel with a smooth intensity profile by externally imposing a transverse focusing field $\mathbf{E}_f$ along the direction of x_2 given by Equation (4.52). This externally imposed electric field is meant to emulate the focusing field created by the charged particles that make up the ion channel.

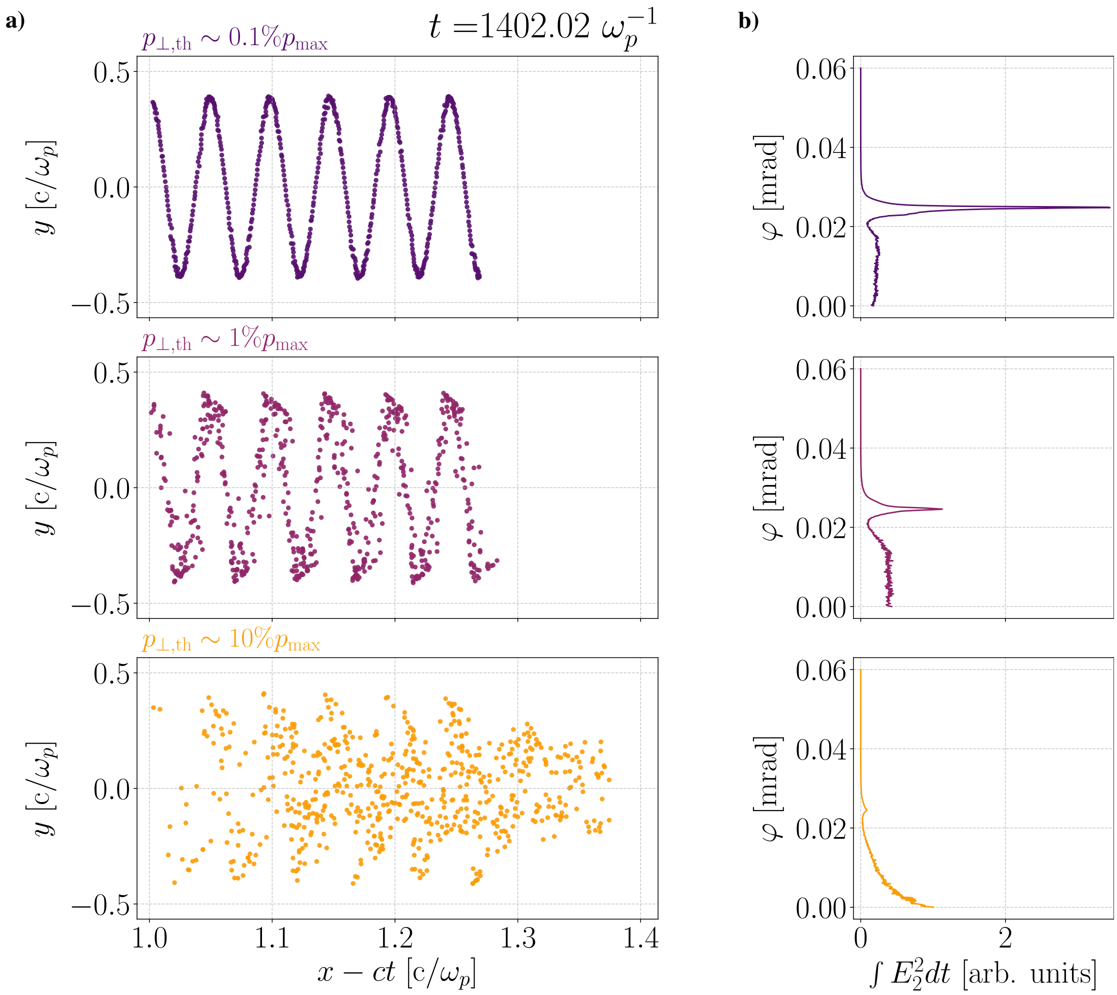

Figure 4.25: a) Snapshots of particle beams with increasing temperatures (from top to bottom) at increasing timesteps (from left to right). b) Angular distribution of the radiated intensity for the 3 particle beams.

In a realistic scenario, using the setup described in Section 4.3, this field would appear self-consistently as the electrons are expelled from the plasma column by the driver beam. In order to show, as self-consistently as possible, that this is a valid way of providing an ion channel suitable for resonantly modulating a particle beam such that it produces radiation in the superradiant regime, we ran simulations with the full set-up: a thin plasma column, a highly energetic particle driver beam, a Bessel laser beam, and a smaller, less energetic particle beam to be modulated in the ion channel and produce radiation. The parameters of the driver and witness beam used in the simulation are summarized in Table 4.1 below:

Parameter	**Driver**	**Witness**
γ	20000	150
u_{th} $[m_e \mathrm{c}]$	$3,3,3$	$0,0,0$
σ_x $[\mathrm{c}/\omega_p]$	3.4 (18 µm)	0.35 (1.9 µm)
σ_y $[\mathrm{c}/\omega_p]$	0.14 (0.80 µm)	0.014 (80 nm)
n $[n_p]$	32	0.02
$K_{\max}$	–	4

Table 4.1: Driver and Witness beam parameters.

The driver beam has the same energy as the SLAC FACET-II particle beam. The plasma density upramp is modelled with a gaussian density profile, starting at $x_1 = 20\ \mathrm{c}/\omega_p$, that grows smoothly until reaching a constant value at $x_1 = 500\ \mathrm{c}/\omega_p$. This profile is described in Eq. (4.63) below:

$$n(x) = \begin{cases} 0 & \text{if } x < 20 \\ n_p \exp\left(-\frac{(x_1-500)^2}{200^2}\right) & \text{if } 20 \leq x < 500 \\ n_p & \text{if } 500 \leq x \end{cases} \tag{4.63}$$

The laser has a normalized vector potential of $a_0 = 0.85$, a phase velocity of $v_\phi = 1.0014\ c$ (slightly exceeding the speed of light), and a laser frequency of $\omega_L = 43.1\ \omega_p$, where ω_p is the plasma frequency. For an 800 nm laser this would correspond to a plasma with frequency $\omega_p = 5 \times 10^{13}$ rad$/s$ and density $n_p = 9 \times 10^{17}$ cm^{-3}. The laser is a Bessel beam approximation whose intensity profile is modelled using two arctangent functions such that it emulates the behaviour of a real Bessel Beam and its intensity grows smoothly with the plasma density, it follows the expression given by Eq. (4.54) below with $x_i = 250\ \mathrm{c}/\omega_p$ (1.3 mm), $x_f = 500\ \mathrm{c}/\omega_p$ (2.7 mm) and $L = 50\ \mathrm{c}/\omega_p$ (0.27 mm). The transverse profile is obtained using a Taylor expansion of the expressions defined in Section 4.3.1 around $x_2 = 0$.

Figure 4.26 shows the spatiotemporal radiation profile obtained under these conditions. It is, in many ways, similar from the ones we saw previously, the only notable difference being the shift in the Cherenkov angle, due to the different parameters used for the laser and the witness particle beam. As we have noted previously, the major bottleneck in these self-consistent simulations is the scale difference between the laser (or modulation) wavelength and distance between the driver and the witness particle beam, therefore, in order to run these simulations we increased the modulation wavelength by about a factor of 3.

In this case, this led to a final K parameter of 4 for our particle beam and to a larger phase velocity, shifting the Cherenkov angle to $\varphi_{\mathrm{Ch}} = \arccos c/v_\phi = 53$ mrad. The reduced K parameter and energy of the witness beam made it easier to avoid non-linear effects that disturb the modulation causing instability in the phase velocity of the perturbations. This allows for a more stable distribution of the points of

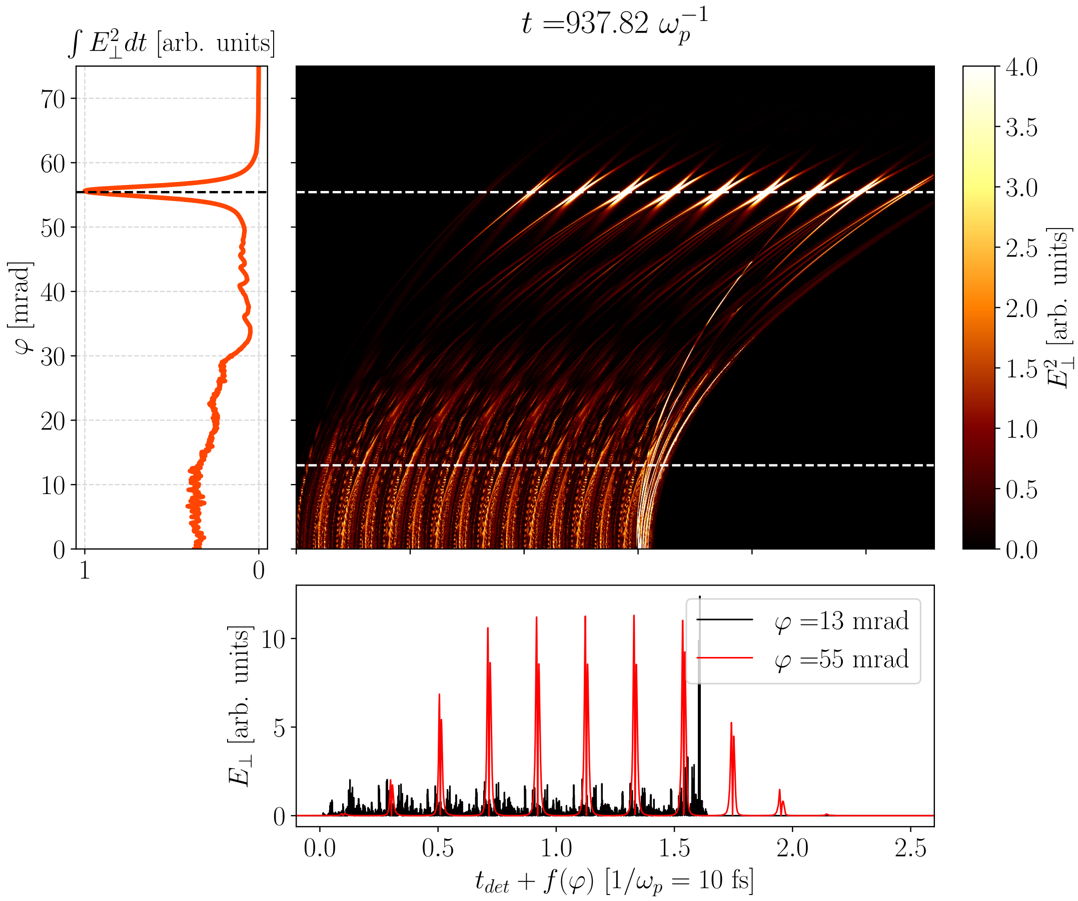

Figure 4.26: Spatiotemporal profile of the radiation obtained in a full self-consistent simulation. The left side panel shows the time integrated spatial profile with a sharp intensity peak at the Cherenkov angle. The bottom panel shows two temporal profiles od radiation taken at different angles (13 and 55 mrad). The temporal axis of these lineouts is shifted with a function $f(\varphi)$ that takes into account the delay at which radiation arrives at larger angles.

accumulation of radiation, leading to the appearance a clean Cherenkov peak in the angular intensity distribution. However, a smaller K parameter also leads to the emission of broader pulses of radiation at the Cherenkov angle. This means that it is easier for the pulses of every particle to converge in the same region, even when other non-idealities such as beam temperature or variable phase speed are present, but leads to an overall larger pulse. In conclusion, there is a trade-off between the robustness of the setup to non-idealities, and the shortness of the superradiant pulses.

4.6 Conclusions and Future Work

In this section, we investigated betatron radiation originating from plasma-accelerated electrons. We made a significant discovery: through the manipulation of the spatiotemporal characteristics of the accelerated particle bunch, we could induce superradiant emission. Our findings revealed that a particle beam featuring sinusoidal modulation with a superluminal phase speed could generate optical shocks along the Cherenkov angle associated with the modulation's phase speed. These optical shocks resulted in ultra-short attosecond-level pulses, with an intensity that scales quadratically with the number of particles in the beam, regardless of interparticle spacing. Additionally, we showed that the spectrum of radiation at the Cherenkov angle comprised numerous high harmonics of the modulation wavelength.

Our rigorous theoretical analysis and computer simulations led to the conclusion that this phenomenon persisted even in cases of non-ideal modulation, such as when the particle beam exhibited energy spread or temperature variations. Additionally, we demonstrated the feasibility of correctly modulating the particle beam through resonant coupling between betatron oscillations and the periodic force exerted by a co-propagating laser pulse with a superluminal phase speed. Our simulations revealed that this process was achievable in the wakeless regime of plasma wakefield acceleration, where a pure ion channel devoid of longitudinal acceleration was created by a high-energy driver particle beam.

5

Conclusions and Future Work

The main computational results of this thesis were obtaiend using the recently developed Radiation Diagnostic for OSIRIS. During the course of this doctoral program, we introduced several enhancements to this code.

In our quest to elevate RaDiO's reliability and stability, we invested effort into debugging and the integration of essential features. This initiative yielded improved code quality, significantly reducing unexpected errors and enhancing the user experience.

Substantial changes were made to the post-processing version of RaDiO to ensure better integration with the OSIRIS framework, which included the adoption of OSIRIS-style input decks and the standardization of file input/output procedures. Moreover, OpenPMD support was incorporated, allowing the code to read trajectory files from other PIC codes. These enhancements boosted the versatility and compatibility of the post-processing version of RaDiO, resulting in its rebranding as RaDi-x.

Furthermore, we integrated additional features into the run-time version, enhancing compatibility with other OSIRIS simulation modes and optimizing performance. Collaborating closely with the UCLA group, particularly with Kyle Miller, we optimized parallelization and introduced support for batch processing of particles on the CPU, leading to a substantial overall performance boost. To enhance the development experience, we prioritized the improvement of code readability to facilitate development, customization, and troubleshooting.

Additionally, we introduced the option to select a subset of radiative species for calculations and to model radiation from ionized particles during simulations, expanding the range of research possibilities. Notably, we empowered the code to model radiation from ionized particles during simulations, broadening the scope of research possibilities. Furthermore, we introduced support for RaDiO in quasi-3D simulations, offering users a new simulation mode for their radiation simulations.

One of the most significant advancements in RaDiO was the introduction of GPU compatibility. The GPU version of the code emerged as powerful tool, opening up new possibilities for exploring radiation emission within Particle in Cell (PIC) codes, especially when dealing with large spatial detectors. Utilizing a single GPU board, we achieve near-instantaneous radiation calculations across millions of spatial cells, a feat previously only achievable when using computer clusters housing hundreds of CPUs.

Throughout the course of the doctoral program, we focused in various aspects of plasma-based radiation sources, with a primary focus on the concept of generalized superradiance. Our explorations encompassed diverse sources where generalized superradiance could unlock the potential to generate ultra-intense short pulses of broadband radiation, with particular emphasis on high-frequency regions.

We started by investigating the previously unexplored domain of radiation generated by particles traversing evanescent fields, such as those existing at the boundary between a laser and an overdense target, a common occurrence in laser-plasma interaction experiments. The degree of spatial localization in the direction normal to the surface, determined by the material skin depth, could be more than an order of magnitude smaller than the wavelength of the exciting laser. In this context, we demonstrated that the interaction between a relativistic particle and these evanescent fields led to the emission of extremely short, broadband radiation pulses.

Our proposed scheme presented a highly promising mechanism for high-frequency radiation emission, featuring a distinct spectral signature conducive to experimental detection. The mechanism, which harnessed moderately relativistic electrons as the sole energy source for generating X-rays, opened up exciting avenues for further research. We exploited the extreme spatial localization of evanescent waves to produce directed X-rays and demonstrated, through theory and particle-in-cell (PIC) simulations in OSIRIS, complemented by the Radiation Diagnostic for OSIRIS (RaDiO), that electrons with $\gamma \simeq 10-100$ scattering across an evanescent wave could produce keV-MeV radiation.

Additionally, we identified that electron bunches with specific spatial distributions could generate a superradiant optical shock. While Bolotowsky and Ginzburg previously explored the creation of optical shocks by tilted electron bunches in transition radiation [61], our research showed that, due to the constructive interference of radiation from each bunch electron, the intensity scaled quadratically with number of bunch particles, akin to superradiance. Furthermore, we found that the intersection position between the electron bunch and the evanescent surface could function as a virtual superluminal particle, dictating critical radiation properties as if it were a single real particle.

Moreover, we investigated betatron radiation originating from plasma-accelerated electrons. Here, we made a significant discovery: through the manipulation of the spatiotemporal characteristics of the accelerated particle bunch, we could induce superradiant emission. Our findings revealed that a particle beam featuring sinusoidal modulation with a superluminal phase speed could generate optical shocks along the Cherenkov angle associated with the modulation's phase speed. These optical shocks resulted in ultra-short attosecond-level pulses, with intensity scaling quadratically with the number of particles in the beam, regardless of interparticle spacing. Additionallt we showed that the spectrum of radiation at the Cherenkov angle comprised numerous high harmonics of the modulation wavelength.

Our rigorous theoretical analysis and computer simulations led to the conclusion that this phenomenon persisted even in cases of non-ideal modulation, such as when the particle beam exhibited energy spread or temperature variations. Additionally, we demonstrated the feasibility of correctly modulating the particle beam through resonant coupling between betatron oscillations and the periodic force exerted by a co-propagating laser pulse with a superluminal phase speed. Our simulations revealed that this process was achievable in the wakeless regime of plasma wakefield acceleration, where a pure ion channel devoid of longitudinal acceleration was created by a high-energy driver particle beam.

Our results offered a promising avenue for enhancing betatron radiation, promising a substantial increase in radiated intensity and a potential elevation of this radiation source to a higher level.

Bibliography

[1]T. E. H. T. Collaboration, "First m87 event horizon telescope results. i. the shadow of the supermassive black hole," 2019.

[2]M. Ferray, A. L'Huillier, X. F. Li, L. A. Lompre, G. Mainfray, and C. Manus, "Multiple-harmonic conversion of 1064 nm radiation in rare gases," *Journal of Physics B: Atomic, Molecular and Optical Physics*, vol. 21, no. 3, p. L31, feb 1988. [Online]. Available: https://dx.doi.org/10.1088/0953-4075/21/3/001

[3]P. M. Paul, E. S. Toma, P. Breger, G. Mullot, F. Augé, P. Balcou, H. G. Muller, and P. Agostini, "Observation of a train of attosecond pulses from high harmonic generation," *Science*, vol. 292, no. 5522, pp. 1689–1692, 2001. [Online]. Available: https://www.science.org/doi/abs/10.1126/science.1059413

[4]S. W. Hell and J. Wichmann, "Breaking the diffraction resolution limit by stimulated emission: stimulated-emission-depletion fluorescence microscopy." *Optics letters*, vol. 19, no. 11, pp. 780–2, jun 1994. [Online]. Available: http://www.ncbi.nlm.nih.gov/pubmed/19844443

[5]J. M. Dawson, "Particle simulation of plasmas," *Reviews of Modern Physics*, vol. 55, no. 2, pp. 403–447, 1983.

[6]F. Tamburini, B. Thidé, G. Molina-Terriza, and G. Anzolin, "Twisting of light around rotating black holes (supplementary information)," *Nature Physics*, vol. 7, no. 3, pp. 195–197, feb 2011. [Online]. Available: http://www.nature.com/doifinder/10.1038/nphys1907

[7]F. Tamburini, B. Thidé, and M. Della Valle, "Measurement of the spin of the M87 black hole from its observed twisted light," *Monthly Notices of the Royal Astronomical Society: Letters*, vol. 492, no. 1, pp. L22–L27, 11 2019. [Online]. Available: https://doi.org/10.1093/mnrasl/slz176

[8]M. Ritsch-Marte, "Orbital angular momentum light in microscopy," *Philosophical Transactions of the Royal Society A: Mathematical, Physical and Engineering Sciences*, vol. 375, no. 2087, feb 2017.

[9]M. Pardal, "Modelling ultra-high frequency x-ray emission in particle in cell codes," Master's thesis, Instituto Superior Técnico, Lisboa, 2018.

[10]M. Pardal, A. Sainte-Marie, A. Reboul-Salze, R. A. Fonseca, and J. Vieira, "Radio: An efficient spatiotemporal radiation diagnostic for particle-in-cell codes," *Computer Physics Communications*, vol. 285, p. 108634, 4 2023.

[11]R. A. Fonseca, L. O. Silva, F. S. Tsung, V. K. Decyk, W. Lu, C. Ren, W. B. Mori, S. Deng, S. Lee, T. Katsouleas, and J. C. Adam, "OSIRIS: A Three-Dimensional, Fully Relativistic Particle in Cell Code for Modeling Plasma Based Accelerators," 2002, pp. 342–351.

[12]R. A. Fonseca, J. Vieira, F. Fiuza, A. Davidson, F. S. Tsung, W. B. Mori, and L. O. Silva, "Exploiting multi-scale parallelism for large scale numerical modelling of laser wakefield accelerators," *Plasma Physics and Controlled Fusion*, vol. 55, no. 12, p. 124011, nov 2013. [Online]. Available: https://doi.org/10.1088%2F0741-3335%2F55%2F12%2F124011

[13]D. A. Deacon, L. R. Elias, J. M. Madey, G. J. Ramian, H. A. Schwettman, and T. I. Smith, "First operation of a free-electron laser," *Physical Review Letters*, vol. 38, pp. 892–894, 4 1977. [Online]. Available: https://journals.aps.org/prl/abstract/10.1103/PhysRevLett.38.892

[14]F. R. Elder, A. M. Gurewitsch, R. V. Langmuir, and H. C. Pollock, "Radiation from electrons in a synchrotron," *Phys. Rev.*, vol. 71, pp. 829–830, Jun 1947. [Online]. Available: https://link.aps.org/doi/10.1103/PhysRev.71.829.5

[15]E. J. N. Wilson, "Fifty years of synchrotrons," *CERN Document Server*, 1996. [Online]. Available: https://cds.cern.ch/record/339572

[16]E. M. McMillan, "The synchrotron—a proposed high energy particle accelerator," *Physical Review*, vol. 68, p. 143, 9 1945. [Online]. Available: https://journals.aps.org/pr/abstract/10.1103/PhysRev.68.143

[17]T. Tajima and J. M. Dawson, "Laser electron accelerator," *Phys. Rev. Lett.*, vol. 43, pp. 267–270, Jul 1979. [Online]. Available: https://link.aps.org/doi/10.1103/PhysRevLett.43.267

[18]L. Cranberg, "The initiation of electrical breakdown in vacuum," *Journal of Applied Physics*, vol. 23, no. 5, pp. 518–522, 1952. [Online]. Available: https://doi.org/10.1063/1.1702243

[19]P. Chen, J. M. Dawson, R. W. Huff, and T. Katsouleas, "Acceleration of electrons by the interaction of a bunched electron beam with a plasma," *American Physical Society*, vol. 54, no. 7, pp. 693– 696, 1985.

[20]E. Esarey, B. A. Shadwick, P. Catravas, and W. P. Leemans, "Synchrotron radiation from electron beams in plasma-focusing channels," *Physical Review E*, vol. 65, p. 056505, 5 2002. [Online]. Available: https://journals.aps.org/pre/abstract/10.1103/PhysRevE.65.056505

[21]Y. Ma, D. Seipt, S. J. D. Dann, M. J. V. Streeter, C. A. J. Palmer, L. Willingale, and A. G. R. Thomas, "Angular streaking of betatron x-rays in a transverse density gradient laser-wakefield

accelerator," *Physics of Plasmas*, vol. 25, no. 11, p. 113105, 2018. [Online]. Available: https://doi.org/10.1063/1.5054807

[22]T. Tajima and J. M. Dawson, "Laser electron accelerator," *Physical Review Letters*, vol. 43, p. 267, 7 1979. [Online]. Available: https://journals.aps.org/prl/abstract/10.1103/PhysRevLett.43.267

[23]A. Rousse, K. T. Phuoc, R. Shah, A. Pukhov, E. Lefebvre, V. Malka, S. Kiselev, F. Burgy, J. P. Rousseau, D. Umstadter, and D. Hulin, "Production of a kev x-ray beam from synchrotron radiation in relativistic laser-plasma interaction," *Physical Review Letters*, vol. 93, p. 135005, 9 2004. [Online]. Available: https://journals.aps.org/prl/abstract/10.1103/PhysRevLett.93.135005

[24]D. Guénot, D. Gustas, A. Vernier, B. Beaurepaire, F. Böhle, M. Bocoum, M. Lozano, A. Jullien, R. Lopez-Martens, A. Lifschitz, and J. Faure, "Relativistic electron beams driven by khz single-cycle light pulses," *Nature Photonics 2017 11:5*, vol. 11, pp. 293–296, 4 2017. [Online]. Available: https://www.nature.com/articles/nphoton.2017.46

[25]B. Miao, J. E. Shrock, L. Feder, R. C. Hollinger, J. Morrison, R. Nedbailo, A. Picksley, H. Song, S. Wang, J. J. Rocca, and H. M. Milchberg, "Multi-gev electron bunches from an all-optical laser wakefield accelerator," *Physical Review X*, vol. 12, p. 031038, 7 2022. [Online]. Available: https://journals.aps.org/prx/abstract/10.1103/PhysRevX.12.031038

[26]A. J. Gonsalves, K. Nakamura, J. Daniels, C. Benedetti, C. Pieronek, T. C. deRaadt, S. Steinke, J. H. Bin, S. S. Bulanov, J. vanTilborg, C. G. Geddes, C. B. Schroeder, C. Toth, E. Esarey, K. Swanson, L. Fan-Chiang, G. Bagdasarov, N. Bobrova, V. Gasilov, G. Korn, P. Sasorov, and W. P. Leemans, "Petawatt laser guiding and electron beam acceleration to 8 gev in a laser-heated capillary discharge waveguide," *Physical Review Letters*, vol. 122, p. 084801, 2 2019. [Online]. Available: https://journals.aps.org/prl/abstract/10.1103/PhysRevLett.122.084801

[27]S. Kneip, C. McGuffey, J. L. Martins, S. F. Martins, C. Bellei, V. Chvykov, F. Dollar, R. Fonseca, C. Huntington, G. Kalintchenko, A. Maksimchuk, S. P. Mangles, T. Matsuoka, S. R. Nagel, C. A. Palmer, J. Schreiber, K. T. Phuoc, A. G. Thomas, V. Yanovsky, L. O. Silva, K. Krushelnick, and Z. Najmudin, "Bright spatially coherent synchrotron X-rays from a table-top source," *Nature Physics*, vol. 6, no. 12, pp. 980–983, 2010.

[28]J. M. Cole, J. C. Wood, N. C. Lopes, K. Poder, R. L. Abel, S. Alatabi, J. S. Bryant, A. Jin, S. Kneip, K. Mecseki, D. R. Symes, S. P. Mangles, and Z. Najmudin, "Laser-wakefield accelerators as hard x-ray sources for 3d medical imaging of human bone," *Scientific Reports 2015 5:1*, vol. 5, pp. 1–7, 8 2015. [Online]. Available: https://www.nature.com/articles/srep13244

[29]S. G. Rykovanov, C. B. Schroeder, E. Esarey, C. G. R. Geddes, and W. P. Leemans, "Plasma undulator based on laser excitation of wakefields in a plasma channel," *Phys. Rev. Lett.*, vol. 114, p. 145003, Apr 2015. [Online]. Available: https://link.aps.org/doi/10.1103/PhysRevLett.114.145003

[30]J. Vieira and J. T. Mendonça, "Nonlinear laser driven donut wakefields for positron and electron acceleration," *Phys. Rev. Lett.*, vol. 112, p. 215001, May 2014. [Online]. Available: https://link.aps.org/doi/10.1103/PhysRevLett.112.215001

[31]J. T. Mendonça and J. Vieira, "Donut wakefields generated by intense laser pulses with orbital angular momentum," *Physics of Plasmas*, vol. 21, no. 3, p. 033107, 2014. [Online]. Available: https://doi.org/10.1063/1.4868967

[32]J. Vieira, J. T. Mendonça, and F. Quéré, "Optical control of the topology of laser-plasma accelerators," *Phys. Rev. Lett.*, vol. 121, p. 054801, Jul 2018. [Online]. Available: https://link.aps.org/doi/10.1103/PhysRevLett.121.054801

[33]J. C. Wood, D. J. Chapman, K. Poder, N. C. Lopes, M. E. Rutherford, T. G. White, F. Albert, K. T. Behm, N. Booth, J. S. Bryant, P. S. Foster, S. Glenzer, E. Hill, K. Krushelnick, Z. Najmudin, B. B. Pollock, S. Rose, W. Schumaker, R. H. Scott, M. Sherlock, A. G. Thomas, Z. Zhao, D. E. Eakins, and S. P. Mangles, "Ultrafast imaging of laser driven shock waves using betatron x-rays from a laser wakefield accelerator," *Scientific Reports 2018 8:1*, vol. 8, pp. 1–10, 7 2018. [Online]. Available: https://www.nature.com/articles/s41598-018-29347-0

[34]S. Kiselev, A. Pukhov, and I. Kostyukov, "X-ray generation in strongly nonlinear plasma waves," *Physical Review Letters*, vol. 93, p. 135004, 9 2004. [Online]. Available: https://journals.aps.org/prl/abstract/10.1103/PhysRevLett.93.135004

[35]D. H. Whittum, A. M. Sessler, and J. M. Dawson, "Ion-channel laser," *Phys. Rev. Lett.*, vol. 64, pp. 2511–2514, May 1990. [Online]. Available: https://link.aps.org/doi/10.1103/PhysRevLett.64.2511

[36]X. Davoine, F. Fiuza, R. A. Fonseca, W. B. Mori, and L. O. Silva, "Ion-channel laser growth rate and beam quality requirements," *Journal of Plasma Physics*, vol. 84, no. 03, p. 905840304, Jun. 2018.

[37]K.-R. Chen, T. C. Katsouleas, and J. M. Dawson, "On the amplification mechanism of the ion-channel laser," *IEEE Transactions on Plasma Science*, vol. 18, no. 5, 1990.

[38]K. R. Chen, J. M. Dawson, A. T. Lin, and T. Katsouleas, "Unified theory and comparative study of cyclotron masers, ion-channel lasers, and free electron lasers," *Physics of Fluids B: Plasma Physics*, vol. 3, no. 5, pp. 1270–1278, May 1991.

[39]I. Kostyukov, S. Kiselev, and A. Pukhov, "X-ray generation in an ion channel," *Physics of Plasmas*, vol. 10, no. 12, pp. 4818–4828, Dec. 2003.

[40]C. S. Liu, V. K. Tripathi, and N. Kumar, "Vlasov formalism of the laser-driven ion channel x-ray laser," *Plasma Physics and Controlled Fusion*, vol. 49, no. 3, pp. 325–333, Mar. 2007.

[41]B. Ersfeld, R. Bonifacio, S. Chen, M. R. Islam, and D. A. Jaroszynski, "Practical considerations for the ion channel free-electron laser," in *Proceedings of SPIE*, vol. 9509, May 2015, p. 95090L.

[42]R. Lichters, J. M. ter Vehn, and A. Pukhov, “Short-pulse laser harmonics from oscillating plasma surfaces driven at relativistic intensity,” *Physics of Plasmas*, vol. 3, p. 3425, 9 1998. [Online]. Available: https://aip.scitation.org/doi/abs/10.1063/1.871619

[43]C. Thaury, H. George, F. Quéré, R. Loch, J.-P. Geindre, P. Monot, and P. Martin, “Coherent dynamics of plasma mirrors,” *Nature Physics*, vol. 4, no. 8, pp. 631–634, Aug 2008. [Online]. Available: https://doi.org/10.1038/nphys986

[44]A. Borot, A. Malvache, X. Chen, D. Douillet, G. Iaquianiello, T. Lefrou, P. Audebert, J.-P. Geindre, G. Mourou, F. Quéré, and R. Lopez-Martens, “High-harmonic generation from plasma mirrors at kilohertz repetition rate,” *Optics Letters*, vol. 36, p. 1461, 4 2011. [Online]. Available: https://www.researchgate.net/publication/51057230_High-harmonic_generation_from_plasma_mirrors_at_kilohertz_repetition_rate

[45]H. Vincenti and F. Quéré, “Attosecond lighthouses: How to use spatiotemporally coupled light fields to generate isolated attosecond pulses,” *Phys. Rev. Lett.*, vol. 108, p. 113904, Mar 2012. [Online]. Available: https://link.aps.org/doi/10.1103/PhysRevLett.108.113904

[46]H. Vincenti, S. Monchocé, S. Kahaly, G. Bonnaud, P. Martin, and F. Quéré, “Optical properties of relativistic plasma mirrors,” *Nature Communications*, vol. 5, no. 1, p. 3403, 2014. [Online]. Available: https://doi.org/10.1038/ncomms4403

[47]K. TaPhuoc, A. Rousse, M. Pittman, J. P. Rousseau, V. Malka, S. Fritzler, D. Umstadter, and D. Hulin, “X-ray radiation from nonlinear thomson scattering of an intense femtosecond laser on relativistic electrons in a helium plasma,” *Physical Review Letters*, vol. 91, p. 195001, 11 2003. [Online]. Available: https://journals.aps.org/prl/abstract/10.1103/PhysRevLett.91.195001

[48]Vachaspati, “Harmonics in the scattering of light by free electrons,” *Physical Review*, vol. 128, p. 664, 10 1962. [Online]. Available: https://journals.aps.org/pr/abstract/10.1103/PhysRev.128.664

[49]S. Y. Chen, A. Maksimchuk, and D. Umstadter, “Experimental observation of relativistic nonlinear thomson scattering,” *Nature 1998 396:6712*, vol. 396, pp. 653–655, 12 1998. [Online]. Available: https://www.nature.com/articles/25303

[50]V. L. Ginzburg and I. M. Frank, “Radiation of a uniformly moving electron due to its transition from one medium into another,” *J. Phys. (USSR)*, vol. 9, pp. 353–362, 1945.

[51]P. Goldsmith and J. V. Jelley, “Optical transition radiation from protons entering metal surfaces,” *The Philosophical Magazine: A Journal of Theoretical Experimental and Applied Physics*, vol. 4, no. 43, pp. 836–844, 1959. [Online]. Available: https://doi.org/10.1080/14786435908238241

[52]C. Couillaud, “Production of x-ray transition radiation with relativistic electrons propagating at grazing incidence,” *Nuclear Instruments and Methods in Physics Research Section A: Accelerators, Spectrometers, Detectors and Associated Equipment*, vol. 495, pp. 171–190, 12 2002.

[53]V. L. Ginzburg and V. N. Tsytovich, “Several problems of the theory of transition radiation and transition scattering,” *Physics Reports*, vol. 49, pp. 1–89, 1979.

[54]J. L. Martins, S. F. Martins, R. A. Fonseca, and L. O. Silva, “Radiation post-processing in PIC codes,” in *Harnessing Relativistic Plasma Waves as Novel Radiation Sources from Terahertz to X-Rays and Beyond*, vol. 7359. SPIE, apr 2009, p. 73590V.

[55]H. Burau, R. Widera, W. Hönig, G. Juckeland, A. Debus, T. Kluge, U. Schramm, T. E. Cowan, R. Sauerbrey, and M. Bussmann, “PIConGPU: A fully relativistic particle-in-cell code for a GPU cluster,” *IEEE Transactions on Plasma Science*, vol. 38, no. 10 PART 2, pp. 2831–2839, oct 2010.

[56]R. Pausch, H. Burau, M. Bussmann, J. Couperus, T. E. Cowan, A. Debus, A. Huebl, A. Irman, A. Köhler, U. Schramm, K. Steiniger, and R. Widera, “Computing angularly-resolved far field emission spectra in particle-in-cell codes using GPUs,” in *Proceeding of IPAC2014*, vol. MOPRI069, 2014, pp. 761–764. [Online]. Available: http://accelconf.web.cern.ch/AccelConf/IPAC2014/papers/mopri069.pdf

[57]R. Pausch, A. Debus, R. Widera, K. Steiniger, A. Huebl, H. Burau, M. Bussmann, and U. Schramm, “How to test and verify radiation diagnostics simulations within particle-in-cell frameworks,” *Nuclear Instruments and Methods in Physics Research, Section A: Accelerators, Spectrometers, Detectors and Associated Equipment*, vol. 740, pp. 250–256, mar 2014.

[58]T. Grismayer, M. Vranic, J. L. Martins, R. A. Fonseca, and L. O. Silva, “Seeded QED cascades in counterpropagating laser pulses,” *Physical Review E*, vol. 95, no. 2, feb 2017.

[59]“Top500 Supercomputer Sites,” www.top500.org, accessed: 2018-10-14.

[60]R. A. Fonseca, J. Vieira, F. Fiuza, A. Davidson, F. S. Tsung, W. B. Mori, and L. O. Silva, “Exploiting multi-scale parallelism for large scale numerical modelling of laser wakefield accelerators,” *Plasma Physics and Controlled Fusion*, vol. 55, p. 124011, 11 2013. [Online]. Available: https://iopscience.iop.org/article/10.1088/0741-3335/55/12/124011https://iopscience.iop.org/article/10.1088/0741-3335/55/12/124011/meta

[61]B. M. Bolotovskiĭ and V. L. Ginzburg, “The vavilov-cerenkov effect and the doppler effect in the motion of sources with superluminal velocity in vacuum,” *Soviet Physics - Uspekhi*, vol. 15, pp. 184–192, 2 1972. [Online]. Available: https://iopscience.iop.org/article/10.1070/PU1972v015n02ABEH004962https://iopscience.iop.org/article/10.1070/PU1972v015n02ABEH004962/meta

[62]J. L. Martins, M. Vranic, T. Grismayer, J. Vieira, R. A. Fonseca, and L. O. Silva, “Modelling radiation emission in the transition from the classical to the quantum regime,” *Plasma Physics and Controlled Fusion*, vol. 58, no. 1, p. 014035, nov 2015. [Online]. Available: https://doi.org/10.1088/0741-3335/58/1/014035

[63]J. Vieira, M. Pardal, J. T. Mendonça, and R. A. Fonseca, "Generalized superradiance for producing broadband coherent radiation with transversely modulated arbitrarily diluted bunches," *Nature Physics*, vol. 17, no. 1, pp. 99–104, Jan 2021. [Online]. Available: https://doi.org/10.1038/s41567-020-0995-5

[64]J. D. Jackson, *Classical Electrodynamics*, 3rd ed. Wiley, 1999, ch. 14.

[65]R. Y. Tsien, "Pictures of dynamic electric fields," *American Journal of Physics*, vol. 40, no. 1, pp. 46–56, 1972. [Online]. Available: https://doi.org/10.1119/1.1986445

[66]S. Kiselev, A. Pukhov, and I. Kostyukov, "X-ray generation in strongly nonlinear plasma waves," *Phys. Rev. Lett.*, vol. 93, p. 135004, Sep 2004. [Online]. Available: https://link.aps.org/doi/10.1103/PhysRevLett.93.135004

[67]A. G. R. Thomas, "Algorithm for calculating spectral intensity due to charged particles in arbitrary motion," *Phys. Rev. ST Accel. Beams*, vol. 13, p. 020702, Feb 2010. [Online]. Available: https://link.aps.org/doi/10.1103/PhysRevSTAB.13.020702

[68]R. Pausch, A. Debus, A. Huebl, U. Schramm, K. Steiniger, R. Widera, and M. Bussmann, "Quantitatively consistent computation of coherent and incoherent radiation in particle-in-cell codes—A general form factor formalism for macro-particles," *Nuclear Instruments and Methods in Physics Research, Section A: Accelerators, Spectrometers, Detectors and Associated Equipment*, vol. 909, pp. 419–422, nov 2018.

[69]A. Borot, A. Malvache, X. Chen, D. Douillet, G. Iaquianiello, T. Lefrou, P. Audebert, J.-P. Geindre, F. Quere, and R. Lopez-Martens, "High-harmonic generation from plasma mirrors at kilohertz repetition rate," *Optics letters*, vol. 36, pp. 1461–3, 04 2011.

[70]R. Lichters, J. Meyer-ter-Vehn, and A. Pukhov, "Short-pulse laser harmonics from oscillating plasma surfaces driven at relativistic intensity," *Physics of Plasmas*, vol. 3, p. 3425, 09 1996.

[71]A. Huebl, R. Lehe, J.-L. Vay, D. P. Grote, I. F. Sbalzarini, S. Kuschel, and M. Bussmann, "Open science with openpmd," Jul. 2017. [Online]. Available: https://doi.org/10.5281/zenodo.822396

[72]A. Davidson, A. Tableman, W. An, F. Tsung, W. Lu, J. Vieira, R. Fonseca, L. Silva, and W. Mori, "Implementation of a hybrid particle code with a pic description in $r-z$ and a gridless description in φ into osiris," *Journal of Computational Physics*, vol. 281, pp. 1063–1077, 2015. [Online]. Available: https://www.sciencedirect.com/science/article/pii/S0021999114007529

[73]F. Li, V. K. Decyk, K. G. Miller, A. Tableman, F. S. Tsung, M. Vranic, R. A. Fonseca, and W. B. Mori, "Accurately simulating nine-dimensional phase space of relativistic particles in strong fields," *Journal of Computational Physics*, vol. 438, p. 110367, 2021. [Online]. Available: https://www.sciencedirect.com/science/article/pii/S002199912100262X

[74]G. Gariepy, J. Leach, K. T. Kim, T. J. Hammond, E. Frumker, R. W. Boyd, and P. B. Corkum, "Creating high-harmonic beams with controlled orbital angular momentum," *Physical Review Letters*, vol. 113, no. 15, oct 2014.

[75]W. Roentgen, "On a new kind of rays," *Nature*, vol. 53, no. 1369, pp. 274–276, Jan 1896. [Online]. Available: https://doi.org/10.1038/053274b0

[76]P. G. O'Shea and H. P. Freund, "Free-electron lasers: Status and applications," *Science*, vol. 292, pp. 1853–1858, 6 2001. [Online]. Available: https://www.science.org/doi/10.1126/science.1055718

[77]C. Jacobsen and J. Kirz, "X-ray microscopy with synchrotron radiation," *Nature Structural Biology*, vol. 5, no. 8, pp. 650–653, Aug 1998. [Online]. Available: https://doi.org/10.1038/1341

[78]E. Esarey, S. K. Ride, and P. Sprangle, "Nonlinear thomson scattering of intense laser pulses from beams and plasmas," *Physical Review E*, vol. 48, p. 3003, 10 1993. [Online]. Available: https://journals.aps.org/pre/abstract/10.1103/PhysRevE.48.3003

[79]P. Catravas, E. Esarey, and W. P. Leemans, "Femtosecond x-rays from thomson scattering using laser wakefield accelerators," *Measurement Science and Technology*, vol. 12, no. 11, p. 1828, oct 2001. [Online]. Available: https://dx.doi.org/10.1088/0957-0233/12/11/310

[80]B. Barwick, D. J. Flannigan, and A. H. Zewail, "Photon-induced near-field electron microscopy," *Nature 2009 462:7275*, vol. 462, pp. 902–906, 12 2009. [Online]. Available: https://www.nature.com/articles/nature08662

[81]J. B. Pendry, "Negative refraction makes a perfect lens," *Physical Review Letters*, vol. 85, p. 3966, 10 2000. [Online]. Available: https://journals.aps.org/prl/abstract/10.1103/PhysRevLett.85.3966

[82]L. J. Wong, I. Kaminer, O. Ilic, J. D. Joannopoulos, and M. Soljačić, "Towards graphene plasmon-based free-electron infrared to x-ray sources," *Nature Photonics 2015 10:1*, vol. 10, pp. 46–52, 11 2015. [Online]. Available: https://www.nature.com/articles/nphoton.2015.223

[83]C. Ziener, P. S. Foster, E. J. Divall, C. J. Hooker, M. H. Hutchinson, A. J. Langley, and D. Neely, "Specular reflectivity of plasma mirrors as a function of intensity, pulse duration, and angle of incidence," *Journal of Applied Physics*, vol. 93, p. 768, 12 2002. [Online]. Available: https://aip.scitation.org/doi/abs/10.1063/1.1525062

[84]B. Malaca, M. Pardal, D. Ramsey, J. R. Pierce, K. Weichman, I. A. Andriyash, W. B. Mori, J. P. Palastro, R. A. Fonseca, and J. Vieira, "Coherence and superradiance from a plasma-based quasiparticle accelerator," *Nature Photonics*, Oct 2023. [Online]. Available: https://doi.org/10.1038/s41566-023-01311-z

[85]A. Liènard, *Champ électrique et magnétique produit par une charge électrique concentrée en un point et animée d'un mouvement quelconque*. G. Carré et C. Naud, 1898.

[86]E. Wiechert, “Elektrodynamische elementargesetze,” *Annalen der Physik*, vol. 309, no. 4, pp. 667–689, 1901.

[87]A. Macchi, “Surface plasmons in superintense laser-solid interactions,” *Physics of Plasmas*, vol. 25, no. 3, p. 031906, 03 2018. [Online]. Available: https://doi.org/10.1063/1.5013321

[88]S. Maier, *Plasmonics : fundamentals and applications*. New York: Springer, 2007.

[89]P. A. Čerenkov, “Visible radiation produced by electrons moving in a medium with velocities exceeding that of light,” *Phys. Rev.*, vol. 52, pp. 378–379, Aug 1937. [Online]. Available: https://link.aps.org/doi/10.1103/PhysRev.52.378

[90]D. Woodbury, L. Feder, V. Shumakova, C. Gollner, R. Schwartz, B. Miao, F. Salehi, A. Korolov, A. Pugžlys, A. Baltuška, and H. M. Milchberg, “Laser wakefield acceleration with mid-ir laser pulses,” *Optics Letters*, vol. 43, p. 1131, 3 2018. [Online]. Available: https://www.researchgate.net/publication/322537398_Laser_wakefield_acceleration_with_mid-IR_laser_pulses

[91]Z. Huang and K.-J. Kim, “Formulas for coherent synchrotron radiation microbunching in a bunch compressor chicane,” *Phys. Rev. ST Accel. Beams*, vol. 5, p. 074401, Jul 2002. [Online]. Available: https://link.aps.org/doi/10.1103/PhysRevSTAB.5.074401

[92]C. Pellegrini, A. Marinelli, and S. Reiche, “The physics of x-ray free-electron lasers,” *Rev. Mod. Phys.*, vol. 88, p. 015006, Mar 2016. [Online]. Available: https://link.aps.org/doi/10.1103/RevModPhys.88.015006

[93]R. H. Dicke, “Coherence in spontaneous radiation processes,” *Phys. Rev.*, vol. 93, pp. 99–110, Jan 1954. [Online]. Available: https://link.aps.org/doi/10.1103/PhysRev.93.99

[94]A. Gover, “Superradiant and stimulated-superradiant emission in prebunched electron-beam radiators. i. formulation,” *Phys. Rev. ST Accel. Beams*, vol. 8, p. 030701, Mar 2005. [Online]. Available: https://link.aps.org/doi/10.1103/PhysRevSTAB.8.030701

[95]A. Gover, R. Ianconescu, A. Friedman, C. Emma, N. Sudar, P. Musumeci, and C. Pellegrini, “Superradiant and stimulated-superradiant emission of bunched electron beams,” *Rev. Mod. Phys.*, vol. 91, p. 035003, Aug 2019. [Online]. Available: https://link.aps.org/doi/10.1103/RevModPhys.91.035003

[96]A. Pukhov, Z.-M. Sheng, and J. Meyer-ter Vehn, “Particle acceleration in relativistic laser channels,” *Physics of Plasmas*, vol. 6, no. 7, pp. 2847–2854, 07 1999. [Online]. Available: https://doi.org/10.1063/1.873242

[97]J. Durnin, J. J. Miceli, and J. H. Eberly, “Diffraction-free beams,” *Phys. Rev. Lett.*, vol. 58, pp. 1499–1501, Apr 1987. [Online]. Available: https://link.aps.org/doi/10.1103/PhysRevLett.58.1499

[98]J. Durnin, "Exact solutions for nondiffracting beams. i. the scalar theory," *J. Opt. Soc. Am. A*, vol. 4, no. 4, pp. 651–654, Apr 1987. [Online]. Available: https://opg.optica.org/josaa/abstract.cfm?URI=josaa-4-4-651

[99]M. Lapointe, "Review of non-diffracting bessel beam experiments," *Optics and Laser Technology*, vol. 24, no. 6, pp. 315–321, 1992. [Online]. Available: https://www.sciencedirect.com/science/article/pii/003039929290082D

[100]A. J. Cox and D. C. Dibble, "Nondiffracting beam from a spatially filtered fabry–perot resonator," *J. Opt. Soc. Am. A*, vol. 9, no. 2, pp. 282–286, Feb 1992. [Online]. Available: https://opg.optica.org/josaa/abstract.cfm?URI=josaa-9-2-282

[101]J. H. McLeod, "The axicon: A new type of optical element," *J. Opt. Soc. Am.*, vol. 44, no. 8, pp. 592–597, Aug 1954. [Online]. Available: https://opg.optica.org/abstract.cfm?URI=josa-44-8-592

[102]J. Arlt and K. Dholakia, "Generation of high-order bessel beams by use of an axicon," *Optics Communications*, vol. 177, no. 1-6, pp. 297–301, Apr. 2000.

[103]J. Arlt, V. Garces-Chavez, W. Sibbett, and K. Dholakia, "Optical micromanipulation using a bessel light beam," *Optics Communications*, vol. 197, no. 4, pp. 239–245, 2001. [Online]. Available: https://www.sciencedirect.com/science/article/pii/S0030401801014791

[104]"Ax1220-c axicon," https://www.thorlabs.com/thorproduct.cfm?partnumber=AX1220-C, accessed on 2023-11-21.

[105]C. Lyu, M. R. Belic, Y. Li, and Y. Zhang, "Generation of diffraction-free bessel beams based on combined axicons," *Optics and Laser Technology*, vol. 164, p. 109548, 2023. [Online]. Available: https://www.sciencedirect.com/science/article/pii/S0030399223004413

[106]W. Lu, C. Huang, M. Zhou, M. Tzoufras, F. S. Tsung, W. B. Mori, and T. Katsouleas, "A nonlinear theory for multidimensional relativistic plasma wave wakefields," *Physics of Plasmas*, vol. 13, no. 5, p. 056709, 05 2006. [Online]. Available: https://doi.org/10.1063/1.2203364

[107]M. Litos, R. Ariniello, C. Doss, K. Hunt-Stone, and J. R. Cary, "Experimental opportunities for the ion channel laser," in *2018 IEEE Advanced Accelerator Concepts Workshop (AAC)*. IEEE, 8 2018, pp. 1–5.

[108]B. Miao, L. Feder, J. E. Shrock, A. Goffin, and H. M. Milchberg, "Optical guiding in meter-scale plasma waveguides," *Phys. Rev. Lett.*, vol. 125, p. 074801, Aug 2020. [Online]. Available: https://link.aps.org/doi/10.1103/PhysRevLett.125.074801